Master's thesis

NTNU
Norwegian University of Science and Technology
Faculty of Engineering
Department of Marine Technology

Stian Røine Brurås

A Survivability Analysis of Two Floating Offshore Wind Turbines in Intact and Damaged Conditions

Master's thesis in Marine Technology
Supervisor: Marilena Greco
Co-supervisor: Mohd Atif Siddiqui
June 2023

NTNU
Norwegian University of
Science and Technology

Stian Røine Brurås

A Survivability Analysis of Two Floating Offshore Wind Turbines in Intact and Damaged Conditions

Master's thesis in Marine Technology
Supervisor: Marilena Greco
Co-supervisor: Mohd Atif Siddiqui
June 2023

Norwegian University of Science and Technology
Faculty of Engineering
Department of Marine Technology

NTNU
Norwegian University of
Science and Technology

NTNU Trondheim
Norwegian University of Science and Technology
Faculty of Engineering Science and Technology
Department of MarineTechnology

MASTER THESIS IN MARINE TECHNOLOGY

Spring 2023

FOR

Stian Røine Brurås

A Survivability Analysis of Two Floating Offshore Wind Turbines in Intact and Damaged Conditions

(En overlevelsesanalyse av to flytende offshore vindturbiner i intakt- og skadetilstander)

Floating Offshore Wind Turbines (FOWTs) represent a young, growing industry with majority of the work focused on development, installation, and improving efficiency. Innovation in floating structures, turbine sizes and mooring designs has also been a major area of interest. As the number of floating units and size increase, chances of accidental events and safety become an important issue.

The present study aims to investigate the survivability of two FOWTs, with semisubmersible floaters, in damaged conditions. In the project thesis, the candidate examined the state-of-the art, including classification rules, identified the field site (Trollvind field) and relevant metocean data for the studies. He performed preliminary analyses on the INO-WINDMOOR 12MW. The available intact model was modified to simulate a ballast-filled compartment. Frequency-domain study was performed in HydroD and the time-domain model consisting of the substructure, tower, and rotor-nacelle assembly was created in OrcaFlex. Numerical convergence and comparison with reference results were examined. The compartment model with tank dynamics was checked against quasi-static ballast and rigid-mass models.

Objective

The master thesis has the overall target to provide insights on the influence of semi-submersible design features on survivability of a FOWT in intact and damaged conditions. Two floater designs will be selected, and proper scaling strategy will be targeted so that the floaters can operate with the same wind turbine.

The work should be carried out in steps as follows; some include part of the work done in the project thesis so to make the MSc thesis a stand-alone document:

1. Provide the background motivation and state-of-the-art relevant for this topic in terms of available studies, existing rules/guidelines for damage scenarios, available prediction tools for studying the behaviour at sea of FOWTs with emphasis on the tool chosen for this analysis. Provide the information on the selected site and on the available metocean data. Base this on the material collected in the project work and complement it when needed.
2. Select the two semi-submersibles and perform proper scaling, if needed, so that they can operate with the same wind turbine; at least for one of the intact floaters reference results should be available for assessment purposes. Based on the selected concepts and operative site, make the needed changes to the mooring-line system. Based on step 1, select the survival scenarios to be investigated, for both storm conditions, abnormal events and damaged conditions. At least one of them should relate to a flooding

scenario, for which both FOWTs can achieve a stable condition in calm water. Select the environmental conditions for the statistical analysis to assess behaviour and survivability based on available standards and recommended practices.

3. Perform the frequency-domain analysis of the floaters in intact and damaged conditions. Check numerical convergence and accuracy through comparison against available intact-floater results. Include a study of internal fluid effects in both intact and damaged conditions. Discuss comparatively the results (e.g., RAOs) for the floaters in intact and damaged conditions.
4. Check the natural periods and other relevant parameters for the FOWT models and perform the time-domain analysis of the FOWTs in damaged conditions. If time permits, assess the mechanisms at the damage opening in a simplified manner. Examine extreme wave conditions assuming parked turbine and assessing effects of second-order wave loads and of wind loads (e.g., on floater motions, mooring-line tensions, etc.).
5. If time allows, for a selected environmental scenario and one floater, compare the instantaneous damage-opening position with the local incident-wave elevation to detect possible water transient phenomena, as error sources in the analysis in step 4.
6. Draw the conclusions from the studies and discuss possible further research steps.

The work may show to be more extensive than anticipated. Some topics may therefore be left out after discussion with the supervisor without any negative influence on the grading.

The candidate should in their report give a personal contribution to the solution of the problem formulated in this text. All assumptions and conclusions must be supported by mathematical models and/or references to physical effects in a logical manner.
The candidate should apply all available sources to find relevant literature and information on the actual problem.
The thesis should be organised in a rational manner to give a clear presentation of the work in terms of exposition of results, assessments, and conclusions. It is important that the text is well written, and that tables and figures are used to support the verbal presentation. The thesis should be complete, but still as short as possible. In particular, the text should be brief and to the point, with a clear language. Telegraphic language should be avoided.
The thesis must contain the following elements: the text defining the scope (i.e. this text), preface (outlining project-work steps and acknowledgements), abstract (providing the summary), table of contents, main body of thesis, conclusions with recommendations for further work, list of symbols and acronyms, references and (optional) appendices. All figures, tables and equations shall be numerated.
The supervisor may require that the candidates, in an early stage of the work, present a written plan for the completion of the work. The plan should include budget for the use of computer and laboratory resources that will be charged to the department. Overruns shall be reported to the supervisor.
From the thesis it should be possible to identify the work carried out by the candidate and what has been found in the available literature. It is important to give references to the original source for theories and experimental results.

Supervisor : Marilena Greco
Co-supervisor : Mohd Atif Siddiqui

Submitted : January 15th 2023
Deadline : June 19th 2023

Marilena Greco
Supervisor

Preface

This thesis marks the end of a five-year master's program in Marine Technology at the Department of Marine Technology, NTNU, with a specialization in marine hydrodynamics. The thesis was written in the spring of 2023.

The thesis has been challenging both theoretically and in terms of computational cost. Topics like fully coupled aero-hydro-servo-elastic time domain simulation and resonant sloshing behavior lie on the border and beyond the curriculum of the five-year master's program. Numerous extensive computations, including tens of complete second-order frequency domain computations and thousands of extensive time-domain simulations, have resulted in months of pure simulation time.

It has been rewarding to see technically challenging topics such as statistical environmental models, optimization problems, finite element modeling, intricate programming scripts, hydrodynamic calculations, and design considerations come together. These components have formed a series of coupled time-domain models whose results can be understood and described based on the knowledge obtained throughout the master's program.

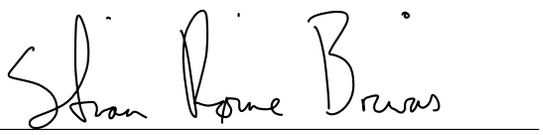

Stian Røine Brurås,

Trondheim, 19th June 2023

Acknowledgment

I express my sincere gratitude to my supervisor, Professor Marilena Greco, for her support and investment in my thesis. From our first meeting through both the preliminary studies and the thesis work, her enthusiasm and commitment have been truly motivating.

I also extend my thanks to my co-supervisor, Dr. Mohd Atif Siddiqui, for his invaluable guidance. His expertise in the topic and availability, even during evenings and weekends, have been greatly appreciated.

Thanks to Ph.D. Candidate Serag-Eldin Abdelmoteleb for providing help with upscaling and taking time to answer any questions related to his work.

Lastly, I want to thank DNV and Orcina. All software with full capabilities has been provided free of charge, and the support teams have shown incredible helpfulness. All questions have been answered rapidly, with astounding technical details and added examples.

Thank you!

Abstract

Wind energy is identified as part of the solution to provide sufficient sustainable, safe, and secure renewable energy. As there are limited available operational sites on land or with shallow depths close to shore, floating offshore wind turbines are required. These turbines face more severe environmental conditions and are associated with higher costs, but also reap the benefits of higher and more stable wind speeds. To reduce the cost to an acceptable level, economies of scale are needed along with serialized production. When the number of turbines increases, so will the number of accidents, production failures, and abnormal events. A clear methodology is therefore necessary to assess whether and to what degree floating turbines should be designed for redundancy.

The main objective of the thesis is to comparatively assess two semi-submersible designs and to develop and use methodologies for studying critical scenarios. To do so, the thesis uses state-of-the-art numerical tools to assess the global response of two different concepts, focusing on substructure design and tower placement. A joint distribution model is created for mean wind speed, significant wave height, and spectral peak period, employing a two-parameter Weibull model, a hybrid log-normal-Weibull model, and a pure log-normal model. Forty years of hourly site-specific metocean data are used to create environmental contour surfaces, describing wind and waves. Several optimization tools are used to upscale a substructure and tailor a mooring system to the selected site.

Hydrodynamic coefficients in potential theory are calculated in the frequency domain using WADAM, including dynamic effects of the internal fluid and full second-order wave excitation forces. A pure potential theory approach is identified as a limitation in the study, although viscous drag forces are included through Morison formulations. Python scripts are used to transfer coefficients and forces to the time domain by including sloshing forces as a frequency-dependent spring force. OrcaFlex is used for fully coupled aero-hydro-servo-elastic time domain simulations, coupled with multiple external Python functions, to enable the use of techniques previously seen in the analysis of damaged ships. Due to the complexity of the models and the novelty of the methodology, extensive testing and verification are performed.

The effects of different levels of ballast filling are studied, along with the effects of internal fluids on linear and quadratic transfer functions. The floating offshore wind turbines are simulated in various scenarios, including operating conditions, survival conditions, and damage conditions. Damage conditions are analyzed in transient and steady-state conditions, focusing on flooding and mooring line failure. The analysis complements and expands previous research by considering additional headings, load cases, and scenarios using new approaches.

Analytical expressions show that the resonant frequencies of internal fluids are well captured within WADAM, but the results confirm that the amplitudes of the sloshing-induced forces are not well described within a linear potential theory approach. Both frequency and time domain calculations show that the applied compartmentalization is conservative and could possibly be enlarged to cover a larger area without compromising redundancy. For selected designs and damage cases, the one-year post-damage survival conditions appear less critical than survival conditions considering intact structures in 50-year storms, which is the most severe scenario. The most striking difference between the concepts appears to be a quasi-static yaw mechanism related to the tower placement, leading to undesirable coupling effects between the rotational degrees of freedom for the peripheral tower design. This effect worsens the response compared to the center tower design, which is already a more conservative design. In the results, the impact of both the quasistatic effects and the dynamic linear sloshing excitation force becomes apparent. The results document both increased and decreased extreme values, mean values, and standard deviations depending on the concept and the selected response variables. This shows the need for further analysis, using experimental or numerical techniques capable of capturing the correct amplitudes of the effects.

Sammendrag

Vindenergi identifiseres som en del av løsningen for å tilby tilstrekkelig bærekraftig, trygg og sikker fornybar energi. Ettersom det er begrenset med passende områder på land eller nær kysten, er det et behov for flytende vindturbiner. Slike turbiner møter kraftigere værtilstander og er assosiert med større kostander, men drar også nytte av kraftigere og mer stabile vindhastigheter. For å redusere kostnadene til et overkommelig nivå, er skalafordeler og serieproduksjon nødvendig. Når antall turbiner øker, vil også antall ulykker, produksjonsfeil og uforutsette hendelser øke. Det er derfor nødvendig med en tydelig metodikk for å vurdere om og i hvilken grad flytende turbiner bør utformes med redundans.

Hovedformålet med oppgaven er å sammenligne to halvt-nedsenkbare flytere samt å utvikle og bruke metoder for å studere kritiske scenarioer. For å gjøre dette bruker oppgaven moderne numeriske verktøy for å vurdere den globale responsen til to ulike konsepter, med fokus på forskjeller i design og tårnplassering. Førti år med værdata brukes til å lage konturlinjer som beskriver vind og bølger. Simultane sannsynlighetsfordelinger som beskriver gjennomsnittlig vindhastighet, signifikant bølgehøyde og bølgeperiode er generert ved å bruke en 2-parameter Weibullfordeling, en hybrid lognormal-Weibull-fordeling og en lognormalfordeling. Flere optimaliseringsverktøy brukes til å oppskalere et flytende understell og tilpasse et forankringssystem til det valgte operasjonsstedet.

Hydrodynamiske koeffisienter fra potensialteori beregnes i frekvensdomenet ved hjelp av WADAM, inkludert dynamiske effekter av intern væske og andreordens bølgekrefter. En ren potensialteoritilnærming identifiseres som en begrensning i studien, selv om viskøse krefter er inkludert ved å bruke Morison-dragkrefter. Python-kode brukes til å overføre koeffisienter og krefter til tidsdomenet ved å inkludere sloshing-krefter som en frekvensavhengig fjærkraft. OrcaFlex brukes til koplete aero-hydro-servo-elastiske tidsdomenesimuleringer, koblet med flere eksterne Python-funksjoner, for å muliggjøre bruk av teknikker tidligere sett i analysen av skadede skip. På grunn av modellenes kompleksitet og nyskapende metoder, utføres omfattende testing og verifisering.

Effekten av ulike nivåer av ballastfylling studeres, og effekten av intern væske på lineære og kvadratiske bølgekrefter undersøkes. De flytende vindturbinene simuleres i ulike scenarioer, inkludert driftstilstander, overlevelsestilstander og skadetilstander. Skadetilstander analyseres både i stasjonære og transiente tilstander, med fokus på vanninnstrømning og svikt i fortøyningssystemet. Analysene komplementerer og utvider tidligere forskning ved å vurdere ytterligere værtilstander, lastetilfeller og scenarier ved hjelp av nye tilnærminger.

Analytiske uttrykk viser at resonansfrekvensene for den interne væsken er godt fanget opp av WADAM, men resultatene bekrefter at amplitudene av sloshing-induserte krefter ikke beskrives godt nok innenfor lineær potensialteori. Både frekvens- og tidsdomeneberegninger viser at de anvendte skottene er konservative og muligens kan utvides for å dekke et større område uten å gå på bekostning av redundansen. For valgte design og skadetilfeller virker ett års overlevelses etter skade mindre kritisk enn overlevelses i intakt tilstand gjennom 50-års stormer, hvilket er det mest alvorlige scenarioet. Den mest tydelige forskjellen mellom konseptene er en kvasi-statisk gir mekanisme relatert til tårnplassering, som leder til uønskede koplede bevegelser i rotasjonsfrihetsgradene av konseptet med periferisk tårnplassering. Dette forverrer responsen sammenlignet med konseptet på sentral tårnplassering, som allerede er et mer konservativt design. I resultatene blir effekten av både den kvasi-statiske effekten og den dynamiske lineære sloshing-ekskitasjonskraften tydelig. Resultatene dokumenterer både økte og reduserte ekstreme verdier, gjennomsnittsverdier og standardavvik avhengig av konseptet og de valgte responsvariablene. Dette viser behovet for ytterligere analyser ved hjelp av eksperimentelle eller numeriske teknikker som er i stand til å fange opp de riktige amplitudene av effektene.

Table of Contents

List of Figures

List of Tables

Acronyms

$\bar{\mathbf{U}}_\mathbf{w}$	Mean wind speed
$\mathbf{H_s}$	Significant wave height
$\mathbf{T_p}$	Spectral peak period
ALS	Accidental limit state
API	Application programming interface
BEM	Blade element momentum
BVP	Boundary value problem
CAPEX	Capital expenditure
CDF	Cumulative density function
CFD	Computational fluid dynamics
ClassNK	Nippon Kaiji Kyokai (Japan-based non-governmental classification society)
COB	Center of buoyancy
COG	Center of gravity
DLC	Design load case
DLL	Dynamic-Link Library
DNV	Det Norske Veritas
DTU	Technical University of Denmark
EIA	U.S. Energy Information Administration
EU	European Union
FEA	Finite element analysis
FEM	Finite Element Method
FLS	Fatigue limit state
FOWT	Floating offshore wind turbine
FPSO	Floating production, storage and offloading
HAWT	Horizontal axis wind turbine
IEA	International Energy Agency
IMR	Inspection, Maintenance & Repair
JONSWAP	Joint North Sea Wave Project
KC	Keulegan–Carpenter
LCoE	Levelized Cost of Electricity
LNG	Liquefied natural gas
LRFD	Load and resistance factor design
MLE	Maximum likelihood estimator
MSL	Mean sea level
NORSOK	Norsk sokkels konkurranseposisjon. (Norwegian continental shelf's competitive position)
NREL	National Renewable Energy Laboratory
NURBS	Non-uniform rational B-spline

O&G	Oil & gas
PDF	Probability density function
PLS	Progressive limit state
PM	Pierson-Moskowitz
QTF	Quadratic transfer function
RAO	Response amplitude operator
RNA	Rotor-nacelle-assembly
ROSCO	Reference OpenSource Controller
Semi-sub	Semi-submersible
SLS	Serviceability limit state
SLSQP	Sequential least squares programming
TLP	Tension-Leg Platform
TSR	Tip-speed ratio
ULS	Ultimate limit state
UMaine	University of Maine
VAWT	Vertical axis wind turbine
VSVP	Variable speed, variable pitch

CHAPTER 1

Introduction

In recent years, an increasing focus has been placed on wind energy as an enabler for shifting the energy mix toward more sustainable alternatives. Floating offshore wind turbines are part of this solution, although they represent numerous challenges for both engineers and economists. With an increasing number of installations, an increasing number of accidents are destined to happen. Several accidents have already occurred at the time of writing involving bottom-fixed offshore wind turbines. During a winter storm in 2022, a freely drifting rudderless chemical tanker collided with a substation at the Hollandse Kust South wind park in the Dutch part of the North Sea (Recharge News 2022). This spring, a high-impact bow collision occurred between a cargo ship and a wind turbine in the Gode Wind 1 wind field in German waters (Recharge News 2023). This speaks to the relevance of the topics analyzed.

This master's thesis focuses on the development of a simplified methodology to analyze the survivability of FOWTs using state-of-the-art numerical tools. To explore the methodology, two different types of semi-submersible FOWTs designs are compared, namely the central and peripheral tower designs. The central tower design is closely based on University of Maine (UMaine) VolturnUS-S, a four-column steel semi-submersible substructure designed to support the 15 MW reference wind turbine by the International Energy Agency (IEA). The peripheral tower design is an upscaled version of the INO WINDMOOR 12MW concept. This substructure is also a steel semi-submersible, but it comprises three columns. The latter substructure was decided to be upscaled to support the same wind turbine as the central tower design, to reduce the number of differences in the comparison. The comparison is performed using different modeling options performed on a set of design load cases from the *DNV-ST-0119* standard.

The main focus of the thesis is to develop a model in which relevant dynamic effects are explicitly included. The work has been done using state-of-the-art modeling tools, such as GeniE, WADAM, and OrcaFlex, along with vast amounts of Python code. Apart from the turbine itself, all modeling has been done within the thesis, built from the ground up using publicly available definitions of the substructures and open-source metocean data. As the models involve explicit modeling of internal fluid domains within the frequency domain calculations, the results are not easily transferred into the time domain. Therefore, a Python module had to be written for reading the text file outputs from the frequency domain calculation, performing re-dimensionalizing of the values, and converting to the time domain software.

To ensure the correctness of the results, extensive testing and sensitivity studies have been performed. For the frequency domain calculations in the exterior fluid domain, mesh convergence studies have been performed both for the hull and free surface discretization. Additionally, several verification tests have been performed in the time domain to ensure that the models behave as expected. These tests are especially important due to the self-written Python module linking the frequency domain and time domain software.

1.1 Objective

The primary objective of the thesis is to comparatively study two different semi-submersible concepts proposed for floating offshore wind applications, focusing on survival in extreme and abnormal situations. Throughout the study, the mechanism of the responses will be investigated, focusing on the effect of internal fluid effects as a secondary objective. To achieve these objectives, extensive modeling and verification must be performed.

1.2 Preliminary study

In the fall preceding this master's thesis, a preliminary study was performed. The study included an investigation of the survivability of the INO WINDMOOR 12 MW FOWT, primarily in the frequency domain. Some of the findings of the preliminary study are included in this thesis, mainly regarding literature study, theory, and methodology. The work of the preliminary study is modified to better suit the subject of the thesis when necessary. No models, environmental data, or results are reused from the preliminary study.

1.3 Structure of the thesis

The thesis is organized with the following structure:

- Chapter 2: Wind energy

  Literature study of the broad concept of wind energy generation.

- Chapter 3: Existing methodology, rules, and guidelines
  - Technical literature study of past work, methods, and regulations relevant for the thesis.

- Chapter 4: Theory

  Presents the needed theory to describe the analyzed problems.

- Chapter 5: Methodology

  Describes the methods and decisions made during the modeling of the problems.

- Chapter 6: Description of concepts

  Defines the properties of the relevant substructures, turbine, tower, and mooring system.

- Chapter 7: Description of selected operational site

  Describes the selected operational site and the site-specific environmental conditions.

- Chapter 8: Definition of design load cases

  Defines the design load cases and damage conditions analyzed in the thesis.

- Chapter 9: Verification of numerical models

  Provides results from both frequency- and time-domain calculations with the main purpose of verifying the response of the different models.

- Chapter 10: Static results

  Presents the results from a quasi-static stability study in intact and damaged conditions.

- Chapter 11: Frequency domain results

  Provides and discusses the results from frequency domain calculations in WADAM.

- Chapter 12: Time domain simulations

  Presents and reflects upon time domain simulations in OrcaFlex.

- Chapter 13: Discussion

  Discusses the combined results from the previous chapters.

- Chapter 14: Conclusions

  Concludes upon the obtained results.

- Chapter 15: Further work

  Presents the recommendations for further studies.

CHAPTER 2

Wind energy

2.1 Wind energy as a solution to the energy crisis

The harvest of wind energy is by no means a new concept. Thousands of years ago, wind power was used for ship propulsion, grain grinding, and pumping water in ancient China, Egypt, and the Middle East. This technology was later brought to Europe and the US by merchants, crusaders, and explorers (EIA 2022). With the emergence of electricity, windmills turned to wind turbines, ideal for producing electricity for rural agriculture. After the second industrial revolution, when electricity became industrialized, grids consisted of low-voltage direct-current cables. This resulted in high losses, which made the transport of electricity over long distances ineffective. As a result, wind turbines were widely used for local power production until the development of more efficient grids, and diesel generators surged forward (M. Hansen 2015). These inventions created the possibility of petroleum-generated electricity and long-range power transportation, decelerating wind power development.

Figure 2.1: Wind mill for water pumping, Kinderdijk - Netherlands
Source: Therin-Weise (n.d.)

Figure 2.2: Steel blade windmill for water pumping, Midwest - US
Source: National Park Service (2019)

During the two world wars and later in the 1970s during the Yom Kippur War and the Iranian Revolution, the world faced excess energy demand and fuel shortages. This led the energy from wind power to resurface due to high energy prices and the desire for energy supply security. At the time of writing, these issues are again at the top of the agenda with the ongoing war in Europe, roaring energy prices, and the inevitable transition to less carbon-intensive energy options. Once again, wind power, along with other renewable sources of energy, is identified as part of the solution.

2.1.1 Why wind power?

Wind energy is a green, renewable energy source that is both sustainable and readily available. Furthermore, wind turbines do not emit air pollutants (SO_x, NO_x, and PM) while operating, and the carbon footprint of production and commissioning is paid back in less than 12 months (Wind Europe 2022a). Looking aside from technical and political issues, over 33,000 TWh of wind power is available in Europe. This corresponds to more than ten times the annual European electricity consumption. Of this power, more than 25,000 TWh is located offshore, and 60% of the offshore wind power is located in areas with water depths exceeding 60 meters (ETIP-WIND 2021).

Furthermore, constructing wind parks is relatively labor intensive, meaning it will generate a lot of employment through fabrication, installation, maintenance, and decommissioning. In addition, a domestic, self-reliant energy supply is desirable for all nations, rather than being dependent on the import of hydrocarbons from other nations. Wind power is also ideal in remote areas and areas with poor grid infrastructure.

A drawback of wind power is the inherent variability of the wind, which shows the need for energy storage or coupling with other forms of power production. Some forms of power production, such as nuclear or coal plants, have a time lag during start-up and shutdown, making them less suitable for coupling with wind power. Other energy sources, such as hydroelectric plants with storage capacities, can be quickly started and integrated with wind power to deliver a stable power supply (M. Hansen 2015). In Norway, 1681 hydroelectric plants are operating, providing 90% of the domestic energy demand, while the last 10% is supplied by wind power. Approximately 75% of the hydroelectric plants have storage capacity, which means they adapt the energy supply relative to the supplied wind power (Norwegian Ministry of Petroleum and Energy 2021).

2.1.2 The future energy mix

After the recent geopolitical events, EU has further accelerated the energy transition. In May 2022, they announced that 50% of the electricity production shall come from wind energy by 2050. From Figure 2.3, one can see that a substantial amount is proposed generated by offshore wind turbines. In the same plan, EU announced the intention to build a total installed capacity of 510 GW from wind power by 2030, which is more than double the 190 GW installed today (Wind Europe 2022a).

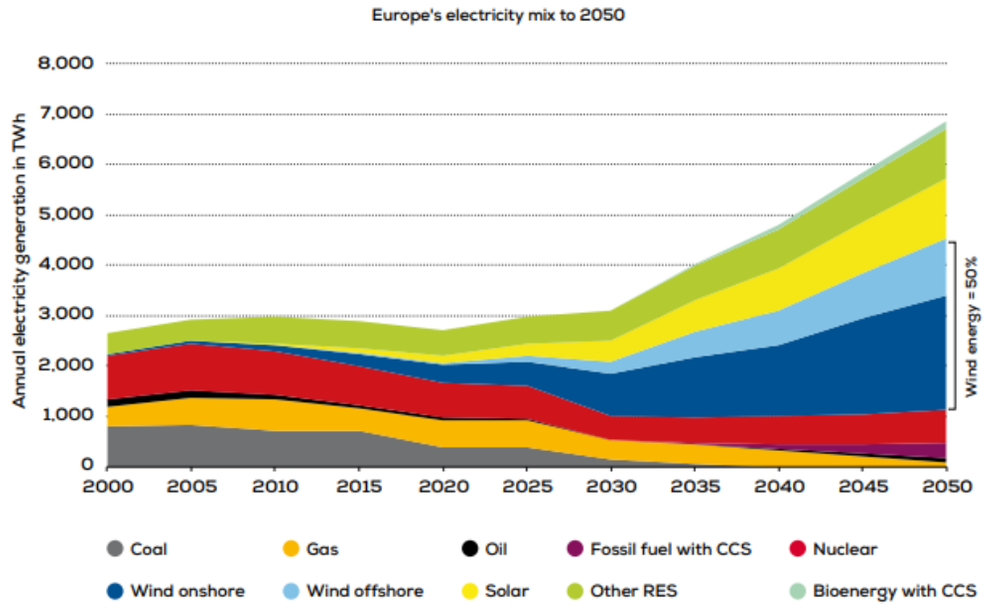

Figure 2.3: Future EU energy mix
Source: ETIP-WIND (2021)

2.1.3 Land-fixed, bottom-fixed or floating

The starting point of the wind power era was through small land-fixed turbines, and even today the majority of the new installations are taking place onshore. In 2021, 81% of all new turbines in Europe were installed onshore. Despite the fact that offshore wind is receiving a lot of attention, only 12% of the total installed capacity in Europe is produced by offshore turbines and only a marginal share by floating turbines (Wind Europe 2022b). Because offshore turbines are typically larger than onshore turbines, the proportion of offshore turbines in terms of quantity is generally lower.

The large share of capacity placed onshore is due to the significantly lower costs involved with onshore development. However, as in all industries, one first develops the most suitable sites. Such sites are characterized by large areas available at a low cost, with high mean wind speeds, low turbulence, and low visual and noise impact on the public. Aside from the higher associated costs, the listed characteristics must be said to describe offshore areas fairly well. In reality, as the amount of land available for wind power generation is limited, it is not the comparison of cost between offshore and onshore that matters in the future; it is the comparison between offshore wind and other forms of renewable power generation.

The majority of offshore wind power development has so far been bottom-fixed turbines placed on monopiles or jacket foundations in shallow water depths (<20 m), with a distance from the shore of fewer than 20 km. These limitations are due to the rapidly increasing cost associated with deeper waters and the need for longer cables as parks are placed further from shore (Twidell and Gaudiosi 2009).

Onshore and especially offshore, one can see rapid growth in wind turbine sizes. The doubling of average rated power from 2 MW to 4 MW took 15 years, while the subsequent double to 8 MW was achieved in only 5 years (ETIP-WIND 2021). At the time of writing, turbines as large as 12-15 MW are expected to be installed in European waters.

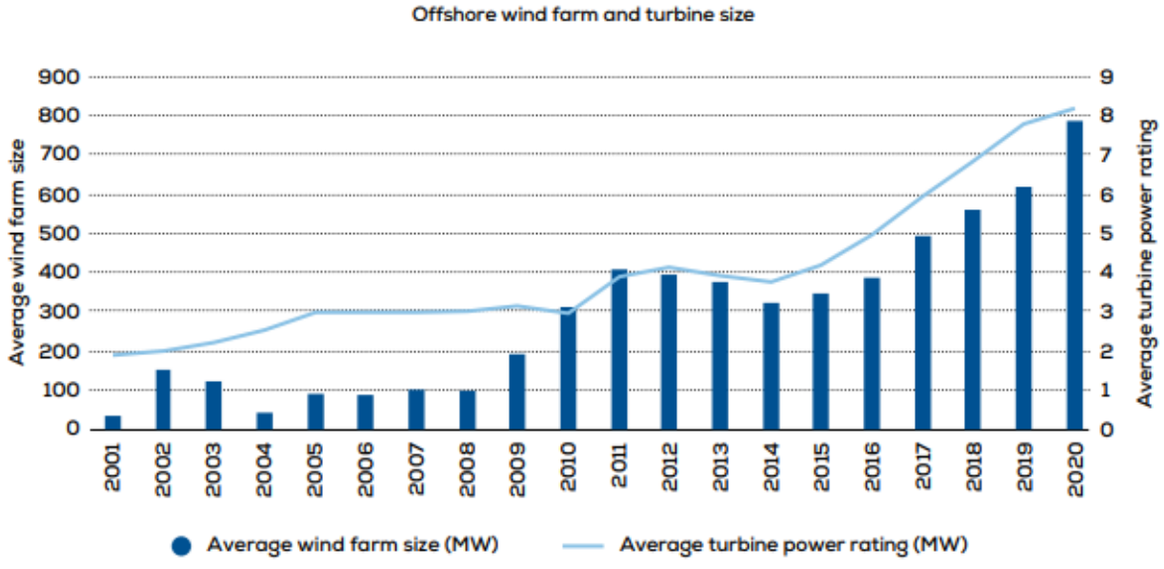

Figure 2.4: Trend of turbine power rating and park sizes in offshore wind generation
Source: ETIP-WIND (2021)

A common trait for both forms of offshore wind is that the installation is a larger portion of the total cost compared to onshore wind. This implies that it is more cost-efficient to install fewer but larger turbines. However, this will also depend on the scalability of the substructure. Larger turbines come with higher hub heights and larger rotor diameters, which leads to larger flexibility and, thus, larger deflections.

The proportion of CAPEX associated with the different components differs greatly between the different types of wind power. When wind turbines move from onshore to bottom-fixed offshore and further to floating offshore, one can see that the turbine itself becomes relatively less costly due to the increasing cost of the remaining components. For a FOWT, the substructure is the most CAPEX intensive component. Figure 2.5 also shows that the installation is a smaller portion relative to the other components in floating offshore wind compared to bottom-fixed wind. This is in part due to the possibility of tow-out to the site, in part due to the increased cost of the substructure, and in part due to the inclusion of anchor and mooring costs in the "Others"-category (ETIP-WIND 2021).

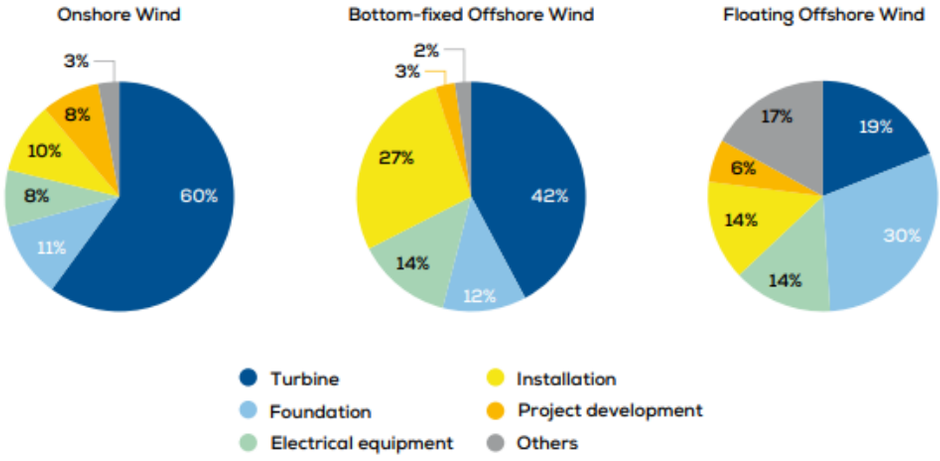

Figure 2.5: Relative component CAPEX in floating offshore wind.
Source: (ETIP-WIND 2021)

There are many trade-offs between onshore and offshore wind, and both concepts have advantages and disadvantages. Usually, the complex and costly installation procedure is considered a disadvantage of offshore wind. However, employing a transportation barge in open water to transport wind turbine blades, which must be transported fully assembled, is far less complex than building roads in remote areas to enable transportation by trucks.

Figure 2.6: Transporation by truck of 58.7 m blades.
Source: (Collett News 2016)

Other advantages of offshore wind are the above-mentioned higher mean wind speeds and lower turbulent components, simple ownership in terms of areas where all offshore areas are government-owned, and practically unlimited wind park sizes. Finally, offshore wind turbines have the advantage of moving the wind turbines away from the public, leading to a lower visual and acoustic impact. Although most of the mechanical noise is eliminated from modern wind turbines, the aerodynamic noise remains. For land-based turbines, a critical noise distance (<40 dB) is achieved at a distance of 250 meters (Twidell and Gaudiosi 2009). In many countries, local residents protest against having wind turbines in their surroundings based on noise complaints, invasion of the ecosystem, and destruction of pastures and hiking areas.

2.1.4 Floating concepts

Different mindsets may govern the design process for offshore wind, especially for floating wind. Either, one can rely on the competence of the onshore wind community and consider the floating offshore wind turbines simply as more complicated onshore wind turbines placed offshore. On the other hand, one can build on the knowledge from the oil & gas (O&G) sector and consider floating offshore wind turbines as offshore structures that happen to support a turbine. Clearly, as will be seen throughout the thesis, the design process involves utilizing knowledge from both communities without disregarding the need for new engineering solutions.

Floating wind turbines remain the most immature and costly option for wind power generation. However, ETIP-WIND (2021) expects a 60% reduction in Levelized Cost of Electricity (LCoE) by 2030 compared to the 2020 level. This cost reduction will mostly be driven by technology maturing, especially the leaner design of floaters and moorings, and better manufacturing in terms of serialized production.

The main functional requirement of any floating structure, including FOWTs, is the ability to remain buoyant in the upright position while fulfilling the serviceability requirement (Moan 1994). The serviceability requirement for a FOWT is to convert the kinetic energy in the wind to electrical energy under all operating conditions. Knowledge from O&G industry has motivated many of the proposed FOWT-concepts, and such concepts are, in most cases, classified in terms of the source of stability. The stability against overturning of a floating structure is mainly resulting from three different sources:

Water plane stabilized:

Restoring stiffness due to a large second moment of area in the water plane, caused by placing the water plane area far from the flotation point.

Ballast stabilized:

Restoring stiffness from the vertical separation of the center of buoyancy and center of gravity

Mooring stabilized:

Restoring caused by taut or pre-tensioned mooring lines anchored to the seabed.

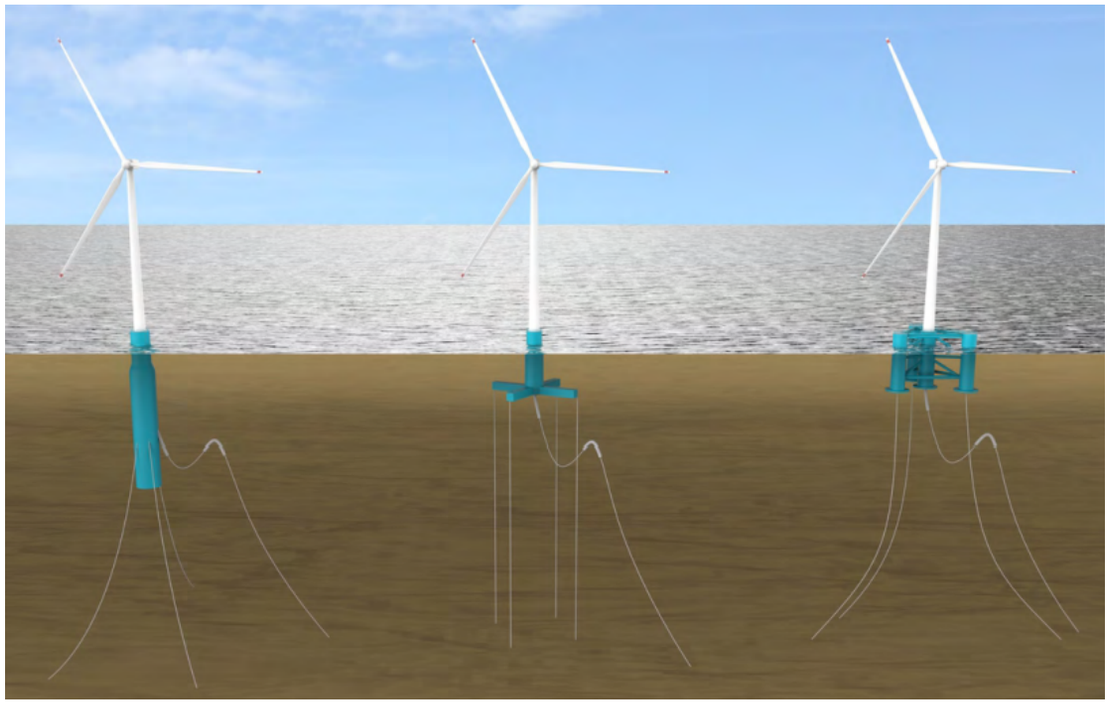

Figure 2.7: Illustration of typical floating concepts
Source: (Offshore Wind Innovation Hub 2020)

The choice of substructure is driven by many different factors. The water depth at the installation site is seen to be the most important design driver due to the minimum depth requirements for the different concepts. Other factors, such as static heel at rated thrust, may also become important. Furthermore, one must consider the ease of fabrication and installation, including the needed depth at the quayside. As opposed to bottom-fixed offshore wind, the fore-aft tower bending mode is no longer the lowest eigenmode. One must carefully examine the rigid-body natural periods with respect to the expected excitation periods. For floating structures, one usually designs for a static heel angle during operation, combined with a static offset in the horizontal modes. Also, the increased misalignment between the rotor plane and the incoming wind speed due to yaw motions must be assessed. Lastly, one must investigate the coupling effects between the rigid body modes, the aerodynamic loads, and the controller actions.

Spar concepts

A spar concept may be described as a slender, cylindrical upright structure. The slender structure is relatively transparent to the waves, but requires a large draft to ensure sufficient buoyancy. Looking back to the three methods of stabilization, one can conclude that the spar concept is evidently ballast stabilized. The center of gravity is lowered by placing the ballast at the bottom of the structure. This creates a large separation between the center of gravity and the center of buoyancy, again causing large restoring moments during overturning.

The response of spar concepts is characterized by small heave motions as a result of the large draft of the floater. An advantage of this is reduced motions and therefore reduced fatigue damage on power cables, umbilical, and moorings. A typical spar concept has long natural periods in the horizontal translational modes dictated by the stiffness of the mooring system. An important feature of spar concepts is short natural periods in yaw, caused by a low radius of gyration and low added inertia when rotating around the vertical axis. Therefore, one should be aware of the coupling effects between yaw and other modes due to the aerodynamic effects. The mooring line configuration often consists of three catenary or taut mooring lines. Additionally, the power cable is often flexible in a lazy wave configuration to uncouple it from vertical motions of the structure (Cruz and Atcheson 2016).

The natural period in heave is usually well above the main energy content of the waves and is often similar to the natural periods in roll/pitch (DNV 2021c). Although long natural periods away from significant wave energy are desirable, collocated heave and roll/pitch natural frequencies may lead to a Mathieu instability (Anaya-Lara et al. 2018). The large and slender structure may also be prone to sizeable global bending loads, which should be investigated during design.

The large draft leads to a large projected drag area that results in large drag loads from currents (DNV 2021c). A large submerged cylinder may also be very susceptible to vortex-induced motions. This may be suppressed by adding strakes, but this further increases the experienced drag loads. Moreover, a large draft also makes SPAR concepts unsuitable for transitional areas between shallow and large depths. Such water depths are in the range of 50-80 m, where it is very costly to build bottom-fixed turbines. It also complicates the installation and mating processes, where one needs a combination of deep and still waters. Aside from the Norwegian fjords, this is a rare combination.

An example of a project applying the SPAR concept is the Hywind Tampen project by Equinor. The project comprises 11 SPAR floaters, each carrying an 8 MW turbine with a 105 m hub height. The substructures consist of concrete, while the towers are made of steel. The substructures have a maximum diameter of 18.6 meters, a draft of 90 meters, and a total displacement of approximately 22,000 tonnes (K. Larsen 2021).

Figure 2.8: Hywind Tampen spar concept
Source: (Aker Solutions 2021)

Tension-Leg Platform (TLP) concepts

The TLP concept is characterized by vertical tendons that provide the main source of stability. Tendons have a large elastic stiffness, typically at least an order of magnitude larger than the hydrostatic stiffness. The tendons are stressed by the buoyancy force being larger than the gravitational force. The large vertical stiffness leads to very limited displacements and short natural periods in heave, roll, and pitch in the lower end of where wave periods would be expected. However, one should be concerned about higher-order sum frequency loads. In the horizontal modes, the restoring effects from the tendons are much softer, and one would expect long natural periods and relatively large mean offsets (DNV 2021c).

Figure 2.9: IBERDROLA TLP concept
Source: (Lifes50+ 2016)

The advantages of the TLP concept are a small footprint on the seabed, limited motions, and potential savings in terms of steel use. On the other hand, such concepts are expensive and complex to install. A TLP may be designed to be self-stabilizing during mating and installation. However, once tethered and lowered to the operational draft, it is dependent on the tendons to provide stability. Losing one or several tendons leads to cap-sizing, and one often enforces a no-slack condition in the analysis (Cruz and Atcheson 2016). If the ULS condition is exceeded, a total loss of the structure would be expected. To my knowledge, no FOWTs of the TLP concepts has been built on a full scale. However, some concepts are considered at various stages, such as the IBERDROLA steel TLP considered in the Lifes50+ project.

Monohull concepts

Monohull concepts are commonly referred to as barge concepts and are characterized by a large waterplane area and a relatively shallow draft. The hydrostatic stability will, in most cases, arise from waterplane stiffness, but it may also be combined with ballast. Such concepts will experience a lot of wave action and will most likely have a heave natural period located in a region with significant wave energy. Measures must also be applied to ensure damping in rotational modes, by, for example, bilge keels (DNV 2021c). Large-amplitude motions at wave frequency in roll or pitch will result in large accelerations in the nacelle, which may be the limiting response variable for a FOWT.

Monohull concepts have a competitive advantage in terms of low minimum water depth during assembly and operation. Still, a simple barge shape is believed to be too susceptible to wave-induced motions (Twidell and Gaudiosi 2009).

Semi-submersible (Semi-sub) concepts

A semi-sub concept is a well-known concept from the O&G industry and is, along with spar concepts, the most frequently proposed concept for floating wind. Common for all semi-sub concepts are the columns, often three or four, placed away from the center to provide a large water plane stiffness. The columns may be joined by braces or pontoons that take up the split forces caused by wave excitation. The tower may be placed in the center of the structure or asymmetrically on one of the columns. The draft of the concepts is modest compared to spar concepts, but will be larger than drafts considered on barge concepts. The relatively modest draft of the semi-sub concepts allows for full assembly at the quayside. The large hydrostatic stability makes towing to the site an effective installation method.

The small waterplane area results in long heave natural periods above the wave periods in regular sea states. However, significant motion for semi-sub-concepts would be expected for long waves in extreme sea states. A catenary mooring system with varying line types is often used for the semi-sub concept. This gives the restoring in the horizontal modes and leads to long natural periods in

surge, sway, and yaw. Advanced hydrodynamic considerations could be included if one identifies a critical design wave, such as designing prominent structural members for cancellation effects at design wave lengths (Cruz and Atcheson 2016). Braces between the columns will be relatively hydrodynamically transparent, and pontoons will be placed at the bottom where wave action is reduced.

Other concepts intended for altering the motions of semi-sub concepts include heave plates, which increase the inertia of the structure during oscillations, dynamic ballast systems to counteract mean aerodynamic thrust, and sharp edges and appendages to increase viscous damping. In terms of materials, steel is the most widely used option in the suggested concepts for FOWT as well as for semi-sub in the O&G industry. Still, Dr. Techn. Olav Olsen has also suggested a concrete concept that is claimed to be more cost-effective and easier to fabricate locally.

Figure 2.10: WindFloat - Principle Power, displaying heave plates on a semi-sub concept.
Source: (Roddier et al. 2010)

Figure 2.11: OO-Star - Dr. Techn. Olav Olsen, concrete semi-sub concept.
Source: (Landbø 2018)

2.2 Turbine concepts

In addition to the numerous types of substructures, there are many options regarding the turbine itself. One of the first mass-produced commercial turbines was the “Danish” wind turbine concept. This was a three-bladed, upwind, horizontal-axis, stall-regulated turbine operating at a fixed speed with an induction generator (Burton et al. 2001). Stall regulation implies that the aerodynamic design of the blades makes the flow separate at a certain rotational speed, and thus eliminates the need for active pitch control of the blades. Upwind means that the rotor plane is placed in front of the tower in the wind direction, and horizontal-axis implies that the rotational axis of the turbine is horizontal.

Many other concepts have emerged, and today most modern turbines are variable speed, variable pitch (VSVP) controlled. VSVP indicates that the turbine aims to maximize power through variable torque and speed when below the rated wind speed and pitches the blades to have constant power production and lower loads when above the rated wind speed. Additionally, most modern turbines still utilize three blades placed upwind, rotating around a horizontal axis. The advantage of a horizontal axis wind turbine (HAWT) is that the blades operate at a constant angle of attack throughout the revolution and therefore may be designed to operate in the optimum configuration delivering a constant torque. Vertical axis wind turbine (VAWT), on the other hand, operate with a constantly changing angle of attack during a revolution and therefore will have a sinusoidal varying thrust and a resulting lower mean power coefficient. The advantage of a VAWT compared to a HAWT is that the drivetrain can be placed on the substructure rather than in the nacelle. This significantly lowers the total structure’s center of gravity and makes the resulting overturning moment lower. This will make the structure inherently more stable and possibly cheaper, as a tonne saved in the nacelle implies several tonnes saved in the substructure. The lower placement of the drivetrain will also make installation less complicated (Cruz and Atcheson 2016).

2.3 Wind harvest areas

The majority of offshore wind power has so far been developed in Europe, in areas such as the North Sea and the Baltic Sea, by the United Kingdom, Denmark, Sweden, and Norway. A map of offshore wind development in the north of Europe is shown in Figure 2.12.Green areas symbolize fully commissioned fields, while yellow, purple, and blue represent preconstruction, planning, and development zones. The map shows that most of the projects are still in the early stages. In other regions, countries such as Japan have expressed a clear intention to develop their wind strategy, and other large countries such as China, South Korea, and the United States have similar plans. The areas on the Norwegian coast, the Japanese coast and the western coast of the USA are all characterized by deep waters, which implies the need for floating concepts. Other factors can differ between locations, such as local laws, geopolitical tensions, and existing infrastructure. For instance, the Jones Act requires the transportation of goods between US ports to be done by ships built, owned, and operated by American citizens. Another example is the Minnan Offshore Shoal Offshore Wind Power Phase I, located on the Taiwan bank at the southern end of the Formosa Strait. This region lies in the middle of the tense conflict between Taiwan and China. When examining suitable wind park locations, such factors must be taken into account.

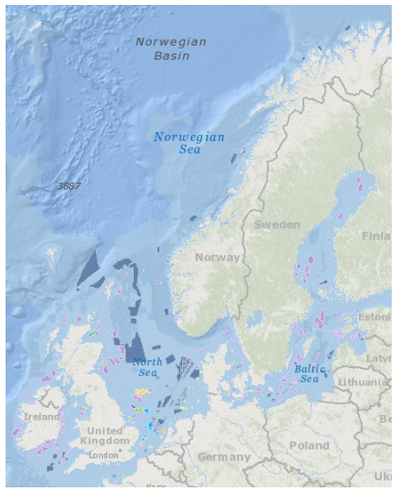

Figure 2.12: North European sites

Source: Extracted from 4C offshore map service

Examples of some major wind farms are presented below:

Dogger Bank

Bottom-fixed wind farm in the southern North Sea, with water depths ranging from 18-63 m. The capacity will be 3.2 GW for the three different phases combined when fully commissioned.

Hornsea 2

Bottom-fixed farm 89 km off the coast of Yorkshire, UK, with a total capacity of 1.3 GW.

Empire Wind 2

Bottom-fixed farm under commissioning outside New York, USA. The farm is planned to produce 2.1 GW using large 15 MW turbines.

Hywind Scotland

World's first floating offshore wind farm. A total capacity of 30 MW, generated by five 6 MW turbines supported by spar substructures.

Hywind Tampen

Floating offshore wind farm currently under construction, aimed at electrifying the Snorre and Gullfaks O&G fields off the coast of Norway. It comprises 11 spar-type FOWT, producing 88 MW in total.

Trollvind

An announced plan by Equinor to build a 1 GW floating wind park at the Troll field to electrify the Troll and Oseberg fields and bring power to shore.[1]

[1] On the 22nd of May 2023, Equinor announced that Trollvind is postponed indefinitely due to inflation-driven increase of CAPEX, and slower than anticipated technology maturing

CHAPTER 3

Existing methodology, rules and guidelines

Although floating structures for wind turbines are a novel technology, several regulatory documents have already been drafted to guide further development. Examples of such rules are offshore standards from, e.g., DNV and NORSOK, well known from the O&G industry. The standards aim to ensure an acceptable level of safety and ease collaboration between stakeholders in a floating offshore wind project (DNV 2021b). The limit state design method is often used to ensure a specific safety level for the design of floating structures. As this method also applies for FOWT it will be presented before discussing specific regulations regarding floating wind.

The design process of FOWTs as defined in IEC (2019b) can be seen in Figure 3.1. The IEC-61400-3-2 standard extends the traditional IEC-61400-3-1 standard, specifically focusing on floating wind power generation concepts. The illustrated design process shows how site-specific environmental conditions are combined in predefined design load cases to estimate the loads on the structure. It further shows how limit state design is applied in an iterative process to evaluate the design.

A noteworthy detail of Figure 3.1 is that the RNA must also be considered in the design spiral for floating wind applications. This implies that RNAs for fixed offshore wind applications may not be usable and that a tailored design may be necessary. Nejad and Torsvik (2021) found that for the 5 MW NREL turbine applied on semi-submersible concepts, both increased and decreased fatigue damage was found for different components. However, this conclusion could not be generalized to larger turbines. In addition, it was concluded that wave-induced loads most likely are of secondary importance compared to wind-induced loads for RNA design.

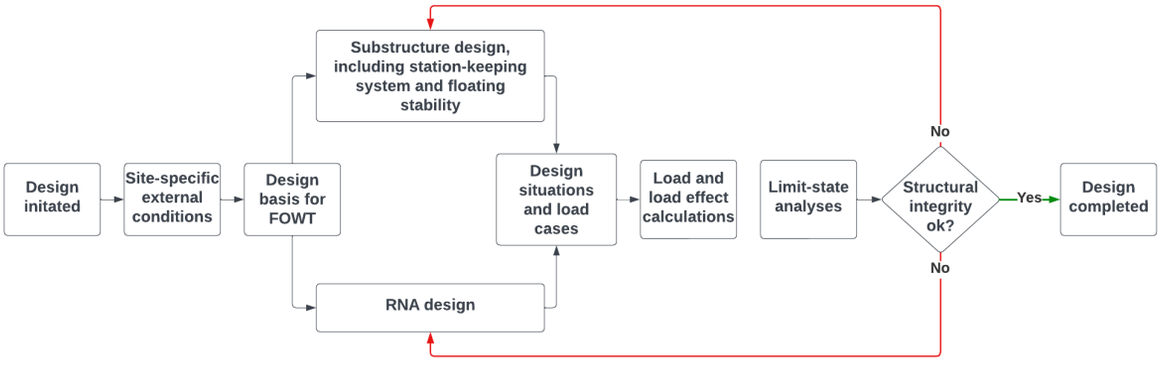

Figure 3.1: Design process of a FOWT
Source: Adopted from IEC (2019b)

3.1 Limit state design

In the structural design of offshore installations, the limit state design method is often used. According to DNV (2021c), a limit state is a condition in which, if exceeded, the structure or a structural component no longer satisfies the design requirements. The most common limit states defined in the structural analysis are:

- Ultimate limit state (ULS)
- Accidental limit state (ALS)
- Fatigue limit state (FLS)

The ULS refers to the maximum load the structure can withstand, typically seen in conjunction with an extreme event with a specified return period. The ALS refers to abnormal events such as explosions, fires, environmental phenomena, or ship collisions above a certain kinetic energy. In addition, the exceedance of a structure's ultimate resistance in damaged conditions and loss of global integrity after local damage or flooding are also included in this limit state. A minor localized damage that escalates to flooding and ultimately to loss of global stability is often referred to as a progressive failure, and the ALS is therefore also referred to as the progressive limit state (PLS) (Moan 2009). FLS is related to the deterioration of a structure due to repeated actions, often seen as crack propagation resulting in fracture. In addition, other limit states can be defined, such as the serviceability limit state (SLS), which relates to the intended use of the structure, e.g., the absence of large deformations and vibration during operation. For all the different limit states, both loads, load effects, and resistance to load effects must be accurately determined (Moan 1994).

The limit state design method is also widely known as the "Load and resistance factor design (LRFD)"-method or the "Partial safety factor"-method, due to the way in which one defines the design criterion (NORSOK 2022).

$$S_d = S_c \cdot \gamma_f \leq \frac{R_c}{\gamma_M} = R_d \tag{3.1}$$

where: S_d = Design action effect
S_c = Characteristic action effect
γ_f = Action factor
R_c = Characteristic resistance
γ_M = Material factor
R_d = Design resistance

The term "action" is defined in NORSOK (2017b) as:

> Assembly of concentrated or distributed forces acting on a structure (direct actions), displacements or thermal effects imposed on the structure, or constrained in it, or environmental influences that may cause changes with time in the material properties or in the dimension of a structure (ISO 2394)

whereas action effects are defined as the global or local response to an action, such as stresses or displacements. These definitions from NORSOK correspond to the terms "loads" and "load effects" in the DNV standards. In Equation 3.1, the characteristic action effect and the characteristic resistance are values from a certain percentile of the respective underlying distributions which represent certain return periods. The probability of failure is defined as the probability of the design action effect exceeding the design resistance. The relation between the characteristic values and the design values is expressed using partial safety factors, which are dependent of the type of action, material, and fabrication method. The partial safety factors are included to account for possible deviations from characteristic values due to the stochastic nature of the variables, the probability of simultaneous occurrence of actions, and possible inaccuracies in the calculation of action effects (NORSOK 2021).

Extreme loading on a FOWT may arise in many different situations and from many different sources as shown in Figure 3.2. In most cases, the dominating thrust force on the wind turbine will occur at the rated wind speed and will be strongly dependent on the controller. Events like emergency stops can introduce extreme transient loads, especially bending moments in the tower. Storm events, where the turbine is parked, may also introduce extreme loads due to the combination of large wave and current loads on the floater and large wind loads on the tower and RNA (DNV 2021c). This shows a difference between the usual analysis performed in the O&G industry, where one often assumes that the most critical events occur during the most extreme environmental conditions. For a FOWT, the most critical situation might just as well occur in less extreme conditions due to aerodynamic loads and controller actions. Consequently, the standards specify that all such loading conditions must be included in the analysis.

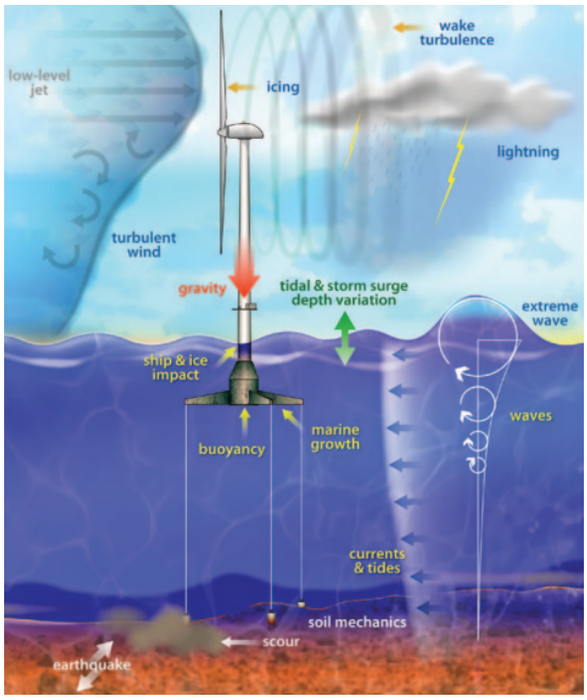

Figure 3.2: Load sources of a floating wind turbine
Source: (U.S. Department of Energy 2010)

3.2 Standards and recommended practices

Several of the DNV standards and recommended practices refer directly or indirectly to wind turbines. For analysis, the general load cases to consider are presented in *DNV-ST-0438 Loads and site conditions for wind turbines*. This standard defines, among other topics, the environmental conditions for the analysis and the methodology for load calculations. It is a general standard for both onshore and offshore turbines and has many similarities to the IEC 61400-1 and IEC 61400-3 standards.

In addition to the load cases defined by *DNV-ST-0438*, *DNV-ST-0119 Floating wind turbine structures* defines further load cases that apply specifically to FOWTs. Furthermore, the standard provides engineering principles, requirements, and guidance for all phases of the life cycle of a floating offshore wind turbine, including design, construction, installation, operating condition, inspection, and maintenance (DNV 2021c). The standard focuses on the support structure, defined as both floater and tower, and the station-keeping system from a structural point of view. For the substructures of fixed offshore turbines, one has to refer to *DNV-ST-0126 Support structures for wind turbines* instead. For other parts of the wind turbines, such as the turbine components itself, defined as the nacelle, rotor, and drivetrain, *DNV-ST-0376 Rotor blades for wind turbines* and *DNV-ST-0361 Machinery for wind turbines* apply. For the controller and potential monitoring systems, it is *DNV-ST-0438 Control and protection systems for wind turbines* that applies.

DNV-ST-0119 specifies requirements to ensure safe design of FOWTs and states that some of these requirements may be based on current industry practices and established principles for floating structures. This implies that some of the regulations are based on experience from the O&G industry, typically other DNV or NORSOK standards. It is allowed to deviate from the stated requirements as long as the safety level is at least as high and all cost-effective risk control measures are implemented. This is an important statement for floating wind concepts, where the economic margins are much tighter than previously seen in the offshore industry. As will be discussed in more detail, the consequences of an accident involving an offshore wind turbine will be much less severe than an accident involving a petroleum installation. Therefore, the design principles of the O&G industry may not be transferable if one wishes to produce cost-effective solutions for floating offshore wind power.

To ensure structural safety, *DNV-ST-0119* defines two different consequence classes which describe the consequences if failure of the structure occurs. The target safety levels assume a ductile failure where the structure may utilize some reserve capacity through plastic deformation (DNV 2021c).

Consequence class 1

Failure is unlikely to lead to unacceptable consequences such as loss of life, collision with an adjacent structure, and environmental harm.

- A structure in consequence class 1 should have a target safety level of a nominal annual failure probability of 10^{-4}

Consequence class 2

Failure may well lead to unacceptable consequences of these types.

- A structure in consequence class 2 should have a target safety level of a nominal annual failure probability of 10^{-5}

A general FOWT-substructure and the associated station-keeping system should, according to DNV (2021c), be designed to meet the requirements of consequence class 1, due to the structure being unmanned when severe loading conditions are expected. This eliminates the risk of personnel during storm events and, therefore, the associated consequences of a failure are mainly economic (DNV 2021c). A special requirement for station-keeping systems without redundancy is that such a system should be defined within consequence class 2. However, if the structure is designed without redundancy in accordance with consequence class 2, the ALS is not required to be considered (DNV 2019a). The standard also states that the need for redundancy in the structure is greater if the technology is immature.

When only a single FOWT is considered, both the ALS conditions and environmental conditions with an annual probability of occurrence less than $2 \cdot 10^{-3}$ are not required to be included in the analysis. However, it may be considered if stakeholders find it relevant from an economic or reputational point of view. If the ALS leads to progressive failure or high economic or societal impact, it must be considered (DNV 2021c). A relaxation of ALS will reduce the extent of the analysis, as damage stability, especially dynamic damage stability, is a complex analysis (Anaya-Lara et al. 2018).

As seen in the discussion above, the specification of whether dynamic response analysis of flooded structures must be performed is somewhat ambiguous. The standards specify damage cases as mandatory design load cases but state that the ALS condition may be omitted if the expected return period is greater than 500 years. The 500-year return period was introduced in the 2021 edition of DNV (2021c), relaxed from 1000 years in the 2018 edition. In the latest edition, it is also specified explicitly that damage stability is not a mandatory requirement for unmanned structures, but that it is advised to perform nonlinear collision analysis and damage stability analysis. It is also specified that if damage stability is considered, one should also consider the stability and buoyancy in damage conditions during temporary conditions such as transport and Inspection, Maintenance & Repair (IMR) operations. Further design conditions for transport and installations are described in *DNV-ST-N001*.

In a ALS scenario, DNV (2019a) differs between stationary and transient load cases, where the former is defined as a load case where the statistical properties are constant in time, and the critical response is due to stochastic environmental processes. The stationary load cases are also defined as redundancy analysis, as it considers the redundancy of the system by ensuring survival in the new steady-state after a damage. On the other hand, the transient analysis is included to ensure that the damage does not lead to a progressive total failure of the structure. For a transient load case, DNV (2019a) states that the simulation time after the abnormal event should be sufficiently long to capture the decay of the system. For a floating structure with catenary mooring lines, at least 600 s is advised. For the transient load cases DNV (2021c) states that the resulting action of the wind turbine control system should be considered. Following the guidance of the same standard, it may be assumed that the state of the system is sufficiently monitored, such that the wind turbine may be shut down in a reasonable time.

As this thesis also considers operational and survival load cases, some requirements for the SLS should also be included. The values given in DNV (2019a) are indicative values applicable at the development phase of a study. For an operational load case, the tilt measured at the tower top should have a mean value of less than 5° and a maximum value of less than 10°. Furthermore, the maximum acceleration measured at the tower top should be less than $0.3g$.

3.3 Possible damage cases for wind turbines

A floating wind turbine consists of several different sub-systems, each consisting of many parts with their respective failure rates. Consequently, a FOWT has many different failure modes, which may result in temporary or permanent loss of operability. The proceeding part will discuss some of the different failure modes associated with the different sub-systems.

Substructure failure

A substructure of a FOWT may fail in several ways, analogously to a floating O&G structure. In this context, the substructure is defined as the floater and, for simplicity, the tower. Generally, failures are divided into either loss of buoyancy, stability, or ability to carry its load. The latter category may be caused by exceedance of the load ULS, where failure modes such as yielding or buckling would be expected. Such failure could occur during extreme events induced by extreme waves or wind. Other failure modes may be related to the deterioration of the load-carrying capacity of the structure, either through fatigue or more extreme events such as fires.

The maximum structural responses in a semi-submersible are often not governed by the maximum wave heights and associated wave periods. Waves with shorter periods often give the governing structural response, e.g., periods with maximum split forces between the columns (DNV 2021b).

Parts of this thesis focus on damage cases related to loss of stability through flooding of compartments. This damage case will also include the loss of buoyancy because a floating structure must remain buoyant to remain stable. The investigated flooding may be caused by several events, where the most probable ones are collisions, wave slamming, cracks due to corrosion, or down-flooding through hull openings. As previously stated, when the number and size of offshore wind parks increase, it will lead to a higher probability of accidents caused by e.g. collisions or fabrication failures.

The doctoral thesis by Kong (2009) investigates the dynamic stability of a damaged ship in beam sea waves, focusing on the time until capsizing. A potential theory approach is used to study the wave-induced ship motions while accounting for water flowing through an opening in the hull. Different flooding scenarios are studied with different methods depending on the compartment filling level and the level of fidelity, namely, a rigid-lump mass model, a shallow-water solver, and a multimodal solver. By so, the thesis considers both the internal dynamics of flooding and the communication between the interior and exterior fluid domains. Kong (2009) also discussed the time and length scales of flooding. For instance, a compartment may be slowly filled by water run-up, causing down-flooding through small non-watertight openings. On the other hand, a compartment may be fully filled in seconds in the case of a collision.

If the level of compartmentalization is sufficient, the damaged ship may reach another equilibrium instead of capsizing. Siddiqui (2020) studied the behavior of ships after a new, damaged equilibrium has been reached. The thesis discusses both the static and dynamic effects of the damage. The static effects are related to loss of buoyancy and metacentric height, which will alter the natural periods of the system. Additional dynamic effects are described as vortex-shedding around and large flow through the opening, as well as sloshing and piston-mode resonance inside the compartment.

For a ship, Siddiqui (2020) found that the hydrodynamical loads differ greatly between the intact and the damaged condition, mainly caused by the piston mode resonance. Another important observation was the effect of air tightness in the compartment. For an airtight compartment, air compression at the top results in a behavior closer to the intact case.

Yu et al. (2022) investigated the collision between the OO-Star concrete semi-submersible with different-sized vessels. In their studies, they found that a collision may lead to both mooring line failure and capsizing. The most critical event was a collision during turbine operation from the opposite direction of the mean wind. In the master's thesis leading to the paper, Rypestøl (2020) found that the collision may also lead to localized hull damage, with subsequent flooding. Depending on the level of compartmentalization, the wind turbine will either capsize or find a new equilibrium.

A design load case considering response after the flooding of a compartment was included in the continued code comparison collaboration in IEA Wind Task 30 presented in Robertson, J. Jonkman, Vorpahl et al. (2014). In their study, several different companies and institutions simulated different load cases involving the OC4-DeepCwind semi-submersible concept, with the overall aim of comparing the results from different aero-hydro-servo elastic codes utilizing different theories in the different parts of the concept. The OC4-DeepCwind semi-submersible, defined in Robertson, J. Jonkman, Masciola et al. (2014) and shown in Figure 3.3a, is designed to support the National Renewable Energy Laboratory (NREL) 5 MW turbine. It is a four-column substructure with three larger radial columns and a smaller center column supporting the tower. The upper part of the radial columns has a diameter of 12 m while the lowest 6 m has an increased diameter of 24 m. The concept features fluid ballast placed in both the upper and lower part of the radial columns as shown in Figure 3.3b.

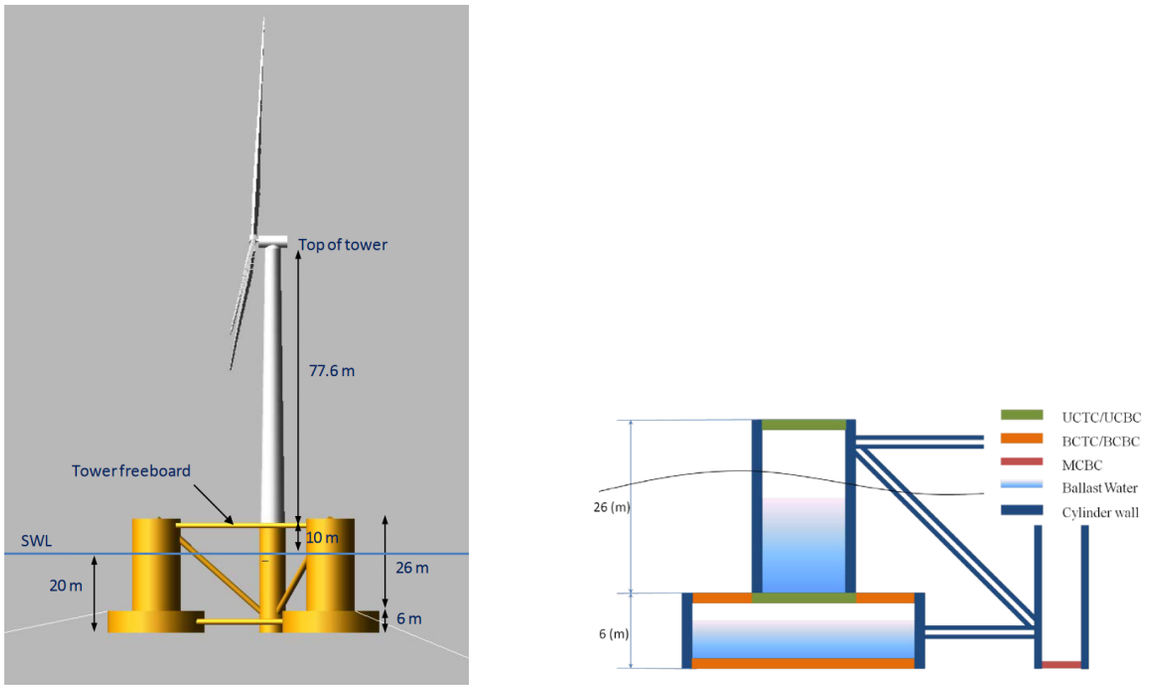

(a) Concept sketch

(b) Ballast filling

Figure 3.3: OC4-DeepCwind concept
Source: Robertson, J. Jonkman, Masciola et al. (2014)

The damage case with flooding in Robertson, J. Jonkman, Vorpahl et al. (2014) is modeled by adding water to the already partially ballast-filled radial columns. The damaged column was not entirely flooded, as compartmentalization of the column was assumed. The paper did not describe the applied compartmentalization and filling levels and included fluid effects. In the simulations, a turbulent wind field with a mean hub speed of 8 m/s and an irregular sea state with (H_s, T_p, γ) = (6 m, 10 s, 2.87) was considered. Their results showed that the effect of flooding on their setup was insignificant and it was debated whether the assumed filling levels were too small.

Global stability

There is an ongoing discussion as to whether a wind turbine should remain buoyant and stable after losing the integrity of the outer hull. The requirement for design against flooding of multiple compartments results from adopting design codes from previous offshore technology to the floating wind turbines. Such design codes are applied to prevent loss of life and environmental harm and may therefore be too strict for FOWTs. Arguments could be made regarding the safety of personnel during the frequent IMR operations, but such operations are limited in terms of environmental variables like other marine operations. Others argue that IMR operations imply that ships travel inside the wind park, increasing the risk of ship collisions. One could also imagine scenarios where wind parks are next to sea lanes, resulting in a higher risk of collision with larger merchant ships. Lastly, the capsize and sinking of a floating offshore wind turbine will have other, less dramatic consequences than the ones discussed above, such as economic and reputational consequences. Local authorities could require that sunken turbines shall be removed due to pollution through lubrication and microplastics or due to navigational hazards, which would be very costly (Cruz and Atcheson 2016). Loss of reputation can be very harmful to companies and their chances of winning contracts and concessions. Moreover, it might also harm the reputation of the floating wind industry, particularly in terms of public and political support.

DNV-ST0119 states that sufficient floating stability for a FOWT is an absolute requirement in intact condition. In other words, it is required that the turbine must remain stable during power production, survival conditions, and wind turbine fault conditions. In general, a consequence class of 1 applies to the event of capsize, since FOWTs are unmanned in severe sea states. Damage stability is, however, not mandatory but shall be considered as an option. During the analysis of the stability, all variable masses should be considered, including internal ballast water.

There is a large difference in whether damage stability is required in the design codes. ClassNK has one of the strictest regulations in terms of damage stability for FOWTs, as specified in ClassNK (2019). This standard explicitly specifies that the structure should be partitioned by watertight decks and bulkheads, ensuring buoyancy and stability in the event of flooding of any compartment at risk of flooding. According to ClassNK a compartment that may be subjected to flooding is any compartment adjacent to the outer hull placed in the range from 5.0 m above to 3.0 m below the free surface. Furthermore, compartments with penetrations below the waterline (e.g. cable penetration), and compartments subjected to reaction forces from mooring lines and any other points where flooding is possible must also be regarded as exposed to flooding. In practice, this implies that most of the submerged structure should be compartmentalized. ClassNK further specifies that the wind turbine should have sufficient stability to withstand wind-heeling moments from any direction and all wave-induced motions when one compartment is flooded. The static waterline after flooding should be below any opening where water may ingress, and the damage stability should not be relaxed by considering the removal of water from the compartment through bailing, ballast adjustment, counterfilling of other compartments, or stabilizing mooring forces.

A transient stability analysis is an analysis of a condition in which an incident occurs. The standard differs between the stability analyzed as quasi-static by integration of moments or as stability in the time domain. The quasi-static method does not include damping from viscous effects or aerodynamic damping and is, in that context, conservative. The quasi-static approach must be taken about the structure's critical heeling axis. The righting moment should be calculated using a large-volume model and should not consider any restoring forces from the mooring system. When considering the static equilibrium between the righting- and overturning moment, it is stated in *DNV-ST0119* that watertight integrity should be ensured at the first intercept. It is also required that the righting moment is strictly positive between the first and second intercepts.

When stability is analyzed by investigating roll and/or pitch responses in the time domain, *DNV-ST-0119* states that nonlinear restoring forces should be considered in an adequate manner. Such nonlinear restoring forces may include changes in the waterplane stiffness at large inclination angles, nonlinear mooring forces, and frequency-dependent spring effects from internal fluids. The latter effect may both be destabilizing from the reduction of the metacentric height or either stabilizing or destabilizing, depending on the phase of sloshing effects. An example of a stabilizing effect due to internal fluid effects is anti-roll tanks, which are occasionally utilized on ships.

DNV-ST-0119 advises that the safety level of the structure may be increased by ensuring that watertight integrity is maintained after a collision or that the structure remains buoyant and stable after damage through adequate compartmentalization. As a non-linear Finite Element Method (FEM) collision analysis, with a deformable ship and FOWT, is extremely computationally expensive, it might be a desirable solution to include compartments around the collision-prone areas.

Turbine Failure

Turbine failures are the type of failure that is expected to occur most frequently. For turbines, a failure is often defined as a permanent loss of the ability to produce power. One often distinguishes between faults and failures, where a fault is an unpermitted deviation from the acceptable operating condition (Isermann and Ballé 1997). Therefore, one should try to detect faults before they become failures, which a supervisory control system may do.

Wind turbine failures may be caused by a failure in any sub-system, such as the generator, the blade pitch actuators, the yaw system, and the gearbox. Other failures, such as blade impacts or overspeeding, may also be critical for the turbines. Sarlak and Sørensen (2016) showed that a broken blade or blade fragment might fly as long as 1000 m for a large turbine operating at a tip speed of 100 m/s.

The investigations of Wilkinson (2011) showed that the pitch actuator system had both the highest failure rate and the highest contribution to lost operating hours. Failure of the pitch actuator is very important for the global loads experienced by the structure. If the failure happens during operation, the control system loses the ability to control the loads on the blade. One would also lose symmetry in the rotor plane, which may lead to greater yaw excitation for the structure.

Mooring line failure

Mooring line failure refers to the failure of the station-keeping system, which for most FOWT consists of catenary or taut mooring lines. As for most failures involving offshore wind turbines, the consequence of a position loss is much less severe compared to a floating hydrocarbon installation with attached risers. The loss of a single mooring line for a system with multiple mooring lines would lead to a horizontal drift of a couple of hundred meters and most probably damage the umbilical and the perhaps the remaining mooring lines. Neighboring turbines are usually placed about 8-10 rotor diameters away to avoid wake interaction. One would, therefore, not consider a mooring line failure as a threat to other installations and could argue for applying the consequence class 1 described in DNV (2021c).

According to DNV (2019a), it may not be straightforward to define the redundancy of the mooring system. As a guidance note, the recommended practice suggests that the dynamic behavior of the FOWT should be investigated, as loss of a mooring line can lead to both increased and decreased tensions in the remaining lines. It is further stated that the mooring system may be defined as redundant if the remaining lines are found to survive a joint sea state with a one-year return period. If this condition does not hold, the structure should be designed according to consequence class 2.

Compared to the rules stated by Det Norske Veritas (DNV), the Japanese laws are found to be much stricter. According to Kikuchi and Ishihara (2019), they require absolute redundancy of the mooring lines in the ALS. In most cases, the practical meaning of this will involve additional lines. As the station-keeping system is a relatively expensive part of the system, this will involve an increased CAPEX.

A design load case considering the loss of a mooring line was included in the code comparison collaboration in IEA Wind Task 30 presented in Robertson, J. Jonkman, Vorpahl et al. (2014). In the load case concerning mooring line loss, they considered a steady uniform wind field with a hub wind speed of 18 m/s combined with aligned regular Airy waves with 6 m height and 10 s period propagating along the mean surge direction of the substructure. At a stage of the simulation, one of the downwind mooring lines with a 60° to the wind-wave direction is lost. Their result describes a transient roll response followed by a large offset in the horizontal plane. The article stresses that the concern in such damage cases is that a large yaw motion is seen, which causes twisting and tangling of the remaining mooring lines. This response was not seen for the analyzed concept, and the drift-off was characterized by a minimal yaw response.

Power cable failure

According to Acteon, a global marine engineering conglomerate, approximately 80% of the economic losses and insurance claims in the offshore wind industry are related to power cable failures (Acteon 2021). Failure modes can be related to several causes, among them installation, manufacturing, fatigue, and ultimate strength. Due to the larger motions associated with floating substructures, failure modes can be related to several additional events. Henrik Reiten, Wind Energy Engineer at 4Subsea, suggested that a rough guideline for horizontal offsets, representing 25-35% of the water depth, can be considered to prevent damage to the power cable (personal communication, May 21st, 2023). However, it is important to note that this estimate requires further examination and confirmation considering factors such as the cable's design and configuration.

CHAPTER 4

Theory

In this chapter, the theory applied in the subsequent modeling and analysis of the FOWTs is presented. First, the theory behind the statistical model of site-specific environmental conditions is presented. In addition, the theory behind the calculation of the loads experienced by the structure is discussed. The focus is on hydrodynamic loads relevant to the exterior domain as well as to internal fluids, although some supporting theory related to aerodynamics and wind turbine control is included as well. Lastly, the representation of the problem in the frequency domain and the time domain is discussed.

4.1 Environmental description

The environmental conditions considered in this thesis comprise the joint action of ocean waves, wind, and currents. This section describes the mathematical formulation of the environmental conditions and how they may be sampled and described statistically.

4.1.1 Waves

In this thesis, it is assumed that ocean waves may be described within linear wave theory. Linear waves are described as sinusoidal functions propagating in time and space. Such waves may be shown to satisfy the free-surface condition of the boundary value problem described in 4.3.1 (Faltinsen 1990). When looking at a real-life sea state, it is apparent that a single sinusoidal wave may not describe the waves. Therefore, a common approach is to consider irregular waves, which is a linear sum of a finite number of sinusoidal waves with varying amplitude and frequency and uniformly distributed phases. Equation (4.1) shows the expression of a long-crested irregular wave, ζ, consisting of N components propagating along the spatial x-direction and in time t. Long-crested means that the crests have an infinite extent and are normal to the direction of propagation.

$$\zeta(x,t) = \sum_{i=1}^{N} \zeta_{A,i} \sin\left(\omega_i t - k_i x + \epsilon_i\right) \tag{4.1a}$$

$$\omega_i^2 = k_i \cdot g \tanh\left(k_i h\right) \tag{4.1b}$$

where: $\zeta_{A,i}$ = Amplitude of component i
ω_i = Circular frequency of component i
k_i = Wave number of component i
ϵ_i = Phase of component i
N = Number of wave components
g = Gravitational acceleration
h = Water depth

The amplitudes of the wave components can be found from the energy content of the corresponding wave spectrum, $S_{\zeta\zeta}$, at the particular frequency. The wave spectrum may be found as a Fourier transform of the autocorrelation of the zero-mean Gaussian surface process. Unlike the time series, the autocorrelation goes to zero as the time separation goes to infinity, which makes it applicable to the Fourier transform. The mathematical result of a Fourier transform yields both positive and negative frequencies, but for practical applications, only the positive part of the spectrum with twice the energy content is considered.

The relation between the spectrum along the frequency axis and the surface process along the time axis may be seen in Figure 4.1. An irregular wave with amplitudes from a wave spectrum is presented in eq. (4.2).

$$\zeta(x,t) = \sum_{i=1}^{N} \sqrt{2S(\omega_i)\Delta\omega}\sin\left(\omega_i t - k_i x + \epsilon_i\right) \tag{4.2}$$

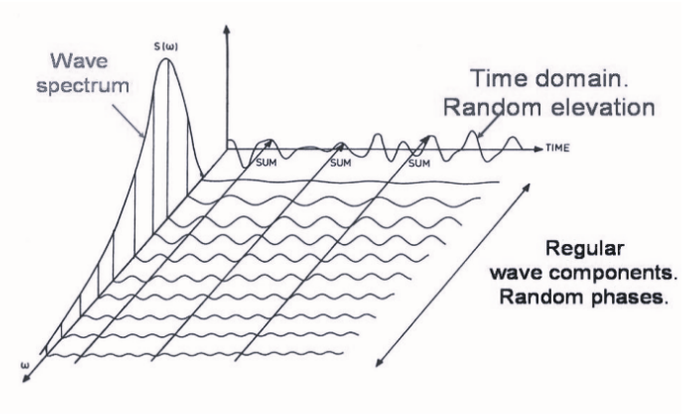

Figure 4.1: Frequency- and time axis of an irregular wave process
Source: Faltinsen (1990)

A commonly applied parameterization of wave spectra in the North Sea is the Joint North Sea Wave Project (JONSWAP) spectra. The JONSWAP spectrum is a modified form of another famous wave spectrum named the Pierson-Moskowitz (PM) spectrum. The difference between them is that the PM spectra consider fully developed sea states, while the JONSWAP spectra consider limited fetch lengths. The PM spectrum is re-obtained from a JONSWAP spectrum by setting the peakedness parameter $\gamma = 1$ in the JONSWAP spectra (Næss and Moan 2012). The parameterization of the JONSWAP spectra may be seen in eq. (4.3). It should be noted that in the original parameterization, the spectrum parameter $\tilde{\alpha}$ was related to the mean wind speed and a wind fetch parameter. In this thesis, the parameterization in terms of $\mathrm{H_s}$ and $\mathrm{T_p}$ given in Næss and Moan (2012) is applied.

$$S^{+}_{\zeta\zeta}(\omega) = \frac{\tilde{\alpha}g^2}{\omega^5}\exp\left[-\frac{5}{4}\left(\frac{\omega_p}{\omega}\right)^4\right]\gamma^{a(\omega)} \tag{4.3a}$$

$$a(\omega) = \exp\left[-\frac{1}{2\sigma^2}\left(\frac{\omega-\omega_p}{\omega_p}\right)^2\right] \tag{4.3b}$$

$$\sigma = \begin{cases} \sigma_a = 0.07 & \text{if } \omega \leq \omega_p \\ \sigma_b = 0.09 & \text{if } \omega > \omega_p \end{cases} \tag{4.3c}$$

$$\tilde{\alpha} = 5.058\frac{H_s^2}{T_p^4}\left(1 - 0.287\ln\gamma\right) \tag{4.3d}$$

where: $S^{+}_{\zeta\zeta}(\omega)$ = Positive-frequency part of wave spectrum
H_s = Significant wave height
$T_p = \dfrac{2\pi}{\omega_p}$ = Spectral peak period
γ = Peakedness parameter

As seen from the wave spectrum parameters, the short-term sea state may be described by three parameters, namely H_s, T_p, and γ. The significant wave height is traditionally defined as the mean of the 1/3 largest wave heights in a sea state. The energy content of the spectrum may also be used to obtain an estimate of H_s as seen in eq. (4.4).

$$H_s \approx H_{m0} = 4\sqrt{m_o} \tag{4.4}$$

where: $m_0 = \int_0^\infty S(\omega)d\omega =$ Zeroth spectral moment.

The spectral peak period is defined as the period where the spectrum takes its maximum value. According to DNV (2018), it may be related to the mean zero-up crossing period of the surface process, T_z, by using the peakedness parameter as shown in eq. (4.5).

$$T_z = T_p\sqrt{\frac{5+\gamma}{11+\gamma}} \tag{4.5}$$

For the assumed zero-mean Gaussian surface process, the mean zero-up crossing period may be found using the standard deviation of the stochastic process and its derivative, which may be expressed using the zeroth and second spectral moments, as shown in eq. (4.6) (Næss and Moan 2012).

$$T_z = \frac{2\pi\sigma_\zeta}{\sigma_{\dot{\zeta}}} = 2\pi\sqrt{\frac{m_2}{m_0}} \tag{4.6}$$

where: $m_i = \int_0^\infty \omega^i S(\omega)d\omega =$ i'th spectral moment

Following DNV (2021c), the peakedness parameter of the JONSWAP spectrum may also be parameterized by the significant wave height and the spectral peak period as presented in eq. (4.7).

$$\gamma = \begin{cases} 5 & \text{for } \dfrac{T_p}{\sqrt{H_s}} \leq 3.6 \\ \exp\left(5.75 - 1.15\dfrac{T_p}{\sqrt{H_s}}\right) & \text{for } 3.6 < \dfrac{T_p}{\sqrt{H_s}} \leq 5 \\ 1 & \text{for } 5 < \dfrac{T_p}{\sqrt{H_s}} \end{cases} \tag{4.7}$$

4.1.2 Wind

For a FOWT, it is crucial to represent the wind field accurately. When considering the wind speed at a fixed point in space, one will see diurnal, seasonal, and yearly variations in wind speed. For Northern Europe, the diurnal cycle of the wind speed peaks around noon and takes its minimum around midnight. The solar heating of the air layers close to the ground causes this pattern. It may change depending on the local terrain and is expected to be less prominent when moving further offshore. Seasonal variations give higher mean wind speeds in the autumn-winter and lower wind speeds in the spring and summer (Cruz and Atcheson 2016). An increasing concern is also placed on the effect of climate change on environmental conditions, especially when considering the placement of wind parks with design lives exceeding 25 years. To distinguish from regular yearly fluctuations, measurements of a minimum of 30 years are advised for such concerns (Cradden et al. 2012).

The wind speed is commonly described as the sum of a mean component and a fluctuating component. Within a single location, the mean component is described only as a function of altitude in a reference system with the x-axis along the mean wind direction, while the fluctuating components have both spatial and temporal variation (Myrhaug 2006).

$$\mathbf{V}(\mathbf{x},t) = \left(\bar{V}(z) + v_x(x,y,z,t)\right)\ \hat{\mathbf{i}} + v_y(x,y,z,t)\ \hat{\mathbf{j}} + v_z(x,y,z,t)\ \hat{\mathbf{k}} \tag{4.8}$$

where: $\mathbf{V}$ = Wind speed vector, as a function of time and space
$\bar{V}$ = Mean wind speed, as a function of altitude
v_i = Fluctuating wind component in i direction, as a function of time and space

The relationship between mean wind speed and height over ground is as expected. When the wind blows over the ground, that be land or water, a boundary layer affects the velocity of the wind. This effect is commonly referred to as wind shear and is an important effect for wind turbines. Taller turbines will experience higher mean wind speeds, which may be considered a non-linearity in the upscaling of wind turbines. For a large turbine, the wind shear also introduces a cyclic turbine loading as the blade passes through a larger wind speed in the top position compared to the bottom position (Cruz and Atcheson 2016). The effect of altitude on the mean wind speed is assumed to be described by the power law profile, as shown in eq. (4.9). The power law is an approximation of the logarithmic profile describing the boundary layer along a flat plate (Burton et al. 2001). The power law factor defines the shape of the profile, and its value is defined according to the wind model applied in the simulated load cases. Sathe et al. (2013) considered the effect of wind profile and atmospheric stability on turbine loads. Although this article used more sophisticated wind profiles than the power law profile, some general conclusions may be reached. The shape of the profile, and hence the power law coefficient, differ greatly depending on the stability of the atmosphere. For the considered profiles, Sathe et al. (2013) found that the choice of the profile had a limited effect on the turbine loads, while the atmospheric stability had a larger effect.

$$\bar{V}(z) = \bar{V}_{10}\left(\frac{z}{10}\right)^{\alpha} \tag{4.9}$$

where: $\bar{V}_{10}$ = Mean wind speed, at 10 m reference height
α = Power law factor

Turbulent oscillations in the wind speed occur at a range of length- and time scales. Usually, turbulence is defined as fluctuations within periods of seconds and minutes. From a wind turbine perspective, such fluctuations are unwanted as they introduce variability in power production, as well as increased loads and fatigue damage. A benefit of offshore wind is higher mean wind speeds and less turbulence due to the low roughness of the ocean surface compared to land (Cruz and Atcheson 2016). For a spatial and temporal description of turbulence, Taylor's frozen turbulence hypothesis is often used. Taylor's hypothesis states that the large-scale turbulent eddies in the wind have no evolvement in time and are instead convected downstream with the velocity of the mean wind speed. Full three-dimensional wind fields may therefore be defined as a time series of 2D turbulent grids of width W and height H. Alternatively, it may be visualized as a 3-dimensional turbulent grid moving through the wind turbine with a velocity equal to the mean wind speed as shown in Figure 4.2. In each grid point, the three wind velocity components are defined. This approach is found to be a good assumption for large wind turbines (Schlipf et al. 2010).

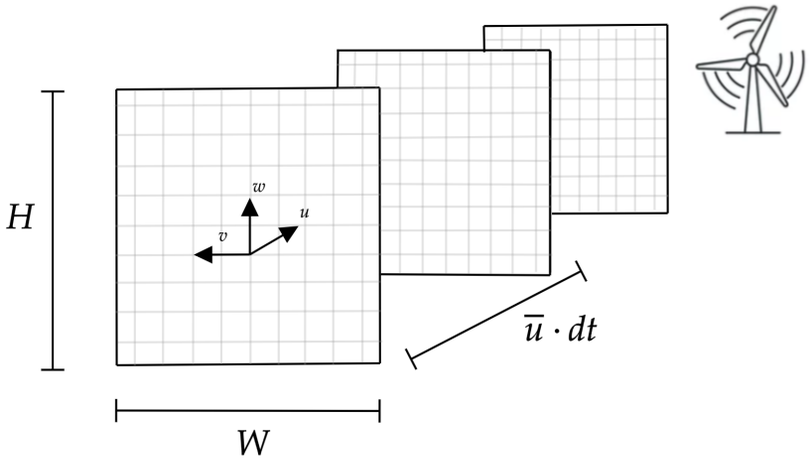

Figure 4.2: Schematic of the frozen turbulence hypothesis

Along the time dimension, turbulence is often described based on a spectral approach, whereas coherence models describe its spatial variation. The IEC recommends applying the Kaimal spectrum, as defined in eq. (4.10). Coherence is defined using the cross-spectral density between the turbulent fluctuations at two points, and it is generally a function of frequency and the separation of the points. E. E. Bachynski-Polić and Eliassen (2019) found that the choice of coherence model significantly impacts the global rigid-body response of the FOWT. This is explained by the time scales of the coherent structures overlapping with the long natural periods of catenary-moored structures.

$$\frac{fS_k(f)}{\sigma_k^2} = 4\frac{\frac{fL_k}{U_{hub}}}{(1+6\frac{fL_k}{U_{hub}})^{5/3}} \tag{4.10}$$

where: f = Frequency, in Hz
S_k = Spectrum, positive frequency side
σ_k = Wind velocity standard deviation
L_k = Integral scale component
U_{hub} = Hub wind speed
k = Direction index

In the Kaimal wind model, the Kaimal spectrum is applied along with an exponential coherence function. It should be noted that the Kaimal wind model only includes coherence in the longitudinal velocity components. The definition of coherence and the exponential coherence function of the Kaimal wind model defined in IEC 61400-1 may be seen in eq. (4.11) (Burton et al. 2001; IEC 2019a).

$$C_{ij}(\Delta r, f) = \frac{|S_{ij}(f)|}{\sqrt{S_{ii}(f)S_{jj}(f)}} = \exp\left[-12\left(\left(\frac{\Delta r \cdot f}{U_{hub}}\right)^2 + \left(\frac{0.12\Delta r}{L_c}\right)^2\right)\right] \tag{4.11}$$

where: C_{ij} = Complex-valued coherence
Δr = Length of projection of separation vector between point i and j on to the plane perpendicular to the mean wind speed
f = Frequency, in Hz
$L_c = 8.1\Lambda$ = Coherence scale parameter
Λ = Turbulence scale parameter

In addition, one defines a turbulence intensity factor, TI, which compares the variations of the wind to the mean wind speed. The turbulence intensity is defined as the ratio of the standard deviation to the mean wind speed.

$$TI = \frac{\sigma}{\bar{V}} \tag{4.12}$$

where: σ = Standard deviation of wind speed

4.1.3 Current

According to DNV (2019b), the current velocity may vary in magnitude and direction in both time and space. The temporal variation is due to turbulent fluctuations, but the recommended practice states that the current may be assumed steady in time for most applications. The current velocity is found as the vector sum of components with various physical origins, such as wind-driven currents, tidal currents, and circulation currents. In the absence of site-specific data, the wind-driven current at the still water level can be assumed to be a function of the mean wind speed at 10 m altitude.

$$v_{c,wind}(z=0) = k\bar{U}_{10} \tag{4.13}$$

where: v_c = Current speed, as a function of submergence
$k \in [0.015, 0.3]$ = Wind current coefficient

The vertical variation of the current velocity in the water column may be taken as a linear profile over the upper 50 m as shown in eq. (4.14).

$$v_{c,wind}(z) = v_{c,wind}(z=0)\left(\frac{d_0+z}{d_0}\right) \quad \text{for } z \in [-d_0, 0] \tag{4.14}$$

where: z = Vertical distance from mean free surface, positive upwards
$d_0 = 50\,\text{m}$ = Current cut-off depth

4.1.4 Hindcast

By hindcasting, one refers to the simulation of historical events using a numerical model. In the context of environmental modeling, these numerical models typically describe the response of the atmosphere and ocean based on a set of initial- and boundary conditions. The input to an environmental hindcast model is typically the results from a global or regional atmospheric reanalysis. Generally, an atmospheric reanalysis is a result of a numerical weather model where one uses historical in-situ measurements of the climate to simulate the environment on a finer grid. As such, the gaps between the measurements are filled in by the numerical model (ECMWF 2020).

NORA10EI

NORA10EI is a regional downscaling of the global ERA-Interim reanalysis in the Norwegian, North, and Barents Seas. The ERA-Interim reanalysis covers the period from 1979-2017 and is continually updated. NORA10EI differs from NORA10 by using the ERA-Interim Reanalysis instead of the ERA-40 (1957-2002) reanalysis. NORA10 have later been extended to the present time using separate operational analyses by ECMWF. The motivation behind making NORA10EI was to have a hindcast from a single data set and not two separate data sets as for the NORA10. Both the NORA10 and the NORA10EI hindcasts use the same wave model, where winds at 10 m altitude are used to force a 50-km resolution wave model, which is further used as boundary conditions for a 10-km wave model. The temporal resolution of the model is 1 hour (Haakenstad, Breivik, Reistad et al. 2020).

NORA3

NORA3 is another hindcast, downscaling the ERA5 reanalysis in the Norwegian, North, Barents, and Baltic seas. ERA5 is a more modern reanalysis compared to ERA-40 and ERA-Interim. The hindcast has a spatial resolution of 3 km and a temporal resolution of 1 hour. The increased resolution of the model is beneficial because extreme values are biased toward lower values for coarser reanalyses (Haakenstad, Breivik, Furevik et al. 2021). Simulations regarding extreme sea states will thus be more conservative when using a hindcast based on a finer resolution.

The NORA3 hindcast has also been used to force a wave model with spatial and temporal resolution similar to the original hindcast. The wave hindcast must be accessed separately from the NORA3 data and is available under the “NORA3 - Winsurfer” project.

4.2 Statistical analysis

Due to the stochastic nature introduced by the randomness in the environmental conditions, statistical analysis must be performed. The environmental conditions, and thus the responses of the FOWT, are governed by aleatory uncertainties. An aleatoric uncertainty is an uncertainty that is inherent in the process, which may not be eliminated with additional information about the process. If the applied data set is of acceptable quality, one can apply statistical inference to infer properties from the stochastic sample to the underlying distribution. The sample quality is inter alia determined by sample size, statistical independence, and identical boundary conditions (Haver 2019).

Due to the dynamic response of FOWTs being determined by a nonlinear combination of the present and past values of multiple parameters, such as the wave height, wave period, and wind speed, a jointly simulated sea state must be applied in the time domain. In the O&G industry, a common approach has been to analyze the structure under the influence of simultaneous environmental variables of a particular return period without taking into account the correlation of the variables. However, by applying a joint distribution of the relevant environmental variables, one can calculate the set of environmental variables expected to occur jointly with a specified return period. When considering the correlation, one obtains a more correct, less conservative approach that allows for leaner designs (Johannessen et al. 2001). For the offshore wind industry, where economic margins are tighter and accidents have less severe consequences, this is especially beneficial.

A long-term condition may be defined as a series of short-term conditions, each weighted by their respective probability. A short-term condition is defined as a condition characterized by the stochastic processes of interest being stationary and homogenous. If the stochastic environmental process is assumed Gaussian, it may be entirely specified by the first- and second-order moments, namely, the mean and variance. For such a condition, a spectrum may fully describe the stochastic processes. In a short-term condition, the wind speed may be considered stationary for reference periods of 10 min to 1 hour. In comparison, waves are typically considered stationary for reference periods of 1 hour to 3 hours. Therefore, a reference period of 1 hour is used for simulations of simultaneous wind and wave fields in the offshore wind community.

4.2.1 Marginal distribution of mean wind speed

For the marginal distribution of the one-hour mean wind speed at 10 m altitude, a two-parameter Weibull distribution is proposed. The Weibull distribution is defined by the shape parameter α_U and the scale parameter β_U. The probability density function (PDF) and cumulative density function (CDF) of the marginal distribution may be seen in eq. (4.15) and eq. (4.16), respectively.

$$f_{U_w}(u) = \frac{\alpha_U}{\beta_U}\left(\frac{u}{\beta_U}\right)^{\alpha_U - 1} \exp\left[-\left(\frac{u}{\beta_U}\right)^{\alpha_U}\right], \quad u \geq 0 \tag{4.15}$$

$$F_{U_w}(u) = 1 - \exp\left[-\left(\frac{u}{\beta_u}\right)^{\alpha_u}\right], \quad u \geq 0 \tag{4.16}$$

4.2.2 Joint distribution of significant wave height and spectral peak period

To estimate sea states of a certain return period, characterized by a combination of a H_s and T_p, a joint probability distribution was formulated using the multiplication rule of probability. This formulation may be done by considering a marginal distribution of H_s, and a conditional distribution of the T_p, as H_s is often characterized as the dominant variable among the two.

$$f_{H_s,T_P}(h,t) = f_{H_s}(h) \cdot f_{T_p|H_s}(t|h) \tag{4.17}$$

Marginal distribution of significant wave height

For the marginal distribution of H_s in the joint distribution of H_s and T_p, a hybrid log-normal-Weibull model may be applied, referred to as the LoNoWe model. This model was first proposed by Haver (1980) and has also been applied in, for example, Moan et al. (2005), Li et al. (2013), and Cheng et al. (2019).

The model is suitable for samples that follow a log-normal model in the lower tail but a Weibull model in the upper tail. The transition point between the two underlying models is defined as another distribution parameter η. It is important to establish a reliable procedure for establishing the value of η, as this may have a significant effect on the extreme values (Moan et al. 2005). The PDF of the LoNoWe model is shown in eq. (4.18), while the CDF is shown in eq. (4.19).

$$f_{H_s}(h) = \begin{cases} \frac{1}{\sqrt{2\pi}\sigma_{H_s} h} \exp\left[-\frac{1}{2}\left(\frac{\ln h - \mu_{H_s}}{\sigma_{H_s}}\right)^2\right] & \text{if } h \leq \eta \\ \frac{\alpha_{H_s}}{\beta_{H_s}}\left(\frac{h}{\beta_{H_s}}\right)^{\alpha_{H_s}-1} \exp\left[-\left(\frac{h}{\beta_{H_s}}\right)^{\alpha_{H_s}}\right] & \text{if } h > \eta \end{cases} \tag{4.18}$$

$$F_{H_s}(h) = \begin{cases} \Phi\left(\frac{\ln h - \mu_{H_s}}{\sigma_{H_s}}\right) & \text{if } h \leq \eta \\ 1 - \exp\left[-\left(\frac{h}{\beta_{H_s}}\right)^{\alpha_{H_s}}\right] & \text{if } h > \eta \end{cases} \tag{4.19}$$

Conditional distribution of peak spectral period

A common choice for the conditional distribution of T_p is the log-normal model. The model is defined by the mean and standard deviation of the natural logarithm of the population variable. The PDF and CDF are shown in eq. (4.20) and (4.21) respectively.

$$f_{T_p|H_s}(t|h) = \frac{1}{\sqrt{2\pi}\sigma_{\ln(T_p)}(h)t} \exp\left[-\frac{1}{2}\left(\frac{\ln(t) - \mu_{\ln(T_p)}(h)}{\sigma_{\ln(T_p)}(h)}\right)^2\right] \tag{4.20}$$

$$F_{T_p|H_s}(t|h) = \Phi\left(\frac{\ln(t) - \mu_{\ln(T_p)}(h)}{\sigma_{\ln(T_p)}(h)}\right) \tag{4.21}$$

where: Φ = Cumulative standard normal distribution

4.2.3 Joint distribution of mean wind speed, significant wave height and spectral peak period

The joint distribution of $\bar{U}_w$, H_s, and T_p may also be formulated using the multiplication rule of probability, shown in equation (4.22). The mean wind speed is chosen as the primary parameter due to the dominant effect on the total load on a FOWT. Therefore, the mean wind speed is formulated by a marginal distribution, while conditional distributions of the significant wave height and peak spectral period are used. The distributions formulated in Section 4.2.2 are hence reused in this model, but the parameters are parametrized considering the mean wind speed as well. The choice of the different distributions and fitting of the distribution parameters is generally based on the work of Li et al. (2013) and Johannessen et al. (2001).

$$f_{U_w,H_s,T_P}(u,h,t) = f_{U_w}(u) \cdot f_{H_s|U_w}(h|u) \cdot f_{T_p|U_w,H_s}(t|u,h) \tag{4.22}$$

Environmental contour lines and surfaces

To find the environmental conditions of a certain return period, the environmental contour method may be used. This method involves a transformation of the physical parameters into a space consisting of independent, standard Gaussian distributed variables. Such a transformation is often done by a Rosenblatt transformation, as illustrated in Figure 4.3. The transformation of the joint distribution of significant wave height and spectral peak period is shown in equation (4.23) while the transformation of the joint model of mean wind speed, significant wave height, and spectral peak period is shown in (4.24).

$$\begin{aligned} \Phi(v_1) &= F_{H_s}(h) \\ \Phi(v_2) &= F_{T_p|H_s}(t|h) \end{aligned} \tag{4.23}$$

$$\begin{aligned} \Phi(u_1) &= F_{U_w}(u) \\ \Phi(u_2) &= F_{H_s|U_w}(h|u) \\ \Phi(u_3) &= F_{T_p|H_s,U_w}(t|h,u) \end{aligned} \tag{4.24}$$

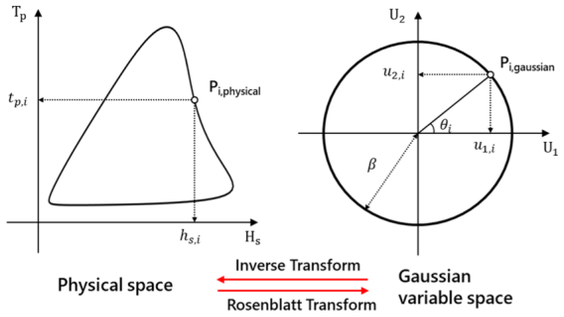

Figure 4.3: Tranformation between physical and standard normal space
Source: Choi et al. (2019)

As the variables in the standard normally distributed space are independent, the probability of a joint event may be found as the product of the individual probabilities. For a joint distribution consisting of two physical random variables (e.g., H_s and T_p), the equiprobable combinations will therefore be circles in the standard normally distributed space. If the extension to three physical random variables is made (e.g., U_w, H_s, and T_p), the equiprobable combinations form a sphere in the physical space. The equiprobable combinations in the standard normally distributed space are hence found by considering circles or spheres with a radius equal to the cumulative standard normal value of the probability associated with the relevant return period.

$$\Phi(\beta) = 1 - \frac{q}{N} \quad \Leftrightarrow \quad \beta = -\Phi^{-1}\left(\frac{q}{N}\right) \tag{4.25}$$

where: β = Radius in standard normally distributed space
q = Annual exceedance probability
N = Number of sea states in 1 year

4.3 Hydrodynamics

Under the continuum hypothesis, where one assumes a fluid to consist of infinitesimal fluid elements, the fluid can be described by a set of macroscopic properties such as density ρ, pressure p, temperature T, and viscosity μ (C. M. Larsen et al. 2009). To describe the dynamics of such a fluid, a velocity field, and the forces acting on it are needed. Said forces will in most cases be limited to body forces, mainly the gravitational force, and surface stresses, consisting of one pressure component and two tangential shear stress components. In an Eulerian description, the velocity field may be described by a three-dimensional vector that varies in both time and space (Newman 2017).

$$\mathbf{u}(\mathbf{x},t) = \mathbf{u}(x,y,z,t) = u(x,y,z,t)\ \hat{\mathbf{i}} + v(x,y,z,t)\ \hat{\mathbf{j}} + w(x,y,z,t)\ \hat{\mathbf{k}} \tag{4.26}$$

By applying the conservation of mass and momentum, adopting a Lagrangian approach in an inertial frame, and assuming the fluid as incompressible and Newtonian, the momentum equations (4.27) along with the continuity equation (4.28) may be derived.

$$\frac{D\mathbf{u}}{Dt} = \frac{\partial \mathbf{u}}{\partial t} + \mathbf{u}\cdot\nabla\mathbf{u} = -\frac{1}{\rho}p + \mathbf{g} + \nu\nabla^2\mathbf{u} \tag{4.27}$$

$$\nabla\cdot\mathbf{u} = 0 \tag{4.28}$$

Together, equations (4.27) and (4.28) comprise a set of four equations and four unknown variables ($\mathbf{u}$ and p). The Navier-Stokes equations are known as fundamental equations in fluid dynamics, and there exists no general analytical solution to the problem. Numerical attempts to solve the problem, commonly known as computational fluid dynamics (CFD), is a very active research area.

4.3.1 Potential flow theory

For marine applications, the fluid referred to is water, which is very well described under the assumption of incompressibility. If one further simplifies the problem by assuming an inviscid fluid (neglecting shear forces), the last term in (4.27) disappears, and the Euler equations remain. The final assumption leading to potential theory is the assumption of an irrotational flow, which means that the curl of the velocity field is zero.

$$\nabla\times\mathbf{u} = 0 \tag{4.29}$$

The two latter assumptions are needed for sufficient simplification of the problem, but it limits the analysis from considering viscous effects like skin friction, flow separation, and vortices. These are effects that are important in e.g., finding the resistance of an advancing vessel or predicting the level of damping during roll motion.

An identity from vector calculus states that the curl of the gradient of a scalar function is equal to zero. Thus, due to the curl of the velocity being zero, it can be described as the gradient of a scalar function ϕ.

$$\nabla\times\nabla\phi = 0 \qquad\qquad \nabla\times\mathbf{u} = 0 \tag{4.30}$$

$$\implies \mathbf{u} = \nabla\phi$$

The scalar function ϕ is referred to as the velocity potential, which simplifies the problem by combining the three unknown velocity components into one scalar. It also facilitates the transition from the continuity equation (4.28) into the Laplace equation and the Euler equations into the Bernoulli equation, using spatial integration. Through the velocity potential, the equation system is reduced from four equations and four unknowns into two equations with two unknowns, where the pressure is found from the velocity potential using the Bernoulli equation (4.32).

$$\nabla \cdot \mathbf{u} = 0 \implies \nabla^2\phi = \frac{\partial^2\phi}{\partial x^2} + \frac{\partial^2\phi}{\partial y^2} + \frac{\partial^2\phi}{\partial z^2} = 0 \tag{4.31}$$

$$p + \rho g z + \rho\frac{\partial\phi}{\partial t} + \frac{\rho}{2}\nabla\phi \cdot \nabla\phi = C \tag{4.32}$$

In eq. (4.32), a coordinate system with a vertical z-axis, positive upwards, is assumed. The constant C is a time-dependent arbitrary constant. The time dependence has been included in the velocity potential following the notation suggested in (Faltinsen 1990).

In potential theory, one aims to solve for the velocity potential, which leads to a boundary value problem. The Laplace equation is an elliptic equation that needs a closed domain with boundary conditions along all boundaries. Although the governing equation itself is linear, the boundary conditions in a free surface wave-body interaction problem do, in general, introduce non-linearities to the problem. Therefore, the problem is often linearized before solving. This is done through a perturbation approach, where the velocity potential, ϕ, and surface elevation, ζ, are rewritten as a power series of the wave steepness, $\epsilon = k\zeta_a$, which is considered small in linear potential theory. Furthermore, boundary conditions are transferred from their instantaneous position to their mean configuration using Taylor expansion (Greco 2022). The linearized boundary conditions applied for solving the boundary value problem are (Faltinsen 1990):

Body boundary condition

The body is considered impermeable. Thus, the fluid velocity must equal the body velocity at the body boundary.

$$\frac{\partial\phi}{\partial n} = \mathbf{U} \cdot \mathbf{n} \quad \text{on the body surface} \tag{4.33}$$

Seabed boundary condition

Similarly to the body, the seabed is considered impermeable. The seabed is also considered stationary, which leads to a simple Neumann boundary condition.

$$\frac{\partial\phi}{\partial n} = 0 \quad \text{on the seabed} \tag{4.34}$$

Kinematic free-surface condition

The kinematic free-surface condition specifies that a water particle initially at the free surface remains at the free surface.

$$\frac{\partial\zeta}{\partial t} = \frac{\partial\phi}{\partial z} \quad \text{on the mean free surface} \tag{4.35}$$

Dynamic free-surface condition

The dynamic free-surface condition states that the pressure on the free surface must be equal to the ambient pressure.

$$\frac{\partial\phi}{\partial t} + g\zeta = 0 \quad \text{on the mean free surface} \tag{4.36}$$

Far-field condition

If the problem is not enclosed by walls or seabed, a far-field condition is applied to provide a closed domain. The far-field conditions state that the radiated potential goes to zero far away.

Radiation condition

In addition, if the problem is in steady-state conditions, a radiation condition is required. This states that the waves are radiated away from the body.

When within linear potential theory, the wave-body interaction problem may be separated into the diffraction and radiation problems. This allows treating potentials with different physical explanations independently and finding the total solution by the superposition principle (Greco 2022). In the diffraction problem, a fixed body exposed to incident waves is examined. The relevant potentials are thus the incident velocity potential, ϕ_0, and the diffracted potential, ϕ_D. The former is connected to the incident waves as the body was not there, while the latter represents the disturbance of the body on the fluid. The velocity potential resulting from a single undisturbed harmonic wave is analytically known, as presented in eq. (4.37), while the diffracted potential must generally be solved numerically, except for simple cases.

$$\phi_0(x, y, z, t) = \frac{g\zeta_a}{\omega} \frac{\cosh\left(k\left(z+h\right)\right)}{\cosh\left(kh\right)} \cos\left(\omega t - kx + \epsilon\right). \tag{4.37}$$

To find the wave excitation loads, the dynamic pressure from the combined potentials is integrated over the body at its mean position, $S_{0,B}$. The loads associated with the incident potential are often referred to as the Froude-Kriloff loads, and the loads related to the diffracted potential are called diffraction loads. Note that the normal vector is pointing into to body. For a three-dimensional body, the load in rigid-body mode j is expressed as (Greco 2022):

$$F_{exc,j}(t) = -\int_{S_{0,B}} \rho \frac{\partial \phi_0}{\partial t} \mathbf{n_j} dS - \int_{S_{0,B}} \rho \frac{\partial \phi_D}{\partial t} \mathbf{n_j} dS = \Re\left\{ \int_{S_{0,B}} -i\omega e^{i\omega t} \rho \left(\varphi_0 + \varphi_D\right) \mathbf{n_j} dS \right\} \tag{4.38}$$

where: $\phi_k = \Re\{\varphi_k(\mathbf{x})\ e^{i\omega t}\}$, where k=0,D.

Alternatively, the excitation forces from the diffraction problem may be rewritten in terms of the incident and radiation potentials through a relation known as the Haskind relation. This formulation reads (Greco 2022):

$$F_{exc,j}(t) = \Re\left\{ \int_{S_{0,B}} -i\omega e^{i\omega t} \rho \left(\varphi_0 \frac{\partial \varphi_j}{\partial n} - \varphi_j \frac{\partial \varphi_0}{\partial n} \right) dS \right\} \tag{4.39}$$

The second problem is called the radiation problem, in which one considers forced oscillations of a body without incident waves. The velocity potential experienced when the body undergoes forced oscillations in rigid-body mode i is denoted ϕ_i, implying a total of six potentials to be solved for a freely floating body. The sum of all radiated potentials is referred to as the radiation potential ϕ_R.

When considering harmonic oscillations of a body, the velocity and acceleration will be perpendicular vectors in the complex plane. Hence, any point in the complex plane is therefore in the span of these complex vectors, and can therefore be expressed as a linear combination. This allows the description of the dynamic pressure forces on the body as coefficients multiplied by the body acceleration and body velocity, respectively. These coefficients depend, inter alia, on the oscillation frequency, and are referred to as the added mass and damping coefficients. As oscillations in any rigid body mode may give forcing to every mode, these coefficients are, in reality, 6 by 6 matrices for a freely floating body. The radiation force of a body in rigid-body mode i due to forced oscillations, η in modes j is described as (Greco 2022):

$$F_{rad,k}(\omega, t) = -\int_{S_{0,B}} \rho \frac{\partial \phi_R}{\partial t} n_k dS = \sum_{j=1}^{6} \left(-A_{kj}(\omega)\ddot{\eta}_j - B_{kj}\dot{\eta}_j\right) \tag{4.40}$$

The actual numerical solution of the boundary value problem (BVP) is found using the boundary element method. This method involves distributing sources with unknown densities on the discretized surfaces and solving integral equations by the use of a Green function. The description of the method may be found in (Faltinsen 1990, Chapter 4).

4.3.2 Higher-order potential theory

In the aforementioned perturbation approach, only terms linearly proportional to the wave steepness were retained. If the analysis is extended to include terms proportional to the wave steepness squared, a better approximate solution is obtained for steeper waves. In addition, the boundary conditions of the physical problem are better satisfied.

$$\phi = \underbrace{\phi_{(1)}}_{\propto\epsilon} + \underbrace{\phi_{(2)}}_{\propto\epsilon^2} + \underbrace{\cdots}_{\mathcal{O}(\epsilon^3)} \tag{4.41}$$

$$\zeta = \underbrace{\zeta_{(1)}}_{\propto\epsilon} + \underbrace{\zeta_{(2)}}_{\propto\epsilon^2} + \underbrace{\cdots}_{\mathcal{O}(\epsilon^3)} \tag{4.42}$$

Although the second-order loads are of smaller magnitudes, their characteristics may be important for the response of floating structures. When second-order effects in an irregular sea state with multiple wave frequency components are investigated, both mean, sum-frequency, and difference-frequency loads arise. The mean and slowly-varying difference frequency forces can be very important for the design of the mooring system (Faltinsen 1990), and difference-frequency effects may also affect wind turbines with long natural periods in heave, roll, and pitch. The sum-frequency effects can, on the other hand, excite elastic vibrations in the tethers of a TLP (springing) and should be investigated in terms of tank sloshing.

The representation of the second-order loads in the time domain is often done using quadratic transfer functions (QTFs). Following the definitions in Engebretsen et al. (2020), the slowly varying excitation force can be written as:

$$\begin{aligned}\mathbf{F^{(2)}}(t) = &\sum_{i=1}^{N}\sum_{j=1}^{N} \zeta_i^{(1)}\zeta_j^{(1)}\mathbf{P_{ij}} \cdot \cos\left(\left(\omega_i - \omega_j\right)t + \left(\epsilon_i - \epsilon_j\right)\right) \\ &+ \sum_{i=1}^{N}\sum_{j=1}^{N} \zeta_i^{(1)}\zeta_j^{(1)}\mathbf{Q_{ij}} \cdot \sin\left(\left(\omega_i - \omega_j\right)t + \left(\epsilon_i - \epsilon_j\right)\right)\end{aligned} \tag{4.43}$$

where: $\mathbf{P_{kl}}$ = Real part of QTF from the interaction between wave components k and l. $\mathbf{P_{kl}} = \Re\left(\mathbf{QTF}(\omega_k, \omega_l)\right)$
$\mathbf{Q_{kl}}$ = Imaginary part of QTF from the interaction between wave components k and l. $\mathbf{Q_{kl}} = \Im\left(\mathbf{QTF}(\omega_k, \omega_l)\right)$
$\zeta_k^{(1)}$ = Linear wave amplitude of wave component k
ϵ_k = Phase angle for wave component k.

The second-order loads may be further subdivided into two contributions, referred to as the quadratic and potential contributions, as shown in eq. (4.44). For completeness, it should also be stated that second-order loads may also arise from second-order body motions, but this is not included in the applied codes (Orcina 2023b).

$$\mathbf{F}^{(2)}(\omega_i, \omega_j) = \underbrace{\mathbf{F}_q(\omega_i, \omega_j)}_{\text{Quadratic part}} + \underbrace{\mathbf{F}_p(\omega_i, \omega_j)}_{\text{Potential part}} \tag{4.44}$$

The quadratic contribution consists of the quadratic terms from the first-order solution of the boundary value problem. In the horizontal translational modes, this contribution may be further separated in the following parts (Engebretsen et al. 2020; Greco 2022). For the remaining degrees of freedom, additional terms arise.

- Pressure loads from the first-order surface elevation relative to the body
- Correction of pressure due to first-order velocity
- Correction of pressure due to the product of gradient of linear pressure and linear motion.
- Contribution from first-order angular motions causing a time-varying normal vector, affecting the first-order forces.

There exist different methods for evaluating the quadratic part of the second-order wave loads:

Pressure integration method

The pressure integration method involves direct integration of the quadratic pressure terms on the instantaneous wetted surface of the hull and is as a result often referred to as the "near-field method". The method is capable of calculating the forces and moments for all degrees of freedom; however, it requires a high degree of mesh refinement, especially close to the mean water line and sharp corners (Engebretsen et al. 2020). For a body with wetted surface S_B and a normal vector pointing inwards, the direct pressure integration may be formulated as (Greco 2022):

$$\mathbf{F} = \int_{S_B} p\mathbf{n}dS = -\rho \int_{S_B} \left(\frac{\partial \phi}{\partial t} + \frac{1}{2}|\nabla \phi|^2 + gz \right) \mathbf{n}dS \tag{4.45}$$

Middle-field method

The middle-field method utilizes the conservation of momentum in a finite control volume surrounding the body. Similarly to the pressure integration method, it provides all six forces and moments but has a better mesh convergence (Engebretsen et al. 2020). The change in fluid momentum inside the control volume is equal to the sum of forces acting on the volume itself, the forces acting on its boundaries and the net flux of momentum passing through the surfaces. For a body enclosed by a finite control volume Ω with normal vector $\mathbf{n}$ pointing out of the volume and into the body, the force may be found as (Greco 2022):

$$\mathbf{F} = -\frac{d}{dt}\left(\int_{\Omega} \rho \mathbf{V} \partial \Omega \right) - \int_{S-S_B} p\mathbf{n}dS - \int_{\Omega} \rho g \mathbf{k} d\Omega - \int_{S} \rho \mathbf{V}(V_n - U_n)dS \tag{4.46}$$

where: Ω = Control volume
S = Control surface
S_B = Part of control surface located on body
$\mathbf{n}$ = Surface vector, positive out of the control volume
$\mathbf{k}$ = Vertical unit vector, positive upwards
V_n = Normal velocity out of control surface
U_n = Normal velocity of control surface

Far-field method

The far-field method is a simplification of the middle-field method, where one also considers the conservation of fluid momentum. The method only provides the horizontal forces and the yaw moment, and only the mean drift along the main QTF diagonal where the difference frequency is zero. The advantage of the method is the lesser computational effort and superior mesh convergence (Engebretsen et al. 2020).

The potential contribution consists of terms from the second-order solution and is only non-zero for $\omega_i \neq \omega_j$. These loads are obtained by considering the incident and diffracted parts of the second-order potential, and most commercial frequency-domain codes apply two different calculation methods. The first method, commonly referred to as the "direct approach", involves the integration of the second-order incident and diffracted potential. The second-order incident potential is analytically known, and hence unproblematic to calculate. Consequently, the main computational effort lies within the diffracted potential.

The alternative method denoted the "indirect approach", utilizes a formulation analogous to the Haskind relations for first-order loads, where the second-order loads are rewritten using the incident potential and the radiation potentials evaluated at the difference or sum frequency (Orcina 2023b). The latter method involves two different integrals, where the first is an integral over a discretized free surface surrounding the body. This component is slow to converge and thus requires a fine mesh over a large surface (Engebretsen et al. 2020). The second integral is over the wetted part of the body and involves both the second-order incident potential as well as the first-order difference frequency radiation potentials. The second computation is much less computationally demanding than the first and is expected to be the dominant contribution.

To reduce the computational burden of the free-surface integral, the frequency domain codes have introduced a three-layer free-surface model. The first layer is a circular portion of the free surface enclosing the body, discretized by panels in the same manner as the body boundary. This region is denoted the "inner region" in WADAM/WAMIT and "panelled zone" in OrcaWave. The integration over this layer is done by summation of the integrand evaluated at the panel centroid multiplied by the panel area. The second layer of the free-surface zone is referred to as the "intermediate region" (WADAM/WAMIT) or "quadrature zone" (OrcaWave), which relies on integration points instead of discretized panels. The integration is performed by using the Gaussian quadrature rule. The outermost layer is referred to as the "far-field" (WADAM/WAMIT) or "asymptotic zone" (OrcaWave), where the integrands are approximated by Fourier-Bessel asymptotic series (Orcina 2023b; WAMIT, Inc. 2013).

Hauteclocque et al. (2012) investigated the effect of different approximations on the calculation of the potential part of the full QTF on a LNG-carrier in both shallow and infinite water depths. Their investigations showed that the elimination of the free-surface integral reduced the computational time to 10 % while providing acceptable results for difference frequencies less than 0.15 rad/s.

Another famous approximation for the second-order difference frequency loads is the Newman approximation. This approximation completely disregards the second-order potential and uses only the mean-drift terms along the main diagonal of the quadratic part of the QTF. There exists a number of different variations of the Newman approximation, although the main idea is the same. The formulation of the Newman approximation given in Faltinsen (1990), presented in equation (4.47), utilizes an arithmetic mean, while the formulation applied in OrcaFlex, equation (4.48), uses a geometric mean. The imaginary part of the QTF, $\mathbf{Q_{ii}}$, is zero on the main diagonal, implying that the secondary difference-frequency loads will always be in phase with the wave component.

$$\mathbf{P_{ij}} = \mathbf{P_{ji}} = \frac{1}{2}\left(\mathbf{P_{ii}} + \mathbf{P_{jj}}\right) \tag{4.47}$$

$$\mathbf{P_{ij}} = \mathbf{P_{ji}} = \begin{cases} sign\{\mathbf{P_{ii}}\}\sqrt{|\mathbf{P_{ii}} \cdot \mathbf{P_{jj}}|} & \text{if } sign\{\mathbf{P_{ii}}\} = sign\{\mathbf{P_{jj}}\} \\ 0 & \text{if } sign\{\mathbf{P_{ii}}\} \neq sign\{\mathbf{P_{jj}}\} \end{cases} \tag{4.48}$$

The use of Newman's approximation comes with two great advantages. The first one is that there is no need for calculating the second-order potential, as only the quadratic terms from the first-order solution are used. Second, the double summation over every wave component in equation (4.43) is reduced to a single summation. This may significantly reduce the computational time during time-domain simulations, especially for a large number of wave components.

4.3.3 Loads due to viscous effects

One of the basic assumptions of potential flow theory is inviscid flow, which prevents the estimation of frictional stresses in the flow. In many problems, this is a good approximation because the normal pressure loads are of main importance. In other cases, like the rolling motion of a ship-shaped vessel or for steady flow around a circular cylinder, the response is governed by viscous effects.

For the floating wind turbines, slender Morison elements are used in addition to the panel model to include viscous drag. Morison's equation is a method originally formulated for calculating wave excitation on circular cylindrical members of O&G structures, but it may also be extended to be used for moving slender elements. The Morison formula is valid for cross sections that are slender compared to the wavelengths ($\frac{\lambda}{D} > 5$), where diffraction effects are negligible. Equation (4.49) shows the complete Morison equation, although only the drag contribution is considered in this thesis. The added mass and excitation force effects of the inertia terms are modeled within the 3D boundary element method.

$$f_N(t) = \underbrace{-\rho C_A A\ddot{\eta} + \rho\left(1 + C_A\right) Aa}_{\text{Inertia terms}} + \underbrace{\frac{1}{2} C_D D v_r |v_r|}_{\text{Drag term}} \tag{4.49}$$

The drag coefficient is, in general, dependent on the level of turbulence, characterized by Reynold's number, the relative motion between the body and waves, characterized by the Keulegan-Carpenter number, and the roughness of the object.

$$C_D = C_D(R_e, KC, \Delta) \tag{4.50}$$

where: R_e = Reynolds number
KC = Keulegan-Carpenter number
Δ = Non-dimensional surface roughness

In DNV (2019b), effect of the Keulegan–Carpenter (KC) number is included by the use of the wake amplification factor. This is a simplified method to adjust the drag coefficients of the steady flow based on the KC number. The formulation is based on a circular cross section, but the recommended practice states that it can be used with the steady-flow coefficients provided for non-circular cross sections. The adjustment procedure is shown in Equation 4.51.

$$C_D = C_{DS} \cdot \psi(KC) \tag{4.51a}$$

$$\psi(KC) = \begin{cases} C_\pi + 0.1(KC - 12) & 2 \leq KC \leq 0.75 \\ C_\pi - 1.00 & 0.75 \leq KC < 2 \\ C_\pi - 1.00 - 2.00(KC - 0.75) & KC \leq 0.75 \end{cases} \tag{4.51b}$$

$$C_\pi = 1.50 - 0.024\left(\frac{12}{C_{DS}} - 10\right) \tag{4.51c}$$

where: C_{DS} = Steady-flow drag coefficient
ψ = Wake-amplification factor

To describe the force by Morison's equation, a good description of the acceleration and velocity field is needed, something that is challenging in steep waves and above the mean free surface. When the drag term is important, an important non-linearity with higher order frequencies is included when integrating the force up to the instantaneous free-surface (Haver 2019). As the horizontal drag force is proportional to the horizontal particle velocity, which takes its maximum under wave crests, it may be important to introduce nonlinear wave kinematics either through second-order surface processes or nonlinear wave theories such as Stokes 5th or stream functions (Orcina 2023a). The second-order surface elevation has higher wave crests, shallower wave troughs, and steeper rises and is often described by introducing a correction to the first-order surface elevation (Haver 2019). For the case considered in this report, an important trade-off is identified. For practical analyses, one has to identify whether the diffraction effects are more important or whether one should use Morison's equation with nonlinear wave kinematics and try to integrate up to the instantaneous surface elevation. For most sea states, the potential theory approach is well suited, but may be unconservative in extreme sea states such as those considered in ALS.

4.4 Damping

There are many other scenarios where viscous effects matters. The rolling motion of a ship-shaped vessel or the steady flow around a circular cylinder is governed by viscous effects. As these drag forces act against and are proportional to the relative velocity between the body and fluid, they act as damping forces on body motions.

For wave frequency motion, the largest damping contribution arises from the free-surface waves radiated from the body. For low-frequency motions, the disturbance of the free surface is far less than for wave-frequency motions, and thus other damping contributions become important. For a FOWT, such damping contributions may be wave drift damping, viscous damping on substructure and mooring lines, and aerodynamic damping. For a semi-submersible with long natural periods, the response will often be governed by such effects.

The wave drift damping is a wave encounter effect on the low-frequency motion, where it is assumed that the vessel velocity is small relative to the wave velocity, such that a quasi-static approach is suitable. By considering the low-frequency motions of the vessels as slowly oscillating forward and backward speeds, the wave drift damping may be considered analogous to the added wave resistance of an advancing vessel. The effect of slow-drift damping is negligible on the standard deviation of the response but not negligible when considering extreme values (Faltinsen 1990).

In OrcaFlex, the low-frequency velocity of the wind turbine is relative to the current velocity applied. As such, the applied wave drift damping includes both the effect of the current on the drift loads, as well as the damping effect on the low-frequency motion. It is also important to mention that the effect is only applied in the translatory horizontal modes, as these are the modes most affected by wave drift (Orcina 2023a).

4.4.1 Internal fluid effects

According to Ludvigsen, Pan et al. (2013), there is an increasing demand to introduce fluid dynamics in compartments for offshore structures related to the petroleum industry, such as floating production, storage and offloadings (FPSOs) and semi-submersibles. The advantages of introducing these effects are a more accurate representation of the global responses and local cross-sectional loads. Designs with internal tanks of large horizontal extent may be severely affected by free surface effects and resonant sloshing modes. In addition, modeling the fluid may be crucial to get a correct representation of the moment of inertia. As most of the support structures for FOWTs are based on designs inspired by knowledge from the petroleum sector, one may assume that the inclusion of internal fluid dynamics may have similar advantages here.

Partially filled compartments may have a significant effect on the global motions if the sloshing periods are in the range of significant wave energy. Moreover, as global motions affect the mean-drift loads, the sloshing may thus affect such loads as well. The interaction between sway motion and internal sloshing was investigated experimentally and numerically by Rognebakke and Faltinsen (2003). Their numerical computations included both a nonlinear and a linearized multimodal approach. In their study, the relative phase between the external and internal wave systems was described, as may be seen in Figure 4.4.

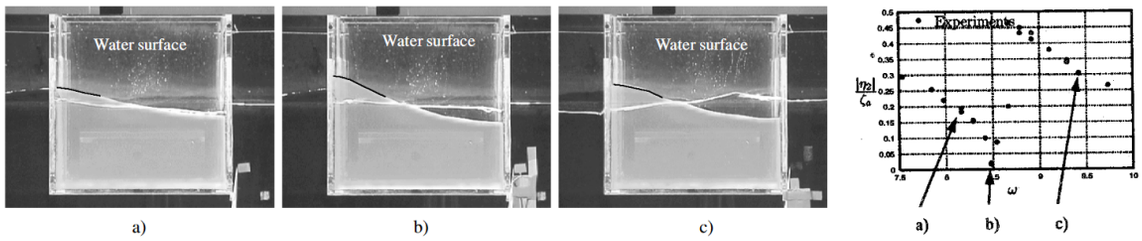

Figure 4.4: Phase between internal and external waves
Source: Rognebakke and Faltinsen (2003)

In Figure 4.4, it is seen that for frequencies lower than the resonant sloshing frequency, the internal wave is in phase with the external wave. At and above the sloshing frequency, a phase of 90° and 180° is observed, respectively. This is in agreement with the phases observed for a damped harmonic oscillator.

When considering linear sloshing, the dynamic effects are introduced as a modification of the added mass matrix. Within linear theory, the damping is zero, as the linear damping is connected with wave radiation. In reality, damping occurs through impacts on the tank roof and viscous effects on the boundary layers around the compartment walls (Rognebakke and Faltinsen 2003). These effects are not captured within linear theory. As a result, one expects the solution of the velocity potential to approach infinity at the exact natural frequency of the tank.

Rognebakke and Faltinsen (2003) suggest formulating the sloshing force as a frequency-dependent spring system as shown in eq. (4.52). In the expression, there exists a distinct separation of the force due to the rigid body acceleration of the mass and the pressure effect of the internal free surface.

$$F_x = m_l \left(-\ddot{\eta}_2(t) + \frac{l}{\pi^2 h} \sum_{i=1}^{N} \ddot{\beta}_i(t) \frac{1}{i^2} (1 + (-1)^{i+1}) \right) \tag{4.52}$$

where: m_l = Fluid mass
$\ddot{\eta}_2$ = Sway acceleration
h = Tank filling height
β = Free surface modes

The linear sloshing calculations made by Rognebakke and Faltinsen (2003) compared generally well with the experimental values. However, close to the natural periods of the internal tank, the response is overpredicted. In addition, for a frequency equal to the natural frequency, the added mass goes to infinity. For a spring formulation of the sloshing force, this implies an infinite spring stiffness. Hence, the linear theory predicts a zero response at the natural period. On the contrary, the experimental values show a non-zero minimum in proximity to the sloshing period.

To prevent double counting, it is important to carefully account for the mass when considering internal fluids such as ballast or accidentally filled compartments. Usually, one considers the internal fluids as "frozen" liquids when the complete draft, center of gravity (COG), and moments of inertia are calculated (Faltinsen and Timokha 2009). However, dependent on the formulation/code, the static fluid mass is considered along with the other hydrodynamic forces as a pressure load. In such an approach, the static fluid mass will be included in the frequency-dependent added mass matrix. In the following, the mathematical models for internal compartments, presented in Ludvigsen, Pan et al. (2013) and Faltinsen and Timokha (2009), are presented.

Dynamic method

The internal BVPs governing the dynamics of waves inside tanks and compartments resembles the exterior BVP to a large extent. Hence, the numerical solver applied to the exterior domain may also be applied to the interior domain without major changes. However, although the solver of the problem may be the same, there exist some important differences between the exterior and interior BVPs. First of all, there exists no incident or diffracted potential in the interior BVPs, and it is thus sufficient only to solve the radiation potentials. Secondly, as the tanks are part of a moving system, the free surfaces of the tanks may have a non-zero mean vertical velocity.

By performing the needed derivative and combining linearized kinematic and dynamic free surface conditions presented in equations (4.35) and (4.36), the linearized combined free surface condition is obtained. The formulation expressed in equation (4.53) is valid for a harmonically oscillating potential with oscillation frequency ω, due to the time derivative of the potential being written as $\frac{\partial \phi}{\partial t} = i\omega\phi$ (Faltinsen 1990).

$$-\frac{\omega^2}{g}\phi + \frac{\partial \phi}{\partial z} = 0, \qquad \text{on the mean free surface} \tag{4.53}$$

The derivation described in Ludvigsen, Pan et al. (2013) introduces an additional term equal to $-\dot{Z}_0$ to equation (4.53), to account for the vertical velocity of the internal mean free surface. When solving the interior BVP, this additional term gives the following particular solution:

$$\phi_p = -\frac{g}{\omega^2}\dot{Z}_0. \tag{4.54}$$

By remembering that the vertical velocity of the internal free surface is a harmonic oscillation in the radiation problem, the time derivative of the particular may be found as:

$$\frac{\partial \phi_p}{\partial t} = -\frac{g}{\omega^2} i\omega \dot{Z}_0 = gZ_0. \tag{4.55}$$

Due to the linearity of the BVP, the solutions may be added following the superposition principle. Hence, using the linearized Bernoulli equation, the total pressure may be found as shown in equation (4.56).

$$p = -\rho\frac{\partial}{\partial t}\left(\phi + \phi_p\right) - \rho g\left(z - Z_0\right) = -\rho\frac{\partial \phi}{\partial t} - \rho g z \tag{4.56}$$

From this result, it is clear that the additional term in the combined free surface condition for an internal tank is canceled when calculating the pressure, and thereby in the forces. Ludvigsen, Pan et al. (2013) therefore argues that the internal tank dynamics may be computed without considering the vertical velocity of the mean free surface, as long as the restoring pressure is calculated in the same manner. This implies that the external solver may be used directly, with the combined free surface condition shown in equation (4.53). Ludvigsen, Pan et al. (2013) refer to Newman (2005), which shows that the vertical added mass and restoring from a tank potential solved without considering the vertical velocity of the mean free-surface is:

$$\hat{a}_{33} = \hat{m} + \rho\frac{g}{\omega^2}\hat{S} \qquad\qquad \hat{c}_{33} = \rho g \hat{S} \tag{4.57}$$

where: $\hat{m}$ = Mass of internal tank fluid
$\hat{S}$ = Free surface area of internal tank fluid

It is clear that an internal tank should not contribute to the vertical restoring coefficient of a vessel, and consequently, the term $\hat{c}_{33}$ should equal zero. In addition, for the added mass coefficient, only the first term is associated with the physical understanding as the force needed to accelerate a certain mass with a unit acceleration. However, when considering their combined force during a harmonic oscillation, it is seen that the terms cancel similarly when computed with a vertical velocity of the mean free surface in the combined free surface condition:

$$\left(-\omega^2\hat{a}_{33} + \hat{c}_{33}\right)\eta_3 = -\omega^2\hat{m}\eta_3 \tag{4.58}$$

The potential damping is not contributing to the internal tank wave dynamics, due to no energy being radiated out of the tank and away from the system.

Completely filled compartments

The approach described in Ludvigsen, Pan et al. (2013), also included a method for handling full compartments. This is an important part of the structure-tank interaction problem, as it is desirable in many cases to operate with either completely filled or emptied tanks. When the tank is completely filled, no surface waves can occur. Therefore, the BVP reduces to solving the Laplace equation, (4.31), with Neumann conditions on all tank surfaces. The problem has no unique solution, meaning that an arbitrary constant may be added to the solutions. Adding a constant pressure will not alter the added mass, but it will change the pressure loads acting on the tank walls.

An important note for filled tanks is that the radiation potentials are not frequency dependent. Furthermore, the added mass for translation modes is equal to the fluid mass, while the moment of inertia is between the values of an equivalent rigid mass and an idealized point mass in the center of the tank (Ludvigsen, Pan et al. 2013).

Quasi-static approach

A simplified approach for including the fluid in internal tanks is a quasi-static method. In such a method, the pressure in the tank is treated as purely hydrostatic in the accelerated reference frame of the geometrical tank center. For the global system, this is equivalent to treating the internal fluid as a point mass at the center of the tank. Consequently, the calculated moments of inertia in the quasi-static approach are lower than in the dynamic approach (Ludvigsen, Pan et al. 2013).

The largest impact of the internal fluid on the global response in the quasi-static approach is a reduction in the transverse and longitudinal metacentric heights. The effect of this is a reduction of static stability and longer natural periods in roll and pitch. For response calculations well above the longest sloshing period, the quasi-static approach is a good approximation (Faltinsen and Timokha 2009).

Sloshing periods

Faltinsen and Timokha (2009) define analytical expressions for the natural sloshing modes of tanks of different geometries. The lowest natural periods associated with these modes will indicate when tank sloshing might become relevant. The tanks considered in this thesis are either rectangular, upright circular cylinders, or annular, sectored upright circular cylinders. Common for all these geometries is that analytical solutions exist to the linearized internal problem with irrotational flow and incompressible fluid.

For a 2-dimensional planar rectangular tank, the natural periods may be found by the following expression:

$$T_i = \frac{2\pi}{\sqrt{\frac{g\pi i}{l}\tanh\left(\frac{\pi i h}{l}\right)}}, \quad i = 1, 2, \ldots \tag{4.59}$$

where: i = Mode number
h = Tank filling height
l = Tank horizontal dimension

Equation (4.59) is a simpliciation of the expression for a 3-dimensional rectangular tank in the case of $i \cdot j = 0$. The full 3-dimensional expression reads:

$$\begin{aligned} T_{i,j} &= \frac{2\pi}{\sqrt{g k_{i,j} \tanh\left(k_{i,j} h\right)}} \\ k_{i,j} &= \pi \sqrt{\left(\frac{i}{L_1}\right)^2 + \left(\frac{j}{L_2}\right)^2}, \quad i + j \neq 0 \end{aligned} \tag{4.60}$$

where: L_1, L_2 = Horizontal dimensions of tank
i, j = Mode number along L_1 and L_2 respectively
h = Tank filling height

4.5 Restoring

For the discussion of the restoring forces acting on a floating body, it is beneficial to treat the discussion about horizontal and vertical modes separately, as the different restoring terms have different physical explanations.

The restoring coefficient in heave is a function of the change in displacement resulting from a vertical displacement of the body, which may easily be explained by Archimedes' principle. For a wall-sided structure, the heave restoring coefficient is directly related to the water plane area, as shown in eq. (4.61).

$$C_{33} = \rho g A_{WP} \tag{4.61}$$

where: A_{WP} = Water plane area

The restoring in the vertical rotational modes, namely roll, and pitch, are of great interest for floating wind turbines. Obtaining a large enough pitch restoring coefficient may be a design driver for a FOWT because it is needed to balance the overturning moment generated by the rotor thrust.

The roll and pitch restoring coefficients for a freely floating body are described by (4.62) and (4.63) for small angles, and may further be reformulated as a function of the transverse and longitudinal metacentric height.

$$C_{44} = \rho g(z_b - z_g) + \rho g \iint_{A_{WP}} y^2 ds = \rho g \overline{GM_T} \tag{4.62}$$

$$C_{55} = \rho g(z_b - z_g) + \rho g \iint_{A_{WP}} x^2 ds = \rho g \overline{GM_L} \tag{4.63}$$

where: z_b = Vertical position of the center of buoyancy
z_g = Vertical position of the center of gravity
$\overline{GM}$ = Metacentric height, where T and L is transverse and longitudinal, respectively.

An effect that should be considered whenever applicable is the free-surface correction terms caused by the free surfaces of the tanks. Through a quasi-static analysis, one can find that the change of the free surface of partially filled tanks during rigid-body rotations reduces hydrostatic stability. This effect is accounted for by considering a virtual elevation of the body's center of gravity and, thus, a reduction of the metacentric heights.

$$\Delta z_g^* = \sum_{i=1}^{n} \frac{\rho_i I_{A,i}}{\rho \nabla} \tag{4.64}$$

where: $I_{A,i}$ = Second moment of area of tank i's free surface, with respect to a reference frame with axes parallel to the global frame with origin in the respective free surface centroid.
ρ_i = Tank i fluid density
ρ_w = Seawater density
∇ = Volume displacement of the vessel, with filled tanks

4.5.1 Mooring systems

A freely floating body has no inherent restoring in the horizontal modes and must therefore rely on a stationkeeping system to provide restoring. In addition to the restoring effect, the mooring lines also provide added inertia and damping to the system.

The mooring lines may be steel-linked chains, steel wire ropes, or synthetic fiber ropes. Aside from TLP-concepts, one often distinguishes between catenary and taut-mooring systems. The former creates the restoring forces by altering the configuration of the catenary shape of the mooring line (Faltinsen 1990). When the floating structure displaces from its static position, the part of the windward mooring line resting on the seabed is lifted and provides additional restoring. In addition, the shape of the already freely hanging catenary is changed, which reduces the line's angle with the horizontal plane at the windward fairlead. This effect will also contribute to added restoring as the horizontal component of the line tension increases. The restoring stiffness is often non-linear and must be treated non-linearly due to the large potential offset seen in surge and sway. In software such as SIMA and OrcaFlex, mooring lines are often modeled by simple bar elements in a finite element analysis (FEA), and the nonlinear system can be solved using a predictor-corrector method such as Newton-Raphson iteration (E. Bachynski-Polić 2022).

Introducing synthetic fiber lines may improve the performance of the system for mooring systems designed for deeper waters. Synthetic fiber lines are lighter, more flexible, and more able to absorb dynamic tensions than chain lines. In addition, they often imply shorter line lengths, lower costs, and a reduced footprint on the seabed (Brown 2005).

Marine growth

For a permanent mooring system, the effect of marine growth must be taken into account. As stated in DNV (2021a), the assumed thickness of the growth is dependent on the location of the structure. In the analysis, marine growth is included by increasing the submerged weight of the line and scaling the drag coefficients. In the absence of site-specific data, data from NORSOK (2017a) may be used. For simplicity, the specification for the Southern North Sea is applied as this is the most conservative region with respect to marine growth thickness. In this region, the marine growth properties presented in Table 4.1 apply.

Table 4.1: Marine growth properties

Depth below MSL (m)	Marine growth thickness (mm)	Marine growth density ρ_{mg} (kg/m^3)
-2 to 40	100	1300
Below 40	50	1300

$$M_{mg} = \frac{\pi}{4}\left[(D_{nom} + 2\Delta T_{mg})^2 - D_{nom}^2\right] \cdot \rho_{mg} \tag{4.65}$$

$$W_{mg} = M_{mg}\left[1 - \frac{\rho_w}{\rho_{mg}}\right] \cdot g \tag{4.66}$$

where: M_{mg} = Mass of margine growth
D_{nom} = Nominal thickness of mooring line
ΔT_{mg} = Marine growth thickness
ρ_{mg} = Marine growth density
W_{mg} = Submerged weight of marine growth

4.6 Aerodynamics

As in hydrodynamics, using aerodynamics for load calculation purposes involves simplifications. This section will introduce the fundamental methods for wind turbine aerodynamics, along with the most important corrections. The theory will only be summarized to the extent needed for explaining the methods applied in this task.

The available power in the wind may be expressed as the flux of kinetic energy through the rotor disk area. The formulation provides a basic understanding of the behavior of the wind turbine power, namely that the power increases with the wind speed cubed and rotor diameter squared.

$$P_0 = \frac{1}{2}\dot{m}u^2 = \frac{\rho}{2}Au^3 \tag{4.67}$$

The relationship presented in eq. (4.67) assumes that wind turbines can extract all the power in the wind, which would imply reducing the wind speed to zero. To obtain an expression for the power of an ideal (i.e. no mechanical losses) wind turbine, one-dimensional momentum theory can be applied. Here, one assumes a rotor disk consisting of an infinite number of blades enclosed by a stream tube. The thrust force on the rotor may either be expressed using conservation of mass and momentum or by applying the Bernoulli equation separately in the control volumes upwind and downwind of the rotor. Using the two expressions for the thrust force, the reduction in wind speed caused by the rotor, referred to as the axial induction factor may be expressed. Further, this may be applied to express the power as the change in kinetic energy across the rotor disk.

$$P = \frac{1}{2}\rho A u^3 4a(1-a)^2 = \frac{1}{2}\rho A u^3 C_p \tag{4.68}$$

$$T = \frac{1}{2}\rho A u^2 4a(1-a) = \frac{1}{2}\rho A u^2 C_T \tag{4.69}$$

The power may be maximized by taking the derivative of the power coefficient, C_p, with respect to the axial induction factor, a. For $a = 1/3$, the maximum power coefficient is found as $C_p = 16/27 = 59.3\%$. This is widely known as Betz' limit, which is the highest theoretical efficiency of an ideal wind turbine.

The rotation of the turbine will also induce a rotational component in the wake opposite of the turbine's rotation. The rotational speed of the turbine is quantified by the tip-speed ratio, which displays the ratio between the tangential blade velocity and the incoming wind speed.

$$\lambda = \frac{\Omega R}{V_0} \tag{4.70}$$

By considering the conservation of angular momentum in annular elements in the rotor disk, one may define a tangential induction factor, a'. The tangential induction represents the added velocity seen by the blades when the wake rotates. The effect of wake rotation introduces an efficiency loss, which decreases with increasing λ.

4.6.1 Airfoils

The local cross sections of the wind turbine consist of specially designed foils to provide the optimal aerodynamic response. The lift force acting on the airfoil section may be explained by the shape of the foil curving the streamlines around it downward. For a streamline to curve, a pressure gradient must be acting. This pressure gradient is due to a pressure difference between the upper and lower surfaces of the foil, which gives a net force upward on the airfoil. The forces on a foil cross-section may be seen in Figure 4.5.

The lift, drag, and moment acting on the foil are often nondimensionalized into respective coefficients, as shown in eq. (4.71) to eq. (4.73). These coefficients are dependent on the angle of attack, Reynold's number, and Mach number. However, the Mach number dependence is commonly disregarded for applications with relatively low inflow velocities, such as wind turbines (M. Hansen 2015). For low angles of attack, the Kutta–Joukowski formulation predicts a linear increase in the lift coefficient equal to $C_L(\alpha) = 2\pi\alpha$. At the same time, the drag is expected to have little variation at low values. The effect of camber in the airfoil may be seen as a non-zero intercept of the lift curve. This relationship holds until the critical angle of attack at which the stall occurs. Stall is characterized by flow separation from the foil surface on the suction side, leading to a rapid decrease in lift and a corresponding increase in drag.

$$C_L = \frac{L/l}{\frac{1}{2}\rho U^2 c} \qquad (4.71) \qquad C_D = \frac{D/l}{\frac{1}{2}\rho U^2 c} \qquad (4.72) \qquad C_M = \frac{M/l}{\frac{1}{2}\rho U^2 c^2} \qquad (4.73)$$

4.6.2 Blade Element Momentum theory

To calculate global and local loads on the wind turbine, the BEM theory is often applied. This theory is an iterative procedure where one requires equilibrium between the forces obtained through the momentum theory and the lift and drag forces acting on the airfoil. In Figure 4.5 the velocities induced by the axial and tangential induction factor are drawn, along with the incoming wind speed and the tangential velocity of the rotor.

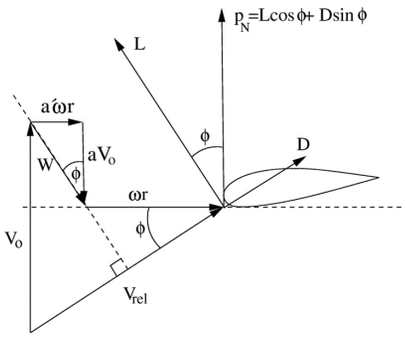

Figure 4.5: Velocity and force components
Source: E. Bachynski-Polić (2022)

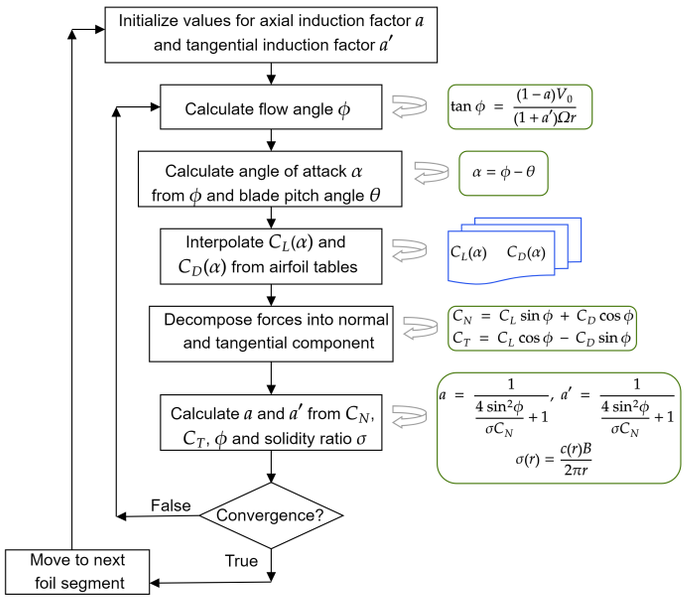

Figure 4.6: BEM iterative procedure
Source: Adopted from text in M. Hansen (2015)

Many corrections exist to the classical BEM method. In the following, only the correction applied in the time-domain prediction tools is discussed. The applied calculations in the different corrections are omitted, but they may be found in the included references.

Prandtl tip and hub loss correction

The general BEM method assumes infinite wingspans and no radial dependency between the elements. As one moves toward the blade tip, the pressure gradient around the wind causes a flow from the pressure side to the suction side of the foil. This disturbs the aerodynamic performance and causes what is known as tip loss. Such a loss is corrected by the Prandtl tip loss factor, which is a factor less than one that increases radially towards the blade tip.

The Prandtl hub loss factor is implemented in a similar way, accounting for the aerodynamic loss caused by vortex shedding at the wind turbine hub. Naturally, the hub loss factor on the blade segments decreases when radially away from the hub (Moriarty and A. Hansen 2005).

Glauert correction

The Glauert correction is a correction applied to the thrust coefficient for high axial induction factors. From the one-dimensional momentum theory, induction factors higher than 0.5 imply negative velocities in the far wake and decreasing thrust. This is unphysical; in reality, the flow passes through the stream tube, which is imagined in momentum theory, leading to a more turbulent wake. Therefore, the thrust coefficient is corrected by an empirical relation for axial induction factors greater than 0.4 (Moriarty and A. Hansen 2005).

Pitt and Peters skewed wake model

The Pitt and Peters correction is commonly applied in commercial BEM codes. It is a static correction factor applied only to the thrust coefficient. The factor is applied when the rotor plane is not perfectly perpendicular to the inflow velocity and results in a higher and lower force on the blades when moving through the upwind and downwind half of the rotor plane, respectively (Ning et al. 2015).

Dynamic inflow model

So far, the discussed BEM method has been quasi-static. This implies that equilibrium has been assumed in both inflow velocity and forces for each time step. In reality, there is a time delay from the occurrence of the wake effect until the system is again in equilibrium. In many BEM software, including those used in this thesis, the dynamic inflow is accounted for by applying the Stig Øye dynamic inflow model. This method uses two filters to predict and describe the induced velocities as a function of the time lags (Orcina 2023a). Including a dynamic inflow model is essential to model the transient response seen when changing the blade pitch of a turbine. Such transients involve large aerodynamic loads, which may affect both ULS and FLS analyses.

Dynamic stall

During the rotation of the rotor, the flow around the blades constantly changes due to turbulence, wind shear, misalignment, and tower shadow. Thus, important flow characteristics such as the local angle of attack and the separation point may behave dynamically. In many commercial codes, the Beddoes-Leishman model accounts for unsteady lift, trailing-edge separation, leading-edge separation, and compressibility issues (M. Hansen 2015).

Tower influence

The presence of the tower leads to reduced wind speed both in front of and behind the tower (Burton et al. 2001). The influence of the tower results in thrust variation occurring with frequencies equal to one and three times the rotor revolution frequency. Most software uses a potential flow formulation to describe the flow field in front of the tower, commonly referred to as the Bak model. The correction leads to a reduction in velocity in front of the tower and an increase in velocity to the sides (Moriarty and A. Hansen 2005). The velocity field behind the tower is characterized by flow separation and thus is harder to model. This is important for downwind turbines and is, in most cases, approximated by empirical formulas (Burton et al. 2001).

4.6.3 Aerodynamic damping

Coupling effects between aerodynamic loads and rigid body motions give important effects, which need to be captured in the analysis. Body velocities change the relative wind speed seen by the rotor and will thus affect the thrust and torque force exerted on the substructure from the turbine. As this force is in antiphase with the rigid body velocity, it is commonly denoted as aerodynamic damping. This damping is important for all offshore wind turbines and especially bottom-fixed turbines, where it may dominate the experienced damping.

4.6.4 Wind turbine control theory

The main responsibility of the turbine is to maximize the power for below-rated wind speeds and limit the loads for above-rated wind speeds. A detailed description of wind turbine control theory is not included in this thesis, but may be found, for instance, in Burton et al. (2001). However, the issue of negative feedback is briefly discussed below, as it is of major importance for FOWTs.

In the above-rated wind speed region of a VSVP turbine, the aerodynamic thrust force decreases with increasing wind speed. A wind turbine moving in the direction of the wind speed will see a lower relative velocity the faster it travels. If the controller responds to this change in relative velocity, the thrust force in the direction of motion will decrease with increasing body velocity. Therefore, the turbine experiences negative damping. A similar effect is seen when moving against the wind, where the increased relative velocity gives a lower resulting thrust force (Anaya-Lara et al. 2018).

Negative feedback is mainly a problem for floating turbines because of the long natural periods in the horizontal modes, giving the controller time to react to the relative motion. One must modify the turbine controller applied to floating substructures to prevent such effects. An example of such a modification may involve detuning the controller to make it too slow to respond to body motions. Otherwise, one might make the controller unable to respond to rigid-body natural periods by applying a notch filter or measuring relative velocity and feeding it back to the controller. This approach was implemented on the Hywind Demo spar floater and turned off to test the effect of negative damping. When the floating motion controller was turned off, a significant increase in pitch response was observed compared to the normal operational state. The turbine had to be shut down to avoid failure (Skaare et al. 2007). A time series of the test is shown in Figure 4.7, where one can see the rapid increase in pitch and that the turbine is shut down at approximately 250 s.

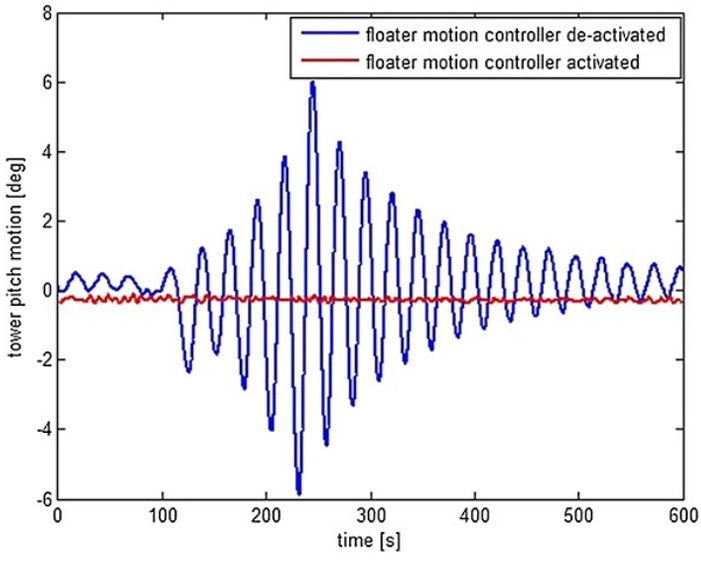

Figure 4.7: Real-life test on Hywind Demo showing negative feedback

4.7 Dynamic simulations

This section describes how the equation of motion may be solved in both the frequency- and time domains to obtain a description of the response of a floating structure.

4.7.1 Frequency-domain simulations

When one assumes that a problem may be analyzed within the linear theory, the frequency domain represents a quick and convenient method for analyzing steady-state behavior. In such a case, the solution to the equation of motion may be found by solving a linear matrix equation with frequency-dependent coefficients.

$$-\omega^2 \left(\mathbf{M} + \mathbf{A}(\omega)\right) \mathbf{X}(\omega) + i\omega \mathbf{B}(\omega)\mathbf{X}(\omega) + \mathbf{C}\mathbf{X}(\omega) = \mathbf{F}^{exc}(\omega) \tag{4.74}$$

$$\mathbf{X}(\omega) = \left[-\omega^2 \left(\mathbf{M} + \mathbf{A}(\omega)\right) + i\omega \mathbf{B}(\omega) + \mathbf{C}\right]^{-1} \mathbf{F}^{exc}(\omega) \tag{4.75}$$

where: $\mathbf{X}$ = Frequency domain response
$\mathbf{M}$ = Generalized mass matrix
$\mathbf{A}$ = Hydrodynamic added mass matrix, frequency dependent
$\mathbf{B}$ = Linear damping matrix, frequency dependent
$\mathbf{C}$ = Restoring matix
$\mathbf{F}$ = Excitation force, frequency dependent

Following Taghipour et al. (2008), equation (4.75) may be used to define transfer functions relative to wave amplitude. The first transfer function, $\mathbf{H}^F$, relates the wave load experienced by the body to the incident wave amplitude as a function of frequency. As the wave excitation force, equation (4.38), is linear in terms of the wave amplitude ζ, this is found by simply dividing the wave excitation force by the wave amplitude.

$$\mathbf{H}^F(\omega) = \frac{\mathbf{F}^{exc}}{\zeta} \tag{4.76}$$

The second transfer function, $\mathbf{H}^{FM}$ relates the wave excitation load on the body to the response of the body. This transfer function is found by dividing the left side of equation (4.75) by the wave excitation load.

$$\mathbf{H}^{FM}(\omega) = \left[-\omega^2 \left(\mathbf{M} + \mathbf{A}(\omega)\right) + i\omega \mathbf{B}(\omega) + \mathbf{C}\right]^{-1} \tag{4.77}$$

By combining the two previous transfer functions, the relationship between incident waves and body motions can be found.

$$\mathbf{H}^M(\omega) = \mathbf{H}^{FM}(\omega)\mathbf{H}^F(\omega) \tag{4.78}$$

4.7.2 Time-domain hydrodynamics

To account for the highly coupled, nonlinear behavior of a floating wind turbine, the solution procedure must be done in the time domain. Examples of important non-linearities may be the quadratic drag loads, non-linear forces imposed by the controller, non-linear elastic structural responses, and higher-order coupling effects.

For instance, the rotor torque imposes a moment on the floater, resulting in a roll response. When the substructure pitches, the rotor plane rotates out of the vertical Y-Z plane, which results in rotor torque-excited yaw responses. Other effects one needs to capture are aerodynamic damping, which may for some modes significant, and negative damping from the controller. The thrust force from the turbine also gives a restoring contribution in yaw, due to part of the turbine seeing a higher inflow velocity (Cruz and Atcheson 2016).

Hybrid frequency-time domain model

The hydrodynamic coefficients obtained through the potential theory analysis are reported in the frequency domain, and must therefore be modified before a time domain simulation can be performed. For convenience, the added mass and damping matrices are split into an infinite frequency term and a frequency-dependent term as shown in equation (4.79).

$$\mathbf{A}(\omega) = \mathbf{a}(\omega) + \mathbf{A}_\infty \qquad \mathbf{B}(\omega) = \mathbf{b}(\omega) + \mathbf{B}_\infty = \mathbf{b}(\omega) \tag{4.79}$$

The last relation in equation (4.79) can be seen by considering the free-surface condition in the limit of infinite frequency, where the velocity potential goes to zero. Consequently, there cannot be any surface wave radiated away from the body. The potential damping of a body is explicitly connected with the squared amplitude of radiated waves, and thus the damping term must go to zero when the frequency of oscillation tends to zero. The infinite frequency added mass on the other hand represents the instantaneous inertial response of the fluid, and should hence be non-zero.

$$\lim_{\omega\to\infty} -\phi + \frac{g}{\omega^2}\frac{\partial\phi}{\partial z} = 0 \implies \lim_{\omega\to\infty} \phi = 0 \quad \text{on the mean free surface} \tag{4.80}$$

Using the definitions presented in equation (4.79) in the frequency domain equation of motion presented in equation (4.74), the following rewriting may be performed:

$$-\omega^2 \left(\mathbf{M} + \mathbf{A}_\infty\right) \mathbf{X}(\omega) + \left(i\omega\mathbf{a}(\omega) + \mathbf{b}(\omega)\right) i\omega\mathbf{X}(\omega) + \mathbf{C}\mathbf{X}(\omega) = \mathbf{F}^{exc}(\omega) \tag{4.81}$$

The relationship between the time and frequency domains can be expressed through the Fourier transform. Specifically, the response of the system in the frequency domain is the Fourier transform of its time-domain response, $\mathbf{x}$, while the inverse Fourier transform allows for the conversion in the opposite direction (Gao n.d.).

$$\mathbf{X}(\omega) = \frac{1}{2\pi}\int_{-\infty}^{\infty} \mathbf{x}(t) e^{-i\omega t} dt \tag{4.82}$$

$$\mathbf{x}(t) = \int_{-\infty}^{\infty} \mathbf{X}(\omega) e^{i\omega t} d\omega \tag{4.83}$$

The multiplication of the hydrodynamic coefficients in the frequency domain transfers to a convolution of a retardation function in the time domain. The convolution represents a fluid memory

effect, where every time step of the solution depends on the integral of all previous time steps. This dependency is due to the previous changes in fluid momentum from the past body motions (Taghipour et al. 2008). The limits of the convolution integral assumes that there is no motion prior to $t = 0$.

$$(\mathbf{M} + \mathbf{A}_\infty)\ddot{\mathbf{x}} + \underbrace{\int_0^t \overbrace{\mathbf{k}(t-\tau)}^{\text{Retardation function}} \dot{\mathbf{x}}(\tau)d\tau}_{\text{Convolution}} + \mathbf{C}\mathbf{x} = \mathbf{f}^{exc}(t) \tag{4.84}$$

$$\mathbf{k}(\tau) = \frac{1}{\pi}\int_0^\infty \left(\mathbf{b}(\omega)\cos(\omega\tau) - \omega\mathbf{a}(\omega)\sin(\omega\tau)\right)d\omega \tag{4.85}$$

By the use of causality, meaning that there must be a motion of the body for there to exist a radiation force, the retardation function can be rewritten using only the potential damping or added mass, respectively.

$$\mathbf{k}(\tau) = \frac{2}{\pi}\int_0^\infty \mathbf{b}(\omega)\cos(\omega\tau)d\omega = -\frac{2}{\pi}\int_0^\infty \omega\mathbf{a}(\omega)\sin(\omega\tau)d\omega \tag{4.86}$$

The relation between the added mass and potential damping is often referred to as the Kramer-Kronig relation:

$$\mathbf{a}(\omega) = -\frac{1}{\omega}\int_0^\infty \mathbf{k}(\tau)\sin(\omega\tau)\,d\tau \tag{4.87}$$

$$\mathbf{b}(\omega) = \int_0^\infty \mathbf{k}(\tau)\cos(\omega\tau)\,d\tau. \tag{4.88}$$

The retardation function may either be found from the frequency-dependent added mass or radiation damping through the approach proposed by Cummins (1962). Both OrcaFlex and SIMA use wave radiation damping to calculate the impulse response function using a Fourier integral equation. To circumvent the larger and larger integral, OrcaFlex utilizes that the impulse response function goes to zero when the time separation goes to infinity. Therefore, the program truncates the integral at a specified cutoff time or a specified cutoff tolerance, which significantly improves the computational performance (Orcina 2023a).

Time-domain implementation of sloshing

There are several aspects of the linear sloshing model that violate the assumptions needed to represent the frequency-domain coefficients in the time domain using the retardation function. For instance, the Kramer-Kronig relations do not hold, as there is no wave radiation damping in the internal problem. This implies the rewriting of eq. (4.85) to eq. (4.88) cannot be done.

Another issue is related to causality. As there is no damping within linear potential flow sloshing theory, the resonant sloshing motion will not decay once excited. This implies that the retardation function will not go to zero for long-time separations.

The implementation of the sloshing force, where the linear response transfer function is used to formulate it as a spring force, is presented in chapter 5.

4.8 Time-domain integration

Integrated dynamic analysis of wind turbines, especially floating wind turbines, is a complicated exercise. To get a full description of the wind turbine, one often refers to a fully coupled aero-hydro-servo-elastic dynamic analysis. The motions, loads, and power output of the system can all be impacted by combined wind and wave loads, making this information essential for assessing the dynamic response (J. Jonkman and Buhl 2007).

The substructure, which is of main importance in the description of hydrodynamic forces, is only a part of the total finite element system. For each time step, the loading and response of every element must be described, including the substructure, the mooring line elements, the tower elements, and the elements of the wind turbine blades.

To describe the time development of the system, a time integration scheme must be applied. There exist many such schemes, both explicit and implicit. An explicit scheme calculates the future state of the system based only on the previous state and the external loads. On the other hand, implicit schemes involve solving a system of equations at each time step. As this equation system may be non-linear, an iterative scheme is often needed. Seen in isolation, this is often more computationally expensive than the more straightforward explicit scheme. However, implicit methods are more stable, sometimes unconditionally stable, allowing larger time steps compared to explicit methods. The Newmark Beta integration methods are commonly used in time-domain simulation codes for structural dynamics. The general Newmark Beta method for a displacement u along a single degree of freedom reads (Næss and Moan 2012):

$$u_{i+1} = u_i + \Delta t \dot{u}_i + (\frac{1}{2} - \beta)\Delta t^2 \ddot{u}_i + \beta \Delta t^2 \ddot{u}_{i+1} \tag{4.89a}$$

$$\dot{u}_{i+1} = \dot{u}_i + (1 - \gamma)\Delta t \ddot{u}_i + \gamma \Delta t \ddot{u}_{i+1} \tag{4.89b}$$

The equation system, as written in eq. (4.89b), is underdetermined, and the equation of motions is used to solve the system. The two parameters γ and β determine the relative weight of the states in the time steps t_i and t_{i+1}, and are important for both the stability and accuracy of the method (Næss and Moan 2012).

Depending on the value of γ, the Newmark Beta methods may have numerical dissipation of energy. For some problems, this may be desirable at high frequencies to dampen spurious high-frequency responses of the finite element system. To limit the damping at low frequencies, there are specialized methods within the Newmark Beta family of methods. One of those methods is the Generalized-α method. This method is specialized to limit low-frequency damping while providing controllable damping at high frequencies (Chung and Hulbert 1993).

There exist several non-linearities in the considered problem, such as the geometric stiffness of the catenary mooring lines, the large deformations of the turbine blades, and the forces exerted on the turbine by the controller. Therefore, an iterative predictor-corrector method is needed. An example of such a method is the modified Newton-Raphson method (Næss and Moan 2012).

4.9 Upscaling

According to Burton et al. (2001), the optimal size of a wind turbine is a debated subject. Those in favor of large wind turbines lean on the economics of scale and the increase in available wind power with increasing wind turbine height. On the contrary, their opponent refers to the "square-cube law". If a geometric scaling of the rotor is performed under the constraint that the tip-speed ratio (TSR) should remain constant, the rotational speed of the turbine is found to be inversely related to the rotor diameter for a constant wind speed, as shown in eq. (4.90).

$$\text{TSR} = \frac{\omega R}{U} \implies \omega \propto \frac{1}{R} \tag{4.90}$$

where: ω = Rotational speed of turbine [1/s]
R = Rotor diameter [m]
U = Incident wind speed [m/s].

Further, the power of a wind turbine can be written as the total available power multiplied by a power coefficient as shown in equation (4.68). As TSR is kept constant, the power coefficient may also be assumed to be constant. Thus, the power is proportional to the rotor area.

$$P \propto R^2 \tag{4.91}$$

Finally, the mass is assumed to be proportional to the length scale cubed times a relevant density. The cost is assumed to be proportional to the mass and hence proportional to the rotor radius cubed. From this reasoning, one can see that the cost of a wind turbine increases with the rotor diameter cubed while the power increases with the radius squared. This is called the "square-cubed law", which ceteris paribus advocates smaller turbine sizes. For FOWTs, the discussion is further complicated. The expensive substructure and mooring system, shown in Figure 2.5, makes it economically sensible to install fewer but larger turbines. Additionally, as noise complaints are much less of an issue offshore, one can increase TSR to reduce the effect of wake rotation.

The upscaling discussed above is referred to as geometric similarity, where all dimensions are increased by the theoretical scaling factors defined as the square root of the ratio of the power rating of the upscaled and reference turbine:

$$s = \sqrt{\frac{P^{\text{US}}}{P^{\text{Ref}}}} \tag{4.92}$$

In reality, a large portion of the recent advancements in FOWTs comprise of upscaling of demonstration projects. However, upscaling of substructures is seldom performed using the theoretical approach described above. For instance, the draft of the substructure may be constrained by the capacity of dry docks or port depths, and the freeboard may be governed by the maximum expected relative wave crest height (Kikuchi and Ishihara 2019). When the wind turbine is upscaled, the substructure must be redesigned to maintain buoyancy and stability. A more refined approach is therefore applying geometrical constraints related to static balance and manufacturing limitations. However, as the substructure and mooring system is affected by large coupled motions, simple upscaling may not be used (Leimester et al. 2016). In terms of dynamic responses, the geometrically upscaled designs may end up with natural periods, e.g., tower bending modes, close to the excitation periods. Furthermore, the static restoring of a theoretically upscaled may be overly conservative, and the steel weight of the hull unnecessarily high (Abdelmoteleb et al. 2022).

As this thesis concerns a comparison of the survivability between an original concept and an upscaled concept, making the stability of the latter overly conservative is undesirable. Therefore, it was decided to apply the optimization-based upscaling method by Abdelmoteleb et al. (2022) to obtain the dimensions of the peripheral tower concept. This method considers the FOWT as a simplified two-dimensional finite element model with surge, heave, and pitch degrees of freedom.

The hydrostatic restoring in heave and pitch, as well as the restoring from the mooring lines, is included as springs in the finite element model. The mass model includes both structural inertia, fixed and floating ballast, and integrated two-dimensional added mass. An illustration of the applied model can be seen in Figure 4.8.

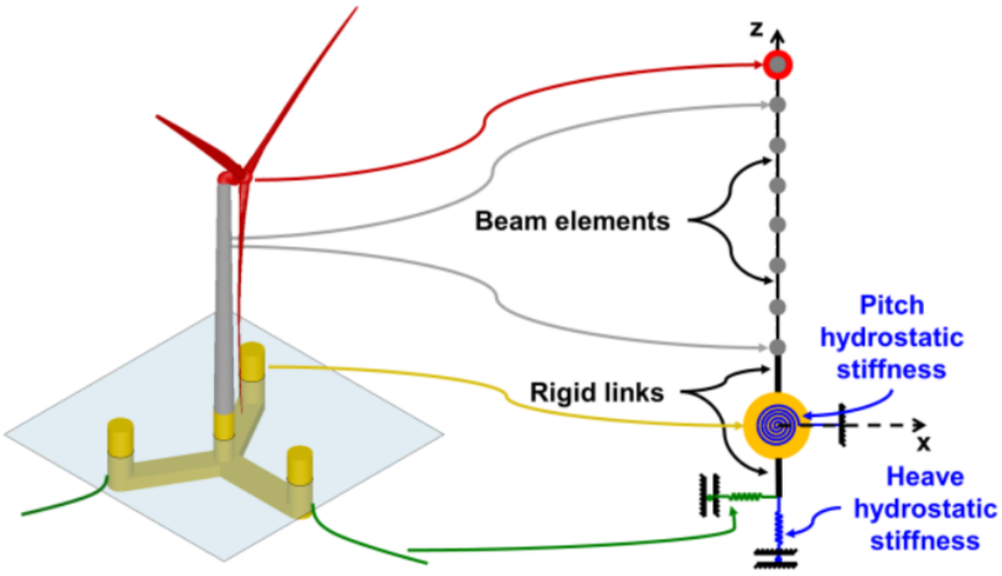

Figure 4.8: Simplified model of FOWT
Source: (Abdelmoteleb et al. 2022)

The objective of the optimization model is to minimize both the steel mass of the substructure and the static pitch during rated thrust, which are found to be contradictory. The constraints of the model are:

- Maximum hull dimension less than 120m
- Minimum natural period larger than 20s
- Stiff-stiff tower configuration
- Static pitch during rated thrust less than 30°

To perform the optimization, a set of structural parameters are defined as a variable while the remaining is either kept constant or derived from other parameters or static balance considerations. The variable parameters are non-dimensionalized by a characteristic parameter and varied in a predefined interval. For the peripheral tower design, the variable parameters are:

- Column-column distance (r_c), ${}^{r_c}/_{r_{c,\mathrm{US}}} \in [0.5 - 1.5]$
- Column diameter, (D), ${}^{D}/_{D_{\mathrm{US}}} \in [0.5 - 1.5]$
- Pontoon width, (w_p), ${}^{w_p}/_{D} \in [0.5 - 1]$
- Pontoon height (h_p), ${}^{h_p}/_{h_{p,\mathrm{US}}} \in [0.5 - 1.5]$

The result of the optimization problem is a Pareto front consisting of minimum steel weight for every maximum allowable static pitch angle. As every unfeasible design is removed from the design space, the user may therefore select the maximum allowable pitch and, as such, obtain the most steel-effective design.

CHAPTER 5

Methodology

The methodology chapter describes how the previously presented theory is combined through different methods to obtain the results. The main focus of the section is to provide reproducible results, by describing the various choices done while modeling in a thorough manner.

5.1 State-of-the-art numerical tools

In this section, some of the state-of-the-art numerical tools available for integrated dynamic analysis of FOWTs will be presented. The programs used or mentioned throughout the project work are included, along with some alternative programs. It should be noted that there are several other programs with similar capabilities.

5.1.1 Geometric modeling and meshing software

GeniE

GeniE is a FEM software for high-level modeling and analysis of structures consisting of beams, plates, and shells. The program is developed as an integrated part of the DNV SESAM suite. GeniE is based on concept modeling, which indicates that the conceptual model is independent of the analysis model. A concept model moves the focus from nodes and elements in general FEM calculations to higher-order modeling of applied loads on actual structural elements. The concept model has dynamic connectivity, meaning that structural connections are updated if a structural part is moved or changed. The conceptual modeling technique and separation of the concept and analysis models result in easy remeshing of the structure, with mapping of loads on new nodes. GeniE also provides the ability to script using JavaScript, which facilitates the creation of parametric models (DNV 2014).

GeniE contains the integration of other SESAM analysis software such as Sestra (Linear structural analysis), Wajac (Hydrostatic and hydrodynamics on fixed offshore frame structures) and Splice (Soil and pile structure interaction). In addition, the program can interact with Usfos, a module for non-linear analysis of the progressive collapse of structures and accidental conditions, and provide code checking of beams and plates according to, e.g., API, NORSOK, Eurocode, and ISO codes.

Rhino

If the modeling aims only to produce a three-dimensional representation of the structure, then all the features of Genie are unnecessary. Rhino is a modeling software for creating NURBS curves, surfaces, and solids and is well suited to mesh three-dimensional structures. The program was originally developed more than 20 years ago to build computer models to aid in shipbuilding fabrication and has integrated support for meshing in the WAMIT GDF format (Rhinoceros 2023).

5.1.2 Potential theory software

WADAM

WADAM (Wave Analysis by Diffraction and Morison Theory) is a DNV program that specializes in calculating hydrodynamic coefficients in the frequency domain. It is capable of solving both first- and second-order problems, where second-order excitation forces may be included by both Newman's approximation and full quadratic transfer functions. WADAM is also capable of solving the linear response of fluid in internal tanks and damaged compartments. WADAM is based on the same theoretical background as the famous WAMIT software and provides the option of outputting results in the WAMIT format. However, it relies on panel models in the SESAM FEM format and not on the WAMIT GDF format.

HydroD

Sesam HydroD is an integrated tool for both hydrostatic and hydrodynamic analysis for ships and offshore structures. HydroD specializes in stability analysis and also works as a hydrodynamic preprocessor for WADAM. Integrating the hydrodynamic modules results in the ability to use the same panel model for different types of analysis.

The program can also model the effect of tanks and damaged compartments, which will be used in this project. Furthermore, the compartments can be automatically filled through the ballasting module to obtain equilibrium. HydroD is also capable of mapping the calculated pressure loads to the finite-element model for further analysis.

OrcaWave

As an alternative to performing potential theory calculations in WADAM, OrcaWave may be used. OrcaWave is a diffraction analysis program created by Orcina, a company well known as the creator of OrcaFlex. Compared to HydroD, the structure has fewer features and provides a simpler interface for the calculation of hydrodynamic coefficients and transfer functions. For this application, OrcaWave delivers capabilities similar to those of WADAM, including second-order hydrodynamics. A great advantage of OrcaWave is the seamless integration with OrcaFlex, but it does not include the option to model internal fluid effects.

5.1.3 Time-domain analysis software

Fast (Fatigue, Aerodynamics, Structures and Turbulence)

FAST is a design tool to model dynamic responses of HAWT with two or three blades. It was developed by NREL and was originally intended for load prediction on land-based and bottom-fixed offshore wind turbines. FAST consists of several modules, each responsible for modeling a separate part of the integrated analysis. The aerodynamic module, AeroDyn, utilizes BEM theory with dynamic stall and dynamic inflow as some of the corrections applied. After adding support for FOWT, the hydrodynamic module (HydroDyn) became of greater importance. This module is a time-domain hydrodynamic code capable of both potential flow theory and Morison elements. It also includes support for irregular waves, second-order wave theory, and current effects. The mooring system is modeled as quasistatic through the MoorDyn module or by a FEA with the FEAMooring module. The remaining modules, ElastoDyn and ServoDyn, model the structural dynamics and the control and electrical system, respectively (Cruz and Atcheson 2016).

SIMA

SIMA is a numerical code developed by MARINTEK, which combines the SIMO and RIFLEX codes. SIMO (SImulation of Marine Operations) is a code created to model the response of offshore structures in the time domain. RIFLEX is a nonlinear FEA code for modeling slender elements such as risers. In SIMA, SIMO is used for the hydrodynamic modeling of large-volume structures, while RIFLEX is applied to slender elements such as wind turbine blades, towers, and mooring lines. SIMA (SIMO-RIFLEX) is often coupled with aerodynamic software such as AeroDyn or HAWC2 (Cruz and Atcheson 2016).

OrcaFlex

OrcaFlex is a program developed by Orcina for the dynamic analysis of marine structures. While originally aimed at analysis for O&G and vessel operations, it has been extended to include offshore wind power. The ability to model vessels with hydrodynamic coefficients, mooring lines, and power cables with FEM formulations and wind turbines with BEM makes it very suitable for performing integrated dynamic analysis of wind turbines.

OrcaFlex also supports external control through their Application programming interface (API), which may be run in either Python or C++. The API allows the definition of external controller functions, which can be used to simulate complex operations and systems such as wind turbine blade pitch actuators, dynamic positioning systems, dynamic ballast systems, and crane operations.

HAWC2 (Horizontal Axis Wind Turbine Code 2nd generation)

HAWC2 is a simulation tool developed for aero-elastic dynamic analysis of bottom-fixed wind turbines. The program is developed by the Technical University of Denmark (DTU) as a commercial code. The modeled loads comprise hydrodynamics, aerodynamics (BEM), and soil mechanics. The structural dynamics are modeled by a multibody system applying Timoshenko beam elements (Cruz and Atcheson 2016).

TurbSim

TurbSim is a program developed by NREL for the simulation of stochastic full-field turbulent wind fields. Its output consists of a series of two-dimensional grids of wind speeds described by three components, using Taylor's frozen turbulence hypothesis described in chapter 4. The software uses a statistical description of the wind using spectra in the frequency domain combined with the inverse Fourier transform (B. Jonkman 2014).

5.2 Environmental data

Several steps must be taken to obtain the relevant environmental data for the selected geographical site to be used in the subsequent time-domain analysis. It was decided to include the intermediate results that provided added information on how the environmental data are modeled in this section. Other intermediate results, such as parameter curve fitting, are included in Appendix A: Environmental modeling. The resulting environmental conditions relevant for the time-domain analysis is presented in chapter 7: "Description of selected operational site". An outline of the environmental modeling may be seen in Figure 5.1. In the figure, U_w, H_s, and T_p refer to the mean wind speed, the significant wave height and the spectral peak period, respectively.

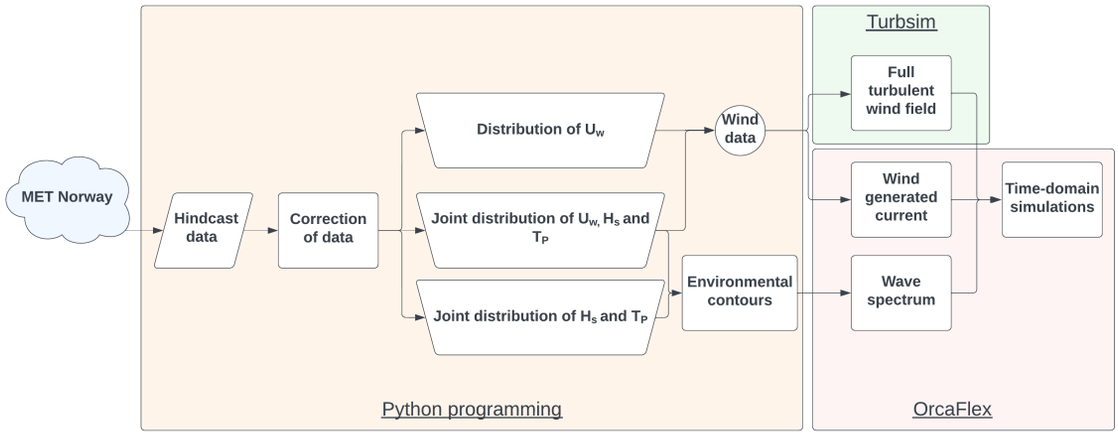

Figure 5.1: Environmental modeling approach.

5.2.1 Hindcast data

To obtain the hindcast data serving as input for the statistical environmental analysis, several different approaches were considered. With the help of Dr. Konstantinos Christakos, the NORA3 and NORA10 data hindcasts were selected.

To download the data, several Python scripts were written to download the files from The Norwegian Meteorological Institute's (MET Norway) THREDDS data server using the OPeNDAP protocol and the xarray-module in Python. The Python scripts were inspired by the MET_wave Python Library (Christakos 2022) provided by Dr. Christakos, but were rewritten to apply the DataFrame objects enabled by the Pandas module instead.

Initially, it was intended only to use the data available through the "NORA3 - Windsurfer" project. However, after inspection of the data set, it was found that the minimum mean wind speed at 10 m was 2 m/s. After consulting with Dr. Christakos, this is assumed to be introduced to the hindcast to force the wave model. Although this would be a conservative approach, it was found to disturb the goodness of fit of the fitted probability distribution. Consequently, the mean wind speed from the original NORA3 data set was used for the mean wind speed and wind direction. As this data set is used as the input to the "NORA3 - Windsurfer" project, and uses measurements from Troll A as one of the reference stations, the wind data should be very representative of the location. The remaining variables are extracted from the "NORA3 - Windsurfer" data set. The location of the Trollvind field was assumed to coincide with the Troll A platform, located at 60°40′1.2″N 3°40′1.2″E. The closest node in the hindcast data sets is located at 60°39′35.99″N 3°41′2.4″E, approximately 1.46 km away. A data set containing wind and wave data from 01.01.1981 to 31.12.2021 was downloaded with a resolution of 1 hour at the specified location. The 41 years of data correspond to 359160 data points, where each data point consists of the following environmental variables:

- Wind speed
- Wind direction
- Significant wave height
- Peak period
- Mean period
- Wave direction

The significant wave height and peak and mean period are specified for the total sea state, as well as for the wind-driven and swell components.

Correction of spectral peak period

The logarithmic spacing in the data for the spectral peak period in the hindcast file causes the distance between adjacent periods in the data set to increase as a function of the period. This must be corrected by uniformly distributing the periods within each bin. The method for correcting the spectral peak period is as described in App. D in (Haver 2019).

$$T_p = 3.244 \exp\left\{0.09525(i - 0.5 - \mathbf{rnd})\right\} \tag{5.1a}$$

$$i = \mathbf{ROUND}\left[1 + \frac{\ln(T_p^*/3.244)}{0.09525}\right] \tag{5.1b}$$

where: T_p^* = Spectral peak period to be corrected
T_p = Corrected spectral peak period
rnd : = Uniformly distributed random variable, $\sim \mathcal{U}(0,1)$
ROUND : = Function rounding the input to the nearest integer

In addition to the procedure described in (5.1), the periods equal to zero in the data set had to be corrected, as these periods imply infinite wave frequencies. These periods were approximated as equal to the lowest physical period in the data set, $T_p^{min} = 2.4s$. This correction was made prior to the correction in eq. (5.1). The effect of the correction can be seen in Figure 5.2.

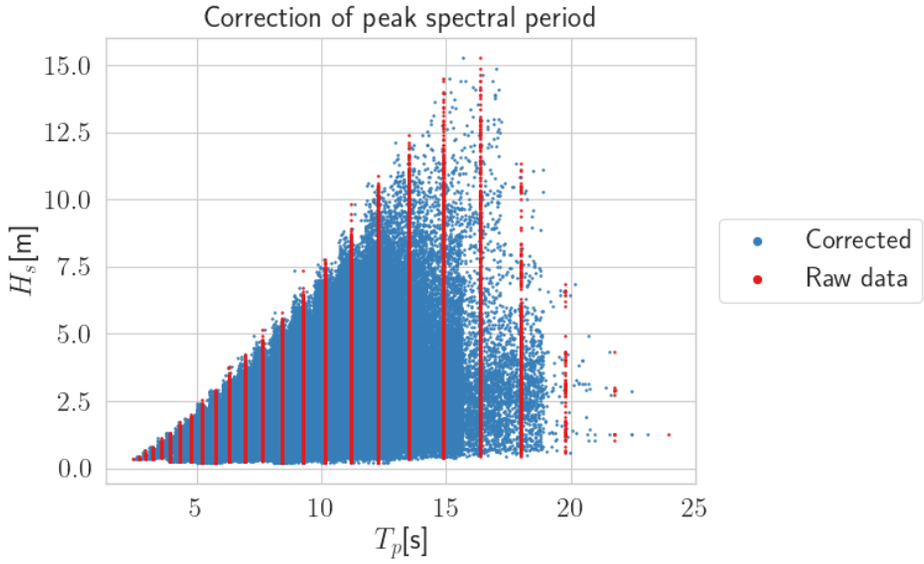

Figure 5.2: Correction of peak spectral period

5.2.2 Marginal distribution of mean wind speed

To model the marginal distribution of the mean wind speed, a two-parameter Weibull distribution was proposed in chapter 4. The distribution parameters were fitted to the sample of wind speeds using a maximum likelihood estimator (MLE) from the Scipy library in Python. The sample data and the fitted distribution are presented in Figure A.1. The linear trend seen in the sample, especially for the highest values, indicates that the Weibull model is well suited. The value of the distribution parameters in eq.(4.15) and eq.(4.16) are shown in Table 5.1.

Table 5.1: Parameters, marginal distribution of mean wind speed

α (Shape)	β (Scale)
1.963898	9.560950

5.2.3 Joint distribution of significant wave height and spectral peak period

Marginal distribution of significant wave height

The LoNoWe model, a hybrid Log-Normal-Weibull model, proposed as the marginal distribution of the significant wave height, was fitted to the data set using an approach described in Aarsnes (2015). To estimate the distribution parameters, the log-normal distribution parameters are fitted using maximum likelihood estimators (MLEs) for the case when $\eta \to \infty$. Further, a for-loop was used to iterate over the value of the shifting point between the Log-Normal model and the Weibull model, considering all values between 0 and 10 m with a step length of 0.01 m. For each iteration, the value of the Weibull parameters was calculated by requiring the CDF to be C^1 continuous. In practice, this means that both the CDF and PDF of the Log-Normal and Weibull distributions must be equal at the shifting point.

$$\begin{aligned} f_{H_s,LN}(\eta) &= f_{H_s,WB}(\eta) \\ F_{H_s,LN}(\eta) &= F_{H_s,WB}(\eta) \end{aligned} \tag{5.2}$$

Using the conditions shown in eq. (5.2), the following expressions for the distribution parameters can be derived:

$$\alpha = \frac{\eta \cdot f_{H_s,LN}(\eta)}{-\ln\left[1 - F_{H_s,LN}(\eta)\right] \cdot \left[1 - F_{H_s,LN}(\eta)\right]} \tag{5.3a}$$

$$\beta = \frac{\eta}{\left(-\ln\left[-F_{H_s,LN}(\eta)\right]\right)^{1/\alpha}} \tag{5.3b}$$

For each value of η, the sum of squared errors between the empirical CDF and the distribution with parameters corresponding to the η-value was calculated. The sum of squared errors was used, since this approach punishes large errors more than smaller errors. As may be seen from Figure 7.2, the majority of the sample is located at low values of H_s. However, in a limit state analysis, the higher values are more of interest. Therefore, the squared error was weighted by the value of the respective significant wave height before summing up. This approach was motivated, although not equal to, the work of Choi et al. (2019). In addition to the weighted sum of squared errors, a χ^2-type test was also performed as described in Moan et al. (2005). This test utilizes the empirical and fitted PDFs, which gave a η value in agreement with the method described above.

The parameters of the hybrid Lonowe models are presented in Table 5.2, and the sample data is plotted againts the fitted distribution in a Weibull scale in Figure A.2. In the plot, a 2-parameter Weibull model fitted using MLEs is included as well, to show the advantage of applying the Lonowe model.

Table 5.2: Parameters, marginal distribution of significant wave height

μ	σ	η	α	β
0.6768	0.6016	3.52	1.3910	2.3153

Conditional distribution of spectral peak period

To fit the conditional distribution of the spectral peak period, the data set was divided into bins of 0.2m width. Inside each bin, MLEs was used to fit the respective log-normal models. Further, a power function (5.4) and an exponential function (5.5) were fitted using the μ and σ parameters in each bin. The fitting was done using a nonlinear least-square method from the Scipy module in Python.

$$\mu_{\ln(T_p)}(h) = a_1 + a_2 \cdot h^{a_3} \tag{5.4}$$

$$\sigma_{\ln(T_p)}(h) = b_1 + b_2 \cdot \exp\left[b_3 \cdot h\right] \tag{5.5}$$

Table 5.3: Parameters, marginal distribution of significant wave height

a_1	a_2	a_3	b_1	b_2	b_3
1.8491	0.2054	0.5947	0.0756	0.2652	0.2623

5.2.4 Joint distribution of mean wind speed, significant wave height and spectral peak period

Conditional distribution of significant wave height

To express the dependence on mean wind speed in the model, the environmental data were arranged into discrete classes of mean wind speeds of 1 m/s width. Inside each wind class, a LoNoWe-model was fitted using the procedure described in Section 5.2.3. The distribution parameters μ, σ, and η were further approximated as fitted functions of the mean wind speed used by the expression provided in eq. (5.8). The remaining distribution parameters are not needed to be fitted as they already are parameterized as shown in eq. (5.3). The raw data and the fitted functions are shown in Figure A.5.

$$\mu(u) = c_1 + c_2 \cdot \left(\frac{1}{1 + \exp\left[c_3 \cdot (u + c_4)\right]}\right) \tag{5.6}$$

$$\sigma(u) = d_1 + d_2 \cdot \left(\frac{1}{1 + \exp\left[d_3 \cdot (u + d_4)\right]}\right) \tag{5.7}$$

$$\eta(u) = e_1 + e_2 \cdot u^{e_3} \tag{5.8}$$

Table 5.4: Parameters, conditional LoNoWe distribution of significant wave height

c_1	c_2	c_3	c_4	d_1	d_2	d_3	d_4	e_1	e_2	e_3
-0.8786	3.8096	-0.1097	-11.9612	0.1674	0.3994	0.2512	-8.9713	1.7427	0.1687	1.2688

To assess the applicability of the method, it is compared to the sample data inside each wind bin. For further comparison, the 2-parameter Weibull model described in Li et al. (2013) is also fitted inside the wind bins. For the relevant metocean data, the LoNoWe model shows a superior fit. The improvement is especially noticeable in the upper tail of the distribution, which is important for predicting extreme values. The comparison for two selected wind bins can be seen in Figure A.5.

Conditional distribution of spectral peak period

Instead of fitting a distribution inside each respective $\bar{U}_w$ and H_s class, the following rewriting of the distribution parameters was done as described in Johannessen et al. (2001). In the equations below, μ_{T_p}, σ_{T_p}, and ν_{T_p} refer to the mean, standard deviation, and coefficient of variance of the spectral peak period.

$$\mu_{\ln(T_p)} = \ln\left[\frac{\mu_{T_p}}{\sqrt{1+\nu_{T_p}^2}}\right] \tag{5.9}$$

$$\sigma^2_{\ln(T_p)} = \ln\left[\nu^2_{T_p} + 1\right] \tag{5.10}$$

$$\nu_{T_p} = \frac{\sigma_{T_p}}{\mu_{T_p}} \tag{5.11}$$

As noted by Li et al. (2013), plotting μ_{T_p} and ν_{T_p} shows that both variables depend primarily on significant wave height, although the variation seems to shift with increasing mean wind speed. The variation of the parameters is shown in Figure 5.3. Based on this variation, the parameterization of T_p in eq. (5.12) was proposed by Johannessen et al. (2001).

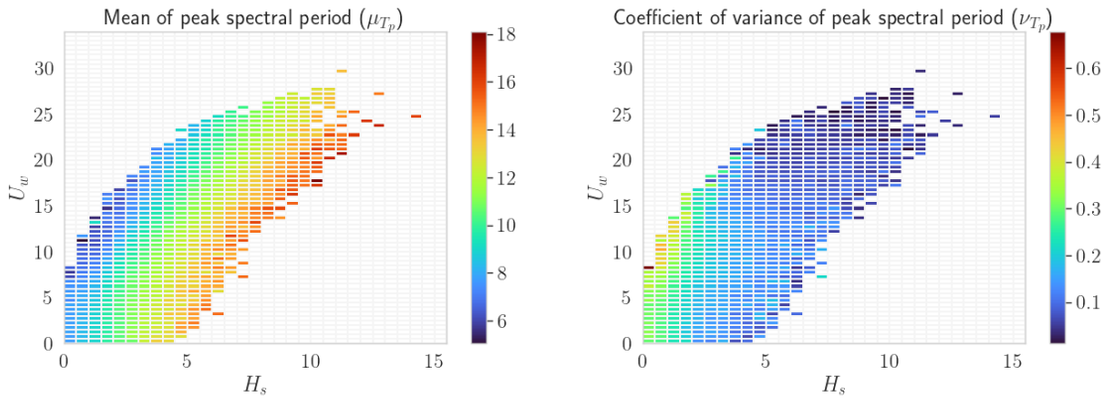

(a) μ_{T_p} (b) ν_{T_p}

Figure 5.3: Variation of μ_{T_p} and ν_{T_p} for different $\bar{U}_w$ and H_s

$$\mu_{T_p} = \bar{T}_p(u,h) = \bar{T}_p(h) \cdot \left[1 + \theta(h) \cdot \left(\frac{u - \bar{u}(h)}{\bar{u}(h)}\right)^{\gamma}\right] \tag{5.12}$$

Equation (5.12) describes the expected T_p for a given $\bar{U}_w$ and a given H_s ($\bar{T}_p(u,h)$) as the expected T_p for the given H_s ($\bar{T}_p(h)$) multiplied by a correction function dependent on $\bar{U}_w$. The correction function adjusts the mean T_p depending on the given $\bar{U}_w$ relative to the expected mean $\bar{U}_w$ for the relevant H_s. The expected spectral peak period and expected mean wind speed for given a given significant wave height were approximated by curve fitting power function, also using the non-linear least squares method. It was not attempted to fit the distribution to wind-wave bins with fewer than 3 observations of T_p. When performing the curve fitting, the intercept of both functions was forced to be positive as negative values for low significant wave heights would be non-physical. The curve fit of $\bar{T}_p$ and $\bar{u}$ may be seen in Figure A.7.

$$\bar{T}_p(h) = i_1 + i_2 \cdot h^{i_3} \tag{5.13}$$

$$\bar{u}(h) = j_1 + j_2 \cdot h^{j_3} \tag{5.14}$$

Table 5.5: Parameters (i, j), conditional distribution of T_p

i_1	i_2	i_3	j_1	j_2	j_3
6.931251	1.215196	0.765027	0.000093	5.785079	0.5782670

To estimate the parameters of the correction function, θ & γ, equation (5.12) was reformulated to express the relationship between the normalized expected spectral peak period and the expected mean wind speed. Subsequently, the relationship was plotted for every class of significant wave heights.

$$\frac{\bar{T}_p(u,h) - \bar{T}_p(h)}{\bar{T}_p(h)} = \theta(h) \cdot \left(\frac{u - \bar{u}(h)}{\bar{u}(h)} \right)^{\gamma} \tag{5.15}$$

Across most significant wave height classes, the plot of the normalized expected mean wind speed and the normalized expected spectral peak period showed a linear relationship. Consequently, the γ-parameter was assumed equal to 1. Furthermore, the slope appeared to vary across the different significant wave heights. Unlike Johannessen et al. (2001), who approximated θ as the mean for all significant wave heights due to the absence of an apparent relationship, the slope of equation (5.15) exhibited a decreasing trend with increasing significant wave height, as can be seen in Figure A.8a. Therefore, it was decided to approximate θ as a power function, using the same method as for some of the other distribution parameters. Due to the negative slope of equation (5.15) for all significant wave height classes, the intercept of equation (5.16) was forced to be less than or equal to zero.

$$\theta(h) = l_1 + l_2 \cdot h^{l_3} \tag{5.16}$$

To test the performance of the power function, the error committed when estimating the expected T_p was calculated as $\epsilon_{T_p} = |\mu_{T_p} - T_p(u,h)|$ in each discrete $\bar{U}_w$-H_s bin. Using the power function as opposed to approximating θ by its mean, reduced the mean error from 0.528 s to 0.406 s and the standard deviation of the error from 0.809 s to 0.544 s. The errors of both approaches are compared in Figure A.9. It should be mentioned that the added accuracy comes with the cost of introducing two additional distribution parameters.

Following the method described by Li et al. (2013), the coefficient of variance was approximated as a function of the significant wave height by curve fitting an exponential function to the estimated coefficient of variance in each significant wave height class. Similarly, for the other parameters, the curve fitting may be found in Figure A.8b.

$$\nu_{T_p}(h) = k_1 + k_2 \cdot \exp(k_3 \cdot h) \tag{5.17}$$

Table 5.6: Parameters (l, k), conditional distribution of T_p

l_1	l_2	l_3	k_1	k_2	k_3
0.034188	0.296374	-0.168203	-0.000001	-0.170107	0.502385

5.2.5 Generation of full wind fields

The full-field turbulent wind files was created using TurbSim. A quadratic grid with side lengths of 250 m, subdivided into 48 points along each edge was created. In the temporal direction, a time step of 0.05 s was used. The Kaimal turbulence model and the IEC coherence model were used, with the IEC 61400-3 standard and a class B turbulence characteristic.

By using the extreme wind model in Turbsim, the inputted reference wind speed is overwritten in favor of the reference wind speed related to the wind turbine class. By using the definition in IEC (2019a), the extreme wind model may be recreated for an arbitrary reference wind speed by using the normal turbulence model with a turbulence intensity of 11% and a power law exponent of 0.11.

5.3 Upscaling

The design space resulting from the substructure upscaling performed by Serag-Eldin Abdelmoteleb is shown in Figure 5.4. In addition to all the considered feasible designs, the Pareto front is included in red. This line consists of the designs which result in the lowest steel mass for the selected static pitch angle. Along this line, several design points are considered, among which DP2 was selected as the basis for this thesis.

An interesting remark made during the upscaling of the concept defined in Silva de Souza (2021) with the constraints considered in this thesis is that the theoretically upscaled design lies outside the design space of feasible models due to insufficient room for ballast to obtain the needed draft.

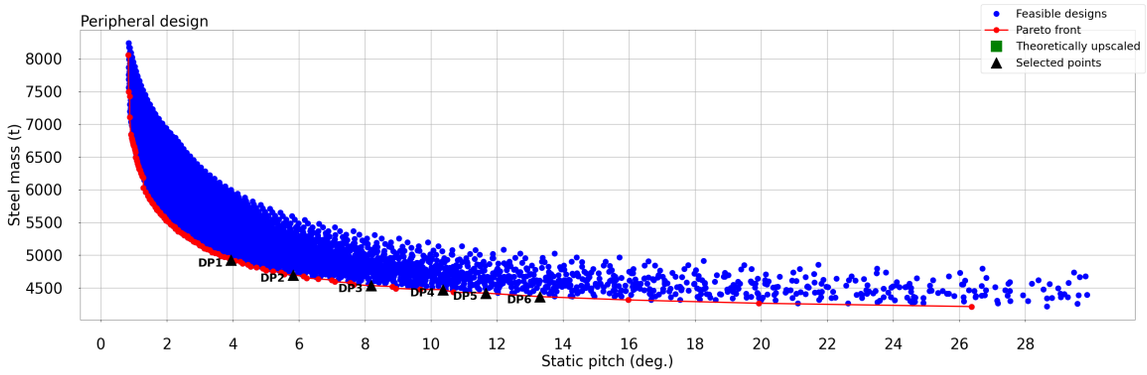

Figure 5.4: Results of upscaling

5.4 Finite element modeling

The modeling and generation of finite-element panel models were performed in Genie. To enable design iterations regarding steel thicknesses, compartments, and mesh refinement, a parametric modeling approach was applied using the JavaScript programming interface of the SESAM program package. Using the parametric script, the workflow presented in Figure 5.5 is performed automatically from a set of input variables.

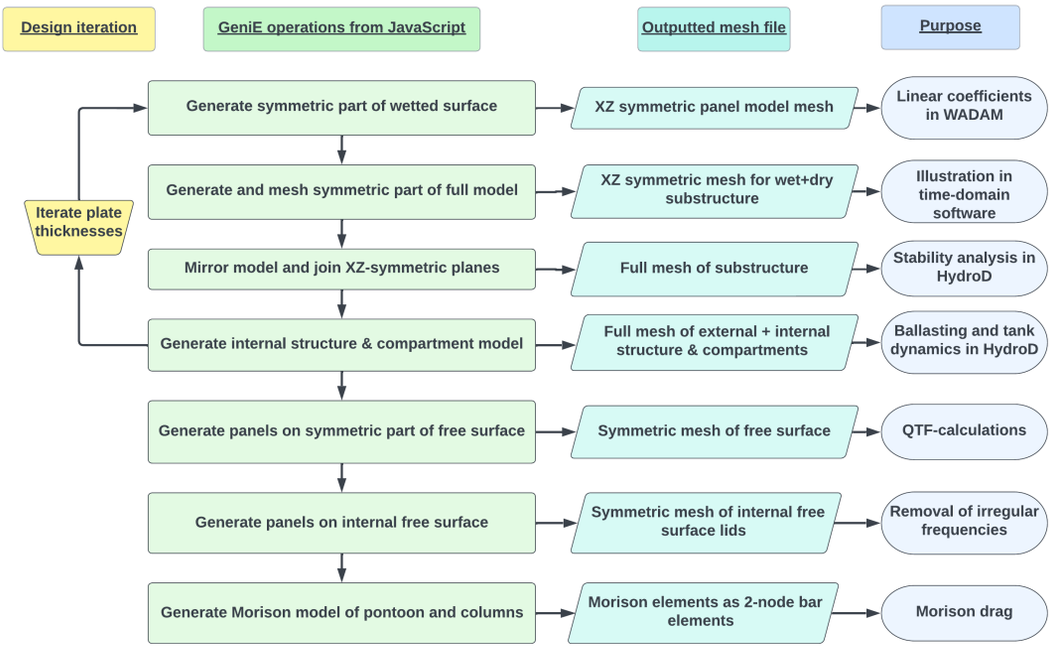

Figure 5.5: Flowchart of geometric modeling in Genie

5.4.1 Hull panel model

The level of discretization of the panel model is decisive in the accuracy of the obtained results. DNV (2019b) states that the diagonal length of the panels should be less than 1/6 of the shortest wave length considered in the analysis and that the discretized water plane area and the volume displacement of the body must be representative of the real structure. Additionally, it is recommended to apply a finer mesh in the proximity of the edges, corners, and mean water line.

For both models, a global mesh density was assigned in GeniE. To comply with the aforementioned DNV recommendations, a finer discretization was applied near critical areas of the model. The size of the panels in the first row near the water line was set to 20 % of the global mesh density. The size of the subsequent panels was increased with a growth factor of 1.25 until the global mesh density was reached. Different meshing algorit¡hms were applied to different faces, as the performance of the algorithms depends on the geometry of the patches.

To verify that the hull panels are sufficiently refined, a convergence study was performed. The convergence study was performed on a subset of periods and headings to reduce computational cost.

In addition to the convergence study, DNV (2019b) advises a comparison of the mean drift force calculated by pressure integration and momentum methods. As the pressure integration method is directly integrated over the hull panels, it is very susceptible to discretization errors. Moreover, as the mean drift loads, in general, require a higher level of discretization, the comparison between the different results is a useful measure of the discretization errors committed. The results of both validations are presented in Section 9.1.

5.4.2 Free-surface model

The free surface models applied in this thesis were created in GeniE. GeniE was preferred over the built-in HydroMesh feature in HydroD, as it could be included in the automated parametric modeling script.

The free surface model was parameterized in terms of radial size and mesh density. In the region of the free surface closest to the body, the same panel size as for the hull was applied. Further away from the body, a transition zone was created where the mesh size was gradually increased until the applied free-surface mesh size was reached.

5.4.3 Compartment model

The collision compartments placed around the mean water line are modeled as specified in DNV (2021c). The placement of the collision compartments also complies with the specifications in ClassNK (2019), which is considered stricter than the DNV standard.

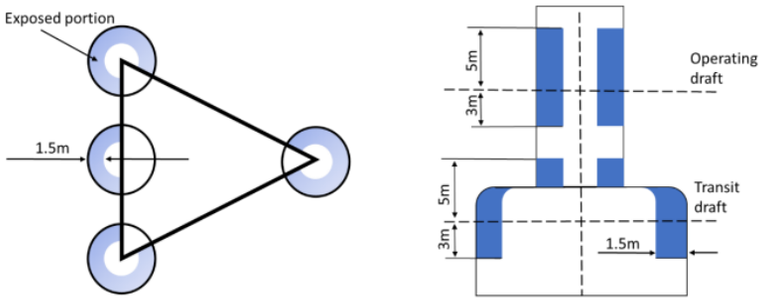

Figure 5.6: Collision-impact risk areas
Source: DNV (2021c)

The standard specifies that the collision-impacted area should be assumed to have a vertical extent of 3 m, in the area that extends from 3 m below to 5 m above the mean water line. For a column, the horizontal extent should be assumed to be 1/8 of the perimeter of the column or 3 m of the length of the pontoon. The impact penetration should be set to 1.5 m in the normal direction of the hull surface. As a transit draft is not included in this analysis, the structure is only modeled to comply with the collision criterion around the operating draft. The standard also specifies that only the exposed sides of the substructure need to be considered as collision-impact-risk areas. However, to maintain a symmetric mass distribution, it was decided to model collision compartments throughout the column.

To ensure the correct draft of both models, the pontoons are partially filled with seawater ballast. To suppress sloshing modes and prevent large free-surface effects, watertight bulkheads were included in the pontoons, running in the longitudinal and transverse directions. Longer pontoons are inherent in the peripheral tower design. Therefore, the same number of bulkheads could not be used for both concepts. The number of bulkheads was instead decided using hand calculations of the first sloshing periods and the reduction in metacentric heights. A single longitudinal bulkhead was modeled in the pontoons of both concepts. In the transverse direction, one and four bulkheads were modeled for the center and peripheral concepts, respectively. This gave metacentric height reductions of 1.4 m and 1.3 m, respectively. The applied compartmentalization can be seen in Figure 5.7.

5.4.4 Mass model

For the displacements obtained in the hydrodynamical analysis to be consistent, the structural inertia of the full structure, and not only the hull, must be included. Therefore, a mass model was assembled from the different parts of the numerical model.

The mass model of the substructures was assembled by assigning a thickness to all plates and using GeniE to calculate their combined inertial properties. As the purpose of the modeling is to make a comparison between the concepts, the same thickness was assigned to all external and internal plates, respectively. A steel density of 7850kg/m^3 was applied for all plates. The steel thicknesses presented in Table 5.7 were adopted as representative thicknesses based on various references investigated in the preceding project thesis, including Luan et al. (2016) and Robertson, J. Jonkman, Masciola et al. (2015), among others. For consistency, the deck beams and braces of both models were included in the calculations, with steel thicknesses similar to the internal plates. It must be stressed that only the internal structure with the purpose of compartmentalization is included. In reality, internal structural elements, such as stiffeners, girders, and frames, must also be added. The external plate thickness is assumed to include the weight of the internal structure by employing the "smeared stiffeners"-approach. However, it is stressed that the plate thickness and needed internal structure should be checked in a detailed structural analysis.

Table 5.7: Plate thickness

Plate type	Thickness
External	40.0 mm
Internal	25.0 mm

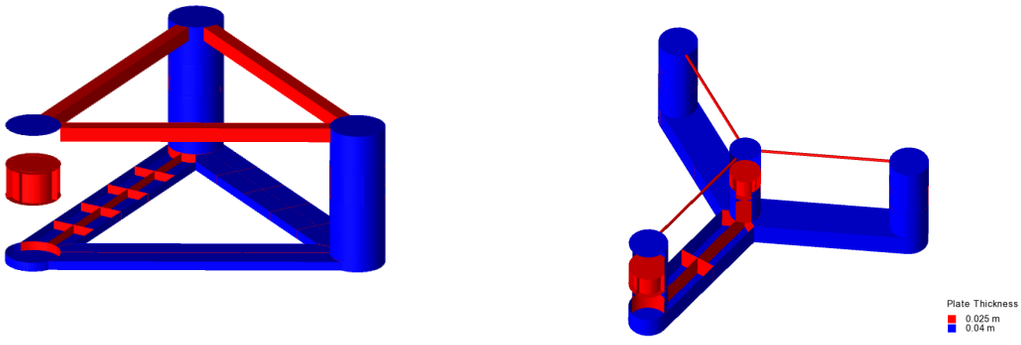

(a) Peripheral tower design (b) Center tower design

Figure 5.7: External and internal plate thicknesses.

To achieve the correct draft, both fixed and fluid ballast was added in the pontoons and the lowest compartments of the columns. Fixed concrete ballast with a density of 2560kg/m^3 was applied in the columns, while seawater ballast was applied in the pontoons, following the work of Abdelmoteleb et al. (2022). Due to the asymmetric tower position of the peripheral tower design, the concrete ballast was applied only in the two columns opposing the tower. The filling height was calculated to counteract the moment caused by the weight of the tower and RNA. As the inertial properties of the center tower design are symmetric, a static equilibrium consideration could not be applied to decide the fixed ballast mass. Therefore, the fixed ballast mass specified by Allen et al. (2020) was applied. For both models, the fluid ballast mass was decided by static equilibrium in the vertical direction. When calculating the static equilibrium, the vertical component of the mooring pre-tension was included. This contribution explains the difference between the FOWT displacement and mass in the following sections. The mass of the combined ballast tanks was calculated by summation of each individual tank mass, and the moment of inertia was calculated using the parallel axis theorem (5.18), disregarding the contribution around the individual tank axes.

$$\begin{bmatrix} I_{XX} & I_{XY} & I_{XZ} \\ I_{YX} & I_{YY} & I_{YZ} \\ I_{ZX} & I_{ZY} & I_{ZZ} \end{bmatrix} = \sum_i \begin{bmatrix} m_i(y_i^2 + z_i^2) & -m_i x_i y_i & -m_i x_i z_i \\ & m_i(x_i^2 + z_i^2) & -m_i y_i z_i \\ \text{sym.} & & m_i(x_i^2 + y_i^2) \end{bmatrix} \tag{5.18}$$

The inertial properties of the tower and the combined RNA were calculated in OrcaFlex with respect to the vessel frame. Similar to Allen et al. (2020), a tower interface modeled as a point mass of 100 tons was included at the bottom of the tower for both models. In the following, the tower interface is regarded as a part of the substructure. The RNA is not axisymmetric with respect to the tower axis. Hence, the horizontal position of the center of gravity of the combined structure depends on the yaw orientation of the RNA. For hydrodynamic modeling, the center of gravity of the RNA was assumed to be in the center of the tower, following the approach applied in Silva de Souza (2021). Decoupling the mass matrix from the RNA orientation ensures that separate frequency domain calculations are not needed for each wind direction. When the correct load case-dependent center of gravity of the RNA is included in the time domain, the FOWTs gets a static trim angle towards the wind direction. As such, it reduces the overturning caused by the rotor thrust force.

It should also be noted from eq. (5.18), that the eccentric tower placement of the peripheral tower concept leads to larger off-diagonal terms in the inertia matrix. As both the tower, RNA and fixed ballast consist of large masses with eccentric positions along the x- and z-axis, I_{XZ}, in particular, becomes large.

The implementation of HydroD prevents the use of internal free-surface on only a subset of the total compartments. As it would be unphysical with a quasi-static free surface for the fixed ballast, the mass contribution of the fixed ballast was included in the mass matrix along with the structural steel mass.

5.5 Hydrodynamic coefficients

The hydrodynamic coefficients were calculated using WADAM through HydroD. A panel model was used, along with a mass model and a compartment model. For the second-order problem, also a panel model of the free surface is needed. For all models, both the quasi-static and dynamic method is used for the internal fluid effects. For all cases considering a model in the intact condition, the full QTFs are calculated. To limit the computational time, the free surface integral is excluded from the full QTF calculation for the cases considering models under damaged conditions.

5.5.1 Effect of discretization of hull panel model

To assess the number of panels needed on the body, a convergence study was performed for both models. Both concepts were analyzed in WADAM using a set of different mesh densities. The results from all analyses were compared in terms of added mass, wave radiation damping, and wave load excitation. In addition, the response amplitude operators and mean drift forces were compared. The mean drift force was only calculated for unidirectional waves. The calculation was performed using pressure integration in the vertical modes and by both the control surface method and far-field integration in the horizontal modes.

To save computational expense, the convergence study was only performed on a limited set of frequencies and wave headings. To model the mooring system, point masses corresponding to the vertical pretension were included at the fairlead positions along with the linearized mooring stiffness in the horizontal modes. The mooring restoring stiffness was calculated in the vessel frame using OrcaFlex and included in the WADAM analysis through an inputted restoring matrix. To obtain meaningful motion transfer functions, viscous damping was included by stochastic linearization using a Morison model and JONSWAP sea state with 3 m significant wave height and a spectral peak period of 10 s.

According to Ferziger and Perić (2012), the discretization error of a numerical solution on a grid size h may be approximated if the convergence is monotonic and asymptotic. When examining the results on different levels of body discretization, it was apparent that these prerequisites did not hold where body discretization introduces small shifts in the natural periods of the body. According to Ferziger and Perić (2012), the discretization error of a numerical solution on a grid size h may be approximated by:

$$\epsilon_h^d \approx \frac{\phi_h - \phi_{\kappa h}}{\kappa^\gamma - 1} \tag{5.19}$$

where: ϵ_h^d = Discretization error of solution on grid size h
ϕ_h = Numerical solution on grid size h
γ = Order of convergence
κ = Mesh refinement factor

The order of convergence may be approximated in the following manner:

$$\gamma = \frac{\log\left(\frac{\phi_{\kappa h} - \phi_{\kappa^2 h}}{\phi_h - \phi_{\kappa h}}\right)}{\log(\kappa)} \tag{5.20}$$

5.5.2 Second-order hydrodynamic forces

To indicate whether the panel model had sufficient refinement to describe the second-order forces, a comparison between the results obtained by direct pressure integration and conservation of momentum was performed. As only one of the methods performs integration over the panels, the agreement between them indicates a sufficiently refined model. Although only first-order potentials are used in the calculation of mean drift forces, they provide added insight into the level of discretization errors as these results converge slower than the first-order coefficients (Orcina 2023b).

To further ensure a satisfactory accuracy of the second-order hydrodynamic coefficients, a mesh convergence study for the free surface mesh was performed. Due to the large computational cost of the analysis, in particular, for the second-order solution, the convergence study was performed on a subset of wave periods and headings.

5.5.3 Morison drag model

A Morison model was introduced to the analysis to obtain a more realistic damping level by including the quadratic drag. In the frequency domain, stochastic linearization was applied to the quadratic terms. The elements were modeled in Genie, using 2-node bar beam elements with the relevant cross-sectional dimensions. The elements were modeled as “Drag only”, meaning that they do not contribute to buoyancy or added mass.

Following the work in Silva de Souza (2021), the drag coefficients of the Morison model are taken as steady-flow coefficients defined in DNV-RP-C205 (DNV 2019b). The drag coefficient for the horizontal cross-flow across the pontoon of the peripheral design lies outside the range defined in DNV-RP-C205. After examining the drag coefficient as a function of aspect ratio for rectangular cylinders in Faltinsen (1990), it was decided to obtain the needed coefficient by constant extrapolation. As a simplification, the dependency of the KC-number was excluded in the frequency-domain analysis. This simplification is justifiable, as only the hydrodynamic coefficients (added mass, potential damping, wave loads) and not the motion RAOs are imported directly into the time-domain simulation software. However, as the first-order body motions are used to calculate the radiated second-order potentials for the full QTFs calculations, a reasonable damping level should be applied. Considerations regarding the KC-number are revised in connection with the time-domain simulations.

To calculate the drag coefficients, tabulated values from DNV-C205 Appendix E were applied. For the pontoons, the tabulated values presented in Figure 5.8 by setting the ratio $T/D = 0$.

2. Rectangle with thin splitter plate

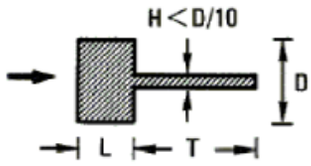

L/D	T/D		
	0	5	10
0.1	1.9	1.4	1.38
0.2	2.1	1.4	1.43
0.4	2.35	1.39	1.46
0.6	2.6	1.38	1.48
0.8	2.3	1.36	1.47
1.0	2.1	1.33	1.45
1.5	1.8	1.30	1.40
2.0	1.6	-	1.33

Figure 5.8: Drag coefficients from DNV-C205

In the HydroD, the preprocessor to the frequency-domain calculations in WADAM, the noncylindrical members with different drag coefficients about the cross-sectional axes may be used. Before the frequency domain calculations, HydroD makes a transformation of the cross-section and coefficients to a cylindrical cross-section with equivalent properties.

In OrcaFlex, only cylindrical elements with a single cross-sectional diameter may be applied. Therefore, the parameters applied in frequency domain calculations must be scaled before being applied in the time domain calculations. For this scaling, the largest cross-sectional parameter from the frequency domain calculations was used, the pontoon width in this context. By keeping the product $C_d \cdot D$ constant in eq. (4.49), the following equivalent drag coefficient may be found:

$$C_D^* = \frac{C_D D}{D^*} \tag{5.21}$$

where: C_D^* = Equivalent drag coefficient
D^* = Equivalent drag diameter
C_D^* = Original drag coefficient
D = Original drag diameter

5.6 Sloshing excitation model

As stated in chapter 4, due to the lack of damping within linear theory, the solution of the velocity potential to approach infinity at the exact natural frequency of the tank. The most intuitive solution to this problem is to add additional damping to the internal domains, but this feature is unavailable in WADAM. Therefore, it was decided to remove frequencies with extreme responses from the list of frequencies considered in WADAM. The selection of extremes for removal is based on a qualitative understanding of the problem. This approach is illustrated in Figure D.1, where the surge RAO for the peripheral tower design, which had the largest extremes, is plotted before and after the removal of extremes. In reality, the expected amplitudes should be based on the results of a CFD-solver applied to the internal domains, where all amplitudes above this level could be removed from the frequency-domain results.

The large effects of internal sloshing are located at a very narrow region of excitation frequencies, where outside this region, one would expect the fluid to behave quasi-static. Hence, it is important to consider a very fine discretization of the frequency axis when solving the radiation problem. When a series of second-order frequency-domain calculations are performed in WADAM, the number of frequencies is limited to a maximum of 60. It is, therefore, difficult to obtain the needed resolution to describe the sloshing phenomena and, at the same time, obtain an acceptable resolution around natural periods and in the asymptotic tail. To overcome this, a subset of periods was manually selected for both concepts, such that the peaks and general trend of the results are captured by piecewise linear interpolation between the selected period. The response described by a very fine discretization is plotted along the response described by the selected periods and presented in Figure D.3 and Figure D.2.

To overcome the challenges associated with including the added mass from the internal boundary value problem in the retardation function, it was decided to model the effect of the linear sloshing as a frequency-dependent spring on the right-hand side of the equation of motion. This method is aligned with the methods described in Faltinsen and Timokha (2009), Jin et al. (2017) and Rognebakke and Faltinsen (2003). As stated in the Faltinsen and Timokha (2009), it is extremely important to keep account of the different mass terms in the problem to prevent double counting. When a WADAM analysis is performed using the quasi-static method, the static mass of the fluid is included in the global mass matrix along with the structural inertia. However, when using the dynamic method, both the static mass and the added mass are added together in the added mass matrix. As shown in chapter 4, the added mass matrix and the global mass matrix are summed linearly in the equation of motion, implying that both approaches are perfectly fine as long as the mass is only included once.

When the effect of the sloshing is included as a frequency-dependent spring force, only the dynamic mass is accounted for. This is the added mass that aligns with the common understanding of the term associated with dynamic pressure effects. The remaining static mass is moved to the mass matrix. The two different mass contributions are calculated by considering the difference between the mass matrices in two separate analyses using the quasi-static and dynamic methods.

The force is modeled by relating the acceleration of the system to the incident wave components using the transfer function described in eq. (4.78). This may further be summed with the wave excitation force for the external problem and used to calculate the total excitation force for each linear wave component.

$$\mathbf{H^T}(\omega) = \omega^2 \mathbf{A}^{\text{int}}(\omega)\mathbf{H^M}(\omega) \tag{5.22}$$

where: $\mathbf{H^T}(\omega)$ = Internal sloshing excitation transfer function
$\mathbf{A}^{\text{int}}(\omega)$ = Internal tank added mass, excluding static contribution

$$\mathbf{F}^{W+T}(t) = \sum_{i=1}^{N} \left(\mathbf{H^T}(\omega_i) + \mathbf{H^F}(\omega_i)\right) \cdot \zeta_i(t, \omega_i) \tag{5.23}$$

where: $\mathbf{F}^{W+T}(t)$ = Combined wave and internal sloshing excitation force
$\zeta_i(t, \omega_i)$ = Wave component corresponding to a discrete circular frequency ω_i

5.7 Interface between Wadam and OrcaFlex

The hydrodynamic coefficients must be transferred from WADAM to OrcaFlex to perform the desired time-domain simulations. Among other formats, such as the format from Ansys AQWA and OrcaWave, OrcaFlex accepts hydrodynamic data in the WAMIT.out format. This human-readable text file contains the output from first- and second-order diffraction and radiation analyzes. WADAM can also export its results in the WAMIT format, leading to a well-tested approach for transferring intermediate results from WADAM to OrcaFlex for common problems.

The introduction of internal tanks prohibits this method, as the hydrodynamic results for each tank are printed in separate files when the WAMIT format is used in WADAM. To overcome this issue, a Python program had to be implemented. Regular expression matching was used to parse the WADAM listing file, which contains all hydrodynamic data for both the outer hull and the internal tanks. As the name and location of the results differ depending on the applied setting in WADAM and the length of the files can approach several hundreds of thousands of lines, this proved cumbersome. The parsed results were saved into a tailored WADAM-result class, where the results were redimensionalized appropriately. To transfer the results to OrcaFlex, a separate routine was implemented, which read the WADAM-result objects and used the OrcaFlex API to change the properties of the relevant OrcaFlex vessel object.

As such, the Python programs implemented provide a method for including internal fluid results calculated by WADAM in time-domain calculations in OrcaFlex, adding value to both programs. Due to the novelty and immaturity of the approach, extensive testing is included in this thesis.

5.8 Mooring system design

The selected site has a far deeper depth than the depths investigated in both Allen et al. (2020) and Silva de Souza (2021). Therefore, a new mooring system fit for the increased water depth had to be designed. As the water depth increase, the added weight and cost of a chain catenary system might become limiting (Brown 2005). Among the two original concepts, the mooring system applied in Silva de Souza (2021) is the only one of a hybrid nature, applying both chain and polyester rope segments. Therefore, this system was applied as a basis for the design of the new mooring system. While chain segments consisting of 130 mm studless links were maintained as in the original report, some changes were made to the polyester segments. The described properties of the polyester segments were not found in any brochure of known manufacturers, and it was decided to use an readily available fiber rope type instead. In reality, the optimal solution may also include additional line types, buoyancy elements, and clump weight, but this would further complicate the optimization problem.

The segments in the original report account for depth-dependent marine growth according to the regulations summarized in Section 4.5.1. For the definition of the mooring line weight and drag coefficients, the original report only reports the compounded properties of the mooring line and the layer of marine growth. By the use of DNV (2021a), the original line parameters were recalculated. Due to the implementation of lines in OrcaFlex, an equivalent diameter must be calculated for chain-type lines. Further, OrcaFlex automatically calculates the buoyancy of the lines using the equivalent diameter, and hence only needs the dry mass per length of the lines. To correctly account for the mass of the marine growth, only the mass equivalent of the submerged weight of the marine growth must be added to the dry line mass. The drag coefficients applied are with respect to the nominal bar diameter of the chain and not the volume equivalent diameter. Furthermore, the drag diameters must be scaled to account for the added diameter introduced by the marine growth.

An optimization problem was defined in Python using the sequential least squares programming (SLSQP) algorithm in the Scipy library and the OrcaFlex API to design the new mooring system. The optimization variables were defined as the radial position of the anchor with respect to the FOWT origin, as well as the length of the lowest chain and polyester line segments. The objective was set to minimize an estimate of the material cost of a single mooring line under a set of constraints. The material cost of a single mooring line is used as a proxy for the full mooring

system cost, which in reality, also must consider the cost of the anchors, the cost of installation, and the life-cycle cost. As material costs are project dependent, market dependent, and difficult to obtain, a normalized relative cost between fiber ropes and chains based on the work of Klingan (2016) was used. Due to the estimates involved and the fact that the cost function is introduced for minimization and not cost estimation, the obtained estimates from the objective function will not be shared.

$$\text{Line cost} = \frac{\pi}{4} \cdot (L_{\text{Chain}} \cdot W_{\text{Chain}} \cdot P_{\text{Chain}} + L_{\text{Polyester}} \cdot W_{\text{Polyester}} \cdot P_{\text{Polyester}}) \tag{5.24}$$

where: L = Length of segment [m]
W = Dry weight of segment [N/m]
P = Normalized, relative price of segments [1/N],

- $\frac{P_{\text{Polyester}}}{P_{\text{Chain}}} = 2.8$.

In principle, a mooring system design should consider both static and dynamic forces. However, as an optimal mooring design is not the aim of this thesis, only static properties were considered in the optimization problem. For completeness, the maximum dynamic loads were examined in the subsequent time-domain analysis. The applied constraints were included by running several OrcaFlex analyzes with different parameters in each iteration of the optimization problem. The applied constraints are listed in the following:

- Static surge offset during rated thrust force less than 18m
- First modal period between 100s and 150s
- Unloaded fairlead pretension between 1000kN and 3500kN
- Fairlead tension during rated thrust less than 5000kN
- Touchdown point more than 25% of mooring line arc length from anchor

The inputted mooring line segments and the results of the optimization are presented in Section 6.5.

5.9 Quasi-static stability analysis

A quasistatic stability analysis was performed in HydroD, considering both concepts in intact and damaged conditions. The analysis involves calculating the needed trim, heel, and draft to balance between the overturning and the righting moment, using the "free trim"-option in HydroD. Complete panel models of the mean wetted and dry hulls are used, and the instantaneous submerged volume is calculated for each heel angle. The free surfaces of the partially-filled internal tanks are represented exactly at every heeling angle, along with the center of gravity. The heeling axis is taken as the most critical for the intact condition. If the compartments are damaged, the heeling axis is still taken as the most critical axis. Still, it must be noted that this axis does not necessarily coincide with the critical axis of the intact structure. The overturning moment in the load cases is simplified by using the thrust force and the moment arm for the given angles of inclination. The thrust force is taken as the maximum thrust experienced in the constant wind tests.

The damage to the compartments is handled using the "Lost buoyancy"-method, which means that the new equilibrium is calculated without considering the buoyancy forces of the damaged compartments. The internal free surface is parallel to the external free surface for partially filled damaged compartments. Non-watertight openings are not considered in the analysis, as such details are excluded from the concept drawing. For further studies, any openings subjected to down-flooding should be examined.

5.10 Time domain simulations

In the time domain simulations in OrcaFlex, the Generalized-α implicit integration scheme with an iterative predictor-corrector algorithm was used. The default value of the numerical damping, equal to 0.4, was used as it provides a reasonable trade-off between computational cost and accuracy (Orcina 2023a). For cases that considered an operating turbine, BEM was applied with unsteady aerodynamics using the Gonzales method. For the blades, the Rayleigh stiffness proportional damping coefficients of the reference IEA-15-240-RWT OrcaFlex turbine model were applied.

Performing time-domain simulations in OrcaFlex implied that several important choices had to be made, where each of which affected both the simulation time and the resulting accuracy of the simulations. To capture important non-linearities, the environmental actions were applied to the structure at the instantaneous position with the instantaneous heading. Wave kinematics was calculated at every time step and at every finite element position. Wheeler stretching was applied to the Morison element extending above the mean free surface, and wave forces were calculated on the entire mooring lines without applying a cutoff depth.

Second-order forces were applied using the QTF modification to avoid double counting of effects. Furthermore, to obtain a reasonable damping level of the slow-drift motions, both the wave-drift damping and maneuvering load options were included in OrcaFlex. These effects do not require additional input data in OrcaFlex and are formulated based on obtained velocities, encounter frequencies, and added mass coefficients (Orcina 2023a). The theory and implementation of these effects are well documented in the Orcaflex online user manual (Orcina (2023a)) and are therefore not reproduced in this thesis.

The computational cost of the time domain simulation is directly related to the selected time step. The needed timestep depends on the time scale of the events that one tries to simulate. Thus, it will depend on the natural periods, accelerations, and deformations that one expects in the analysis. In this analysis, the wind turbine itself is the most difficult element to simulate, with large accelerations, large blade deflections, and low natural periods. To estimate the effect of the selected time step on an operating turbine, a sensitivity study was performed. A 10 min steady-state joint full field wind-wave sea state at rated wind speed was simulated for the center tower design with time steps of $\Delta t \in [0.05, 0.025, 0.01, 0.005]$ s. Based on the results of the study, presented in Table C.1 in Appendix C, a time step of $\Delta t = 0.025$ was selected for the cases with an operating turbine. In the cases considering a parked turbine, a higher time step of 0.05 s was applied. In these cases, each blade was also represented as a rigid body to limit the size of the FEM system. With this formulation, the distributed wind load is still captured, but not any elastic deformation of the blades. The load cases that consider a sudden loss of a mooring line combined with a controlled turbine shutdown are characterized by a transient occurring over a short time scale. Therefore, the time step was refined to $\Delta t = 0.005$.

5.10.1 Wind turbine controller

In the calculations in the time domain, the Open Source Reference Controller (ROSCO) described by Abbas, Zalkind, Pao et al. (2022) and Abbas, Zalkind, Mudafort et al. (2023) was applied. The bladed-style controller python wrapper developed by Orcina was applied as the interface between the ROSCO controller and OrcaFlex. However, the dynamic-link library and the corresponding IN-file were upgraded to the versions corresponding to ROSCO version 2.7. For all simulations with an operating turbine, the floating mode was enabled, along with wind speed estimation and pitch saturation.

5.11 Modeling of transient effects

This section describes how transient damage and abnormal events are implemented and simulated in the time-domain calculations.

5.11.1 Inflow/outflow model

The ingress/egress model is a simple model that handles the connection between the interior and exterior fluid domains. It is a simplified formulation based on the work of Kong (2009). The inflow/outflow model consists of a flooding model, which handles the flow through an opening, and a floodwater model, which handles the effect of the internal water on the global FOWT motions. An illustration of the problem may be seen in Figure 5.9

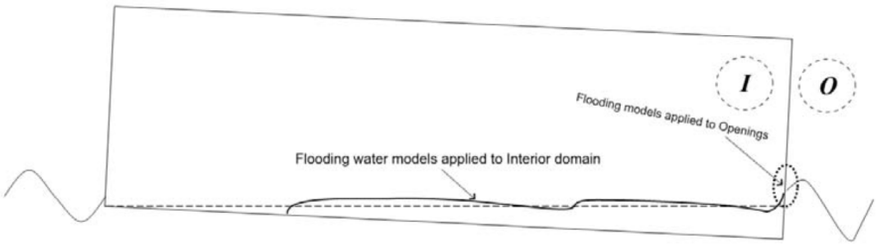

Figure 5.9: Flooding and floodwater model
Source: Kong (2009)

The applied flooding model is a hydraulic model based on the Bernoulli equation. The validity of the model is limited to slow, quasi-steady flooding through a small opening (Kong 2009). For intermediate or larger openings, the integral hydraulic model presented in Kong and Faltinsen (2008) or the hull reshape method presented in Kong and Faltinsen (2010) can be used.

The simplified hydraulic method is a well-known problem in fluid mechanics, often referred to as flow through an orifice. It is still assumed that the flow is steady and irrotational and that the fluid is incompressible and inviscid. By applying the Bernoulli equation along the streamline passing from a point of infinite distance but of equal vertical position as the opening in the external domain to the vena contracta, the following relation may be defined. Note that subscripts "∞" and "O" refer to values outside and at the opening, respectively.

$$z_\infty + \frac{p_\infty}{\rho g} + \frac{u_\infty^2}{2g} = z_O + \frac{p_O}{\rho g} + \frac{u_O^2}{2g} \tag{5.25}$$

where: z_i = Vertical position of point i in the global reference frame ($z_\infty = z_O$)
$p_i = \rho g h^i$ = Pressure
u_i = Fluid velocity

The external and internal pressures are assumed to be purely hydrostatic relative to the instantaneous external and internal free surfaces, respectively. It is further assumed that the air pressure inside the column is equal to the ambient pressure, and any air compression effects from increased filling levels are disregarded. In the case of waves, the diffracted component of the free surface elevation is neglected. The fluid velocity at the point placed in the external domain is also assumed to be negligible. This implies that the fluid velocity due to wave kinematics is neglected. The internal pressure head includes the effect of the internal free-surface staying parallel to the external free surface. By using the definitions of the pressure heads, h^e and h^i, presented in Figure 5.10, Torricelli's law which gives the velocity through the opening, is obtained. The version of the law presented includes a signed velocity, representing that the flow may travel in both directions through the opening.

$$u_O(t) = \sqrt{2g \cdot |h^e(t) - h^i(t)|} \cdot \text{Sign}\left(h^e(t) - h^i(t)\right) \tag{5.26}$$

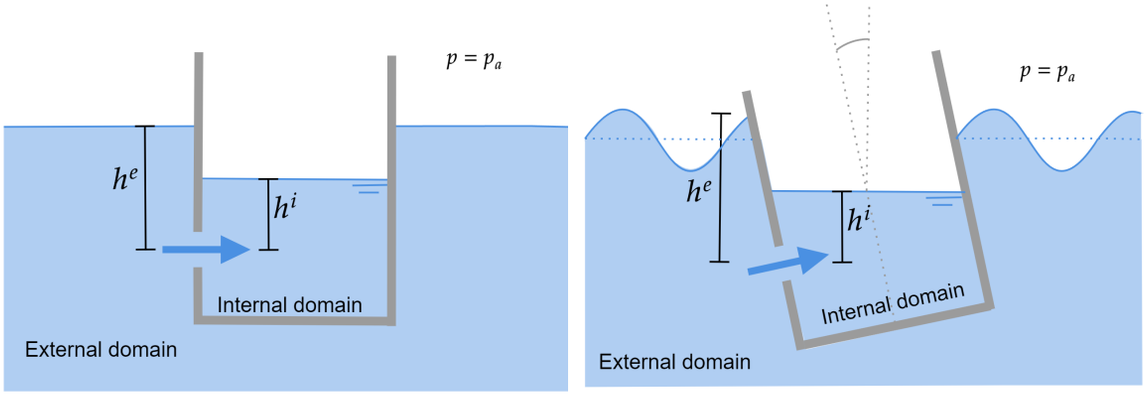

(a) Fixed body in still water

(b) Floating body in incident waves

Figure 5.10: Illustration of pressure head in flooding model

The instantaneous volume flux, $\dot{Q}(t)$, of floodwater passing through the opening is found as the instantaneous velocity at the opening multiplied by the area of the opening. As the area of the vena contracta may be smaller than the opening area, a discharge coefficient is introduced. According to Kong (2009), the discharge coefficient varies between 0.5 and 1, depending on the boundary of the opening. For a sharp opening in a plane wall, the discharge coefficient takes the value of $\mu = 0.63$ (Kong 2009).

$$\dot{Q}(t) = \mu A u_O(t) \tag{5.27}$$

where: $\mu = {}^{A_c}/_{A}$ = Discharge coefficient
A = Opening area
A_c = Area of the vena contracta

The accumulation of floodwater in the column is found by integrating the volume flux that passes through the opening. The effect is then included in the time-domain calculation as a point load corresponding to the rigid lumped mass. A limitation of OrcaFlex is that only the magnitude and direction of the load may be changed in time and not the point of attack. Therefore, the point of attack is taken at the center of the compartment, in the body fixed reference frame. This enables the point of attack to move with the rigid body with respect to the global reference frame, but the point of attack may not move in the body fixed reference frame depending on the compartment filling level. The magnitude of the point load is calculated as the inertial load of the internal water in the accelerated compartment frame.

$$\mathbf{F}_f(t) = -\rho \int_0^t \dot{Q}(\tau) d\tau \cdot (a_z(t) + g)\hat{\mathbf{k}} \tag{5.28}$$

where: $\mathbf{F}_f$ = Point load due to internal water
$a_z(t)$ = Vertical component of acceleration of compartment frame, positive upwards
g = Scalar gravitational acceleration
$\hat{\mathbf{k}}$ = Vertical unit vector, positive upwards

Some of the time-domain simulations use hydrodynamic coefficients from the frequency-domain calculations of the body in the damaged equilibrium with partially filled compartments. In these frequency-domain calculations, the damaged compartments have a mean filling level corresponding to an internal free surface coinciding with the external free surface. When the flooding model described in this section is to be used together with hydrodynamic coefficients already considering the mean compartment filling, it must be subtracted from the mass term of eq. (5.28), as presented in eq. (5.29). In that case, the mean filling level is inputted to the flooding model as an initial condition.

$$\mathbf{F}_f(t) = -\left(\rho \int_0^t \dot{Q}(\tau) d\tau - \bar{m}^{int}\right) \cdot (a_z(t) - g)\hat{\mathbf{k}} \tag{5.29}$$

Combining the frequency-domain solution with internal tank dynamics and the inflow/outflow model may be regarded as an extension of the rigid lumped mass model for internal floodwater. In this sense, the linear dynamic horizontal sloshing effects of the mean configuration are combined with the nonlinear quasi-steady vertical effect of the change in compartment filling. Due to the surge-pitch and sway-roll couplings and the eccentric location of the damaged compartment, both the horizontal sloshing and the inflow/outflow may give excitation in the vertical rotational modes.

However, due to the nature of the time-domain calculations applied in this thesis, the transition from intact to damaged condition with turbine shutdown may not be modeled using both the flooding model and the internal sloshing results. This would require changing the added mass coefficients, wave load excitation transfer functions, and the stiffness matrix. It was initially attempted to implement such a model with the help of the Orcina support team, using the "Restart analysis"-feature in OrcaFlex, but it had two important shortcomings. A "Restart analysis" means that the state of the model is saved at a certain stage of the simulation, allowing it to be restarted again. A powerful feature of this type of analysis is that changes can be made to the finite element model during the restart. When the simulation is restarted, the position and velocity of all elements are maintained, but the properties of the new model are applied to further calculate the time history.

The first of the two shortcomings lies in the implementation of the Reference OpenSource Controller (ROSCO) wind turbine controller using the Dynamic-Link Library (DLL) and the python wrapper. Although the rotor state is transferred correctly in terms of rotational speed and blade pitch, the controller state is not transferred. Consequently, a clear transient is seen in the rotor's response following the restart. Second, if the data obtained in the hydrodynamic radiation problem are changed during a restart analysis, the time history of the retardation function is cleared. This implies that the pressure effects of prior body motions are not modeled correctly. Running a transient simulation under these limitations would imply too large assumptions for the results to have any credibility. The implementation of the flooding model in OrcaFlex is presented in Figure 5.11. Note that the external Python routine is called on every time step after the flooding is initiated.

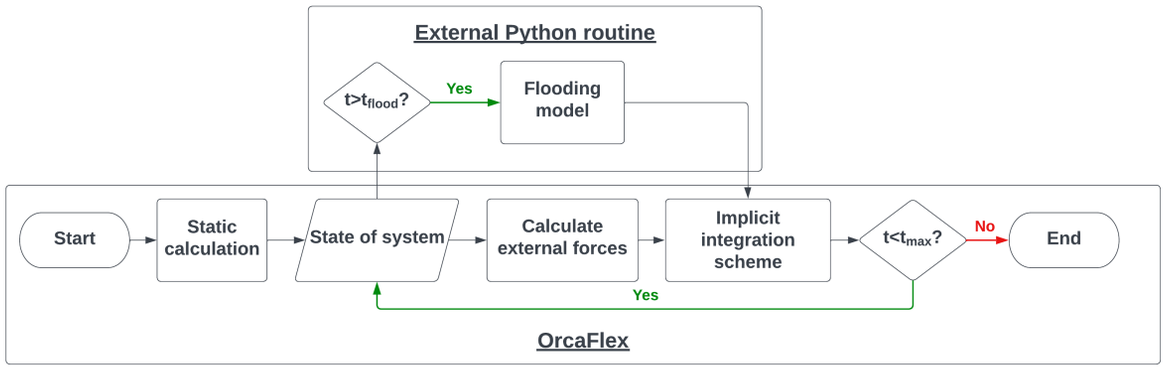

Figure 5.11: External flooding model in OrcaFlex

5.11.2 Wind turbine shutdown

An extension was written to the Python wind turbine controller to model the shutdown of the wind turbine. A turbine shutdown time and strategy are inputted into the OrcaFlex model. If the simulation time is below the shutdown time, the control is handled by ROSCO. When the shutdown time is reached, the extended Python controller pitches the blades until feathered with a pitch rate depending on the shutdown strategy, and the generator is disconnected by setting the applied torque to zero. All shutdown strategies consider one-stage shutdowns, meaning a constant pitching rate is applied. The pitching rates applied in this thesis correspond to those investigated by Jiang et al. (2015).

- Normal shutdown
  - Pitching rate: $1\,^{\circ}/_{s}$
- Controlled shutdown after occurrence of fault
  - Pitching rate: $2\,^{\circ}/_{s}$
- Emergency shutdown
  - Pitching rate: $8\,^{\circ}/_{s}$

The mechanism behind the turbine shutdown is drawn in Figure 5.12. The velocities and forces in the figure are as defined in Figure 4.5. When the blades are pitched into the incident wind speed, the angle of attack becomes negative. This causes a reversal of the lift force, and hence reversal of the normal and tangential forces in the rotor plane. The effect of this is both a torque load, slowing the turbine, and a thrust force acting against the incident wind. The lift and drag coefficient curves for one of the foil segments used in the time-domain simulations are presented in Figure 5.13. In the plot, the reversal of the lift force is apparent. It should be mentioned that this foil segment appears to have a camber, resulting in a positive lift coefficient even for a small negative angle of attack.

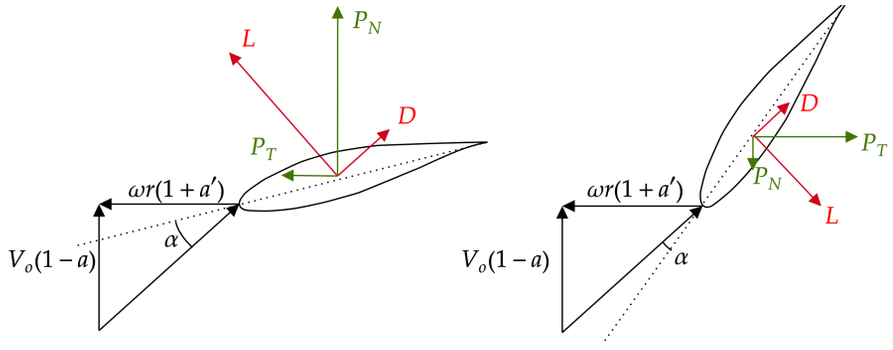

Figure 5.12: Change of aerodynamic forces from blade pitching

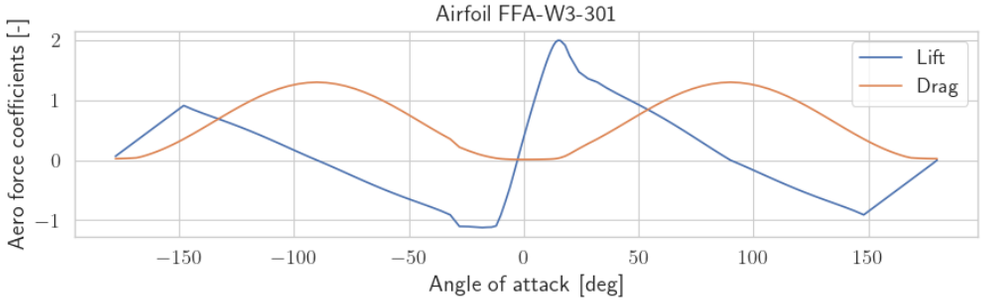

Figure 5.13: Lift and drag coefficients as a function of angle of attack
Source: Adopted from IEA (2022)

5.11.3 Mooring line failure

During the simulations concerning intact conditions, the end nodes of the three 1D dimensional FEM models representing the mooring lines have a slave connection to the substructure at the fairlead positions. To model the loss of a mooring line, the end node of the windward mooring line is released during the simulation. This will result in a transient condition, as the restoring matrix of the system is suddenly changed. The windward mooring line was chosen as this is the most heavily loaded line. Other causes and situations may also lead to the loss of different lines, changing the transient response. As previously discussed in Section 3.3, twisting and tangling of the remaining mooring lines are undesirable following the loss of a mooring line.

CHAPTER 6

Description of concepts

To perform the analysis, two different semi-submersible substructures with different configurations were considered. Both substructures comprise wall-sided, constant-diameter columns and pontoons with rectangular cross-sections. In addition to structural dimensions, the substructures differ by the number of columns and the placement of the tower.

For the definition of the turbine, tower, and UMaine VolturnUS-S substructure, several sources must be visited to obtain sufficient accurate information. In addition to the original report by Allen et al. (2020), the IEA has a GitHub repository (IEA 2022). This repository includes input files that are continuously tested, updated, and maintained. Therefore, it is suggested that the repository should supersede the original report if any discrepancies are observed. In the following, the deviations from the report by Allen et al. (2020) are clearly marked. Furthermore, Orcina has created a report and a numerical model for the RNA, tower, and UMaine VolturnUS-S substructure in OrcaFlex. Orcina states clearly that their report and model are based on their interpretation of the information they had available at the time of writing. Therefore, the Orcina report and model are only used as a guide to model the system in OrcaFlex, and all values used are based on the latest information from IEA.

6.1 Frame of reference

According to DNV (2021b), FOWTs using a semi-submersible substructure must be considered as a compliant structure in all degrees of freedom, where compliant implies rigid-body displacements of several meters or degrees. Unlike ship-shaped structures where the surge axis is naturally defined by the longitudinal axis of the structure, the surge and sway axes might not be as easily defined for a FOWT. However, the axes may be defined by the mooring system. In this thesis, surge, sway, and heave motions are defined as motions along the x, y, and z axes of the body, respectively. Roll, pitch, and yaw are defined as rotations about the same axes. Body-fixed coordinate systems for the peripheral and center tower designs are shown in Figure 6.3 and Figure 6.5, respectively. The definition of the directions of the applied wind and wave conditions is defined as shown in Figure 6.1. The global coordinate system, illustrated in black, coincides with the body-fixed coordinate system when the body is in the initial position. The red dot indicates the position of the tower.

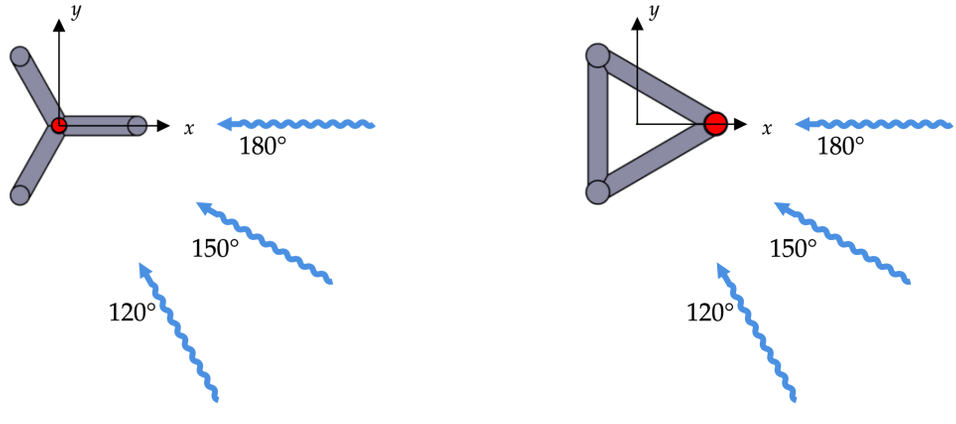

(a) Center tower design

(b) Peripheral tower design

Figure 6.1: Definitions of wind and wave directions

6.2 Wind turbine (RNA)

The wind turbine investigated in this thesis is the IEA Wind 15-MW reference wind turbine (IEA-15-240-RWT), which is the product of a IEA-facilitated collaboration between NREL, Technical University of Denmark (DTU) and UMaine. The wind turbine is a 3-bladed upwind turbine with a low-speed direct drivetrain. The controller utilizes variable speed and variable collective pitch control. Following the definitions created by the IEC, the turbine is class 1B.

Table 6.1: Wind turbine aerodynamic performance

Parameter	Unit	Value
Power rating	MW	15.0
Specific power	W/m	332*
Cut-in wind speed	m/s	3.0
Rated wind speed	m/s	10.87*
Cut-out wind speed	m/s	25.0
Min. rotor speed	rpm	5.0
Max. rotor speed	rpm	7.56
Max. tip speed	m/s	95
Design TSR	-	9

* Changed from Allen et al. (2020)

In Table 6.2, the rotor diameter is reported as 242.2 m as defined in the Github repository. This differs from the rotor in Allen et al. (2020), where the diameter is defined as 240 m. This is caused by the effect of the prebend on the blade arclength, which was not considered in the original report. Further, both values differ from the diameter reported in OrcaFlex, which considers the effect of the rotor precone, lowering the reported diameter. By setting the rotor precone to zero in OrcaFlex, the rotor diameter agrees with the value reported in the Github repository. As an extension of this discrepancy, the specific power decreases due to the larger area swept by the rotor, and the rated wind speed increases to maintain the same TSR.

Table 6.2: Wind turbine geometrical dimensions

Parameter	Unit	Value
Rotor diameter	m	242.2*
Hub height	m	150
Hub diameter	m	7.94
Hub overhang	m	12.03*
Blade prebend	m	4
Rotor precone	deg	-4
Shaft tilt	deg	6

* Changed from Allen et al. (2020)

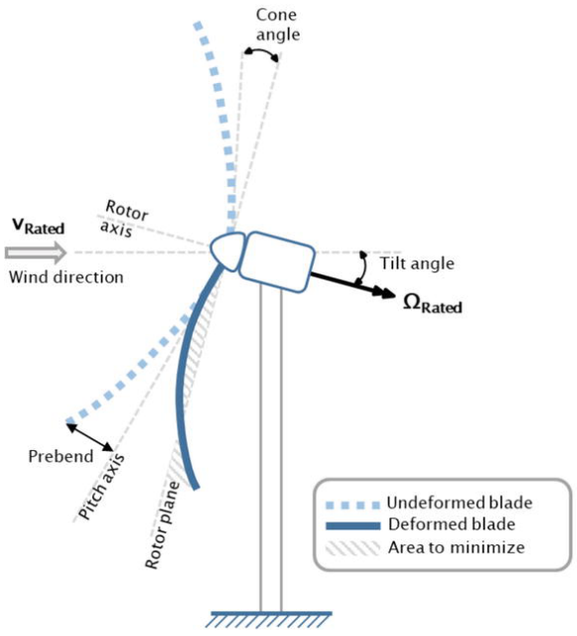

Figure 6.2: Illustration of geometrical dimensions
Source: Sartori et al. (2020)

For the definition of the inertial properties of the RNA, the values given in Gaertner et al. (2020) were found to have several inconsistencies, as pointed out in the Github repository. The values presented in Table 6.3 are therefore based on the documentation available at the Github repository.

Table 6.3: Wind turbine inertial properties

Component	Mass (te)	COG[a](m)	I_{XX} [b]($\mathrm{kg\,m/s^2}$)	I_{YY} [b]($\mathrm{kg\,m/s^2}$)	I_{ZZ} [b]($\mathrm{kg\,m/s^2}$)
Blades	205.25	(-11.42, 0.00, 5.55)	3.493×10^8	1.747×10^8	1.747×10^8
Hub	69.36	(-11.42, 0.00, 5.55)	9.735×10^5	6.200×10^5	6.200×10^5
Nacelle	675.18	(-4.53, -0.14, 4.10)	9.913×10^6	1.086×10^7	1.036×10^7
RNA	949.78	(-6.52, -0.10, 4.52)	4.783×10^8	3.154×10^8	3.164×10^8

[a] COG relative to tower top
[b] Moment of inertia relative to COG

6.3 Tower

According to the Github repository, there was an error in the optimization script used to design the FOWT-specific tower in the original report. As a result, the natural frequency of the first fore-aft and side-side bending modes coincided with three times the blade passing frequency causing tower resonance during operating conditions. The tower was therefore redesigned to increase the bending stiffness, causing the mass to increase.

When designing the tower in OrcaFlex, it was discovered that the latest definition of the tower geometry did not match the reported tower mass with the reported density. After integrating the distributed mass in the OpenFast files available in the GitHub repository, the reported tower mass appeared to be correct. Thus, the definition of the tower geometry appears to be inconsistent. Orcina's solution to the problem is to keep the defined tower geometry but to scale the density until the reported tower mass is obtained. As no detailed structural analysis will be performed on the tower, this approach is also applied in this thesis.

The geometry of the tower is defined by discrete sections of uniform thickness, owing to certain assumptions made in the optimization script regarding the manufacturing of steel towers. Usually, a tower section is produced by rolling a trapezoidal shape into a conical section, which results in the constant thickness of the tower sections.

Table 6.4: FOWT-specific tower geometry

Arc length [m]	Outer diameter[m]	Thickness [mm]	Arc length	Outer diameter	Thickness
0	10	88.528	65.001	10	36.876
13	10	88.528	78	10	36.876
13.001	10	78.377	78.001	10	26.873
26	10	78.377	91	10	26.873
26.001	10	68.146	91.001	10	17.749
39	10	68.146	104	10	17.749
39.001	10	57.782	104.001	10	9.911
52	10	57.782	117	10	9.911
52.001	10	47.297	117.001	10	7.936
65	10	47.297	129.386	6.5	7.936

6.4 Substructures

The definitions of both substructures, but especially VolturnUS-S, have undergone several iterations. Therefore, different values for the parameters may be found when investigating different sources. The specific properties of the substructures applied in this thesis are presented in the following.

6.4.1 Peripheral tower design

The body-fixed coordinate system of the peripheral tower design is presented in Figure 6.3. The coordinate system is located in the water plane, at the geometrical center of the structure.

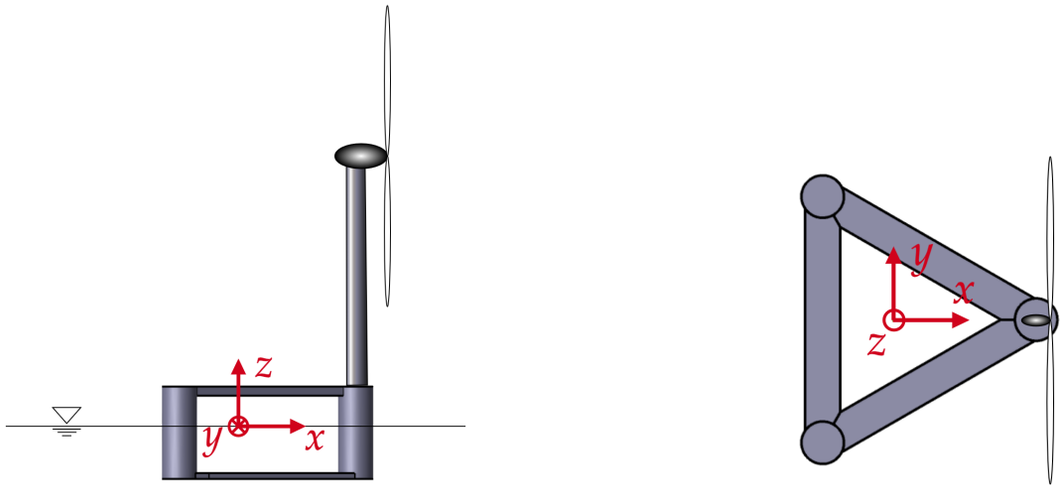

(a) Elevation view (b) Plan view

Figure 6.3: Body fixed coordinate system - Peripheral tower concept.

In Table 6.5, the main geometrical properties of the concept are presented. The values are the result of the upscaling presented in chapter 5.

Table 6.5: Peripheral tower design - geometric properties

Parameter	Unit	Value
Displacement	m^3	13176
Center-center column distance	m	77.32
Column diameter	m	13.32
Pontoon width	m	11.1
Pontoon height	m	2.24
Deck beam width	m	3.5
Deck beam height	m	3.5
Draft	m	20
Freeboard	m	15
Fairlead depth	m	14

Furthermore, the individual and combined inertial properties of the different subsystems are presented in Table 6.6. Note that the radius of gyration of the different parts corresponds to the mass of the respective part.

Table 6.6: Peripheral tower design - inertial properties

	Mass (te)	Center of gravity (m)			Radius of gyration (m)		
		x_g	y_g	z_g	R_{xx}	R_{yy}	R_{zz}
Steel hull	4247.85	0	0	-6.82	29.64	29.64	37.52
Solid ballast	5063.13	-22.3	0	-16.44	38.62	0	38.62
Fluid ballast	1431.15	0	0	-19.68	19.62	19.62	27.74
Tower interface	100	44.56	0	15	0	0	0
Full substructure	10842.12	-10.00	0	-12.81	34.90	29.04	40.00
Tower	1483.41	44.56	0	56.66	30.6	30.6	4.96
Nacelle	675.28	44.56	0	148.46	3.83	4.01	3.91
Rotor + hub	274.61	44.56	0	150.61	35.44	25.25	25.38
Full structure	13275.31	0	0	6.5581	55.651	55.402	40.9

In Table 6.7, the applied drag coefficients are shown. The coefficients for OrcaFlex are scaled to the equivalent cylindrical diameter as described in Section 5.5.3.

Table 6.7: Morison drag coefficients for peripheral tower design

	HydroD				OrcaFlex			
	D_y (m)	D_z (m)	$C_{D,y}$ (-)	$C_{D,z}$ (-)	D_y^* (m)	D_z^* (m)	$C_{D,y}^*$ (-)	$C_{D,z}^*$ (-)
Columns	13.32	$\sim$	1	$\sim$	13.32	$\sim$	1	$\sim$
Pontoons	2.24	11.1	1.6	2.1	11.1	11.1	0.32	2.1

• In the utilized models, the cross-sectional z direction of the pontoons correspond to the global z direction. The drag diameter is defined as the diameter of the extent of the cross-section perpendicular to the flow direction.

• HydroD uses X as the axial cross-sectional direction, while OrcaFlex uses Z. The coefficients in Table 6.7 are renamed so $Y - Z$ defines the cross-sectional plane.

The coordinates of the anchor nodes in the global reference system and the fairlead nodes in the body-fixed reference system are presented in Table 6.8. These coordinates are part of the results of the mooring system optimization tool.

Table 6.8: Fairlead and anchor coordinates for peripheral tower design

Mooring line	Azimuth [deg]	Fairlead position [m]			Anchor position[m]		
		x	y	z	x	y	z
1	0	51.25	0.00	-14	1084.81	0.00	-300.00
2	-120	-25.63	-44.38	-14.00	-542.41	-939.48	-300.00
3	120	-25.63	44.38	-14.00	-542.41	939.48	-300.00

In Figure 6.4, several natural periods of the combined peripheral tower design concept are presented. In addition, the wind and wave spectra corresponding to a normal sea state at rated wind speed are included. The shaded regions illustrate the location of the 1P and 3P excitation periods. For this concept, the natural period of longitudinal sloshing is found to coincide with periods of significant wave energy for the given sea state. It also coincides with the 1P periods of the rotor, but this is not expected to be as critical for the excitation of sloshing. The natural periods of the tower are as presented in Allen et al. (2020)

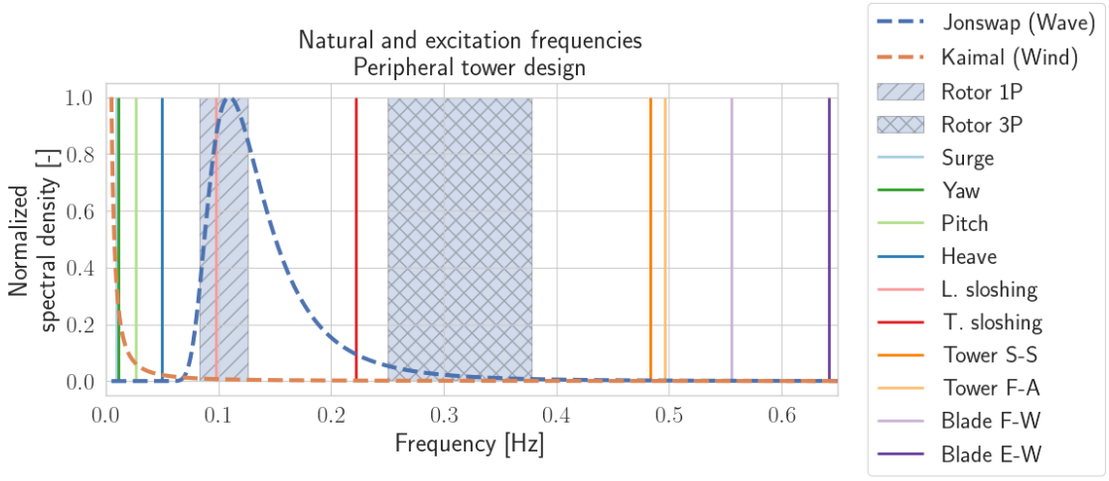

Figure 6.4: Important frequencies - Peripheral tower design
L=Longitudinal, T=Transverse, S-S = Side-Side, F-A=Fore-Aft, F-W=Flap-wise, E-W=Edge-wise

6.4.2 Central tower design

The UMaine Volturn US-S reference platform, hereby referred to as Volturn US-S, is a four-column semi-submersible substructure. It is designed by the University of Maine to support a 15 MW turbine created by the IEA. In Figure 6.5, the body-fixed coordinate system of the center tower design is shown.

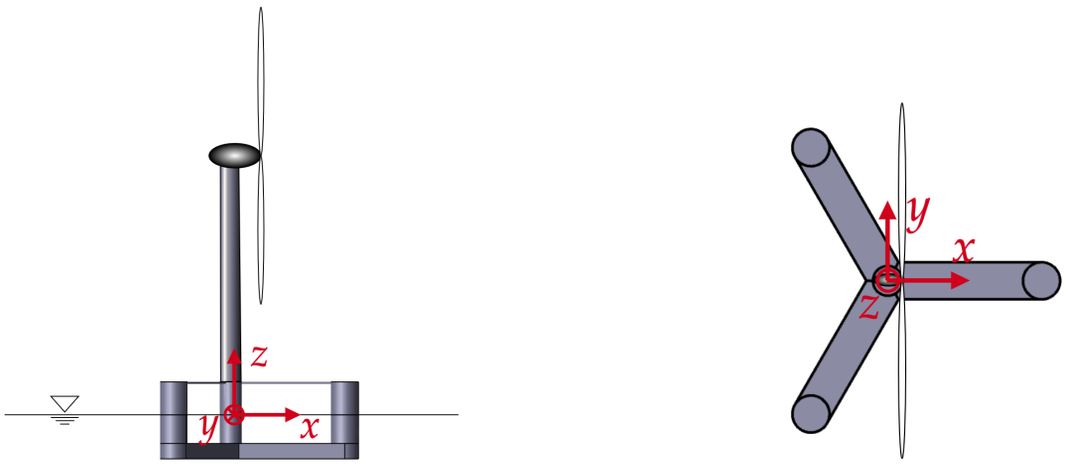

(a) Elevation view (b) Plan view

Figure 6.5: Body fixed coordinate system - Center tower concept.

In Table 6.9, the main geometrical properties of the design of the center tower are presented. It should be noted that the concept has a larger displacement compared to the design of the peripheral tower. This displays the lean design of the latter, resulting from the optimization model. The draft, freeboard, and fairlead depths are equal, as this is used as constraints in the optimization of the peripheral design.

Table 6.9: Center tower design geometric properties

Parameter	Unit	Value
Displacement	m^3	20206
Central-radial column distance	m	51.75
Center column diameter	m	10
Radial column diameter	m	12.5
Pontoon width	m	12.5
Pontoon height	m	7
Brace diameter	m	0.9
Draft	m	20
Freeboard	m	15
Fairlead depth	m	14

The inertial properties of the VolturnUS-S floater are as described by Allen et al. (2020), while the inertial properties for the tower and RNA were calculated using OrcaFlex. When comparing the radius of gyration, the larger mass of the center tower design must be taken into account. Further, the lower vertical position of the center of gravity should be noted.

Table 6.10: Center tower design inertial properties

	Mass (te)	Center of gravity[a](m)			Radius of gyration[b](m)		
		x_g	y_g	z_g	R_{xx}	R_{yy}	R_{zz}
Steel hull	4218.99	0	0	-7.88	30.15	30.15	39.59
Solid ballast	2540	0	0	-18.65	36.59	36.59	51.75
Fluid ballast	11189.19	0	0	-16.77	19.10	19.10	27.01
Tower interface	100	0	0	15	0	0	0
Full substructure	18048	0	0	-14.78	29.43	29.43	34.58
Tower	1483.41	0	0	56.66	30.6	30.6	4.96
Nacelle	675.28	0	0	148.46	3.83	4.01	3.91
Rotor + hub	274.61	0	0	150.61	35.44	25.25	25.38
Full structure	20481.37	0	0	-2.0	45.908	45.818	32.628

[a] Relative to origin.
[b] Relative to own COG.

Similarly, as for the other concept, the drag coefficients for the center tower design are shown in Table 6.11. The drag coefficient for OrcaFlex is scaled in the same manner, using the approach described in Section 5.5.3.

Table 6.11: Morison drag coefficients for center tower design

	HydroD				OrcaFlex			
	D_y (m)	D_z (m)	$C_{D,y}$ (-)	$C_{D,z}$ (-)	D_y^* (m)	D_z^* (m)	$C_{D,y}^*$ (-)	$C_{D,z}^*$ (-)
Center column	10	$\sim$	1	$\sim$	10	$\sim$	1	$\sim$
Radial columns	12.5	$\sim$	1	$\sim$	12.5	$\sim$	1	$\sim$
Pontoons	7	12.5	1.68	2.55	12.5	12.5	0.94	2.55

• In the utilized models, the cross-sectional z direction of the pontoons correspond to the global z direction. The drag diameter is defined as the diameter of the extent of the cross-section perpendicular to the flow direction.
• HydroD uses X as the axial cross-sectional direction, while OrcaFlex uses Z. The coefficients in Table 6.11 are renamed so $Y - Z$ defines the cross-sectional plane.

In Table 6.12, the coordinates of the anchors and fairleads are presented. As for the other concept, the anchor coordinates are in the global coordinate system while the fairleads are defined in the body-fixed system. As the mooring line lengths are equal and the fairleads are located at the columns, the coordinates for the center tower design are shifted radially compared to those for the peripheral design.

Table 6.12: Fairlead and anchor coordinates for center tower design

Mooring line	Azimuth [deg]	Fairlead position [m]			Anchor position[m]		
		x	y	z	x	y	z
1	0	58.00	0.00	-14	1091.56	0.00	-300.00
2	-120	-29.00	-50.23	-14.00	-545.78	-945.32	-300.00
3	120	-29.00	50.23	-14.00	-545.78	945.32	-300.00

As for the peripheral concept, the important natural periods are presented along with characteristic excitation periods in Figure 6.6. From this plot, the concept appears well-designed, with natural periods away from significant excitation. It may also be seen that both concepts have a stiff-stiff tower design.

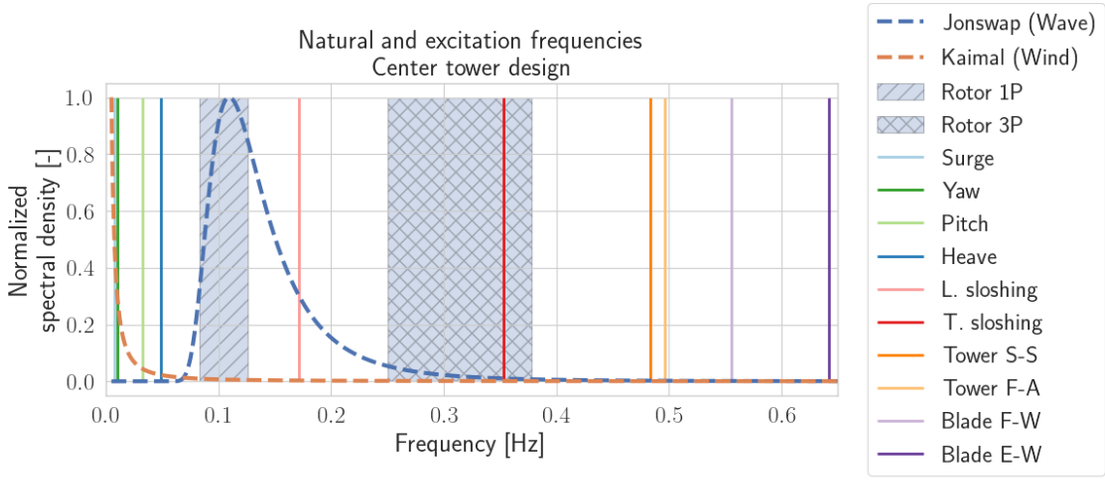

Figure 6.6: Important frequencies - Peripheral tower design
L=Longitudinal, T=Transverse, S-S = Side-Side, F-A=Fore-Aft, F-W=Flap-wise, E-W=Edge-wise

6.5 Mooring system

For all mooring line types, a Coulomb friction coefficient is taken conservatively as $\mu = 0.5$ in both the lateral and axial directions. Segment lengths, segment types, and marine growth thicknesses considered in the analysis are presented in Table 6.13. The segment lengths are products of the mooring system optimization tool, along with the anchor and fairlead coordinates.

Table 6.13: Mooring line optimization result

Segment number*	Type	Length [m]	Marine growth [mm]
1	Chain	25	100
2	MoorLine Polyester	85	100
3	MoorLine Polyester	337.35	50
4	Chain	659.05	50

* Segments are numbered from fairlead to anchor

The parameters for the mooring line segments used in the optimization tool are presented in further detail in Table 6.14.

Table 6.14: Properties of mooring line segments

	Chain	MoorLine Polyester
Type	130 mm, R4 studless	195 mm, sheated
Equivalent diameter [m]	0.234	0.150
Mass per length [kg/m] (0mm / 50mm / 100mm)	336.4 / 353.6 / 377.7	24.4 / 46.0 / 60.7
Axial stiffness [MN]	1443.0	228.0
Normal added mass coefficient [-]	1.0	1.0
Tangential added mass coefficient [-]	0.5	0.0
Normal drag coefficient [-] (0mm / 50mm / 100mm)	2.4 / 4.2 / 6.1	1.2 /1.8 / 2.4
Normal drag diameter [m]	0.130	0.195
Tangential drag diameter [m]	0.041	-
Tangiential drag coefficient [-] (0mm / 50mm / 100mm)	1.15 / 2.0 / 2.9	-
Minimum breaking load	15.560	10.791

In the mean static configuration, each mooring line has a total pretension of 1260.73 kN, where the vertical component is 746.36 kN. The mass equivalent of the combined vertical pretension is 228.32 t, which corresponds to 1.1 % and 1.69 % of the displacement of the center and peripheral tower design, respectively. This is equivalent to a vertical displacement of 0.5 m and 0.53 m for the two concepts.

The force-displacement curves for the total mooring system and for a single mooring line were calculated using a series of static analyses in OrcaFlex through the Python API. The linearized stiffness of a single mooring line, calculated using the difference in force resulting from a ± 1 m offset around the mean configuration, was found to be 13.68 kN/m and 50.5 kN/m in the vertical and horizontal directions, respectively.

The total mooring restoring stiffness acting of the system, calculated using the "Report mooring stiffness"-feature in OrcaFlex, was found to be 41.03 kN/m and 77.38 kN/m in the vertical and horizontal translation modes, respectively. These values are in agreement with the combined stiffness of three mooring lines in a 120° configuration with the individual stiffnesses calculated in Python and presented above.

The vertical stiffness of the mooring system corresponds to 0.91 % and 0.97 % of the vertical hydrostatic restoring stiffness for the center and peripheral tower design, respectively. From these results, it is apparent that vertical pretension should be considered when the needed ballast mass is calculated, but the vertical stiffness may be disregarded in the frequency domain calculations.

Using the same mooring lines for both concepts ensures equal pretension and stiffness in the translational modes. However, as the fairlead positions differ in the radial direction, the stiffness in the rotational modes will be different. The complete mooring restoring stiffness matrices for the center and the peripheral tower are shown in eq. (6.1) and (6.1) respectively. The matrices are calculated using the aforementioned OrcaFlex feature and have kN, m, and rad as force, length, and angle units.

$$k^{Moor,C} = \begin{bmatrix} 77.4 & 0 & 0 & 0 & 989.6 & 0 \\ 0 & 77.4 & 0 & -989.6 & 0 & 0 \\ 0 & 0 & 41.0 & 0 & 0 & 0 \\ 0 & -991.0 & 0 & 1.46E+05 & 0 & 0 \\ 991.0 & 0 & 0 & 0 & 1.46E+05 & 0 \\ 0 & 0 & 0 & 0 & 0 & 1.95E+05 \end{bmatrix} \tag{6.1}$$

$$k^{Moor,P} = \begin{bmatrix} 77.4 & 0 & 0 & 0 & 748.3 & 0 \\ 0 & 77.4 & 0 & -748.3 & 0 & 0 \\ 0 & 0 & 41.0 & 0 & 0 & 0 \\ 0 & -749.6 & 0 & 1.27E+05 & 0 & 0 \\ 749.6 & 0 & 0 & 0 & 1.27E+05 & 0 \\ 0 & 0 & 0 & 0 & 0 & 1.70E+05 \end{bmatrix} \tag{6.2}$$

The mooring stiffness matrices presented above show two important effects of the mooring system. First, it is seen from the matrices that the mooring system introduces surge-pitch and sway-roll coupling. Second, by comparing the roll-roll and pitch-pitch entries of the matrices to the restoring coefficients described in Section 4.5, one can see that the mooring system has a large contribution to the rotational restoring. For the center tower concept, the mooring stiffness in roll and pitch corresponds to 5.55 % of the hydrostatic restoring, while it corresponds to 7.94 % for the peripheral tower design. As rotational restoring may be design-driving for a FOWT, this is important to include in the analysis.

CHAPTER 7

Description of selected operational site

In this chapter, the selected operational site is presented. In addition, the results of the site-specific environmental model are included.

7.1 Operational area

The operational area considered for the thesis is the proposed location of the aforementioned Trollvind park by Equinor. Trollvind is, as the name suggests, located in the proximity of the Troll O&G field. The intended capacity of the park is 1 GW, which implies a minimum of 67 wind turbines if a 15 MW turbine is chosen. The project aims to supply power to the Troll and Oseberg field, which today are electrified by power cables from shore[1]. The wind park may also supply the Bergen region with renewable power (Equinor 2022).

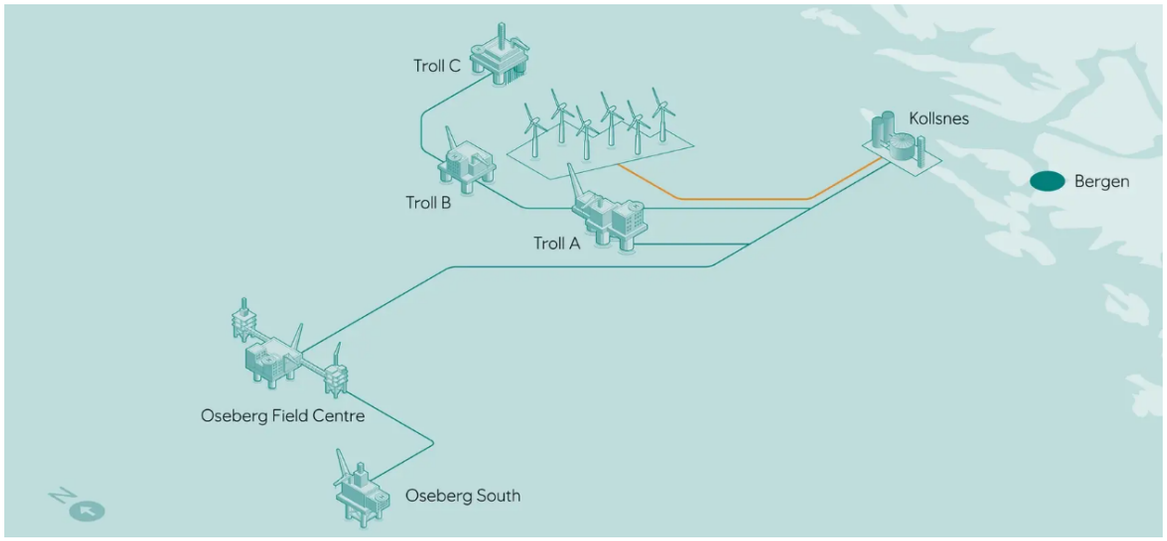

Figure 7.1: Illustration of the proposed Trollvind offshore wind turbine park
Source: (Equinor 2022)

The water depth at the Troll field is in the range of 300-340 m, which implies that a floating wind park is the only viable solution. The field is located about 65 km from Kollsnes, where the power cables from Troll are connected to the main grid, and approximately 80 km from Gulen, where the crane base for the construction of Hywind Tampen has been built. This is beneficial as one knows that it is possible to lay power cables to shore and that there is a suitable offshore base within towing distance.

[1] At the 22nd of May 2023, Equinor announced that the development of Trollvind is postponed.

7.2 Site-specific environmental conditions

By using the obtained environmental data, several metrics may be constructed to obtain an understanding of the conditions at the selected site. As the site is considered as a potential site for FOWTs, one would ideally desire high mean speeds, with low turbulence and mild wave and current conditions. Generally speaking, this is, of course, contradictory, as high wind speeds are correlated with harsh sea states.

By taking the 1-hour wind speed at 10 m altitude, using the power law to obtain the wind speeds at the hub height, and assuming that the wind conditions correspond to the 1-hour mean with zero turbulence, the maximum theoretical power at the site can be estimated. In addition, the wind speed over the entire swept area is assumed to be equal to the hub height wind speed.

Under these assumptions, the mean annual wind power density is found to be 0.0196 GWh/m^2 across all 41 years of data, with a standard deviation of 0.0021 GWh/m^2. For a turbine with the dimensions considered in this report, this corresponds to a mean yearly theoretically available power of 884.78 GWh. Furthermore, by interpolating the power coefficient as a function of wind speed, from the rotor performance tables developed by the IEA, the produced power may be found. By this approach, the mean annual power produced is found to be 85.48 GWh, with a standard deviation of 3.68 GWh. The increased standard deviation relative to the mean is most likely due to the variability of extreme wind speeds, where the theoretically available power increases while the power production goes to zero. Under the presented assumptions, the results indicate a mean annual capacity factor of 65.01% with a standard deviation of 2.8%. This will clearly be the upper bound of the capacity factor, as the assumptions made regarding zero turbulence and constant wind speeds across the rotor disk do not hold. In the obtained results, the generator efficiency of 95.76% is included, but any other losses are not accounted for.

Figure 7.2 shows a scatter plot of H_s and T_p, along with histograms of their relative occurrences. As expected, most of the significant wave heights are located towards mild sea states, but extreme values are also apparent. One can also see that the wave height is limited for short spectral periods, as expected due to wave breaking.

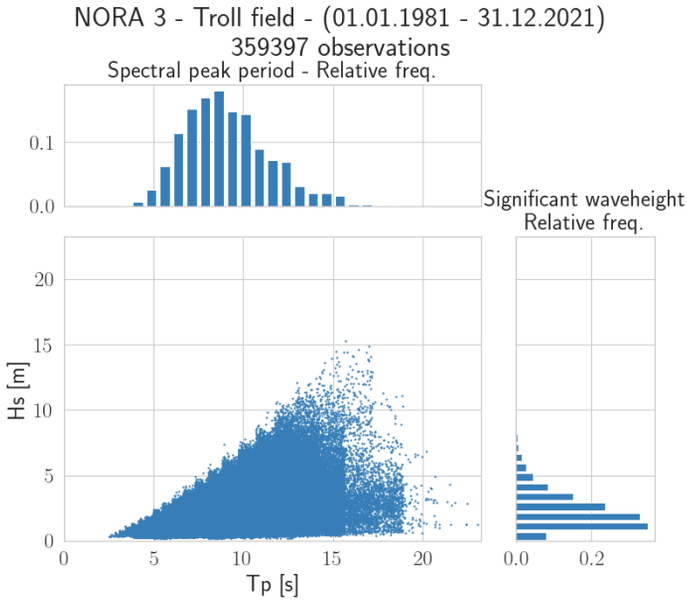

Figure 7.2: Scatter plot and relative frequency of significant wave height and spectral peak period

In Figure 7.3, monthly variations in the data set are displayed. As expected, the data set shows more severe environmental conditions in the winter and autumn, compared with the spring and summer. One can also notice a larger spread in the data in the winter months, quantified by the spread between the 10- and 90 percentiles.

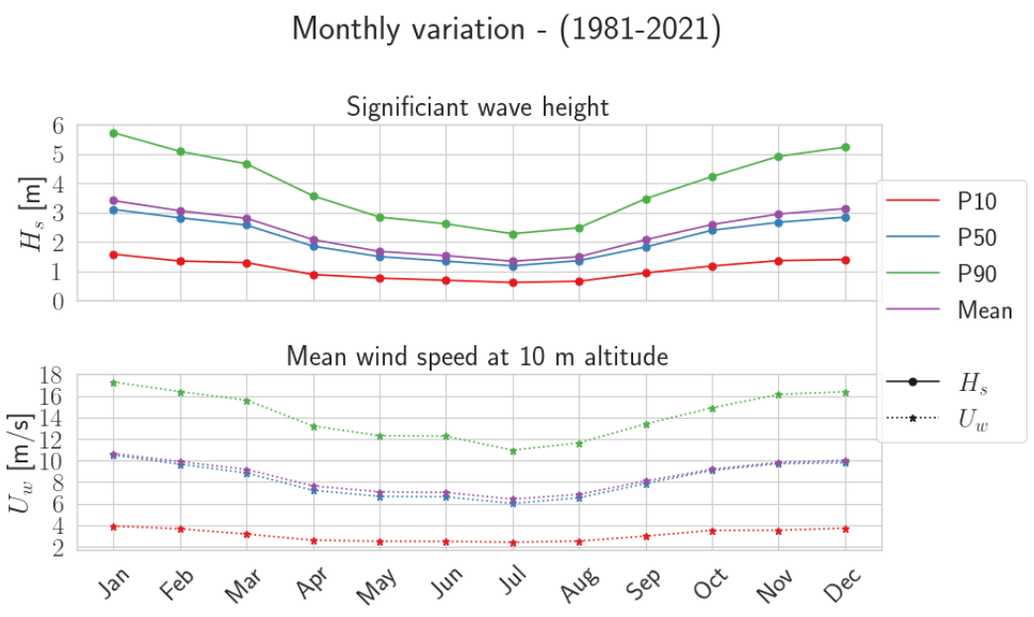

Figure 7.3: Monthly variation in wave heights and mean wind speeds

Looking at the wind directions presented in the wind rose in Figure 7.4, one can see that the most frequent wind direction is from the north or south. The direction of the wind rose is defined as the direction from which the wind blows. The radial scale of the wind rose is the relative occurrence and the colors show wind speeds. This is also the direction where the most extreme wind speeds occur. An interesting observation is the almost complete lack of eastern winds. This may be explained by the prevailing westerlies blowing eastward in the atmospheric Ferrel cell (Brittanica n.d.).

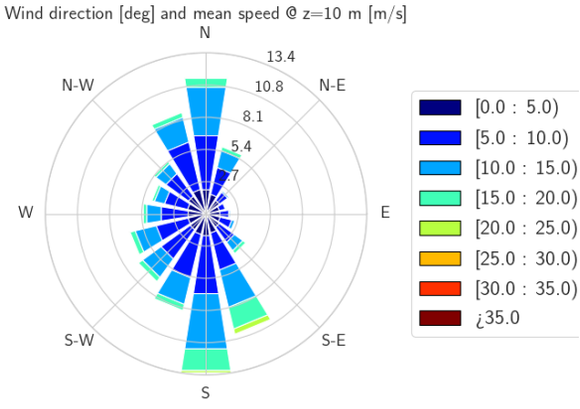

Figure 7.4: Mean wind direction vs. mean wind speed at 10 meter altitude. Wind direction is defined as the direction from which the wind blows

Figure 7.5 shows windroses of both significant wave height and spectral peak period versus the wave direction. Note the opposite definition of direction compared with the wind. The plot shows that most of the waves align with the wind, traveling from or toward the north. Expected wave action is not seen traveling from the coast of Bergen towards the wind speed. This is associated with the limited fetch length of only 60 km. Furthermore, from the wave periods, the longest waves are found traveling toward the shore. This is explained by swell from the North Sea.

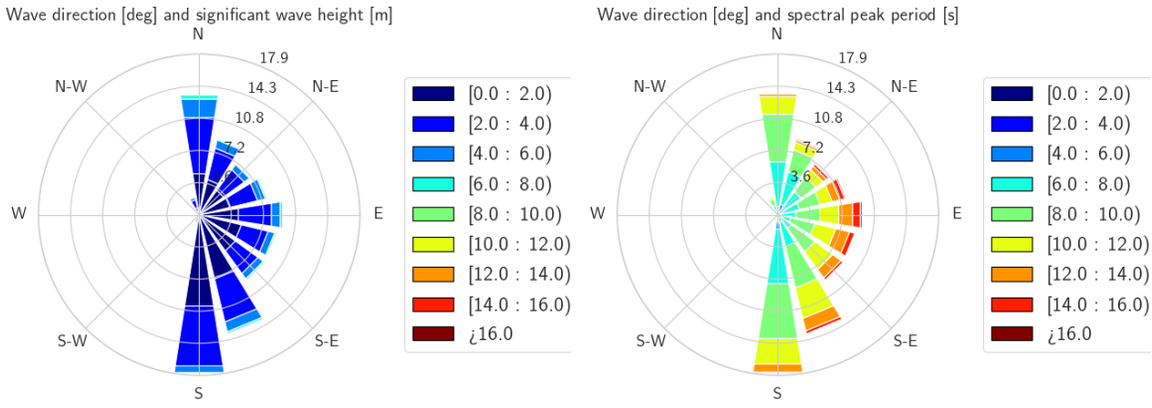

(a) Wave direction versus significant wave height

(b) Wave direction versus spectral period

Figure 7.5: Wave direction versus significant wave and spectral peak period. The wave direction is defined as the direction of propagation.

Normal Sea State (NSS)

In normal sea states, the significant wave height and the spectral peak period are taken as their expected values conditional on the wind speed at 10 m altitude.

For the wind speeds considered in the load cases applying the normal sea state, the following values are found:

Table 7.1: Normal sea states

Number	U_w^{hub} [m/s]	$U_w^{10\,m}$ [m/s]	H_s [m]	T_p [s]	γ [-]	$U_c^{0\,m}$ [m/s]
1	8.59	5.88	1.67	9.11	1	0.18
2	10.59	7.25	1.87	9.13	1	0.22
3	12.59	8.62	2.12	9.18	1	0.26
4	25	17.11	4.82	10.32	1.41	0.51

Severe Sea States (SSS)

For severe sea states, the environmental contour method is applied. For the selected wind speeds, discrete points along the 50-year H_s-T_p contour are selected. Ideally, every point on the contour line should be investigated because of the dynamic amplification seen at selected wave periods. Again, to limit the total number of load cases, it is assumed that, for a given wave period, the response increases with increasing significant wave height. This is a reasonable assumption, which makes it sufficient only to consider the upper half of the environmental contour. In addition, because the thesis focuses on the global response of the structures, and the structures have rigid-body natural periods in the high-period tail of the wave spectra, the main focus is on long spectral peak periods. For each relevant wind speed, a total of six discrete sea states are selected along the conditional environmental contour. The number in the name of the severe sea states refers to the wind speed, which corresponds to the wind speeds from the NSS, while the letter corresponds to the selected H_s-T_p pair along the contour. The selected sea states are tabulated in Table 7.2 to Table 7.5, and the corresponding environmental contours are presented in Figure B.1 to Figure B.4 in the Appendix.

Table 7.2: Severe sea state 1

#	H_s [m]	T_p [s]	γ [-]
1A	5.34	7.95	5.00
1B	7.33	12.42	5.00
1C	8.25	16.9	1.61
1D	7.33	20.24	1.00
1E	5.34	25.78	1.00
1F	1.71	28.08	1.00

Table 7.3: Severe sea state 2

#	H_s [m]	T_p [s]	γ [-]
2A	5.68	8.14	5.00
2B	7.72	12.59	1.71
2C	8.65	16.95	1.00
2D	7.72	20.10	1.00
2E	6.68	22.70	1.00
2F	1.80	27.47	1.00

Table 7.4: Severe sea state 3

#	H_s [m]	T_p [s]	γ [-]
3A	5.98	8.29	5.00
3B	8.00	12.63	1.85
3C	8.92	16.83	1.00
3D	8.00	19.85	1.00
3E	5.98	22.25	1.00
3F	2.01	26.67	1.00

Table 7.5: Severe sea state 4

#	H_s [m]	T_p [s]	γ [-]
4A	8.58	9.99	5.00
4B	10.23	13.23	2.70
4C	10.92	16.25	1.10
4D	10.23	18.34	1.00
4E	7.28	20.05	1.00
4F	5.03	20.73	1.00

Extreme Sea States (ESS)

Extreme sea states are used in load cases that investigate the survival of a parked turbine. If an intact structure is considered, the sea states with 50-year return periods are used. For damaged structures, it is sufficient to ensure survival over a year, which calls for sea states with a one-year return period. The environmental contours from which the sea states are selected are calculated using the joint probability distribution of significant wave height and spectral peak period. The load cases consider unconditional mean wind speeds with the same return periods, thereby disregarding the covariance between wind and waves. Similarly, as for the severe sea states, the extreme sea states are tabulated in Table 7.6 and Table 7.7, and plotted in Figure B.5 and Figue B.6.

Table 7.6: 1-year extreme sea state

#	H_s [m]	T_p [s]	γ [-]
1yA	7.52	9.13	5.00
1yB	10.36	12.42	3.72
1yC	11.70	15.43	1.75
1yD	10.36	16.93	1.00
1yE	5.55	17.76	1.00
1yF	2.68	20.04	1.00

Table 7.7: 50-year extreme sea state

#	H_s [m]	T_p [s]	γ [-]
50yA	9.14	9.71	5.00
50yB	12.85	13.70	3.88
50yC	14.60	17.48	1.63
50yD	12.85	19.24	1.00
50yE	5.73	19.91	1.00
50yF	1.02	27.03	1.00

CHAPTER 8

Definition of design load cases

The selection of load cases, along with the assumptions made during their definitions, was dictated by the simulation time of the time-domain simulations. A simulation of an operating turbine in irregular waves and turbulent wind, with unsteady aerodynamics and full QTFs had a simulation wall time of approximately 10 hours on the applied setup. Although batch processing was applied over several threads, the number of cases had to be limited.

DNV (2018) defines a series of design load cases which covers all aspects of the design life of a wind turbine. Furthermore, DNV (2021c) defines additional design load cases specific for FOWT. The load cases are in general separated into ultimate strength and fatigue load cases.

The design load cases specify the environmental conditions to be applied in the analysis. These environmental conditions are specified by the following parameters:

- Mean wind speed
- Turbulence model
- Sea state (H_s, T_p)
- Wind and wave directionality
- Current
- Water level

For load cases involving operating conditions, a range of wind speeds is defined, all of which are to be simulated. However, DNV (2018) allows for only investigating the rated wind speed, 2 m/s above and below the rated wind speed and the cut-out speed for load cases involving ultimate strength.

It is also specified that the worst combination of aligned and misaligned wind and waves should be considered. As both substructures are symmetric in sectors of 60°, only wind/wave directions between 120°-180° were investigated. This is a simplification for the peripheral tower design, where the placement of the tower limits the symmetry. As will be seen, the direction chosen appears conservative for this concept. For the misaligned wind and wave directions, it was decided only to investigate misalignments of ±30° to reduce the number of simulations. This assumption may qualitatively be justified by the direction of the wind and waves presented in Figure 7.4 and Figure 7.5. In these plots, it may be seen that the largest wind speeds, largest significant wave heights, and longest spectral peak periods occur along the North-South or South-North direction. In principle, also the time correlation between the direction will also matter. Across all simulations, only long-crested waves were applied. This is also an assumption, as one could expect bidirectional wind-driven waves and swell. Generally, in the O&G sector, long-crested waves are considered conservative. However, it is debated whether this assumption holds for offshore wind, due to the large aerodynamic damping from the rotor.

Due to a lack of site-specific data, some simplifications were made related to the current and water level. For the current, it was considered purely wind-driven by the model proposed by DNV (2019b). For the water depth, only the mean water level was considered. Due to the large depth of the selected location, this is considered a justifiable simplification.

8.1 Definition of intact and damaged conditions

Figure 8.1 shows the compartmentalization of both substructures with the filling levels associated with the intact condition. The blue and orange filling of the compartments show the liquid and solid ballast, respectively. In addition, the collision compartment around the still water line may be seen in all columns.

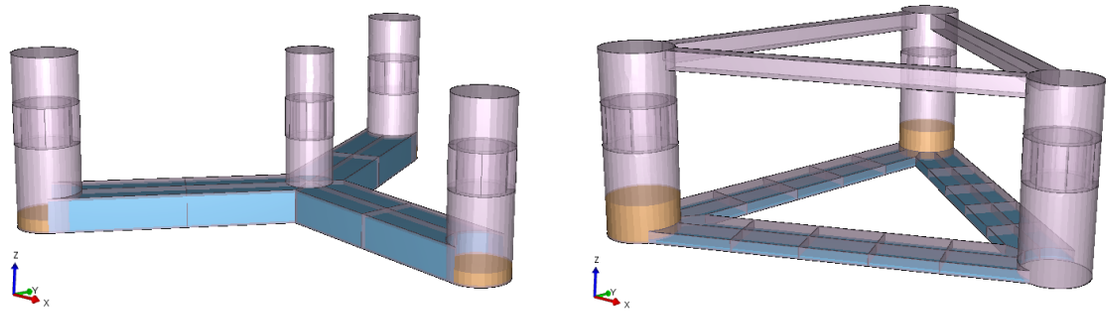

(a) Center tower design (b) Peripheral tower design

Figure 8.1: Compartments, with filling levels corresponding to the intact condition.

The filling levels of ballast shown in Table 8.1, do not consider any reduction of compartment volume due to internal structure such as frames or stiffeners. The remaining volume subjected to external flooding is thus overestimated and conservative.

Table 8.1: Ballast filling levels in intact condition

	Center tower concept	Peripheral tower concept
Fluid ballast, placed in pontoons	92.32%	29.03%
Fixed ballast, placed in columns	15.90%	41.85%

In the analysis a "two-compartment" philosophy will be adopted, which means that the damage cases will consider pairwise flooding of two compartments. This is to safeguard against the event of damage occurring at the watertight bulkhead separating two compartments.

To obtain a complete analysis of the damage cases in all relevant environmental conditions, with a sufficient number of random seeds, only two damage conditions will be selected for the time-domain calculations. In general, all time-domain cases will be calculated using the quasi-static method. For the worst cases, the effect of sloshing and transient behavior will be analyzed.

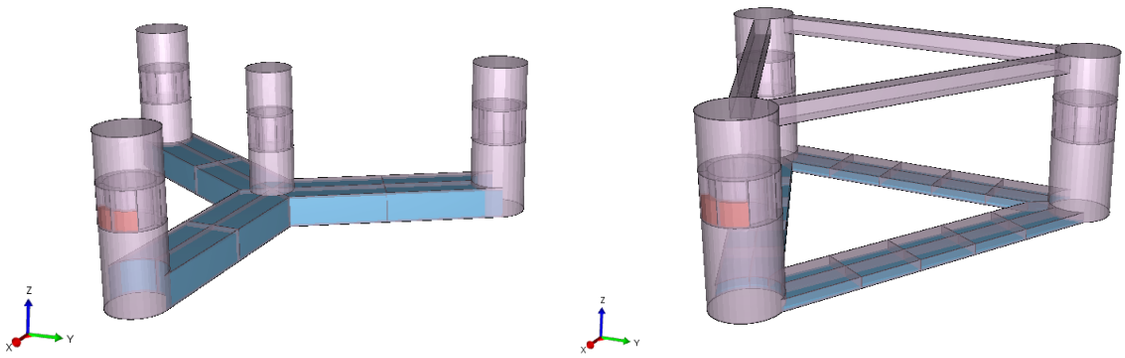

(a) Center tower design (b) Peripheral tower design

Figure 8.2: Damage case 1: Two damaged column compartments

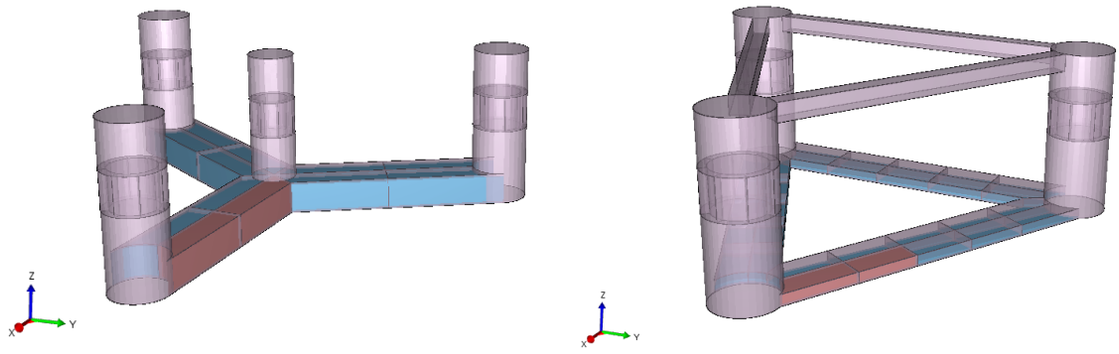

(a) Center tower design

(b) Peripheral tower design

Figure 8.3: Damage case 2: Two damaged pontoon compartments

8.2 Simulated load cases

In this section, the simulated load cases are defined. All load cases are selected from *DNV-ST-0437* and *DNV-ST-0119*, focusing on load cases considering ultimate strength and damaged conditions. The computational cost of the simulations was much larger than anticipated, as running simulations over multiple simultaneous processes increased the computational time of the respective simulations. Furthermore, the implementation of the wind turbine controller in OrcaFlex is not safe for parallel processing and therefore the controller DLL could not be shared between processes. This appeared to further slow down the simulations with an operating turbine. The longest simulations took almost 48 hours, which resulted in months of continuously running simulations day and night.

Consequently, the number of random seeds had to be reduced. It was decided to run two random seeds across all load cases and all combinations of environmental actions to understand the behavior of the systems and identify critical combinations. For critical combinations, five random seeds were simulated to obtain a better estimate of the expected extreme values. It is stressed that the number of seeds should be increased to be able to estimate the extreme values with confidence. As a reference, DNV (2018) recommends a minimum of six random seeds for fatigue calculations, and it is also recommended to check the variability of estimates obtained from different seeds.

According to DNV (2021b), the critical response of a transient response arises as an effect of the transient itself. For a stationary load case, the critical load is due to the stochastic process resulting from the combined action of the environmental conditions. From these definitions, it is concluded that the need for several random seeds is less in a transient load case compared to a stationary load case. In addition, all transient conditions are performed in relatively mild sea states, which further indicates that a reduced number of seeds may be sufficient.

8.2.1 Power production

Within the load cases considering an operating turbine, DLC 1.6 was chosen. This is a stationary load case that considers the operating wind speeds, along with the 50-year conditional severe sea states. Further, it considers only aligned wind and wave directions, from multiple directions. Only wind-driven current aligned with the mean wind direction is included.

Typically, the control system limits the operation of the turbine in environmental conditions close to the cutoff speed, if such conditions are design-driving (DNV 2019a). However, in this analysis, it is assumed that the turbine operates at the sea states conditional to the cut-out wind speed. The response obtained from these simulations should be considered during the development of the control strategy.

The main reason for including this operational load case in an analysis of ultimate strength, accidental condition, and abnormal events, is that it may be design-driving in terms of mooring line capacity. The combination of severe sea states, considerable current speeds, and maximum rotor thrust often results in the largest mean mooring line tensions (DNV 2019a). The load case is also identified as a critical load case in terms of dynamic stability (DNV 2021b), and is a useful reference for the other conditions.

As OrcaFlex only allows starting the simulation with a stationary turbine, long simulations must be considered. In the first 400 s, the wind speed is ramped from zero to the operating wind speed. This allows a controlled start-up of the turbine, preventing simulation failure due to turbine speed overshooting. In the subsequent 400 s, turbulent wind and irregular waves are simulated, allowing the transient phase of the simulation to die out. After this transient, a full stationary one-hour sea state is simulated.

Taking into account the four different wind speeds, along with the six sea states at each wind speed and the three wind directions, this results in 72 simulations of 4400 s per floater design, per random seed. Therefore, only 2 random seeds are considered for every wave heading due to time constraints. As the different wind and wave directions use the same realization of the wind and wave processes, this is a reasonable approach for determining the worst heading. When the worst combination of sea state and directions is identified for a selected set of response variables, three additional realizations with different random seeds are analyzed. A diagram showing the analysis of the load case is shown in Figure 8.4.

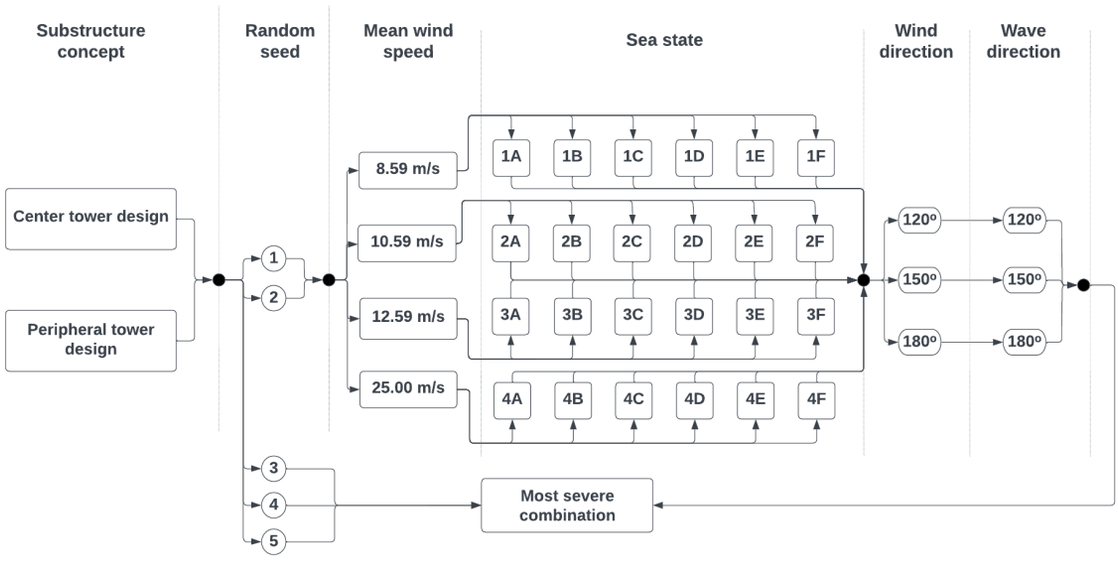

Figure 8.4: DLC 1.6 schematic

8.2.2 Parked turbine in storm conditions

The selected DLC considering a parked turbine in storm conditions is DLC 6.1. The wind speed considered in this load case is the 50-year wind speed. This wind speed is simulated along with selected sea states from the joint 50-year H_s-T_p contour. The load case also specifies that a 50-year current should be included, which is considered as the current driven by the 50-year wind speed in this analysis. Both aligned and misaligned wave and wind directions are considered, with a misalignment of ±30°. DNV (2018) specifies that both nacelle yaw misaligned and slippage of the yaw control system should be considered. This was excluded from the analysis, as it would increase the number of simulations by several multiples. Similarly to the previously described load cases, a 400 s start-up followed by a 400 s transient and 1-hour steady-state duration was simulated. The schematic of the load case is shown in Figure 8.5.

This load case was selected as it is considered design-driving for several of the system components. For the RNA, the 50-year wind load may introduce extreme loads on the blade bearings. It is also expected to result in extreme tower-bending moments. For the floater and mooring system, the hydrodynamic loads from the large sea states and the large current speed are expected to result in design-driving loads (DNV 2019a).

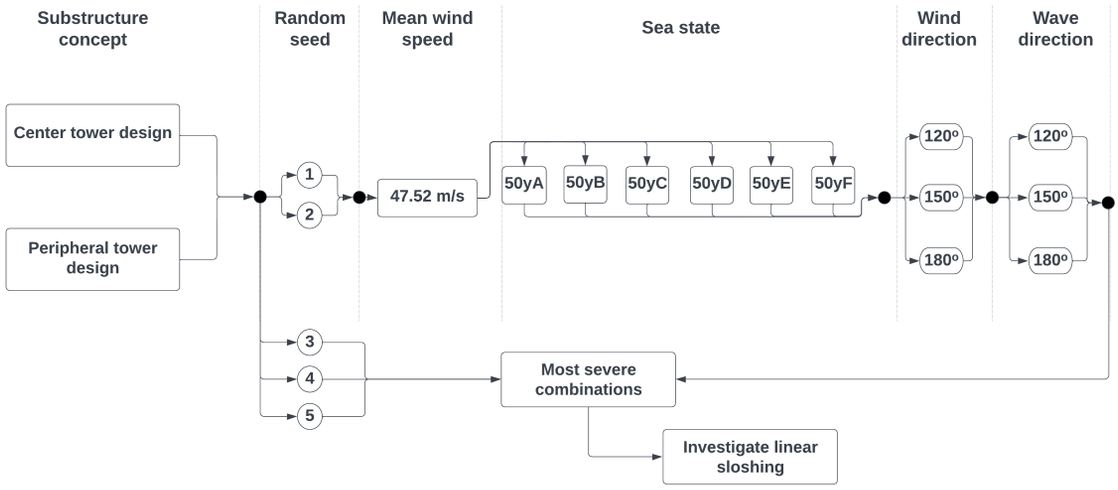

Figure 8.5: DLC 6.1 schematic

8.2.3 Parked turbine after occurrence of fault

The load cases considering a parked turbine after the occurrence of either a fault or a damage is floating-specific, and is also referred to as redundancy check conditions. In these conditions it is assumed that the system has reached a new equilibrium after the accidental event has occurred and the turbine has been shut down. Two separate load cases are decided, considering flooded compartments and the loss of a mooring line. The aim of the analysis is to check surviability time of one year, which is assumed to be sufficient until the structure may be repaired or decommissioned.

Flooded structure

The stationary load case considering a flooded structure is DLC 7.5. For this load case, the 1 year extreme mean wind speed is considered along with a series of unconditional joint H_s-T_p sea state with a return period of 1-year. Several directions are considered with wind-wave misalignment. For each concept, both damage case presented in Section 8.1 are considered. The simulation is performed with 400 s for the transient to die out, followed by 3600 s of steady state. An overview of the load case is presented in Figure 8.6.

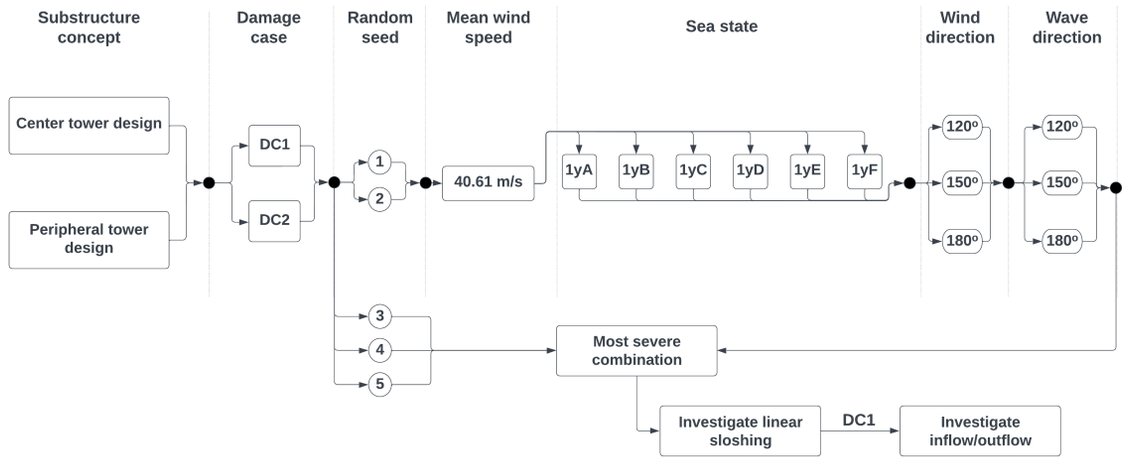

Figure 8.6: DLC 7.5 schematic

All the initial simulations are performed using the quasi-static model. For the most severe cases, the effect of sloshing as well as ingress/egress will be investigated.

Loss of mooring line

To analyse the stationary redundancy condition after the loss of a moorine line, DLC 7.4 was selected. Similarly as DLC 7.5, this loading condition considers the 1-year extreme wind speed with the corresponding unconditional joint sea state. In DNV (2021b) wind-wave misalignment is specified. However, as the results from DLC 6.1 shows that the largest offset and mooring tension occurs for aligned wind and wave action, only such cases will be considered. This is due to time constraints, at it is stressed that the full combination of wave and wind directions should be considered. The schematic of the load case is included in Figure 8.7.

As vessels in OrcaFlex in reality is modeled as a rigid body located at a certain point with an attached drawing, care must be placed to prevent the mooring lines from passing through the external hull. This is taken care of by including shape elements fixed to the location of the columns in the body reference frame. The sole purpose of these elements are to prevent lines from passing through the body, and they do not affect the simulation in any other way.

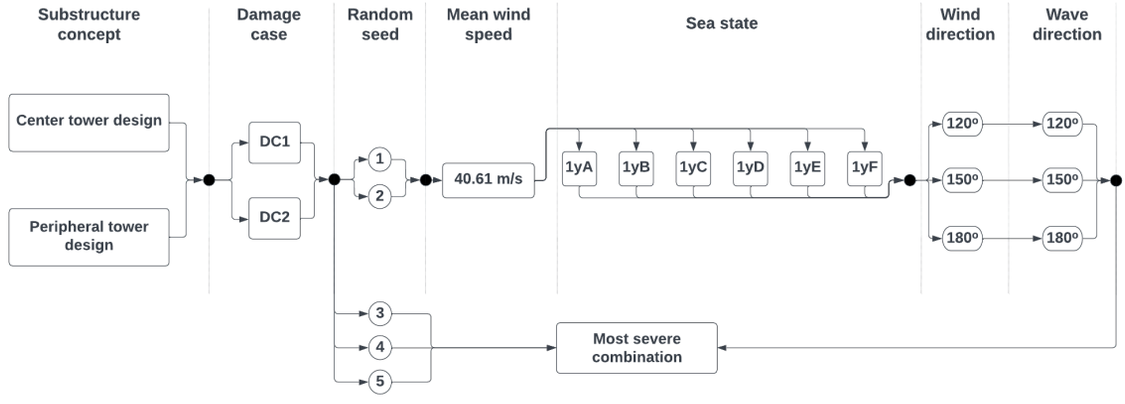

Figure 8.7: DLC 7.4 schematic

8.2.4 Emergency stop

The load case involving an emergency stop of the turbine is DLC 5.1, specified in DNV (2018). It is a transient load case that utilizes the normal turbulence model with the operating wind speeds, along with the normal sea states. According to the standard, only aligned wind and wave directions are considered from multiple directions. As for the other load cases, the schematic is shown in Figure 8.8 below.

The emergency shutdown of the turbine is initiated after a 400 s undesirable transient phase simulation, where the blades are pitched until feathered with a pitch rate of 8 °/s. In addition, the generator is disconnected by setting the generator torque to zero. The transient phase related to the shutdown is simulated for 600 s after the shutdown is initiated.

The emergency shutdown of the turbine can introduce an extreme load on the system. The abrupt pitching of the structure will result in large bending moments at the base of the tower due to the overhang of the RNA (DNV 2019a). The emergency shutdown of the turbine will also require a large restoring moment. DLC 5.1 is also defined as a critical transient stability load case by DNV (2021c).

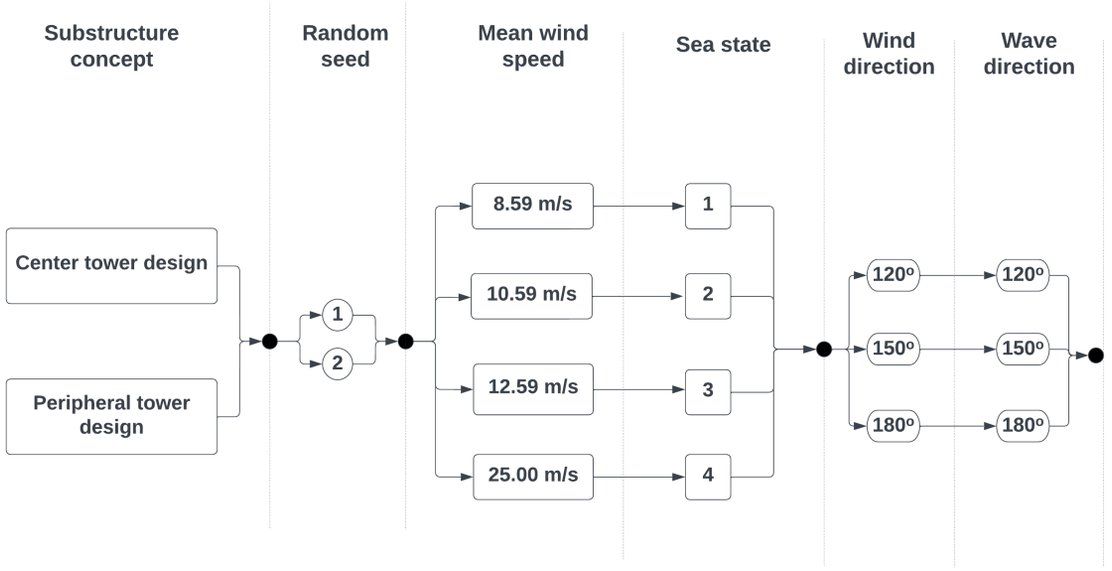

Figure 8.8: DLC 5.1 schematic

8.2.5 Operating turbine with shutdown due to occurrence of fault

When simulating the transient stages of the damage conditions, DNV (2021b) specifies that the response of the control system should be included. Therefore, these load cases include a controlled turbine shutdown, with a pitch rate of 2 °/s, initiated ten seconds after the damage occurs. Both of the following load cases use a start-up time of 400 s before a transient failure of 600 s is simulated.

Flooded structure followed by turbine shutdown

In Figure 8.9, the setup of the analysis regarding DLC 2.8 is shown. As two damage conditions are used, along with misaligned wind and waves, this is a computationally demanding load case.

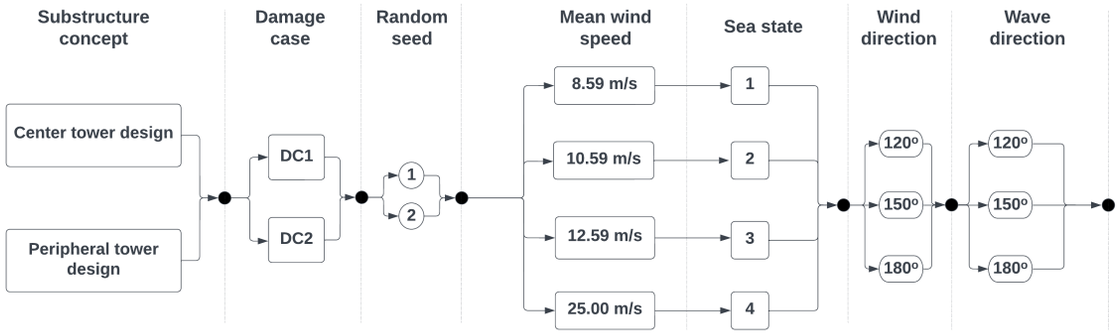

Figure 8.9: DLC 2.8 schematic

Loss of mooring line followed by turbine shutdown

Similarly, the setup of DLC 2.6 is presented in Figure 8.10. The main difference between this analysis and DLC 2.6 is that only aligned wind and waves are considered. This, along with only one damage condition, lightens the computational burden. It is rementioned that the Coulomb friction coefficient is taken as $\mu = 0.5$ in both the axial and tangential directions. This coefficient is expected to influence the offset of the damaged system and is hence taken conservatively in this study.

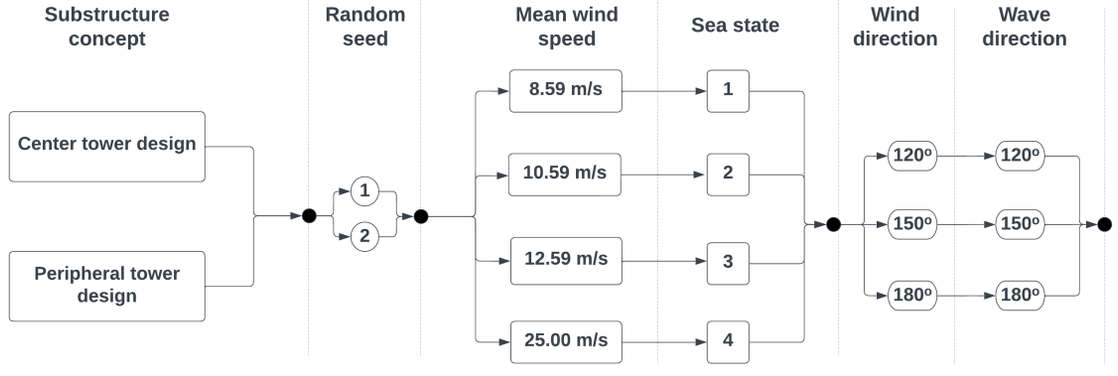

Figure 8.10: DLC 2.6 schematic

CHAPTER 9

Verification of numerical models

This section provides numerical results with the main purpose of providing confidence in the different models. The verification results include convergence studies and time-domain simulations. As the thesis considers many different results in both frequency and time domains for two separate concepts in a set of loading conditions, only selected results that provide added understanding to the problems at hand are presented. To limit the length of the chapter, some of the plots are placed in Appendix C.

9.1 Panel model convergence study

The panel model convergence study includes repeated hydrodynamic frequency-domain calculations on a set of panel models with increasing levels of refinement. The results of a perfect panel model are also included for the hydrostatic results presented in Table 9.1. This corresponds to a hull with perfectly circular columns, implying a panel model with infinitesimal panels.

Table 9.1: Hydrostatic results, panel model convergence study

	Unit	Center tower design				Peripheral tower design			
Panel size	m	1.8	1.2	0.8	∞	1.8	1.2	0.8	∞
Number of panels	#	1254	2953	6686	∞	1436	3190	7097	∞
Volume displacement	m^3	20086.1	20155.7	20185.2	20206.3	13085.6	13135.0	13156.8	13176.0
Waterplane area	m^2	439.085	443.439	445.359	446.694	413.283	415.92	417.03	418.04
Vertical COB	m	-13.659	-13.640	-13.632	-13.626	-13.271	-13.257	-13.251	-13.245

Note that the number of panels refers to the positive Y side of a YZ-symmetric model.

The hydrostatic results are found to converge to the limiting values. This implies that a sufficiently accurate hydrostatic description of the body is obtained, which is important for correctly calculating the restoring in the vertical modes.

9.1.1 Estimated discretization error

In this subsection, the convergence of the hydrodynamic coefficients is investigated. The radiation and diffraction problem is solved for the panel refinement levels listed in Table 9.1. The full results are presented in Appendix C, and only the estimated discretization errors for selected diagonal terms are presented in this section. The discretization errors are estimated using the approach described in Section 5.5.1. It should be noted that the convergence study is performed with all masses gathered in the global mass matrix and without including the free surface correction in the stiffness matrix.

The estimated discretization errors of the added mass coefficients, presented in Figure 9.1 show an acceptable convergence across all the considered wave periods. The decreasing long-period asymptotic value for the heave diagonal added mass with increasing panel model refinement seen in Figure C.1b and Figure C.5b is similar to the trend seen in Silva de Souza (2021).

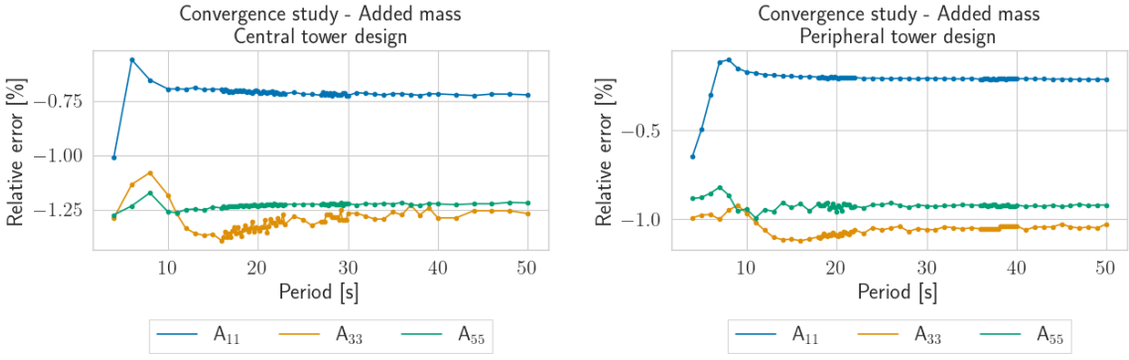

(a) Center tower design (b) Peripheral tower design

Figure 9.1: Relative discretization error - Added mass

For the remaining estimated discretization errors of the radiation damping and wave load excitation, presented in Figure 9.2 and Figure 9.3, a lack of convergence may be seen around the natural periods of the respective degrees of freedom. The small differences in added mass and hydrostatic restoring associated with the level of discretization of the panel model cause the resonance periods to shift. In these cases, the convergence is no longer monotone and asymptotic, and the discretization error may not be estimated.

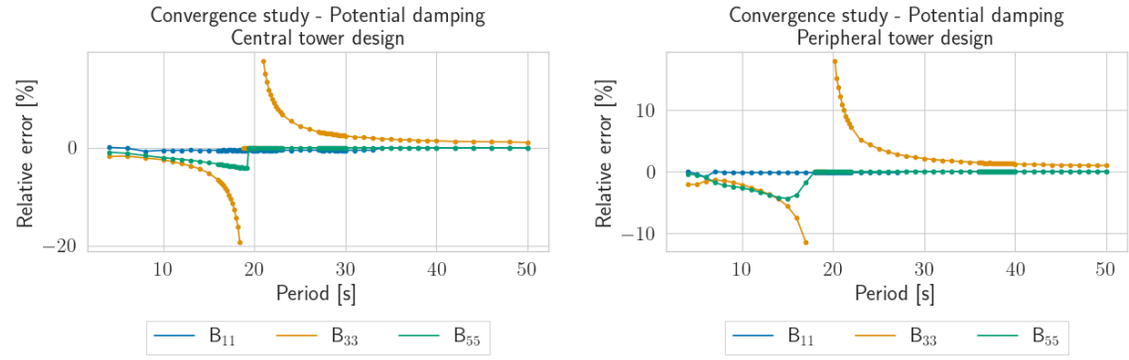

(a) Center tower design (b) Peripheral tower design

Figure 9.2: Relative discretization error - Potential damping

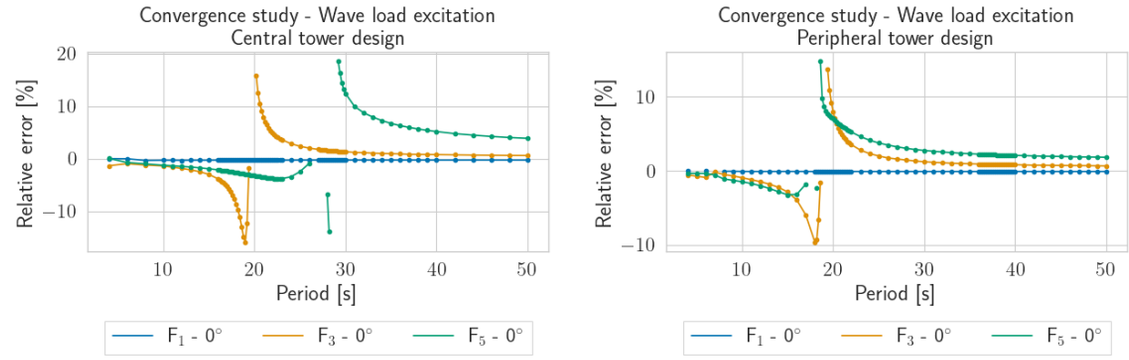

(a) Center tower design (b) Peripheral tower design

Figure 9.3: Relative discretization error - Wave load excitation

9.1.2 Comparison against reference results

The hydrodynamic data available from the IEA GitHub for the UMaine VolturnUS-s semi-submersible was used to compare the obtained results and reference results. An advantage of using these results compared with more traditional published results is that the offshore wind community continuously uses these open-source files, and potential errors are usually quickly discovered. The results only include the hydrodynamic coefficients, not the RAOs. However, as the applied structural mass matrix differs from the reference results, the RAOs are not expected to coincide fully. Nevertheless, the hydrodynamic coefficients are sufficient to ensure the same level of accuracy in the discretized panel model.

It should be noted that the reference result is calculated using WAMIT, while this thesis utilizes WADAM. However, this should not introduce any differences between the results, as WADAM is built upon the same method as WAMIT. By inspecting the IEA's WAMIT input files, it was found that 2766 panels were used to discretize the symmetric part of the substructure. Furthermore, it was found that their calculations use the higher-order method used in WAMIT (ILOWHI=1). This means that the panels are not limited to plane quadrilateral panels, as they are in the lower-order method. According to WAMIT, this provides a more accurate solution in most cases (WAMIT, Inc. 2013). The WADAM calculations used in this thesis use the lower-order panel method, and some differences in the order of convergence may therefore be seen. The WAMIT results also use a constant wave frequency spacing instead of a constant period spacing, as in this thesis. This results in a different finer discretization at lower periods and a coarser discretization at longer periods. The structure is also oriented differently in two conditions, where the coordinate system applied in the IEA calculations is rotated 180° with respect to the coordinate system used in this report. The reference results also consider a water depth of 200 m, as opposed to the 300 m. This will change the velocity potentials in the fluid, especially when considering long wave periods in the diffraction problem. In addition, as the phases are defined relative to wave crests, it may give additional discrepancies. The effect of the water depth on the wavelengths is calculated by solving the non-linear dispersion relation and is shown in Figure 9.4.

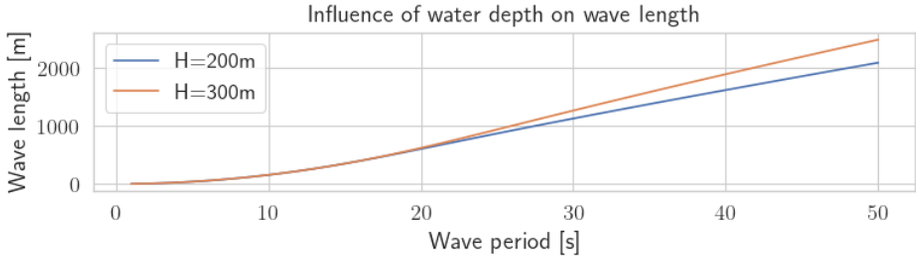

Figure 9.4: Effect of water depth on wave length

In Figure C.9 to Figure C.12, the coefficients from the radiation problem are compared with the reference results. For these results, all coefficients perfectly coincide with the reference results except for the added mass in heave. The zero-frequency limit appears higher than in the reference results for the heave added mass. This is believed to be from a discretization error, as the panel size convergence study shows a similar trend. The convergence study results for the heave added mass, presented in Figure C.1b, shows that the asymptotic zero-frequency limit for the heave added mass decreases with increasing panel refinement. Although the reference results use a comparable number of body panels, the applied higher-order panel method may lead to faster convergence.

The amplitude and phase of the forces from the diffraction problem are compared in Figure C.13 to Figure C.15. In terms of amplitudes, the results obtained in this thesis perfectly coincide with the reference results. Some differences are seen in the phases for the rotational degrees of freedom. As these differences occur only for long wave periods, it might indicate that the results may be influenced by the difference in water depth. However, it must be interpreted together with the amplitude, which goes to zero for long periods. This difference is therefore not investigated any further.

9.2 Comparison of mean drift force calculation methods

This section compares the mean drift forces obtained by multiple calculation methods. In the plotted results, "PI" and "PI*" refer to the pressure integration method with and without increased panel discretization close to the mean free surface, respectively. Details of the discretization around the mean free surface may be found in Section 5.4.1. The remaining line, labeled "FF", refers to the far-field conservation method. As discussed in Section 4.3.2, agreement between direct pressure integration and conservation of momentum methods indicates an acceptable level of panel refinement.

For the mean drift results in surge, presented in Figure 9.5, the effect of increased discretization close to the mean free surface is apparent. These results approach the results obtained through the far-field method, which indicates that the effect of modeling errors is small. The largest differences between the different calculation methods are seen at high wave frequencies, which correspond to short wavelengths. This is expected as the panel size is relatively larger compared to the wavelengths, and discretization errors are, therefore, of larger importance. The exact same results are obtained in sway and are therefore not reported in the thesis. For the yaw results, presented in Figure 9.6, the results show a good agreement for all considered wave frequencies.

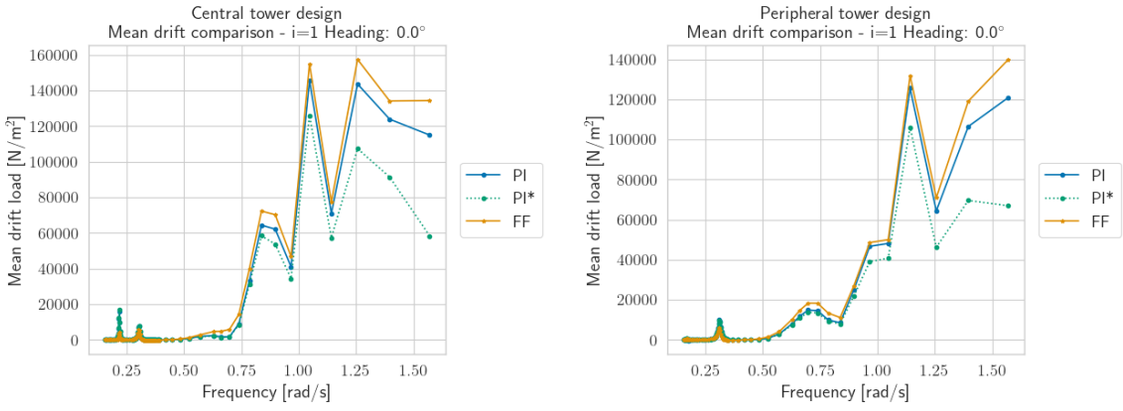

(a) Center tower design

(b) Peripheral tower design

Figure 9.5: Comparison of surge mean drift loads - 0° heading

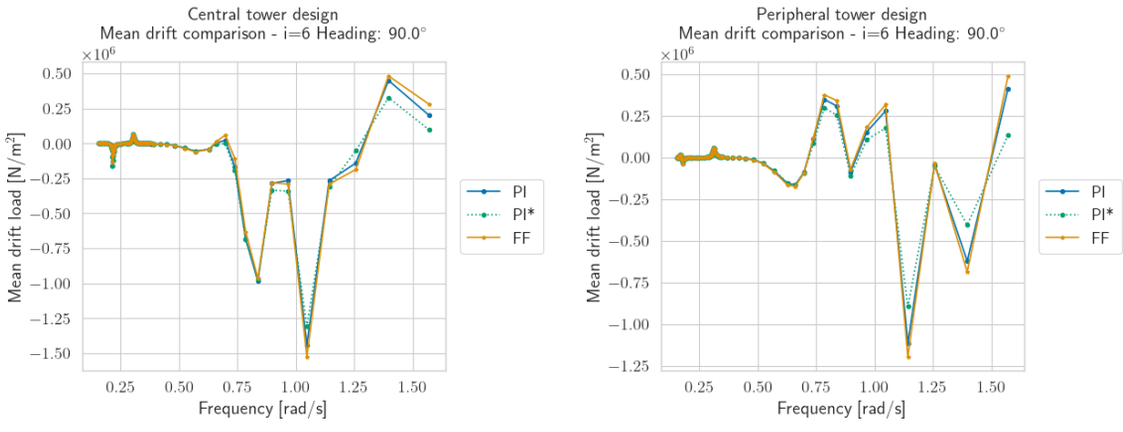

(a) Center tower design

(b) Peripheral tower design

Figure 9.6: Comparison of yaw mean drift loads - 90° heading

9.3 Verification of QTFs and free-surface model

A study of the effect of the extent and refinement of the free-surface model on the QTFs was performed. Due to the added computational cost of computing multiple QTFs, only uni-directional waves with propagation directions coinciding with the global x-axis were considered. In addition, only the difference frequency components less than or equal to 0.15 rad/s were calculated. In the study, the frequency components between 0.2 and 1.25 rad/s were discretized with a 0.05 rad/s resolution. The quadratic parts of the second-order loads were calculated using the "middle-field" method with a prismatic control volume enclosing the body, as this method has a faster convergence than the "near-field" method.

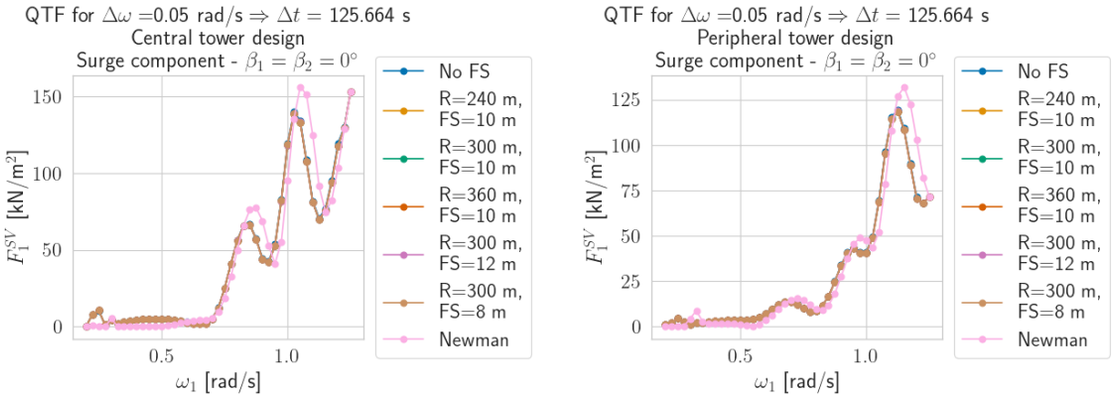

(a) Center tower design

(b) Peripheral tower design

Figure 9.7: Comparison of surge difference frequency loads - $\Delta\omega = 0.05$rad/s

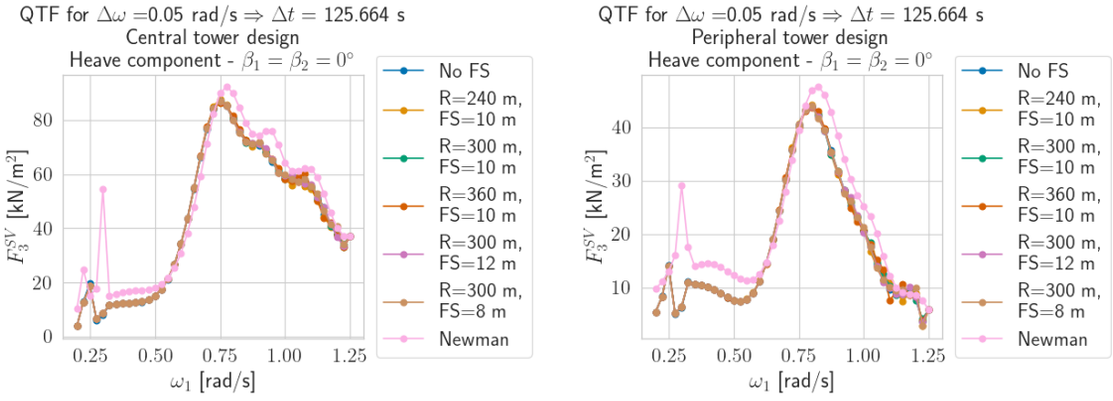

(a) Center tower design

(b) Peripheral tower design

Figure 9.8: Comparison of heave difference frequency loads - $\Delta\omega = 0.05$rad/s

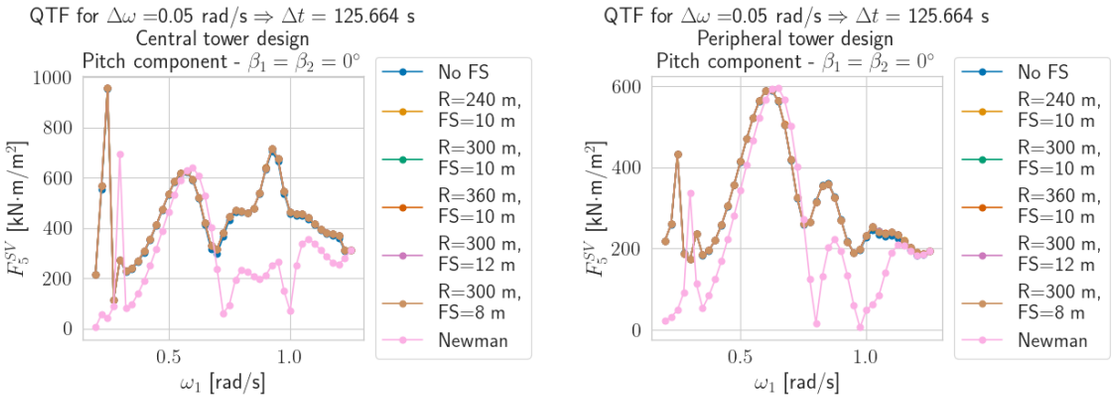

(a) Center tower design

(b) Peripheral tower design

Figure 9.9: Comparison of pitch difference frequency loads - $\Delta\omega = 0.05$rad/s

From the results presented in Figure 9.7-Figure 9.9 several remarks may be made. First of all, for the calculations involving the full QTFs with the free-surface integral, one can see a very small dependency on the selected mesh parameter. Neither the mesh size, nor the horizontal extent of the mesh appears to affect the calculated results, which indicates that the QTFs have converged for the applied hull panel size. By combining the results presented in this section with the coinciding mean drift force for different calculation methods presented in the previous section, the confidence in the calculated QTFs is elevated.

Further, one can see that disregarding the free-surface integral gives results coinciding with the full formulation of the full QTF. This assumption also significantly reduced computational effort, almost halving the wall time of the calculations when using multiprocessing.

At last, the application of Newman's approximation must be discussed. For the surge QTFs, Newman's approximation appears to be a reasonable assumption, although the approximation overestimates the second-order forcing. It is also noticed that the peaks are shifted towards higher frequencies. This involves shifting the peak towards lower spectral densities when compared with wave spectra for extreme sea states, which may affect the extreme mooring line response.

The remarks regarding the surge QTF are also generally valid for the corresponding results in heave. However, it is observed that Newman's approximation predicts a peak in second-order heave excitation at the natural frequencies in heave. This excitation is small compared to linear wave excitation, but it might have significance at high sea states. For the second-order pitch excitation moment, the largest differences are seen. Newman's approximation appears to underestimate the pitch excitation around typical wave spectral peak periods. This region is clearly dominated by linear excitation, but it is nevertheless undesirable to underpredict the excitation, especially for pitch which may be a critical response variable for FOWTs.

9.4 Rigid-body natural periods

To understand and verify the behavior of the fully coupled models, decay tests were performed in the time domain. The decay tests were performed by applying a force or moment at the body center for a certain amount of time before suddenly setting the force or moment to zero. The natural period was calculated by doing a discrete Fourier transform of a sectioned part of the time history, illustrated by green dotted lines, and selecting the most protruding period of the transformed signal. The sway and roll decay test results gave similar results as surge and pitch, respectively, and are therefore not included here.

For the surge decay test, presented in Figure 9.10 below, a natural period of 130.06 s and 104.28 s is found for the center- and peripheral tower concept, respectively. The mooring system used for the concepts differs only in the radial position of the fairlead, and the same translational stiffness is therefore obtained. The lower natural period of the peripheral tower design is due to lower structural- and hydrodynamic added mass compared to the center tower design. It is further noticed that both concepts fulfill the constraints of the mooring system optimization, with natural periods between 100 s and 150 s.

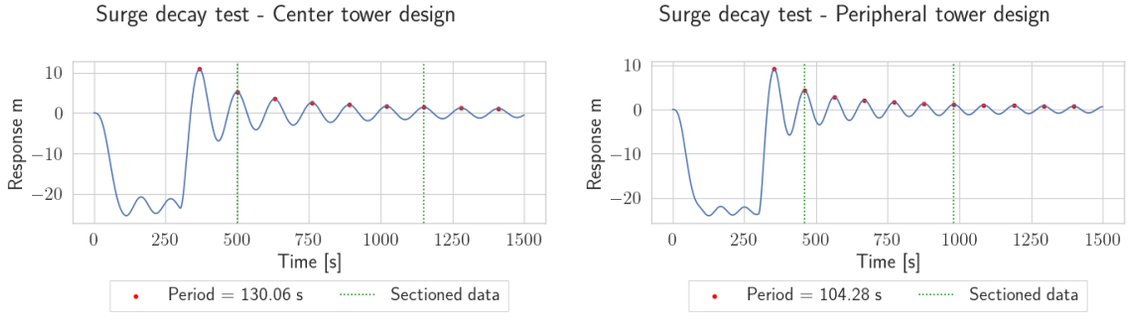

(a) Center tower design

(b) Peripheral tower design

Figure 9.10: Decay tests - Surge

The heave decay tests give corresponding results between the two models, with heave natural period of 20.6 s and 20.14 s. The similarity of the natural periods in heave might appear surprising, considering that the combined steel- and ballast mass of the peripheral tower concept is only 65% of the center tower design and that the waterplane areas are comparable. However, it may be better understood when investigating the ratio of the heave added mass to the structural mass at the natural period. For the center tower design, this ratio equals $A_{33}/M = 1.36$ while it equals $A_{33}/M = 2.24$ for the peripheral tower concept. This major difference between the concepts is well described by the two-dimensional added mass coefficients for rectangular cross-sections in an infinite fluid found in Faltinsen (1990). In his presentation of the results, Faltinsen (1990) states that: "If the body is long in the oscillation direction, the added mass is much smaller than the displaced mass". In that sense, the cross-section of the pontoons applied for the peripheral tower design has a much greater resemblance to a flat plate than the center tower design, which implies a higher ratio of A/M in the direction normal to the plate.

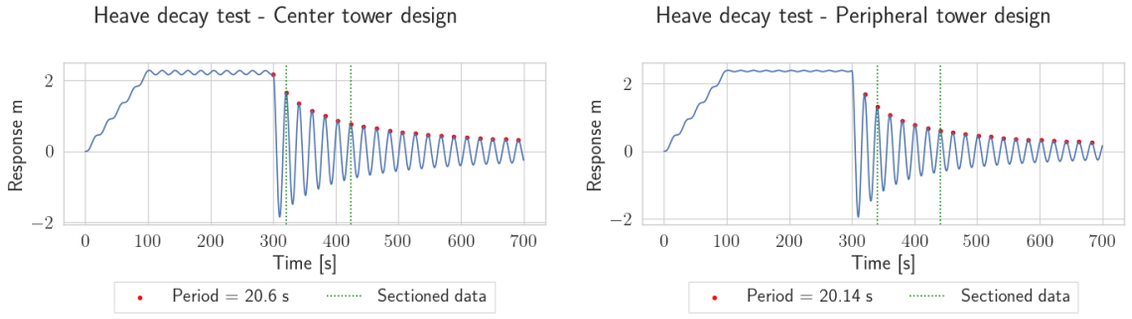

(a) Center tower design

(b) Peripheral tower design

Figure 9.11: Decay tests - Heave

The decay tests in pitch document natural periods of 30.56 s and 37.76 s for the center- and peripheral tower design, respectively. Unlike the translational mass of the concepts, the moments of inertia are of a more comparable magnitude. The relatively heavy tower and RNA, and opposing fixed ballast, has an eccentric position both in the horizontal and vertical directions, leading to a large pitch moment of inertia. The main reason behind the longer pitch natural period for the peripheral tower design is the smaller pitch restoring stiffness compared to the center tower design. For completeness, it is mentioned that while the roll natural period perfectly coincides with the pitch natural period for the center tower design, it is found to be 36.46 s for the peripheral tower design. Asymmetric properties of the system cause this difference, such as the difference in roll- and pitch moment of inertia caused by the already discussed eccentric placement of the tower along the x-direction. When discussing the decay in the rotational modes, the reduction in metacentric height due to internal free surfaces must be mentioned. By running separate decay tests without including this quasi-static free surface correction, the natural period in pitch was found as 28.3 s and 35.8 s for the center- and peripheral tower, respectively. This shows that the quasi-static inclusion of the internal free surfaces shifts the natural period approximately two seconds towards longer periods, which may be an important change in the system's characteristics.

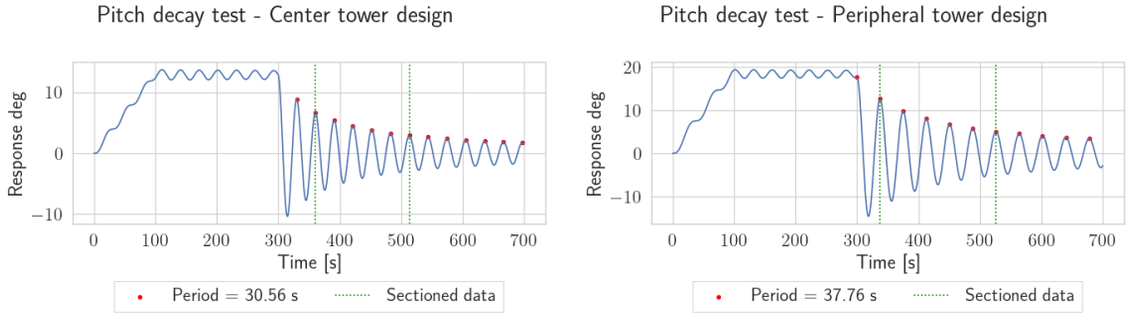

(a) Center tower design

(b) Peripheral tower design

Figure 9.12: Decay tests - Pitch

To compare the yaw decay tests, the inertia and stiffness are dissected in the same manner as above. The cause of the difference in yaw stiffness is the difference in radial placement of the mooring line fairleads in the body's coordinate system. This difference amounts to a 12.5% reduction of yaw stiffness for the peripheral tower concept compared to the center tower concept, which ceteris paribus leads to an increased natural period.

The steel- and ballast masses of both concepts are practically equal, with a difference of only 1.8%. However, as also seen for the heave response, the pontoon design majorly affects the obtained added inertia. The ratio of yaw added mass to yaw moment of inertia is $A_{66}/I_{zz} = 1.2$ for the center tower design, while it is only $A_{66}/I_{zz} = 0.66$ for the peripheral tower design. The center tower design has a pontoon height of 7 m, compared to a height of 2.24 m for the peripheral tower design. By assuming that the added inertia in yaw may be found as the 2-dimensional added

mass multiplied by the distance to the rotational axis, this difference may be understood using the previously discussed 2-dimensional results from Faltinsen (1990). It is hence seen that the smaller added mass offsets the reduced stiffness, leading to a net reduction in the yaw natural period for the peripheral tower design compared to the center tower design.

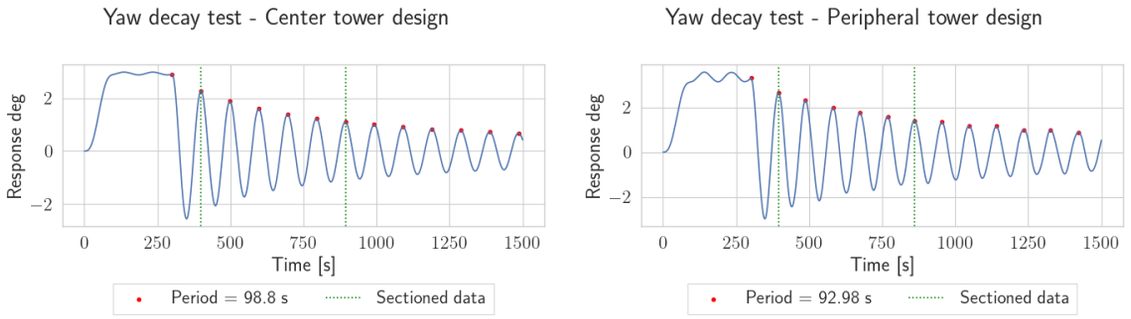

(a) Center tower design

(b) Peripheral tower design

Figure 9.13: Decay tests - Yaw

9.5 Constant wind tests

The constant wind test is performed for both concepts, in addition to a fixed rotor. For the floating application, the wind speed estimator mode and the floating specific feedback mode are applied with a value of 2 in the ROSCO controller. For the fixed turbine, the two separate tests are made with and without the wind speed estimator. For all simulations involving the wind speed estimator, the performance table from Github is applied. The results presented in Figure 9.14 show that the rotor response is identical between the two floating concepts. This is desirable, as it reduces the variability of the results to differences caused by the substructure itself.

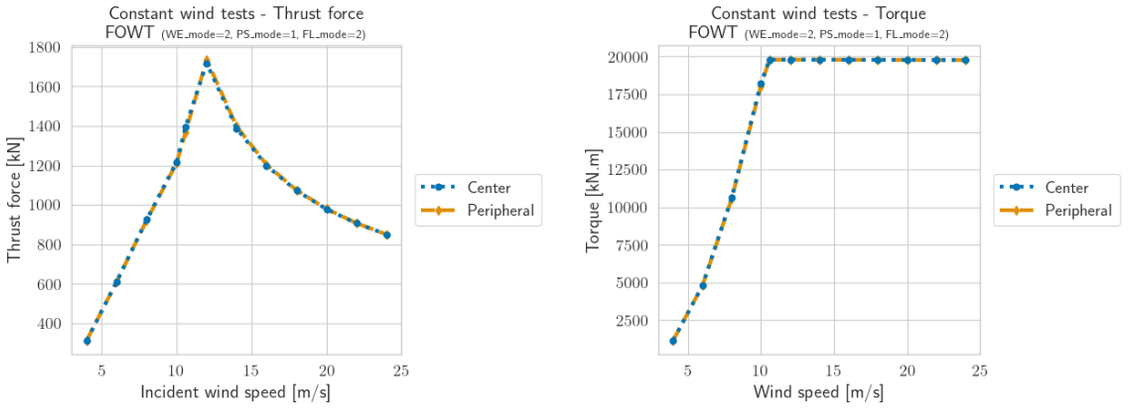

(a) Thrust force

(b) Torque moment

Figure 9.14: Constant wind tests

An interesting observation from Figure 9.14a is that the peak thrust does not occur at the rated wind speed. To investigate this further, several constant wind tests with a fixed rotor were performed, varying the settings of the wind turbine controller. The results showed that the shift of the peak thrust is caused by the peak shaving mechanism applied by the controller when pitch saturation and wind speed estimation are used together. The results of these investigations may be seen in Appendix F.

9.6 Regular wave test

Regular wave tests were performed to ensure that the models had the expected response in the time domain and to ensure thereby that the frequency-domain results were transferred correctly. As discussed in Section 5.7, a series of self-made Python programs performs the transfer of intermediate frequency domain results to the time-domain calculations. Thorough documentation of the results is therefore included in the thesis. The shape of the transfer functions is further discussed in chapter 11.

It must be stressed that for the sake of comparison, the time-domain model used for the regular wave tests employs the same mass matrix as the frequency-domain results. This mass matrix disregards the eccentric center of gravity of the RNA, and assumes that the horizontal position of the center of gravity coincides with the horizontal position of the tower top. The reasoning behind this choice is elaborated on in Section 5.4.4.

Apart from the obtained amplitudes at the resonant regions, the time-domain results coincide well with the frequency-domain results. At the natural period in heave, roll, and pitch, the frequency-domain calculations severely overestimate the response. To investigate the cause of this difference, several variations of the regular wave tests were performed. The results showed that the lower damping in the frequency domain was two-folded, where both the stochastic linearization of damping applied in WADAM and the drag forces on the mooring line affected the results. By using the linearized damping matrix from the frequency domain results and zeroing the drag coefficients on the mooring lines, the frequency domain RAOs was reobtained in the time domain. Including only one of these modifications failed to recover the RAOs fully. This illustrates the importance of modeling the problem in the time domain to obtain an estimate of the response. Some results of the investigations are presented in Figure 9.15 to Figure 9.18, while the remaining results can be found in Section C.4.

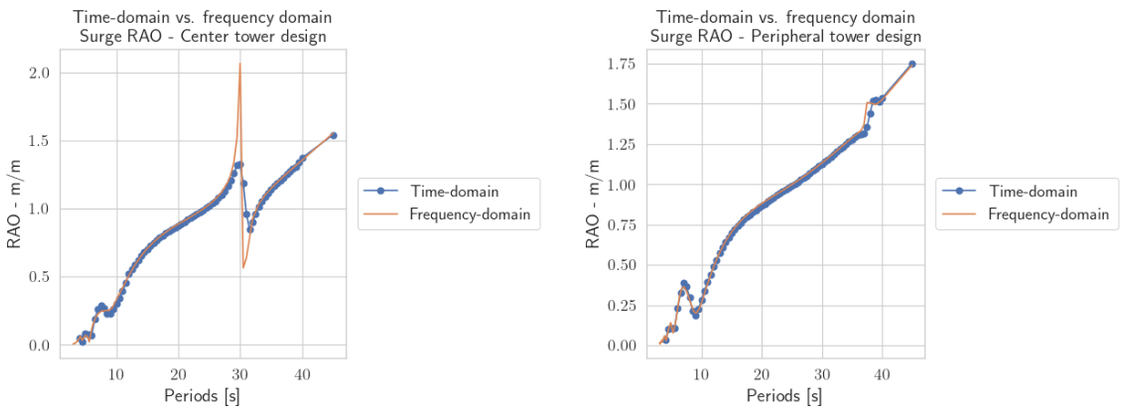

(a) Center tower concept

(b) Peripheral tower concept

Figure 9.15: Frequency- and time-domain surge RAO comparison

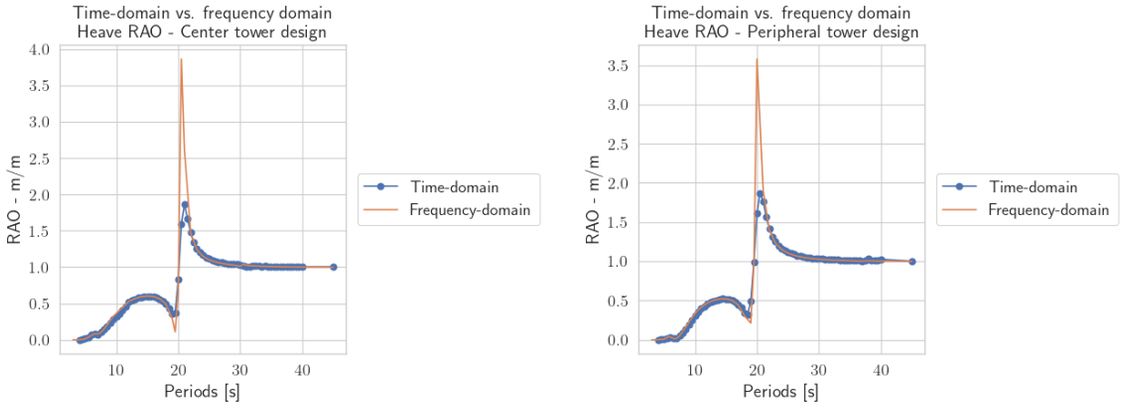

(a) Center tower concept (b) Peripheral tower concept

Figure 9.16: Frequency- and time-domain heave RAO comparison

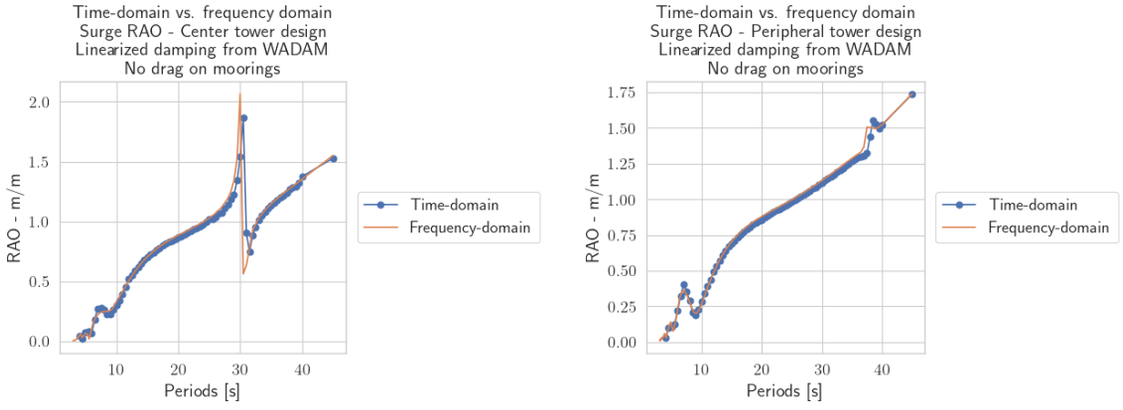

(a) Center tower concept (b) Peripheral tower concept

Figure 9.17: Frequency- and time-domain surge RAO comparison, with linearized damping matrix from WADAM and drag-less mooring lines

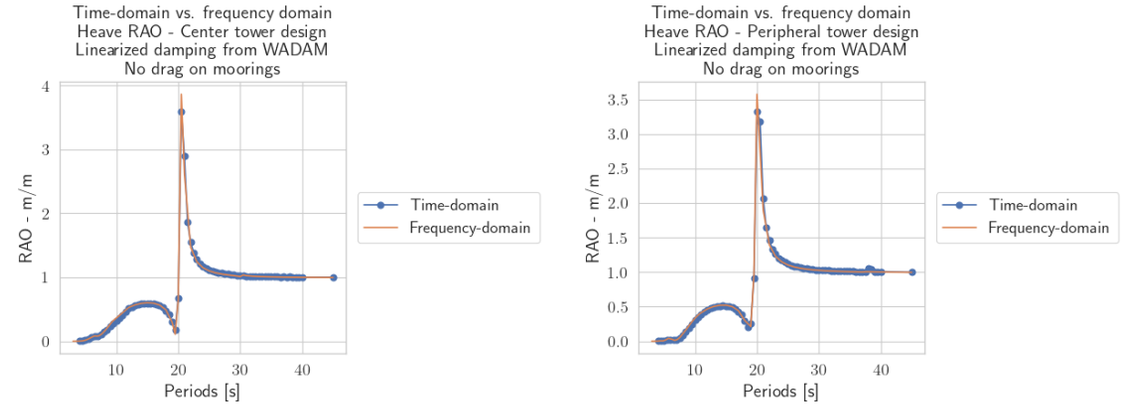

(a) Center tower concept (b) Peripheral tower concept

Figure 9.18: Frequency- and time-domain heave RAO comparison, with linearized damping matrix from WADAM and drag-less mooring lines

9.7 Control of motion RAOs with sloshing excitation

The results presented in Figure 9.19 and Figure 9.20, show different sets of RAOs calculated with two separate formulations of the sloshing. The results plotted in blue represent the case of including the effect of the internal fluid completely in the added mass matrix. This is the default method in WADAM. The results plotted in red represent the case where the static mass is placed in the global mass matrix, whereas the dynamic compartment added mass is included as a frequency-dependent spring. The complete agreement between the two methods acts as a verification of the implemented methods.

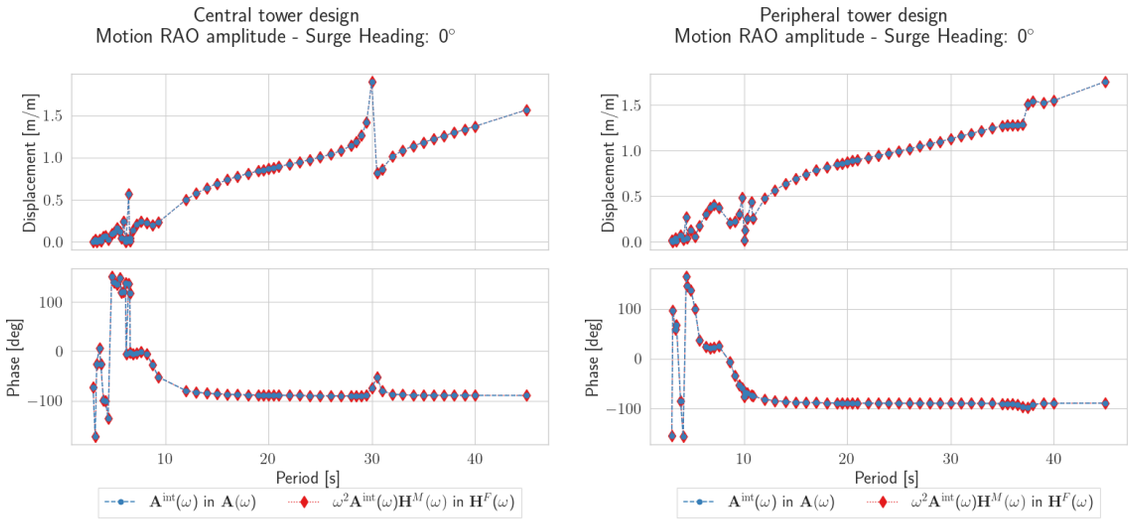

(a) Center tower design

(b) Peripheral tower design

Figure 9.19: Surge RAO comparison

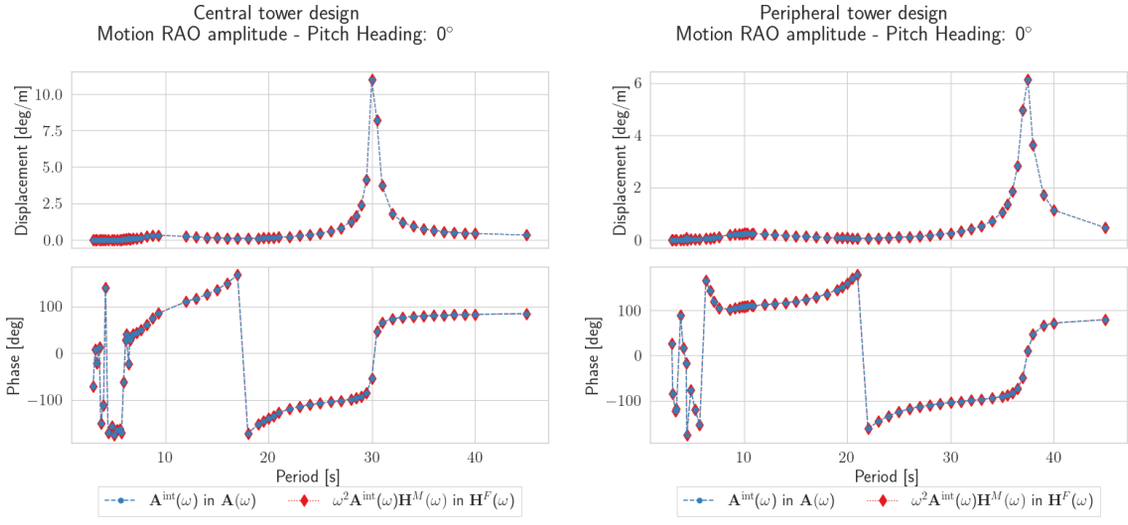

(a) Center tower design

(b) Peripheral tower design

Figure 9.20: Pitch RAO comparison

9.8 Inflow/outflow model tests

The validation of the inflow/outflow model is based on simple tests where one has an intuitive understanding of the physical response. The test was only performed for the center tower concept, and they consider an imagined scenario where a 90° sector of the column may be flooded from 3 m below the column to the column top.

The first test considered is the flow through a sudden opening in one of the columns located below the mean free surface without the influence of other environmental conditions. The pitch response of the substructure, the external and internal pressure heads, and the flux and volume of the floodwater volume are shown in Figure 9.21. The definitions of the external and internal pressure heads are as previously shown in Figure 5.10.

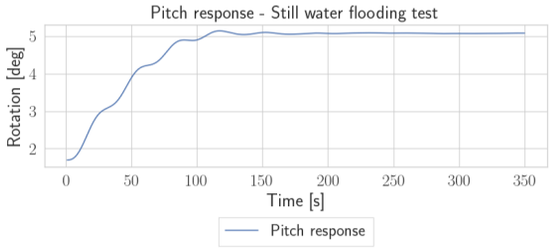

(a) Platform pitch response

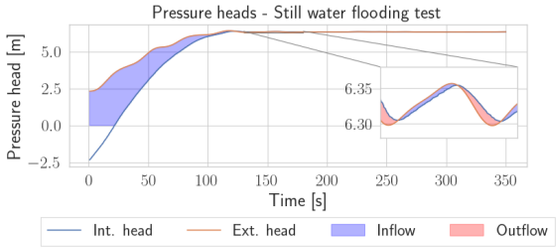

(b) Pressure heads

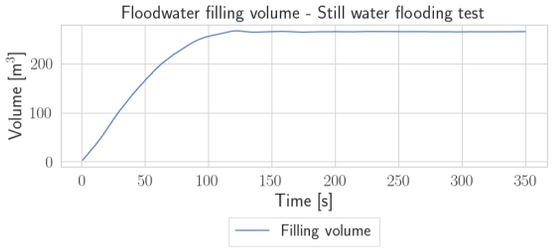

(c) Floodwater filling volume

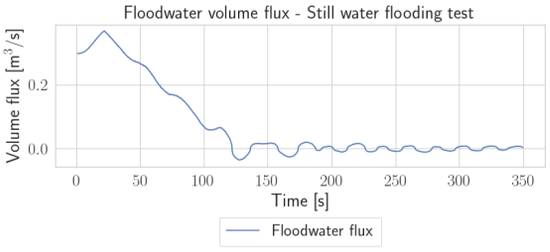

(d) Volume flux

Figure 9.21: Flooding model test - Still water

The still water flooding test displays behavior that gives a physical meaning. Flooding of the radially placed compartment causes a slow change in the system's pitch angle until a new equilibrium is reached. The pitch of the structure lowers the opening relative to the free surface, which increases the external pressure head. After some time, the internal fluid rises above the opening, causing a positive internal pressure head. This causes a reduced volume flux through the opening. During some time periods, the internal pressure head is larger than the external pressure head, which causes outflow through the opening.

The second test is presented in Figure 9.22. It considers an opening placed above the mean free surface, with the structure free to move in incident regular waves. In this case, the linear wave response is seen together with the quasi-static response of the flooding. The relative motion between the incident waves and the body causes a larger variation in the external pressure head, and the body motion also affects the internal pressure head, since the internal free surface is assumed to be parallel to the external free surface. When the structure has reached its new equilibrium, the incident waves cause increased fluid exchange between the internal and external domains.

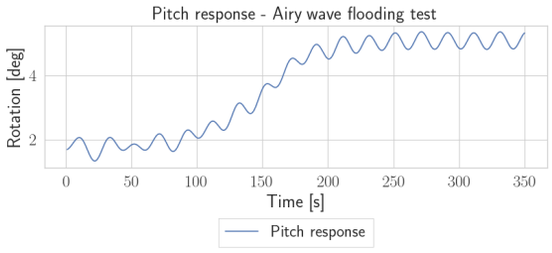

(a) Platform pitch response

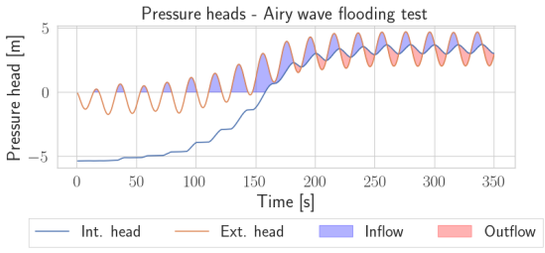

(b) Pressure heads

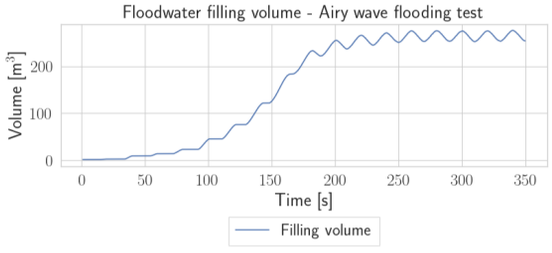

(c) Floodwater filling volume

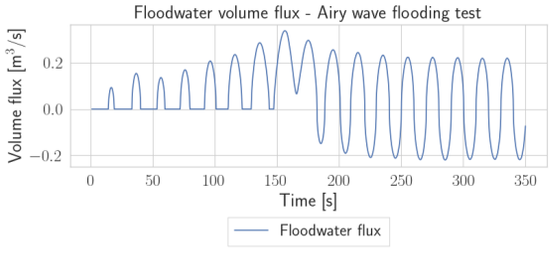

(d) Volume flux

Figure 9.22: Flooding model test - Airy waves

CHAPTER 10

Static results

In this chapter, the results of the quasi-static stability analysis are presented. Several compartments were investigated in case of flooding to see if the structure had enough reserve buoyancy to remain floating. The beams or braces connecting the columns were assumed to not contribute to any buoyancy. The center of gravity of the RNA was assumed to be located in the center of the tower top. As the center of gravity depends on the yaw orientation of the RNA, it may both improve and worsen the responses considered in the quasi-static analysis. In this chapter, the heeling angle is defined at the angle about which the external moment from HydroD is acting, e.g., the critical axis, which must be balanced by the righting moment. By trim, one refers to the rotation about the perpendicular horizontal axis. The restoring moments provided by the mooring lines are excluded as specified in DNV (2021b).

10.1 Quasi-static stability of center tower design

In Table 10.1, the different parts of the pitch and roll restoring coefficients are presented. From the table, one can see that the stability of the structure is completely provided by the water plane moment. The free surface corrections in the table are the corrections calculated by HydroD for the exact compartment geometries.

Table 10.1: Pitch and roll restoring contributions, center tower design

Separation of COB and COG	Water plane moment	Free surface correction	Total
$-2.36 \cdot 10^9$ Nm/rad	$5.00 \cdot 10^9$ Nm/rad	$-3.96 \cdot 10^8$ Nm/rad	$2.24 \cdot 10^9$ Nm/rad

In Figure 10.1, the restoring moments for the intact and damaged cases are shown. The damage appears to have a modest effect on the restoring moments, but it is noted that damage case 1 removes the symmetrical behavior of the restoring. At the point where the restoring moment deviates from the remaining curves, a large trim angle occurs, eventually leading to a capsizing. The intercepts between the simplified overturning moment and the restoring moments are illustrated as dots in Figure 10.1 and tabulated in Table 10.2.

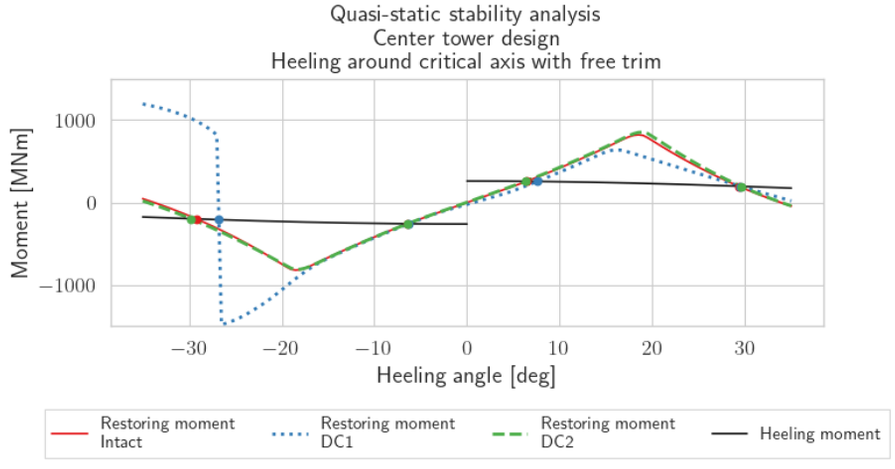

Figure 10.1: Righting moment curves for intact and damaged conditions, center tower design

Table 10.2: First and second intercepts, center tower design

	Negative heel		Positive heel	
	1st intercept	2nd intercept	1st intercept	2nd intercept
Intact	-6.61°	-29.06°	6.61°	29.16°
DC1	-6.46°	-26.78°	7.74°	29.29°
DC2	-6.61°	-29.66°	6.47°	29.44°

The work done by the righting and overturning moment is calculated by integration of the moment curves from Figure 10.1. The results, presented in Table 10.3, show that the work done by the righting moments is greater than 1.3 times the work done by the heeling moment, fulfilling the requirements of DNV (2021b).

Table 10.3: Quasi-static stability by integration of moment curves, center tower design

	Negative heel			Positive heel		
	Righting [MJ]	Heeling [MJ]	Ratio	Righting [MJ]	Heeling [MJ]	Ratio
Intact	-222.01	-121.50	1.82	223.29	121.84	1.83
DC1	-307.56	-112.90	2.72	181.47	122.54	1.48
DC2	-226.27	-123.59	1.83	233.17	122.79	1.90

Additional damage cases

The first additional damage case considered for the center tower design was total flooding of the center column supporting the tower. As the center of buoyancy for this column is collocated with the global center of buoyancy, the damage does not result in any inclination of the structure. The new damaged equilibrium is found at an increased draft of 2.76 m. The relatively modest change in draft from the total loss of a column results from the smaller diameter of the center column compared with the radial columns. As this column carries the load of the tower and the RNA, the structural implication of damage should be carefully investigated. Depending on the location and size of the damage, the remaining column cross section may not have enough resistance against buckling and yielding.

Further, the loss of a full pontoon is investigated. Again, the structure is found to survive with a relatively modest equilibrium change. When assuming that all four compartments of the pontoon parallel with the x-axis are flooded, an increased draft of 0.44 m and a trim of 1.1° are experienced. Due to the symmetric placement of the pontoon, a zero heel angle is maintained. Damage to the other pontoon would lead to a non-zero heel angle but also a corresponding reduction of the inferred trim angle. The modest result of such severe damage is mainly due to the filling level of fluid ballast already placed in the pontoons in intact condition. In fact, a total simultaneous loss of the outer hull integrity of all three pontoons would be survived with a draft similar to the draft experienced during the flooding of the center column.

With the compartmentalization considered in this thesis, the compartments located in the radial columns below the collision compartments are the only critical compartments. Flooding of one of these compartments leaves the structure without enough reserve buoyancy to remain in an upright equilibrium, which causes the analysis to fail in HydroD.

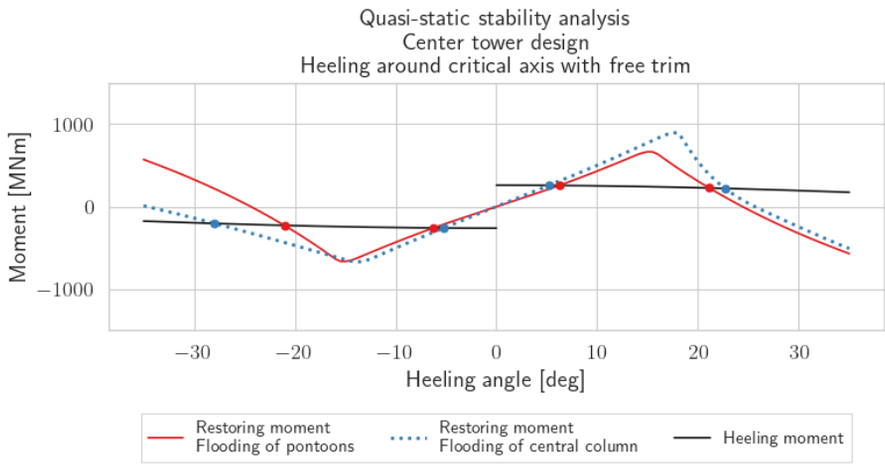

Figure 10.2: Righting moment curves for extreme damage conditions, center tower design

10.2 Quasi-static stability of peripheral tower design

In the same way as for the center tower concept, the different terms of the pitch and roll restoring coefficients are presented in Table 10.4. This concept is also completely stabilized by the waterplane moment. When comparing the values between the concepts, the smaller displacement of the peripheral tower design should be considered. The metacentric height of the peripheral tower design is 10.65 m, compared to 10.92 m for the center tower concept.

Table 10.4: Pitch and roll restoring contributions, peripheral tower design

Separation of COB and COG	Water plane moment	Free surface correction	Total
$-2.62 \cdot 10^9$ Nm/rad	$4.23 \cdot 10^9$ Nm/rad	$-1.80 \cdot 10^8$ Nm/rad	$1.43 \cdot 10^9$ Nm/rad

The calculated righting moments for the peripheral tower design are presented in Figure 10.3. The same abrupt behavior is seen at larger heeling angles for the case with damage to the column. This indicates a capsizing, which is further supported by the large change of trim occurring at this heeling angle. Looking at the cures, and the intercepts presented in Table 10.5, the lesser restoring of the peripheral tower is apparent.

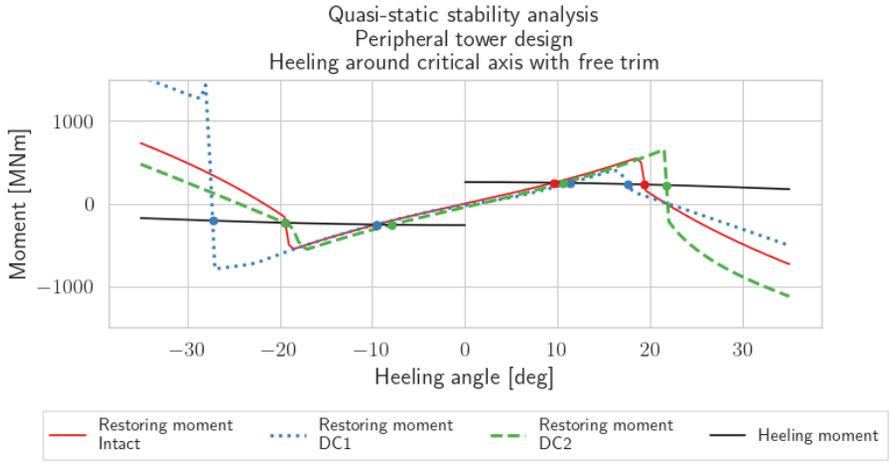

Figure 10.3: Righting moment curves for intact and damaged conditions, peripheral tower design

Table 10.5: First and second intercepts, peripheral tower design

	Negative heel		Positive heel	
	1st intercept	2nd intercept	1 intercept	2nd intercept
Intact	-9.86°	-19.38°	9.85°	19.38°
DC1	-9.85°	-27.23°	11.59°	17.49°
DC2	-8.19°	-19.28°	10.87°	21.74°

The quasi-static stability assessment of the peripheral tower concept is presented in Table 10.6. Looking at the positive heel moment, which appears critical, all cases fail the stability criterion of a ratio between the righting and overturning moments of 1.3. However, in some limit state analyzes, a safety factor of 1 is used for damaged structures. In that case, damage case 2 passes the quasi-static criterion.

Table 10.6: Quasi-static stability by integration of moment curves, peripheral tower design

	Negative heel			Positive heel		
	Righting [MJ]	Heeling [MJ]	Ratio	Righting [MJ]	Heeling [MJ]	Ratio
Intact	-88.80	-84.51	1.05	88.85	84.51	1.05
DC1	-185.95	-114.54	1.62	55.5	76.92	0.72
DC2	-99.99	-84.74	1.18	103.03	93.89	1.09

The increased restoring seen for the second damage case can be related to two separate reasons. First, since the program uses the "lost buoyancy" method, the center of buoyancy of the total structure will be elevated, making the structure more stable by reducing the negative contribution in the first column of Table 10.4. Second, the compartments are fully filled, eliminating the relevant compartments' free surface correction.

Additional damage cases

Similarly, as for the center tower design, the peripheral tower design has enough reserve buoyancy to reach a new static equilibrium after the complete flooding of an entire pontoon. In this case of flooding of the pontoon running between the tower column and the leftmost rear column, the orientation is more extreme with an increased draft of 2.74 m and a trim and heel angle of 4.21° and −7.32°, respectively. In terms of static equilibrium, the structure remains floating in the event of flooding of all three pontoons. However, such a damage condition leads to a symmetric increased draft 8.32 m. As seen in Figure 10.2, it is likely that a capsize will occur in this condition. Damage to one of the column compartments below the collision compartments leads to a total loss of the structure, similar to the center tower design.

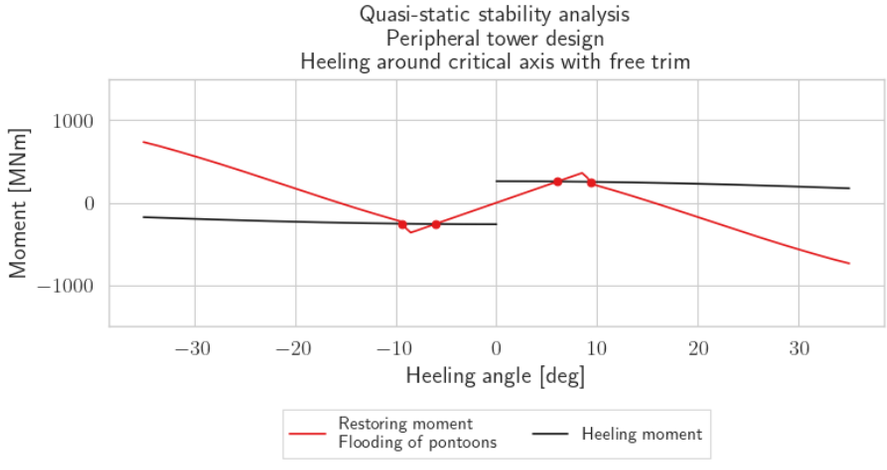

Figure 10.4: Righting moment curves for an extreme damage condition, peripheral tower design

CHAPTER 11

Frequency-domain results

In this chapter, the results obtained in the frequency-domain calculations are presented. To reduce the length of the thesis, only selected results are presented here. Additional frequency domain results can be seen in the results presented in the convergence study in Appendix C.

11.1 Heave added mass from linear sloshing

During the calculation of the hydrodynamic coefficients in the frequency domain, an unphysical behavior was seen in the heave added mass. For cases that considered the effect of internal fluids using the dynamic method, the internal tanks gave an added mass that increased with increasing periods instead of approaching an asymptotic value. The plotted results for the combined external and internal added mass can be seen in Figure E.1. Linear sloshing should not affect the vertical motions, as the pressure effect of the internal wave system should average to zero in the vertical direction.

The reason behind the increasing added mass is believed to be from the calculation method applied in WADAM. As described in chapter 4, the internal coefficients are calculated using the external solver by disregarding the vertical velocity of the mean free surface. These coefficients are later corrected by the method described in Ludvigsen and Pan (2015). The use of this method of correction is confirmed by the developers of WADAM in DNV, who further confirmed that the long-period asymptotic value of the added mass contribution from the internal tanks should be equal to the mass of the tank fluid (DNV support team, personal communication, May 16, 2023). A possible explanation of the result is found by looking at the combined linearized free surface condition, shown in eq. (4.53). In the long period limit, this equation reduces to a Neumann condition in the direction perpendicular to the free surface and may therefore be interpreted as a fixed wall. Combined with the correction term in Ludvigsen and Pan (2015), this may cause issues for long periods.

As the obtained added mass in heave when using the dynamic methods is unphysical, the values obtained through the quasi-static method are used for diagonal and off-diagonal terms involving heave responses.

11.2 Effect of compartment model in intact condition

To verify that the modeling of the mass is consistent between the different models, a comparison of the responses is performed. The comparison includes the following models:

- Global mass matrix

  The combined inertia of structural steel, concrete ballast, and fluid ballast, defined by its mass, center of gravity, and radii of gyration.

- Static fluid ballast, without free-surface correction

  The inertia of the structural steel and concrete ballast is modeled by a mass matrix as in the former model. The fluid ballast is included by assigning filling ratios to the ballast tanks in the pontoons. The free-surface correction of the restoring coefficients is not included, nor are the internal tank dynamics.

- Static fluid ballast, with free-surface correction

  Similar to the previously defined model, but including the correction of the restoring terms due to the internal free surface.

- Dynamic fluid ballast

  The structural inertia and fixed concrete ballast are modeled by a mass matrix, while the fluid ballast is modeled with appropriate filling ratios and internal free surfaces. The solver for internal tank dynamics is applied.

To understand the effect of the free surface correction due to the internal free surfaces, some hand calculations were performed (not shown here). The free surface correction from each separate tank was estimated by calculating the second moment of the free surface area as described in equation (4.64). In the hand calculations, the ballast tanks were idealized as rectangular tanks with length and width corresponding to half the pontoon length and width, respectively. These hand calculations verified the previously discussed free surface corrections in the restoring coefficients from WADAM, which also led to changes in the pitch natural period.

The transfer functions for the linear surge response are presented in Figure 11.1. For both cases, one can observe the effect of using the dynamic method for internal fluids as sloshing responses for both concepts. The first sloshing periods are seen to agree well with the predictions from the analytical expressions. Furthermore, a large surge-pitch coupling is observed for the center tower design, while it is more modest for the peripheral tower design. An explanation of surge-pitch coupling is found in both the added mass and the restoring matrices. The restoring matrix introduces a coupling due to the eccentric positions of the fairleads. Although a slightly different fairlead position has been used, it is not expected to make this large of a difference. The long-period asymptotic value of the A_{15}-term of the center tower design is almost three times that of the peripheral tower design. For comparison, the ratios of the long-period asymptotic values of the A_{11} and A_{55} terms are 1.57 and 0.93, respectively. This difference may be caused by the larger vertical projected area of the pontoons for the center tower design when moving in the surge direction. Due to the large submergence of the pontoons, this will induce cause pressure loads with a moment arm to the axis of rotation. It should be mentioned that the pitch response is excessively large in the frequency domain due to the linearization of the damping. As documented in the regular wave tests presented in Figure 9.15, the effect is much less severe in the time domain.

The surge responses at long periods are seen to exceed the expected value of 1 for both concepts. This is caused by seabed influence and the mooring system. Waves with periods of 45 s have wavelengths approaching several kilometers for the given water depth of 300 meters, making the deep water assumption invalid. As a verification, a frequency-domain calculation was performed in OrcaWave without the linearized mooring stiffness in infinite water depths. This test showed the expected asymptotic behavior.

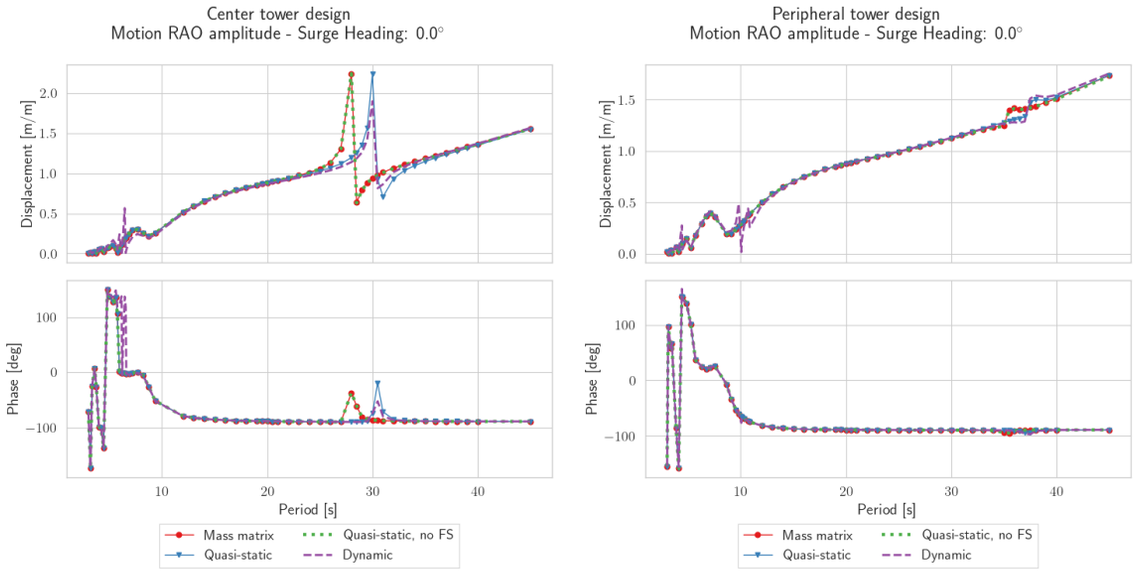

(a) Center tower design

(b) Peripheral tower design

Figure 11.1: Surge RAO comparison

The minimum seen in the heave motions for periods just below the natural period is connected with cancellation effects in the excitation. This is clearly seen in the plot of the heave wave excitation forces, presented in Figure C.3b and Figure C.7b in the appendix. The long-period asymptotic response is as expected for a floating structure.

In the comparison of linear heave response for the different models, a difference is seen in the response at the natural period between the models using the quasi-static and dynamic methods. The difference is most noticeable for the center tower design, where it amounts to approximately 0.5 m/m lower response for the dynamic compartment model. The difference is caused by an added mass effect of the internal fluid.

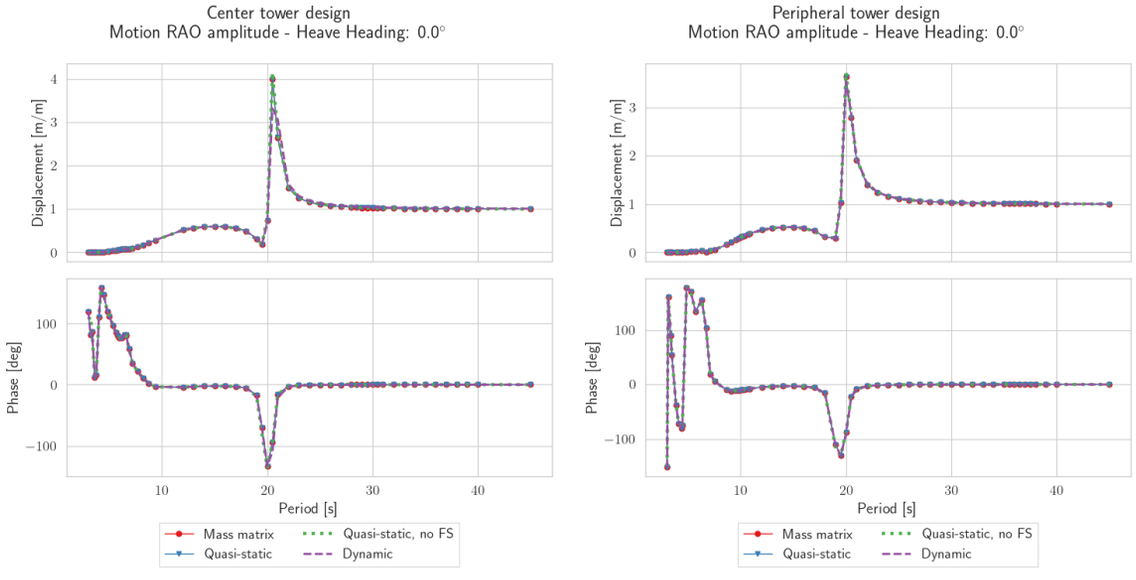

(a) Center tower design

(b) Peripheral tower design

Figure 11.2: Heave RAO comparison

The linear pitch response shows a clear effect of the correction introduced to the metacentric height as a result of the internal free surfaces. This correction is introduced in the results using the quasi-static and dynamic methods for the internal fluids. It is further documented by the case that uses the quasi-static method without internal free surfaces. These results are seen to coincide perfectly with the traditional mass matrix approach.

One should be careful with comparing the responses directly from the RAOs, as they depend on how well the discretized wave periods align with the natural periods. As both the added mass and wave excitation are smooth functions at these periods, it will not influence the time-domain results as OrcaFlex uses interpolation between the discretized periods.

The coupling between surge and pitch is also seen in the phase for long periods, which tends to $\pm 90°$ for both degrees of freedom. The different signs are connected with the definition of the phase.

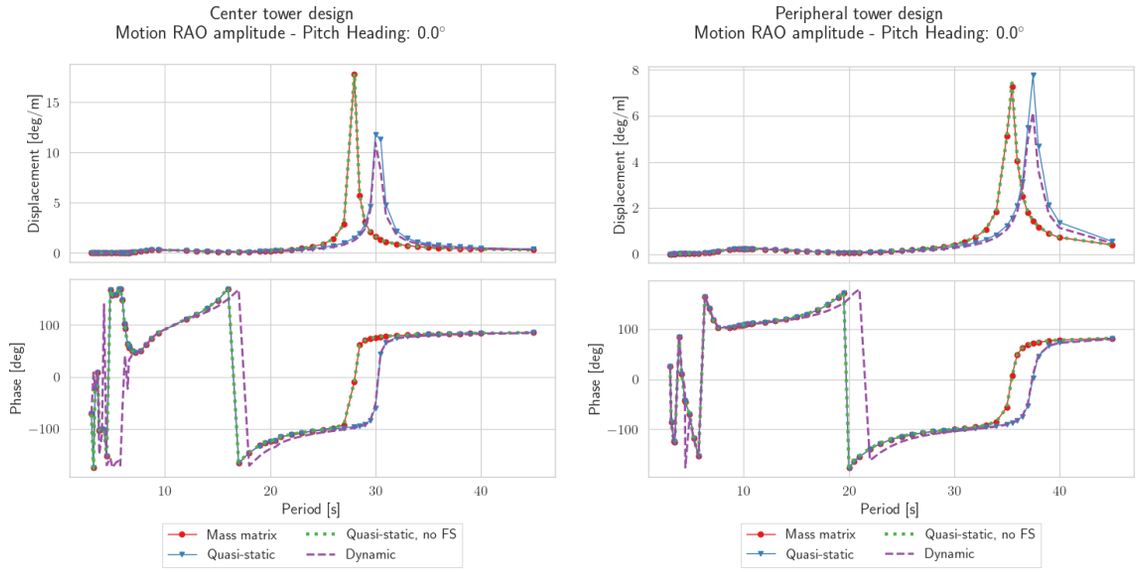

(a) Center tower design

(b) Peripheral tower design

Figure 11.3: Pitch RAO comparison

11.3 Effect of damage cases

In Figure 11.4, the linear surge RAO is compared for the different damage cases. The calculations are performed with the bodies in intact or damaged equilibrium positions, tabulated in Table 11.1.

Table 11.1: Damaged equilibriums

	Center tower design			Peripheral tower design		
Damage case	Vertical displacement	Heel	Trim	Vertical displacement	Heel	Trim
DC1	-0.24	0	0.75	-0.24	0	1.21
DC2	-0.46	0.89	-0.12	-0.65	-1.12	2.70

In general, it must be stated that the localized damages have little effect on the results. This is expected, as the damaged compartments' horizontal extent and filling volume are small compared to the fluid ballast in intact condition. No exchange of fluid between the internal and external domains is captured in these calculations. Some small changes in amplitude may be seen in the zoomed-in portion of the plot, but the sloshing amplitude is not expected to be well captured in potential theory. The most noteworthy difference is the slightly lower natural period in pitch, visual through the surge-pitch coupling, caused by the changes described in chapter 10. As no differences from those already mentioned were seen in the other responses, they are omitted here.

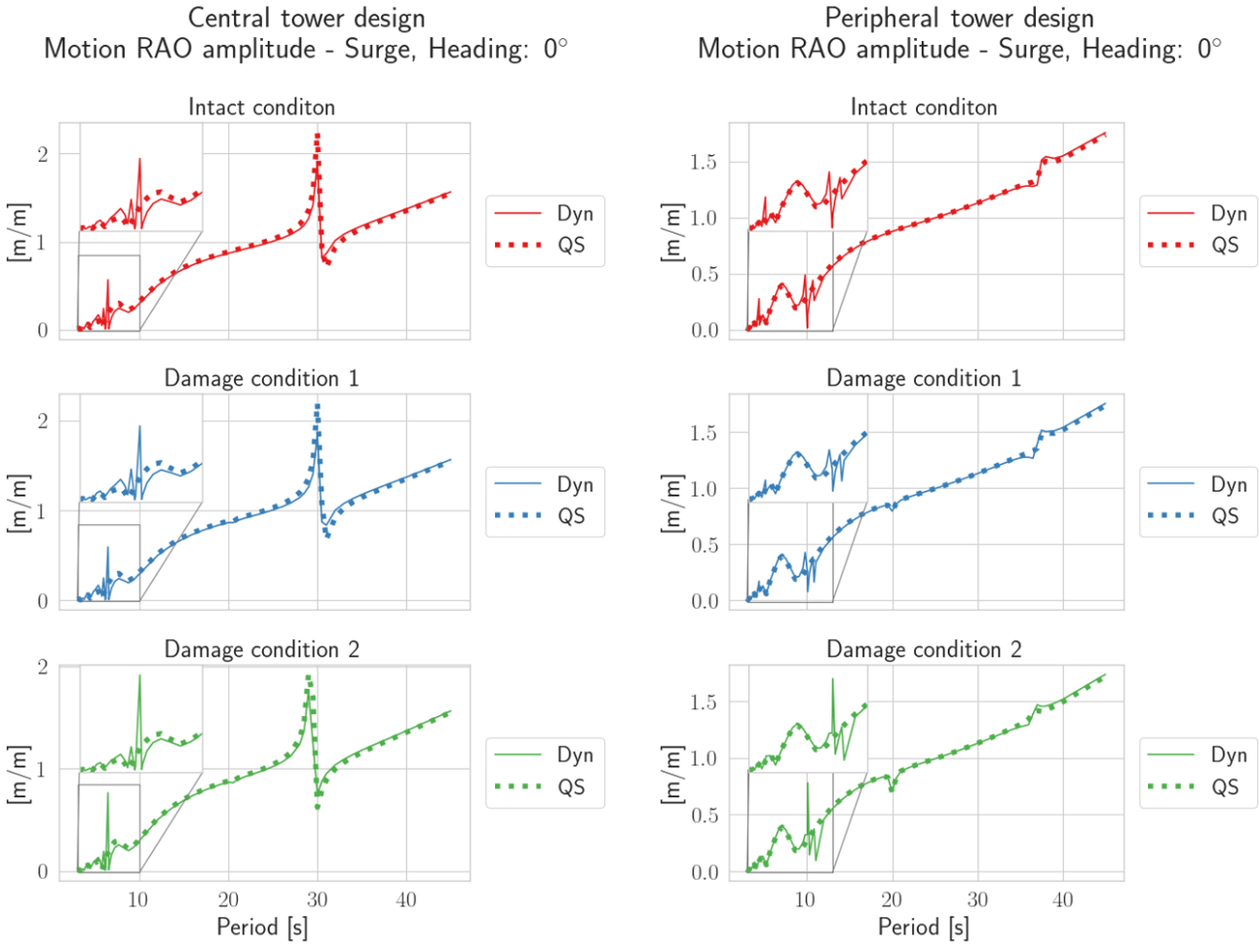

(a) Center tower design

(b) Peripheral tower design

Figure 11.4: Surge RAO

11.4 Sloshing excitation model

The section provides frequency domain results specifically related to the effects of linear sloshing.

Effect of sloshing on load RAOs

Figure 11.5 and Figure 11.6 show how the load transfer functions are changed by introducing the internal sloshing as a frequency-dependent spring. The wave excitation and sloshing spring force are plotted both separately and combined. As expected from the nature of sloshing, the effect is very localized around the resonant sloshing periods. For other periods, the internal fluid behaves quasi-statically, and almost no effect is seen on the load RAOs. This is in agreement with the theory presented in Faltinsen and Timokha (2009).

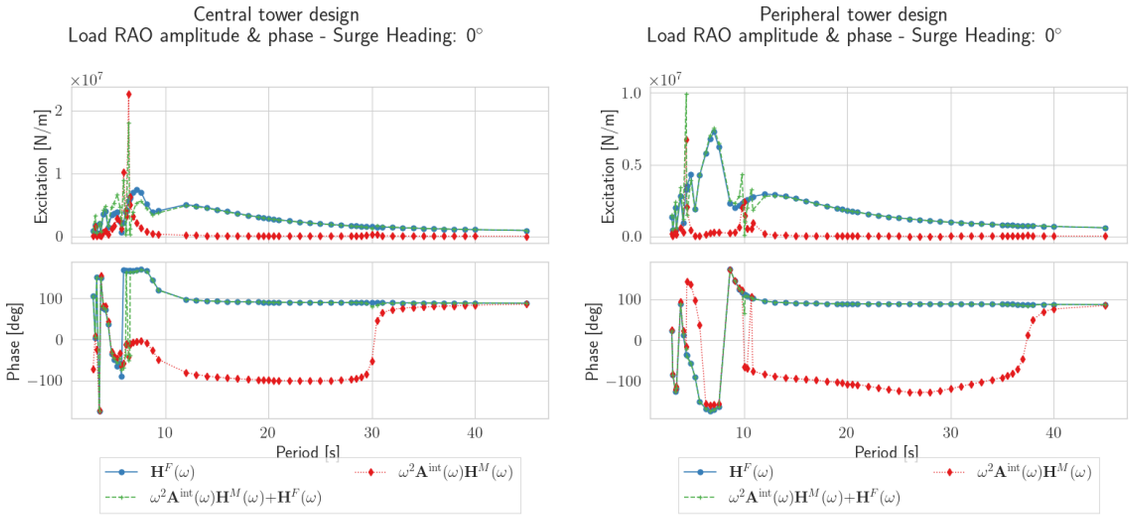

(a) Center tower design

(b) Peripheral tower design

Figure 11.5: Wave load excitation in surge comparison

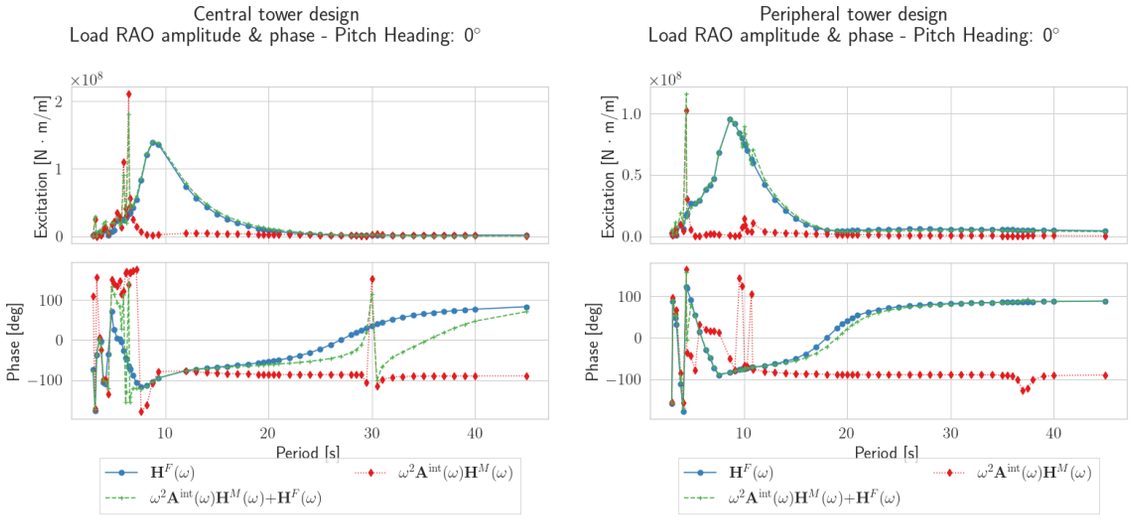

(a) Center tower design

(b) Peripheral tower design

Figure 11.6: Wave load excitation in pitch comparison

11.5 Effect of sloshing on QTFs

In Figure 11.7 and Figure 11.8, the full QTFs is plotted using both the quasi-static and the dynamic methods for internal fluids, for the center and peripheral tower concepts, respectively. In general, the two methods provide the same results for both concepts. However, it is noted that a small difference is observed along the main diagonal at $\omega_1 = \omega_2 \approx 1.1 rad/s$. This corresponds to a period of $5.71s$, which is the longest sloshing period. As the sloshing-induced motion may affect the ability to generate waves, the changes in the QTFs may have physical meaning. For the peripheral tower design, the same effect is not seen.

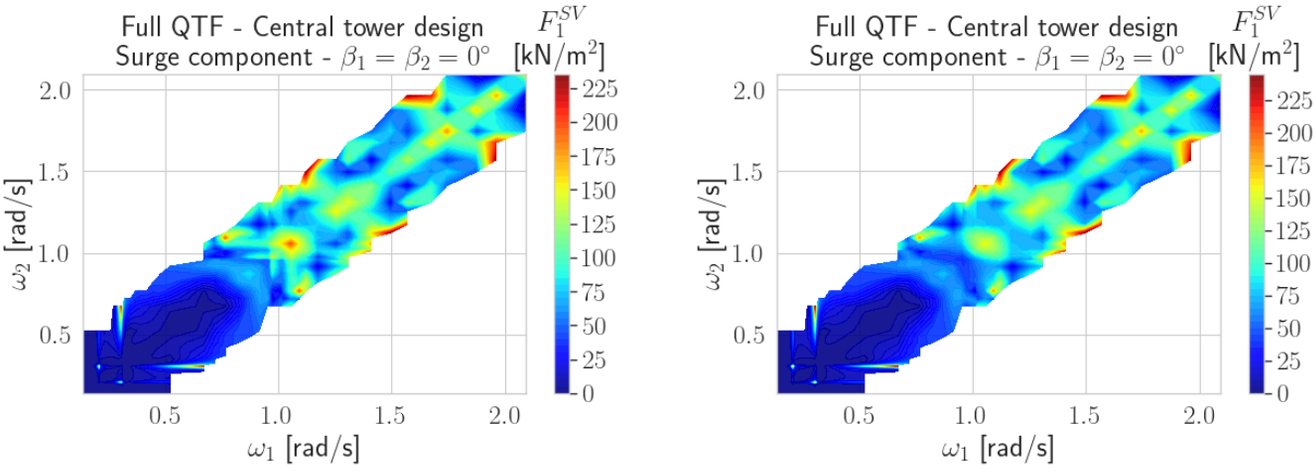

(a) Dynamic method

(b) Quasi-static method

Figure 11.7: Surge component - full QTF, Center tower design

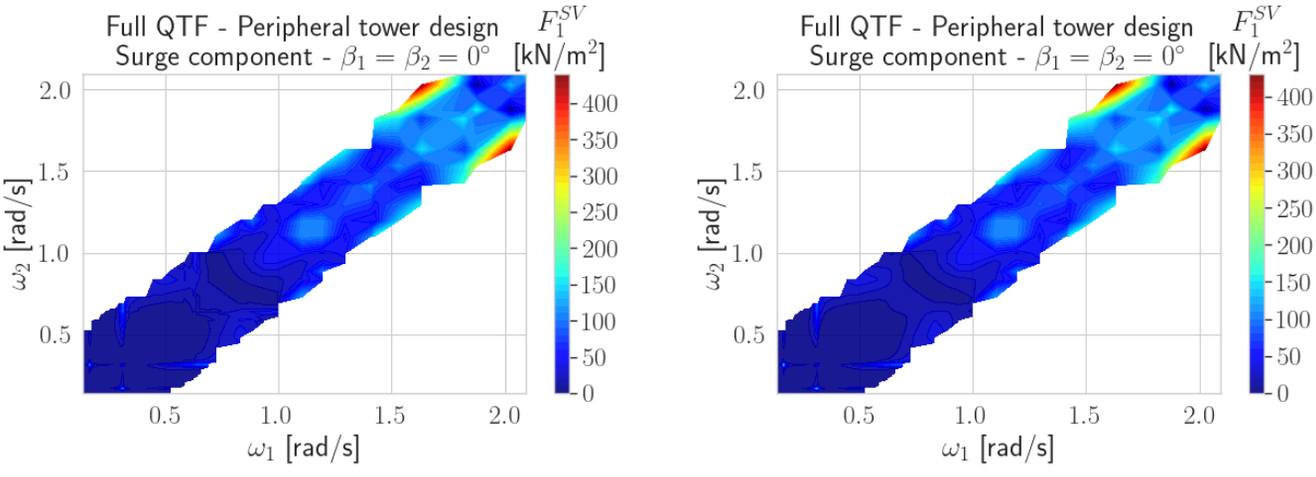

(a) Dynamic method

(b) Quasi-static method

Figure 11.8: Surge component - full QTF, Peripheral tower design

Based on the results of the time-domain simulations, the effect of the linear sloshing on the yaw QTF must be investigated. This quadratic moment component is presented below for wave components of 150°. The results from the center tower design show a clear difference in the moment caused by the interaction between waves with frequency $\omega \approx 1 rad/s$ and $\omega \approx 1.3 rad/s$. Some differences are also seen along and towards the main diagonal.

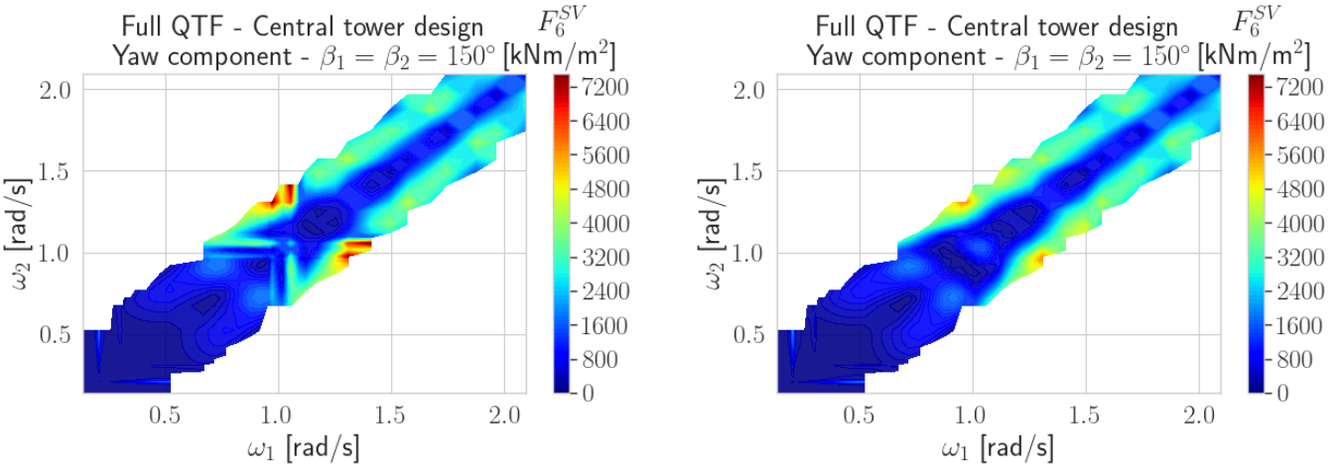

(a) Dynamic method

(b) Quasi-static method

Figure 11.9: Yaw component - full QTF, Center tower design

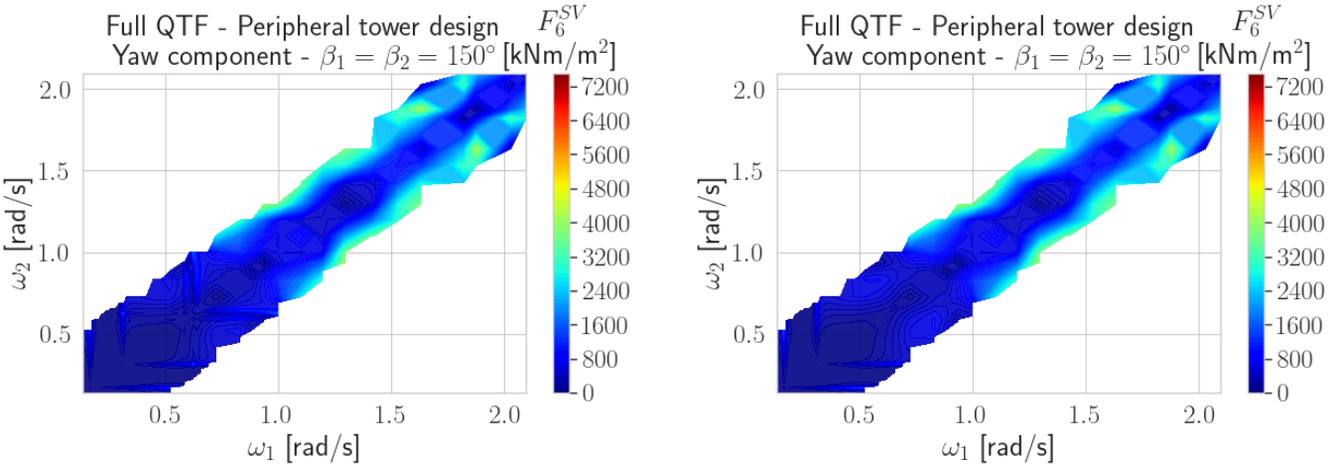

(a) Dynamic method

(b) Quasi-static method

Figure 11.10: Yaw component - full QTF, Peripheral tower design

11.6 Effect of ballast filling levels

To investigate the effect of changing the filling level of the ballast in the intact condition, several linear frequency-domain calculations were performed. In the different calculations, the tank filling was changed from completely empty to fully filled in steps of 25%. To maintain the same draft of the substructure, changes in the fluid ballast were counteracted by modifying the level of fixed ballast until vertical equilibrium was obtained.

In Figure 11.11a, the added mass of the tanks is derived from WADAM as a function of period. The output from WADAM included both the dynamic and static effect of the internal fluid as an added mass effect, which implies that the "mass"-effect of the ballast is modeled in the added mass matrix instead of the mass matrix.

As predicted by analytical formulations of the resonant sloshing period for simple three-dimensional geometries presented in Section 4.4.1, the filling level is inversely proportional to the first sloshing period. The difference in added mass, and consequently motion response, is connected with how well the applied discretization of the wave period axis aligns with the resonant sloshing periods. Any conclusion about the level of the responses may not be drawn from linear theory, as the response is governed by nonlinearities at the sloshing period. Changes in pitch responses, visual through the surge-pitch coupling, are connected with changes in the moment of inertia and the center of gravity caused by the exchange of fluid ballast with fixed ballast.

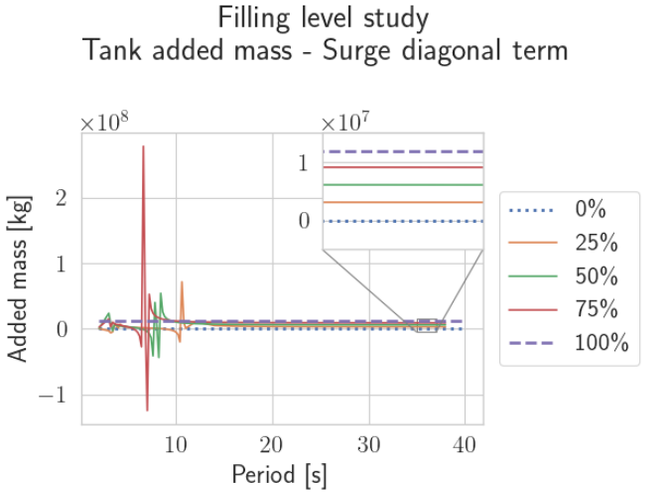

(a) Added mass of ballast water, surge diagonal component

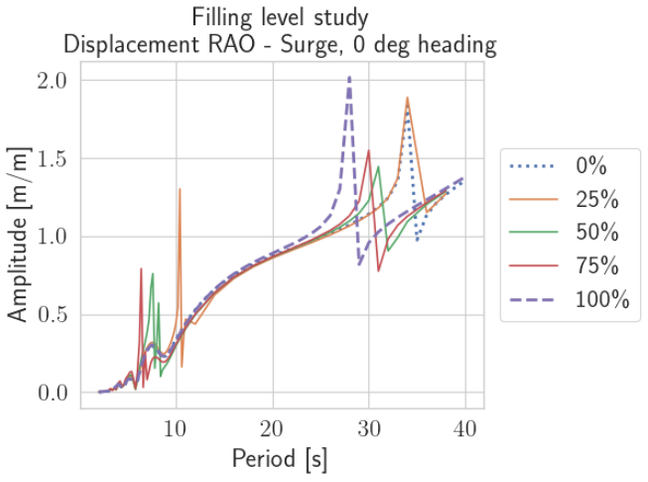

(b) Displacement RAO in surge

Figure 11.11: Comparison of ballast filling levels, center tower design

CHAPTER 12

Time-domain simulations

During post-processing of the results, some important response variables have to be identified. In this thesis, the focus lies on rigid body motions, as well as global structural responses in tower and mooring lines. As the analysis consists of several wind and wave directions, the horizontal translations will be quantified by an offset defined as the Pythagorean sum of the surge and sway response. The vertical rotation will be quantified by considering the absolute maximum value of the roll and pitch response. The mean and standard deviation of the degree of freedom with the absolute maximum rotation will also be presented, that be, of either the roll or pitch response. For the tower bending moment, the magnitude of the combined fore-aft and side-side contributions will be considered at the tower base. The axes around which this magnitude acts will generally be different for different loading conditions.

It is important to note the use of the mean and standard deviation. The mean and standard deviations of a response variable refer to the mean value and variability in the time series. The mean and standard deviations of seeds refer to the mean and variability of the statistics obtained across different seeds. For the cases with different wind and/or wave directions, the same random wind and wave seed is applied. This allows to see the effect of the different directions without the added variability of the random wind and wave processes. Cases sharing the same seed number and wind speed utilize the same turbulent wind file as well to be able to see the effect of the different sea states without the variability of the wind processes.

The results are explained and discussed when presented, as this was found to give the clearest representation of the results. A more general discussion of the results and limitations is given in chapter 13.

12.1 Power production (DLC 1.6)

The results from the time-domain simulations considering DLC 1.6 are presented in this section. As discussed in the methodology and shown in Figure 8.4, two random seeds were analyzed for every combination of mean wind speeds, wind directions, and sea states. As prescribed by DNV (2018), only aligned wind and wave directions are considered. The repeated simulations with multiple random seeds amount to a total of 318 4000 s time-domain simulations and almost 400 GB of time series results.

Maximum vertical rotation

In the following, the maximum vertical rotation obtained within DLC 1.6 is presented. As seen in Table 12.1, the maximum vertical rotation occurs in the same sea state for both concepts, namely severe sea state 3D presented in Table B.3 and Table 7.4. This is a high sea state placed at the long-period side of the highest sea state for the given environmental contour. From the constant wind tests, this wind speed was also found to give the largest rotor thrust. As expected from the quasi-static, the peripheral tower shows a large response in terms of mean value and maximum. The mean values are, however, found to be significantly smaller than the intercepts found in chapter 10. This is explained by the fact that the true center of gravity of the RNA is considered, which counteracts the moment from the thrust force. In addition, the restoring from the mooring lines is included, which is non-negligible as described in chapter 6.

Table 12.1: Vertical rotation, DLC 1.6

	Center tower design		Peripheral tower design	
Sea state	3D		3D	
Mean hub wind speed [m/s]	12.59		12.59	
Significant wave height [m]	8.00		8.00	
Spectral peak period [s]	19.85		19.85	
Wind direction [deg]	180		180	
Wave direction [deg]	180		180	
Maximum rotation DOF	Pitch		Pitch	
	Mean of seeds	Std.dev of seeds	Mean of seeds	Std.dev of seeds
Maximum rotation [deg]	7.00	0.21	8.83	0.31
Mean rotation [deg]	3.68	0.05	5.49	0.07
Std. dev. of rotation [deg]	0.94	0.03	1.12	0.06

Maximum horizontal offset

The horizontal offset is presented in Table 12.2. The results show that the center tower design experiences a larger maximum and mean offset compared to the peripheral tower design. A possible explanation of this may be the larger projected drag area caused by taller pontoons and an additional column. The maximum value occurs for the same combination of environmental conditions for both concepts. This is the steepest sea state considered in the load case, conditional to the largest wind. The QTFs shown in Figure 9.7, shows an increase in the quadratic force with increasing frequency, connected with the body's ability to generate waves. Seen in connection with the quadratic dependency on the wave amplitude, this is a plausible explanation. It could be expected that the maximum offset should occur in connection with the maximum thrust, but the current sea state introduces larger wind loads on the tower and has a larger wind-driven current. The maximum offset occurs for a wind and wave direction aligned with a mooring line, although different from 180°. This shows the need for analyzing additional directions.

Table 12.2: Maximum horizontal offset, DLC 1.6

	Center tower design		Peripheral tower design	
Sea state	4A		4A	
Mean hub wind speed [m/s]	25.00		25.00	
Significant wave height [m]	8.58		8.58	
Spectral peak period [s]	9.99		9.99	
Wind direction [deg]	120		120	
Wave direction [deg]	120		120	
	Mean of seeds	Std.dev of seeds	Mean of seeds	Std.dev of seeds
Maximum offset [m]	50.748	3.873	43.737	3.577
Mean offset [m]	31.485	0.094	25.432	0.878
Std. dev. of offset [m]	4.858	0.172	4.366	0.263

Maximum mooring line tension

The maximum mooring line tension occurs at the same sea state as the maximum offset, but for an aligned wind and wave direction of 180°. At this heading, the entire horizontal restoring is provided by a single mooring line. The maximum value is far less than the minimum breaking load presented in Table 6.14.

Table 12.3: Maximum mooring line tension, DLC 1.6

	Center tower design		Peripheral tower design	
Sea state	4A		4C	
Mean hub wind speed [m/s]	25.00		25.00	
Significant wave height [m]	8.58		10.92	
Spectral peak period [s]	9.99		16.25	
Wind direction [deg]	180		180	
Wave direction [deg]	180		180	
	Mean of seeds	Std.dev of seeds	Mean of seeds	Std.dev of seeds
Maximum tension [kN]	5369.60	697.60	5066.24	373.30
Mean tension [kN]	2955.03	6.88	2705.06	42.62
Std.dev of tension [kN]	386.41	23.8	497.60	18.72

Maximum tower base bending moment

The largest tower base bending moment occurs in the same steep sea state, with aligned wind and waves. The peripheral tower shows the largest maximum and mean value, which may be seen in connection with the larger vertical rotation. A larger rotation out of the horizontal plane will give a larger overhang of the RNA and tower, causing a larger bending moment. By using the tower geometry defined in Table 6.4, the bending stress can be calculated. This disregards the contribution from the axial stress and shear stress, which should be included when evaluating the Von-Mises criterion against yielding. For the maximum bending moments presented in Table 12.4, the pure bending stress is found as 94.73 MPa and 110.72 MPa for the center and peripheral tower design, respectively. This value is much lower than the yield strength of structural steel.

Table 12.4: Maximum tower base bending moment, DLC 1.6

	Center tower design		Peripheral tower design	
Sea state	4A		4A	
Mean hub wind speed [m/s]	25.00		25.00	
Significant wave height [m]	8.58		8.58	
Spectral peak period [s]	9.99		9.99	
Wind direction [deg]	120		150	
Wave direction [deg]	120		150	
	Mean of seeds	Std.dev of seeds	Mean of seeds	Std.dev of seeds
Maximum moment [MNm]	641.37	76.5	749.68	44.63
Mean moment [MNm]	181.85	0.58	257.54	0.80
Std.dev of moment [MNm]	92.56	0.81	112.89	2.2

Maximum nacelle acceleration

In Table 12.5, the maximum nacelle accelerations observed within DLC 1.6 is presented. The nacelle acceleration is only included for this load case, as a check of the SLS. The acceleration is quantified as the magnitude of the translational acceleration components in all directions. For both concepts, the maximum value occurs for the sea states with the shortest spectral peak period, conditional to the maximum wind speed. As previously stated, this is a rather extreme sea state with high and steep waves.

Table 12.5: Maximum nacelle acceleration, DLC 1.6

	Center tower design		Peripheral tower design	
Sea state	4A		4A	
Mean hub wind speed [m/s]	25.00		25.00	
Significant wave height [m]	8.58		8.58	
Spectral peak period [s]	9.99		9.99	
Wind direction [deg]	120		150	
Wave direction [deg]	120		150	
	Mean of seeds	Std.dev of seeds	Mean of seeds	Std.dev of seeds
Maximum acceleration [m/s^2]	3.401	0.183	3.200	0.924

By comparing the maximum acceleration to the gravitational acceleration, values of $0.35g$ and $0.33g$ are found for the center and peripheral design respectively. Hence, both concepts exceed the SLS value of $0.3g$ described in chapter 3.

12.2 Parked turbine in storm conditions (DLC 6.1)

Similarly, as in the previous load case, two random seeds were performed for all combinations of environmental actions. Only considering a single mean wind speed compared to four separate wind speeds reduces the number of simulations seen in isolation, but this reduction is countervailed by the inclusion of wind-wave misalignment. In total, 250 simulations are performed, amounting to 200 GB of results.

In the extreme wind speeds considered in this load case, the peripheral tower design showed an unexpected yaw response. A mean yaw response is expected for the cases with either 120° or 150° wind and/or wave directions, but not in the case of aligned wind and waves from the 180° direction.

To understand the behavior, several variations of the load case were performed. Through the investigation, it was found that the behavior does not occur when considering only the combined wave and current conditions of the load case. This rules out yaw drift as the cause of the behavior. Furthermore, it was observed for cases considering only the turbulent wind, without waves and current. This strongly suggests that the wind loading on the tower and RNA causes the yaw moment. For inspection of the time series, it appears to be a quasi-static effect caused by a small rotational displacement in a roll. As the point of attack of the wind force has a vertical distance from the roll axis, a small roll angle will introduce a yaw moment arm between the wind force and the restoring force. As it is assumed quasi-static, the restoring force will balance the excitation force, but their separation leads to a pure torque acting on the system. The moment arm increases further with increasing yaw displacement, which appears to give a yaw excitation that increases faster than the yaw restoring from the mooring system. Simulations with joint wind and waves acting from the opposite direction, with the tower placed away from the wind direction, do not show large yaw motions. The mechanism, with the tower illustrated by the red dot, is illustrated in Figure 12.1.

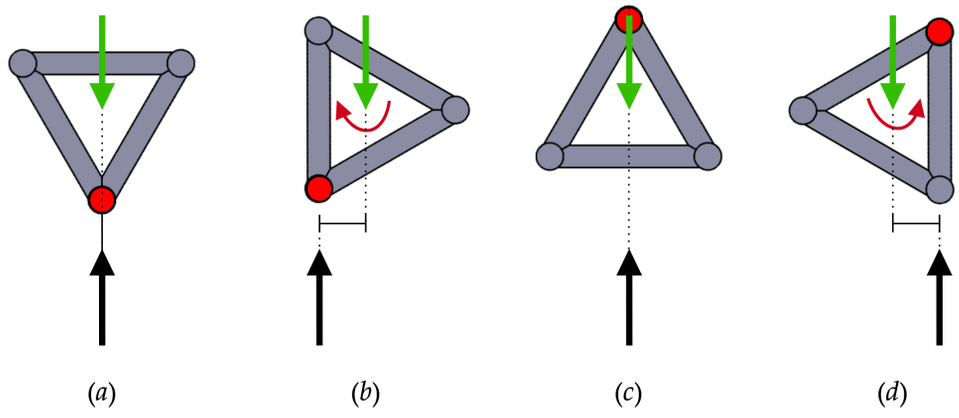

Figure 12.1: Proposed mechanism behind extreme yaw responses

Further testing show that both increased roll and pitch stiffness and increased yaw stiffness appear to reduce the mean yaw angle. This further indicates that this is a quasi-static instability and that the concept lacks sufficient restoring stiffness. An interesting remark is that simulating the peripheral tower concept without introducing the quasi-static internal free-surface correction to the stiffness matrix gives a far-less yaw response. This shows the importance of including the effect. A final simulation was performed, where all environmental actions were suddenly turned off. In this case, the structure decays back to its original equilibrium. Increasing the roll and pitch restoring stiffness may be done by either increasing the water plane stiffness or by lowering the center of gravity. The former can be obtained by increasing the distance between the columns, while the latter can be obtained by changes in ballast or eventual weight savings in the tower and the RNA. To increase yaw stiffness, the mooring system must be modified. To achieve an increase in yaw stiffness for the given substructure, a "crowfoot" connection consisting of delta lines could be applied. This method is commonly applied for SPAR concepts and was also proposed by J. Jonkman and Buhl (2007) in the case of a yaw instability observed on a barge-type FOWT during blade fault simulations.

Maximum vertical rotation

The maximum rotation for both concepts occurs in a sea state with misaligned wind and wave forces, causing a large roll response as presented in Table 12.6.

Table 12.6: Maximum vertical rotation, DLC 6.1

	Center tower design		Peripheral tower design	
Sea state	50yA		50yC	
Mean hub wind speed [m/s]	47.52		47.52	
Significant wave height [m]	9.14		14.60	
Spectral peak period [s]	9.71		17.48	
Wind direction [deg]	180		180	
Wave direction [deg]	150		150	
Maximum rotation DOF	Roll		Roll	
	Mean of seeds	Std.dev of seeds	Mean of seeds	Std.dev of seeds
Maximum rotation [deg]	7.843	0.749	17.689	0.853
Mean rotation [deg]	2.441	0.109	10.459	0.156
Std.dev of rotation [deg]	1.499	0.070	2.177	0.148

As a dominating roll response was not aligned with the expected response, it was further investigated. Simultaneous time series for the roll and yaw responses in the sea states of maximum vertical rotation is presented in Figure 12.2. These results show that the large roll responses are due changes in the excitation due to yaw motions. As illustrated with red dotted lines in Figure 12.2a, the maximum absolute roll response occurs at times with maximum yaw response. The larger yaw response is caused by the inclined angle of the waves. When the yaw response is larger, the body-fixed y-axis rotates towards the wind speed, acting along the global x-direction. This causes a large overturning moment from the wind forces acting on the tower and RNA. For the peripheral tower design, a larger mean yaw angle occurs from the mechanisms described above. Consequently, a large mean roll angle is also observed.

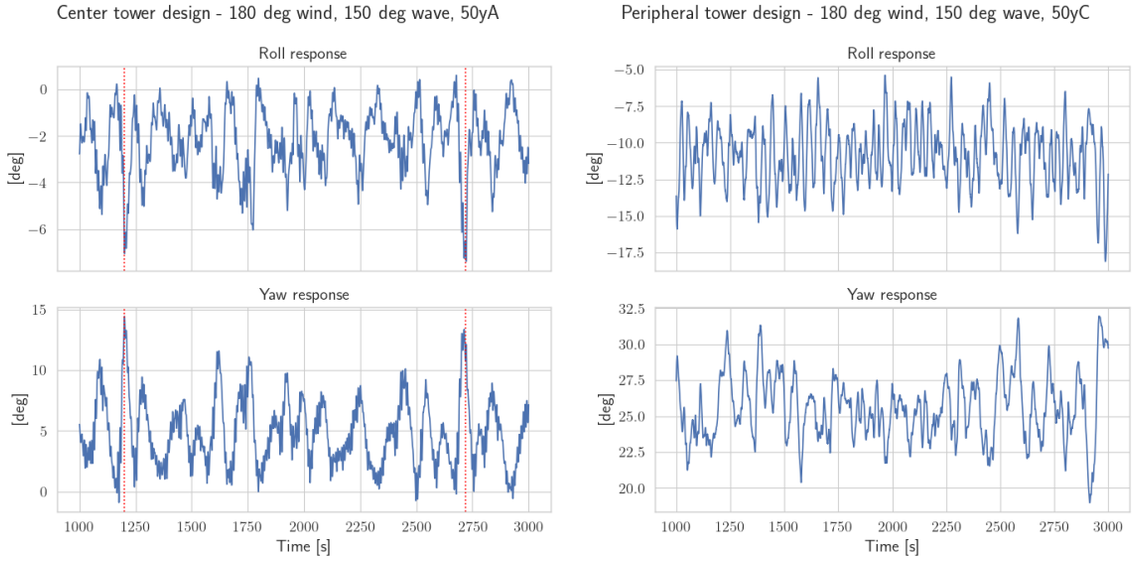

(a) Center tower design

(b) Peripheral tower design

Figure 12.2: Roll and yaw time series for sea states with maximum vertical rotation

Maximum horizontal offset

The same trend as for DLC 1.6 is observed for the maximum horizontal offset. The most critical sea states are characterized by high and steep waves. Even larger values are seen in this case, as both wave height, wind speed, and current are increased. The largest response is seen for the center tower design, which is approaching a value of 25% of the water depth, equivalent to 75 m. This was the rule of thumb to prevent damage to the power cable discussed in chapter 3.

Table 12.7: Maximum horizontal offset, DLC 6.1

	Center tower design		Peripheral tower design	
Sea state	50yA		50yA	
Mean hub wind speed [m/s]	47.52		47.52	
Significant wave height [m]	9.14		9.14	
Spectral peak period [s]	9.71		9.71	
Wind direction [deg]	120		150	
Wave direction [deg]	120		120	
	Mean of seeds	Std.dev of seeds	Mean of seeds	Std.dev of seeds
Maximum offset [m]	73.069	2.479	66.498	4.795
Mean offset [m]	53.102	0.605	46.543	0.551
Std.dev of offset [m]	5.673	0.343	5.536	0.455

Maximum mooring line tension

The maximum mooring line tension occurs in the same environmental conditions for both concepts. This is the sea state with the largest significant wave height along the 50-year environmental contour. This might indicate that the extreme response is governed by wave action. The maximum mooring line tension is still below the minimum breaking strength presented in Table 6.14.

Table 12.8: Maximum mooring line tension, DLC 6.1

	Center tower design		Peripheral tower design	
Sea state	50yC		50yC	
Mean hub wind speed [m/s]	47.52		47.52	
Significant wave height [m]	14.6		14.6	
Spectral peak period [s]	17.48		17.48	
Wind direction [deg]	180		180	
Wave direction [deg]	180		180	
	Mean of seeds	Std.dev of seeds	Mean of seeds	Std.dev of seeds
Maximum tension [kN]	9026.11	582.34	9394.44	696.69
Mean tension [kN]	4032.32	30.12	4315.29	34.10
Std.dev of tension [kN]	1059.47	17.18	1029.36	15.84

Maximum tower base bending moment

The maximum tower base bending moments occur at very different sea states for the two concepts, placed at each spectral period extrema of the environmental contour. The reason behind the larger bending moment for the peripheral tower design is still believed to be due to the large overhang of the tower and RNA. Inspection of the time series shows that the extreme bending moment occurs simultaneously with extreme vertical rotations.

The second random seed has an extreme tower base bending moment of 1055 MNm, close to the mean of all seeds presented in Table 12.9. On inspection of the time series, it is found that the simultaneous axial force at the same location is −22.33 MN. Using the values for the tower cross-section presented in Table 6.4, the combined stress of both loads at the compression side equals 164 MPa, where the axial force contribution amounts to only 8 MPa.

Table 12.9: Maximum tower base bending moment, DLC 6.1

	Center tower design		Peripheral tower design	
Sea state	50yA		50yF	
Mean hub wind speed [m/s]	47.52		47.52	
Significant wave height [m]	9.14		1.02	
Spectral peak period [s]	9.71		27.03	
Wind direction [deg]	180		120	
Wave direction [deg]	150		150	
	Mean of seeds	Std.dev of seeds	Mean of seeds	Std.dev of seeds
Maximum moment [MNm]	751.62	46.66	1050.99	237.10
Mean rotation [MNm]	238.66	4.42	559.65	14.90
Std.dev of rotation [MNm]	123.11	2.52	138.46	48.67

Effect of sloshing

In Table 12.10, the effect of linear sloshing is presented. For all the selected response variables, the same five random seeds are re-simulated using the first- and second-order forces, including the effect of linear sloshing. Looking at the result, the differences are surprisingly larger based on the similar results obtained in the frequency-domain calculations. OrcaFlex's "Compare data"-feature was used on the respective time-domain models, which confirmed that the only difference between them was in the wave excitation forces.

The most surprising result is the reduced vertical rotations. For the center tower design, the maximum rotation for the case with sloshing occurs in the pitch degree of freedom. The magnitude is comparable to the maximum pitch response for the quasi-static model, while the absolute maximum roll response is reduced to 4.56°. This appears to be caused by a reduced mean yaw angle of only 0.48° compared to 4.8° for the other model across all seeds. A reduced yaw angle eliminates the extreme wind load-induced roll responses previously discussed. The variability in the yaw response, quantified by the standard deviation, is approximately equal for the two models. This suggests that a mean drift load may be causing the difference, and possibly the differences in the yaw component of the QTFs presented in chapter 11.

It is further noted that the results considering linear sloshing show an increased horizontal offset, quantified by the maximum value, the mean value, and the standard deviations. Looking at the surge RAOs from the frequency domain, this is more easily accepted. The linear sloshing also causes the center tower concept to exceed the criterion for power cable damage.

Table 12.10: Effect of sloshing on time-domain response in DLC

		Center		Peripheral	
		QS	Dyn	QS	Dyn
Vertial rotation [deg]	Max	7.84	5.89	17.69	14.34
	Mean	2.44	1.39	10.46	8.70
	Min	1.36	1.33	2.18	1.68
Offset [m]	Max	73.07	78.64	66.50	70.58
	Mean	53.10	57.53	46.54	49.45
	Std.dev	5.67	6.38	5.54	6.17
Tower BM [MNm]	Max	751.62	732.66	1050.99	1047.91
	Mean	238.66	204.04	559.65	559.68
	Std.dev	123.11	112.20	138.46	138.07
Mooring tension [kN]	Max	9026.11	9958.17	9394.44	8700.80
	Mean	4032.32	4862.72	4315.29	4727.89
	Std.dev	1059.47	1252.11	1029.36	769.09

12.3 Parked turbine after the occurrence of compartment flooding (DLC 7.5)

This section presents the results which consider the steady-state response after the flooding of internal compartments. The major part of the results uses the quasi-static model in the damaged static equilibrium with the mean compartment filling levels. For the most severe combinations of environmental conditions, the effect of sloshing is investigated. The effect of inflow/outflow of the damaged compartment is also analyzed for damage case 1 using the hydraulic flooding model. These calculations are not performed for damage case 2, as the relevant compartments will be completely flooded during the entire simulations.

The combination of several damage cases and wind-wave misalignment made this load case the most computationally demanding part of the thesis. More than 500 simulations have been performed, producing almost a gigabyte of data each.

12.3.1 Damage case 1: Column flooding

Maximum vertical rotation

In the simulations of column flooding using the quasi-static model, the maximum vertical rotation occurs in steep sea states. For the center tower design, the maximum rotation occurs in the pitch degree of freedom. The time series shows the same mechanism as before, where in this case an opposite yaw response rotates the body-fixed x-axis towards the mean wind speed. For the peripheral tower design, the same extreme mean yaw angles are seen, which results in a large maximum and mean roll angle. This is described by the same quasi-static mechanism as described in Figure 12.1.

Table 12.11: Maximum vertical rotation, DC1 - DLC 7.5

	Center tower design		Peripheral tower design	
Sea state	1yA		1yB	
Mean hub wind speed [m/s]	40.61		40.61	
Significant wave height [m]	7.52		10.36	
Spectral peak period [s]	9.13		12.42	
Wind direction [deg]	120		180	
Wave direction [deg]	150		180	
Maximum rotation DOF	Pitch		Roll	
	Mean of seeds	Std.dev of seeds	Mean of seeds	Std.dev of seeds
Maximum rotation [deg]	6.989	1.107	12.797	1.908
Mean rotation [deg]	2.048	0.088	6.975	1.084
Std.dev of rotation [deg]	1.073	0.024	1.660	0.283

Maximum horizontal offset

For the horizontal offset, the same general trend is seen as in the previous load cases. The maximum offset is larger for the center tower design, and it occurs in a steep sea state with an angle to the global x-axis. The values are significantly lower than those seen in DLC 6.1, as all environmental conditions are lower. Furthermore, the values are larger than those observed for DLC 1.6 even though the operating conditions consider more severe significant wave heights. This suggests that the extreme wind speed and associated current are relatively more important for the offset.

Table 12.12: Maximum horizontal offset, DC1 - DLC 7.5

	Center tower design		Peripheral tower design	
Sea state	1yA		1yB	
Mean hub wind speed [m/s]	40.61		40.61	
Significant wave height [m]	7.52		10.36	
Spectral peak period [s]	9.13		12.42	
Wind direction [deg]	120		150	
Wave direction [deg]	120		120	
	Mean of seeds	Std.dev of seeds	Mean of seeds	Std.dev of seeds
Maximum offset [m]	59.45	2.95	53.27	2.23
Mean offset [m]	38.99	0.31	33.96	0.21
Std.dev of offset [m]	5.05	0.25	4.63	0.13

Maximum mooring line tension

As expected from the smaller horizontal offsets, the mooring line tensions are smaller than the tensions found in DLC 6.1. It is seen that although the maximum tension is larger for the center tower design, the peripheral tower design shows a larger mean value. However, this mean value is associated with a larger variability, as quantified by the standard deviation of the seeds.

Table 12.13: Maximum mooring tension, DC1 - DLC 7.5

	Center tower design		Peripheral tower design	
Sea state	1yB		1yC	
Mean hub wind speed [m/s]	40.61		40.61	
Significant wave height [m]	10.36		11.70	
Spectral peak period [s]	12.42		15.43	
Wind direction [deg]	180		180	
Wave direction [deg]	180		180	
	Mean of seeds	Std.dev of seeds	Mean of seeds	Std.dev of seeds
Maximum tension [kN]	6438.32	382.30	6355.89	412.86
Mean tension [kN]	3356.24	9.19	3424.26	79.63
Std.dev of tension [kN]	564.62	7.34	665.49	19.13

Maximum tower base bending moment

While the center tower design shows a relatively small maximum tower base bending moment, the largest extreme value for all cases occurs for the peripheral design. This is explained by the larger overhang caused by the larger vertical rotations of the substructure, combined with significant wave action.

Table 12.14: Maximum tower base bending moment, DC1 - DLC 7.5

	Center tower design		Peripheral tower design	
Sea state	1yA		1yD	
Mean hub wind speed [m/s]	40.61		40.61	
Signficant wave height [m]	7.52		10.36	
Spectral peak period [s]	9.13		16.93	
Wind direction [deg]	180		150	
Wave direction [deg]	150		180	
	Mean of seeds	Std.dev of seeds	Mean of seeds	Std.dev of seeds
Maximum moment [MNm]	634.85	44.09	1136.32	103.43
Mean moment [MNm]	166.20	5.76	484.24	16.96
Std.dev of moment [MNm]	90.77	0.58	154.42	35.04

Effect of sloshing and flooding

In this section, the results of further investigation of the damage case using both the sloshing model and the combined sloshing and flooding model are presented. For each approach, five additional simulations were performed for the sea states that gave the maximum of the selected response variables. The results show the same general differences as the comparison for DLC 6.1. For the vertical rotation, the flooding model appears to counteract some of the reduction from the dynamic fluid model. The increased vertical rotations caused by the environmental actions cause an increased external pressure head, which again increases the compartment filling levels. This further worsens the experienced vertical rotation.

Both the dynamic sloshing and the combined models show a larger horizontal offset for both concepts, where the dynamic sloshing model appears to be the cause. From the horizontal offset, the center tower design shows the expected increase in mooring line tension. The response for the peripheral tower design shows a response that is more difficult to explain, as the maximum values decreased while the mean values increased.

Table 12.15: Effect of sloshing and flooding, DLC 7.5 - DC1

		Center			Peripheral		
		QS	Dyn	Dyn+FM	QS	Dyn	Dyn+FM
Rotation [deg]	Max	6.99	4.64	4.93	12.80	10.92	12.65
	Mean	2.05	0.90	0.99	6.97	6.35	7.23
	Std.dev	1.07	0.99	0.99	1.66	1.43	1.59
Offset [m]	Max	59.45	64.04	64.03	53.27	63.02	62.72
	Mean	38.99	41.85	41.85	33.96	39.14	38.57
	Std.dev	5.05	5.62	5.63	4.63	6.11	6.11
Tower BM [MNm]	Max	634.85	521.76	520.75	1136.32	1029.03	915.62
	Mean	166.20	134.80	135.20	484.24	471.11	497.37
	Std.dev	90.77	74.55	74.71	154.42	135.46	81.64
Mooring tension [kN]	Max	6438.32	8237.82	8239.12	6355.89	6139.70	6264.21
	Mean	3356.24	3939.08	3939.88	3424.26	3617.74	3700.14
	Std.dev	564.62	900.19	900.57	665.49	526.37	549.07

12.3.2 Damage case 2: Pontoon flooding

Maximum vertical rotation

Compared to the case of column damage, the maximum vertical rotation in the case of damage to the pontoons shows diverging results. The vertical rotation is reduced in terms of maximum and mean values for the center tower design, whereas the opposite is seen for the peripheral design. This may be connected with the lower intact filling level of the pontoons for the latter. A difference in the sea state for which the maximum value occurs is further noted, similarly as for the maximum tower bending moment in DLC 6.1.

Table 12.16: Maximum vertical rotation, DC2 - DLC 7.5

	Center tower design		Peripheral tower design	
Sea state	1yA		1yF	
Mean hub wind speed [m/s]	40.61		40.61	
Significant wave height [m]	7.52		2.68	
Spectral peak period [s]	9.13		20.04	
Wind direction [deg]	120		120	
Wave direction [deg]	120		120	
Maximum rotation DOF	Roll		Pitch	
	Mean of seeds	Std.dev of seeds	Mean of seeds	Std.dev of seeds
Maximum rotation [deg]	5.18	0.49	14.38	0.74
Mean rotation [deg]	1.43	0.03	8.87	0.08
Std.dev of rotation [deg]	1.01	0.05	1.65	0.16

Maximum horizontal offset

The horizontal offset of both concepts does not appear to be affected by the different damage locations. The maximum offsets are observed for the same combination of environmental actions, with similar magnitudes. Therefore, the results discussed for the previous cases also hold here.

Table 12.17: Maximum horizontal offset, DC2 - DLC 7.5

	Center tower design		Peripheral tower design	
Sea state	1yA		1yB	
Mean hub wind speed [m/s]	40.61		40.61	
Significant wave height [m]	7.52		10.36	
Spectral peak period [s]	9.13		12.42	
Wind direction [deg]	120		150	
Wave direction [deg]	120		120	
	Mean of seeds	Std.dev of seeds	Mean of seeds	Std.dev of seeds
Maximum offset [m]	59.10	3.09	53.07	2.18
Mean offset [m]	38.84	0.32	33.64	0.21
Std.dev of offset [m]	4.99	0.22	4.63	0.13

Maximum mooring line tension

As a direct result of the similar horizontal offsets, similar mooring line tensions are observed as well. Similarly as for the previous damage cases, the maximum occurs with aligned wind and waves acting parallel to a mooring line. The maximum value occurs in sea states with larger significant wave heights compared to the maximum offset, which again suggests that the response variable is more affected by direct wave action.

Table 12.18: Maximum mooring tension, DC2 - DLC 7.5

	Center tower design		Peripheral tower design	
Sea state	1yB		1yC	
Mean hub wind speed [m/s]	40.61		40.61	
Significant wave height [m]	10.36		11.70	
Spectral peak period [s]	12.42		15.43	
Wind direction [deg]	180		180	
Wave direction [deg]	180		180	
	Mean of seeds	Std.dev of seeds	Mean of seeds	Std.dev of seeds
Maximum tension [kN]	6377.42	378.62	6500.27	415.38
Mean tension [kN]	3355.09	8.93	3546.19	7.89
Std.dev of tension [kN]	552.97	6.67	690.00	11.76

Maximum tower base bending moment

Following the general trend of the results, similar values are seen for the tower base bending moment. It is, however, noted that the extreme value of the peripheral tower design is lowered and is, for this case, lower than the values seen in both damage case 1 and DLC 6.1.

Table 12.19: Maximum tower base bending moment, DC 2 - DLC 7.5

	Center tower design		Peripheral tower design	
Sea state	1yA		1yD	
Mean hub wind speed [m/s]	40.61		40.61	
Significant wave height [m]	7.52		10.36	
Spectral peak period [s]	9.13		16.93	
Wind direction [deg]	180		150	
Wave direction [deg]	150		180	
	Mean of seeds	Std.dev of seeds	Mean of seeds	Std.dev of seeds
Maximum moment [MNm]	554.83	52.39	987.22	165.94
Mean moment [MNm]	145.87	1.02	501.95	14.55
Std.dev of moment [MNm]	73.93	1.73	108.05	36.51

Effect of sloshing

The effect of sloshing in damage case 2 follows the previously discussed results. A reduction in the vertical rotation is observed, although this reduction is less for the peripheral tower design than observed for the other cases.

Table 12.20: Effect of sloshing on time-domain response in DLC 7.5 - DC2

		Center		Peripheral	
		QS	Dyn	QS	Dyn
Rotation [deg]	Max	5.18	4.61	14.38	14.24
	Mean	1.43	1.51	8.87	8.88
	Min	1.01	0.97	1.65	1.60
Offset [m]	Max	59.10	64.43	53.07	57.54
	Mean	38.84	42.21	33.64	36.39
	Std.dev	4.99	5.72	4.63	5.33
Tower BM [MNm]	Max	554.83	535.76	987.22	928.00
	Mean	145.87	183.76	501.95	495.70
	Std.dev	73.93	82.25	108.05	108.72
Mooring tension [kN]	Max	6377.42	7108.09	6500.27	6450.97
	Mean	3355.09	3871.46	3546.19	3782.07
	Std.dev	552.97	694.25	690.00	591.54

12.4 Parked turbine after the occurrence of mooring line loss (DLC 7.4)

Based on the observed yaw behavior of the peripheral tower design, it was suspected that the twisting of the remaining mooring lines described in Robertson, J. Jonkman, Vorpahl et al. (2014) could be observed. This load case was therefore included in the thesis as more of a qualitative study of the behavior of the system after the loss of a mooring line. Hence, only two random seeds are applied as this is deemed sufficient to understand the general trend of the behavior but not to get a precise estimate of the extreme values.

The twisting behavior was observed in all cases, for all seeds except one, considering a wind direction of 180°. The development of the yaw drift appears towards both sides, giving yaw displacements of ±180°. The inconsistency of the single random seed suggests that a more thorough analysis should be performed. It was not observed for any of the cases concerning wind directions of 120°or 150°, and not observed for any cases considering the center tower design.

The maximum observed horizontal offset was found to be 1094 m and 1080 m for the center and peripheral tower concepts, respectively. This implies that a total loss of the power cable will occur. The maximum bending moment, mooring tension, and vertical rotation were comparable to DLC 7.5, and thus less than DLC 6.1.

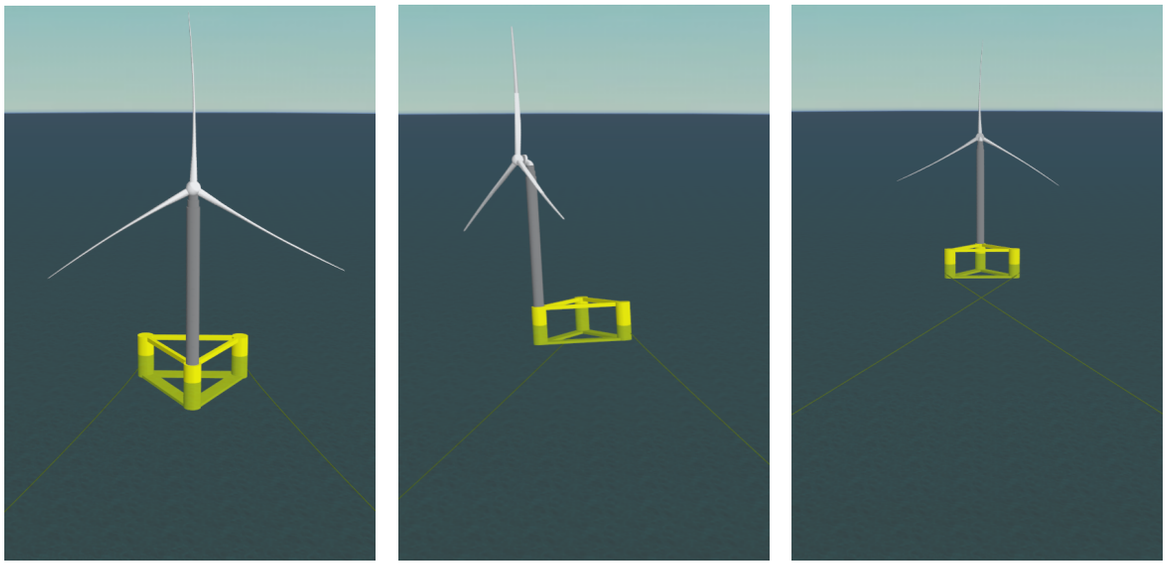

(a) T=0.0 s (b) T=112.0 s (c) T=400 s

Figure 12.3: Mooring line twisting - peripheral tower design

12.5 Emergency stop (DLC 5.1)

Figure 12.4 shows the maximum vertical rotation after the emergency shutdown is initiated. The height of the bars is determined by the mean value of the seeds, whereas the black line shows the distance between the seeds. The figure includes all the analyzed directions and wind speeds. Similar to the differences seen in previous load cases, the peripheral tower design experiences a larger maximum rotation during the emergency shutdown. This is connected to the results seen in the analysis of quasi-static stability, where the peripheral tower design has a lower area under the restoring moment curve.

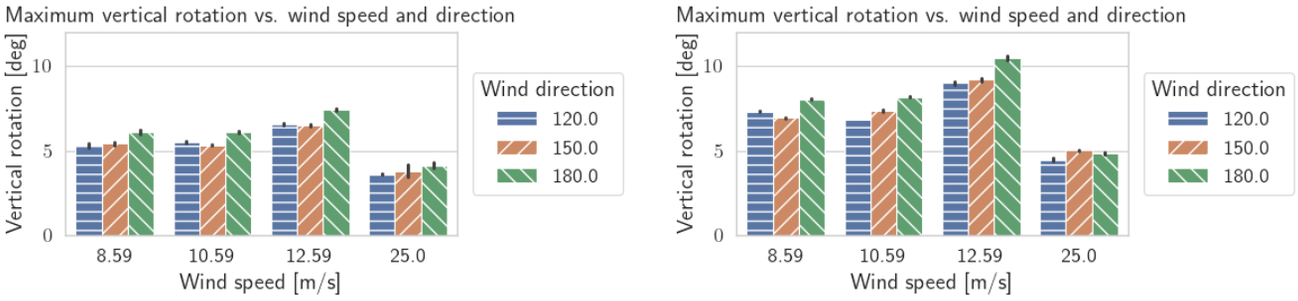

(a) Center tower design

(b) Peripheral tower design

Figure 12.4: Maximum vertical rotation, DLC 5.1

In Figure 12.5, the time series of the pitch responses of the load case identified as the most critical in Figure 12.4 is shown. The lower pitch restoring stiffness of the peripheral tower design is evident throughout all stages of the shutdown. Before the shutdown is initiated, the negative pitch angle is several degrees lower compared to the center tower design. Moreover, the maximum response during the shutdown, as well as the mean value of the decay, is consistently larger than the center tower design. The longer pitch natural period, also connected to the reduced stiffness, is also apparent in the plot.

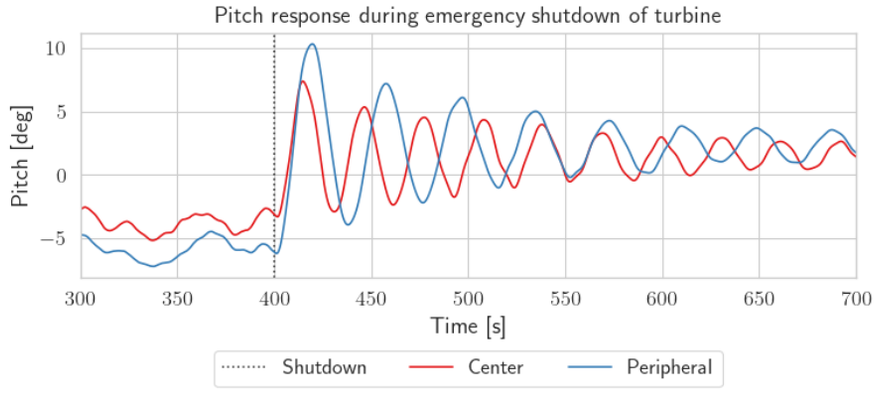

Figure 12.5: Comparison of pitch response following emergency shutdown

The large transient pitch response is caused by the reversal of rotor thrust, as illustrated in Figure 5.12. The rapid pitching of the blades results in a negative angle of attack and, consequently, a negative rotor thrust. The thrust reversal occurs rapidly and acts at the system like a pitching moment impulse which causes a pitch decay. At the beginning of the decay, one can see that the response is dominated by the response to the thrust reversal impulse before the pitch response to the incident waves becomes more visible. Selected time steps from the simulations with the center tower design are presented in Figure 12.6. Note the large deformation of the blades out of the rotor plane at the time of maximum thrust reversal, while the substructure has not yet had time to respond. The total elapsed shutdown time is approximately 20 s.

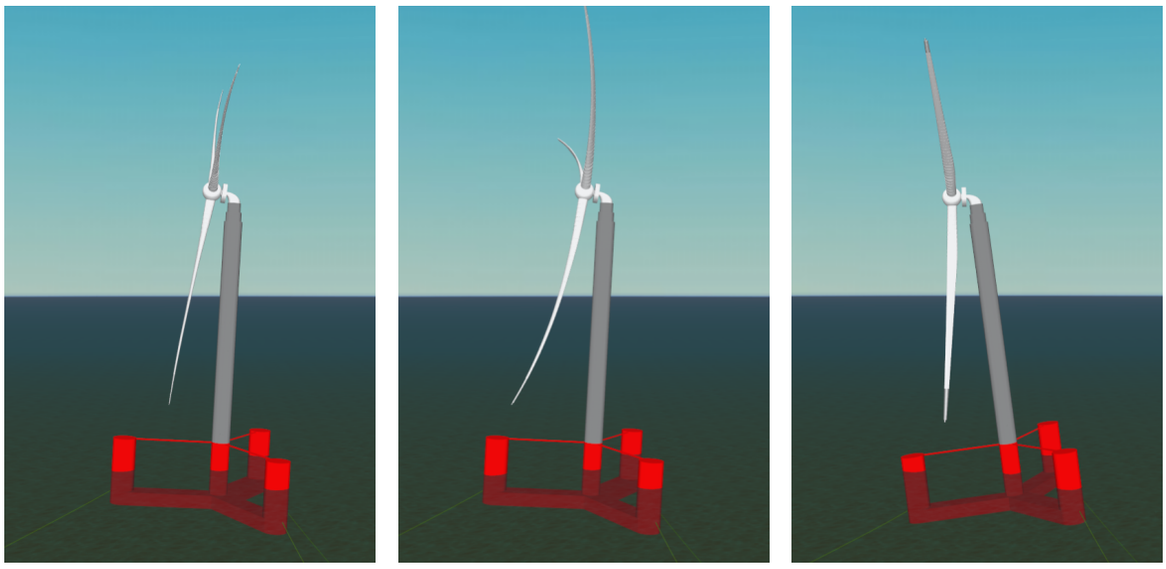

(a) Before shutdown (T=400.0 s)

(b) Max thrust reversal (T=402.5 s)

(c) Max pitch response (T=414.8 s)

Figure 12.6: Emergency shutdown snapshots, Center tower design

Investigation of the maximum tower bending moment and maximum mooring line tension indicates that the emergency shutdown load case is not critical for these response variables. The maximum tower base bending moments across all simulations are 496.5 MNm and 550.8 MNm for the center and peripheral tower design, respectively. The maximum value occurs simultaneously with the largest pitch amplitude at the beginning of the decay for both concepts. The variation of the moment is large between the different wind speeds, with a clear maximum seen for a mean wind speed of 12.59 m/s. This wind speed gives the largest thrust force and, consequently, the largest change in loading when the is reversed. For different wave headings, very similar results are obtained. The mooring line tensions are reduced by the shutdown as the large thrust from the rotor is no longer acting.

12.6 Flooding of structure followed by shutdown (DLC 2.8)

The simulations performed for this load case aim to study the transient effects of flooding in a simplified manner by considering the instantaneous hydrostatic pressure at the opening. Large deterministic transient effects are included, which are expected to dominate the loading in the transient. The effect of more severe environmental conditions in the steady-state damaged equilibrium is considered with multiple random seeds in DLC 7.5. The controlled shutdown strategy applied in both this load case and DLC 2.8 stops the turbine in approximately 50 s, which is more than double the time compared to the emergency shutdown in DLC 5.1.

12.6.1 Damage case 1: Column flooding

In terms of vertical rotation, both concepts experience the maximum in the environmental conditions consisting of a mean wind speed of 12.59 m/s with aligned waves from a direction of 180°. This is the same combination identified as critical for the other transient cases.

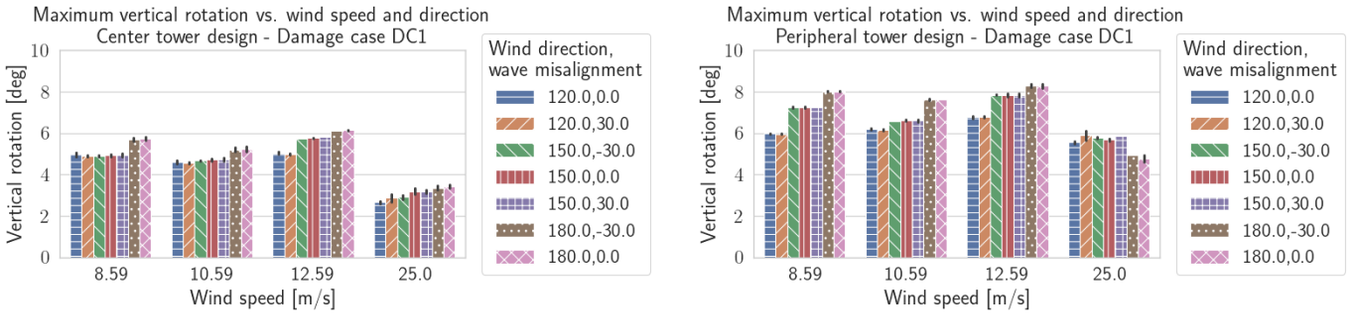

(a) Center tower design

(b) Peripheral tower design

Figure 12.7: Maximum absolute vertical rotation, DC1 - DLC 2.8

During post-processing, it was seen that the large overturning due to the rotor thrust lifts the compartmentalized part of the column out of the water. Consequently, flooding does not occur before the rotor is shut down and the pitch decay starts. The time series of the pitch response, floodwater volume, and floodwater flux are presented in Figure 12.9 to Figure 12.10. Neither of the response variables showed a critical value within this load case.

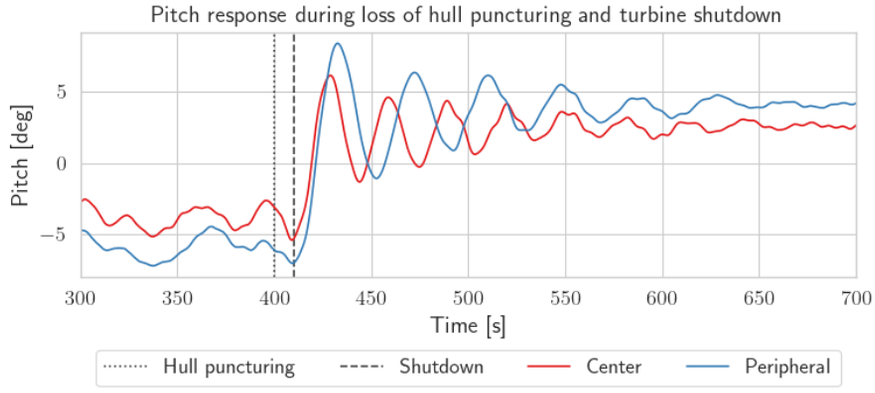

Figure 12.8: Comparison of pitch response following hull puncturing and turbine shutdown

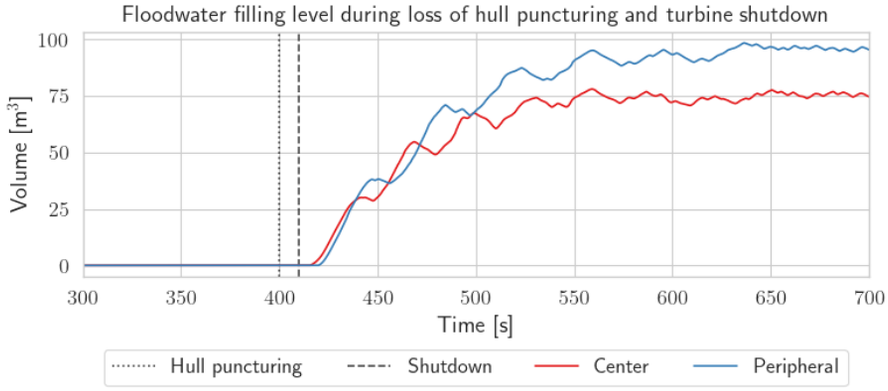

Figure 12.9: Comparison of floodwater filling volume following hull puncturing and turbine shutdown

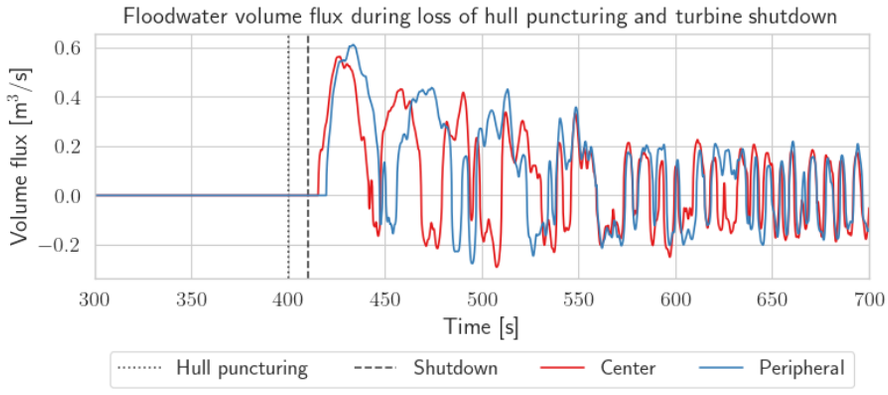

Figure 12.10: Comparison of floodwater flux following hull puncturing and turbine shutdown

12.6.2 Damage case 2: Pontoon flooding

In the following, the results from transient simulations of sudden pontoon flooding are presented. Due to the large submergence of the pontoons, the external pressure head is always larger than the internal pressure head. Hence, only inflow occurs until the compartment is completely filled.

An important variable for this load case is the pontoon ballast filling level in the intact case. This filling level is above 92% for the center tower design, which makes flooding of the remaining volume rather insignificant. As a result, the dynamic response is governed by the shutdown of the turbine. The new damaged equilibrium is characterized by a small additional trim angle about the y-axis. No significant heel angle about the x-axis is obtained, as the compartments are located close to the axis.

By looking at the intact ballast filling level percentage of the peripheral tower design, a larger response could be expected, but this must be seen in conjunction with the compartment volume itself. The added compartmentalization of the pontoons of this design makes the floodable volume less, and the obtained response is less critical compared to other load cases.

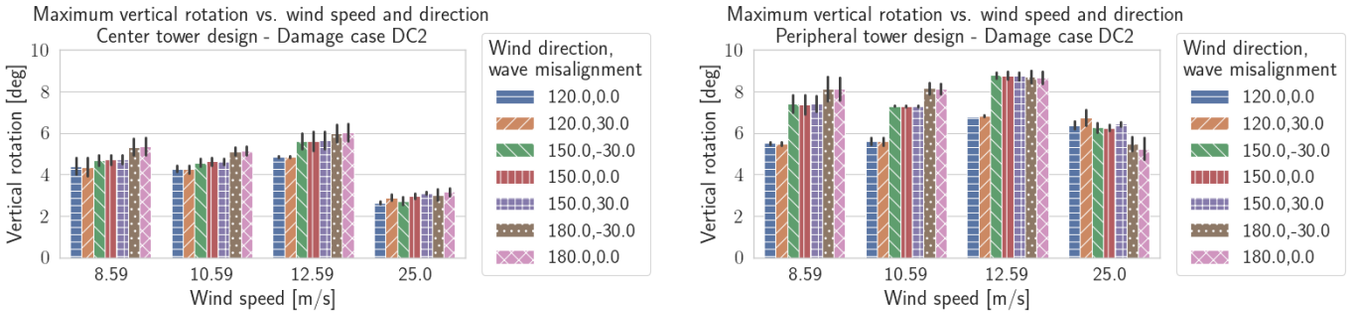

(a) Center tower design

(b) Peripheral tower design

Figure 12.11: Maximum absolute vertical rotation, DC2 - DLC 2.8

Across all environmental conditions for both DC1 and DC2, the maximum tower base bending moment and fairlead mooring line tension are much lower than seen for the other cases. The maximum observed bending moment was equal to 464.6 MNm, occurring on the peripheral tower concept in damage condition 1. The maximum observed mooring line tension was observed for the center tower design in damage condition 2, equal to 2975.9 kN.

12.7 Loss of mooring line followed by shutdown (DLC 2.6)

This load case was analyzed as the transient counterpart to DLC 7.4. The analysis of the load case focuses on the transient response in the rotational degrees of freedom, in addition to the tower base bending moment. Other response variables analyzed for the other load cases, such as mooring line tensions and offsets, are not relevant for this load case. Clearly, the offset will be large for this load case, but this is analyzed in more severe environmental conditions in DLC 7.4.

The maximum vertical rotation for both concepts occurs for the same environmental conditions as for the emergency shutdown of the turbine. This condition consists of a mean wind speed of 12.59 m/s, the expected conditional sea state, and aligned wind and wave directions equal to 180°.

The time series of simulations with the most critical pitch responses are shown in Figure 12.12. Generally speaking, the responses bear a lot of similarities with the results seen for emergency shutdown, although two main differences are noticed. First, the maximum rotation is lower than for the emergency shutdown, which appears to be caused by the lower pitching rate associated with the shutdown. Second, the loss of the mooring line appears to give an additional negative rotation. This is as expected, as the mooring lines provide a non-negligible portion of the rotational restoring. Due to the larger radial distance to the mooring line fairleads, the center tower design losses experience a larger loss of rotational restoring than the peripheral tower design. However, it also has a larger initial restoring which makes the situation less critical.

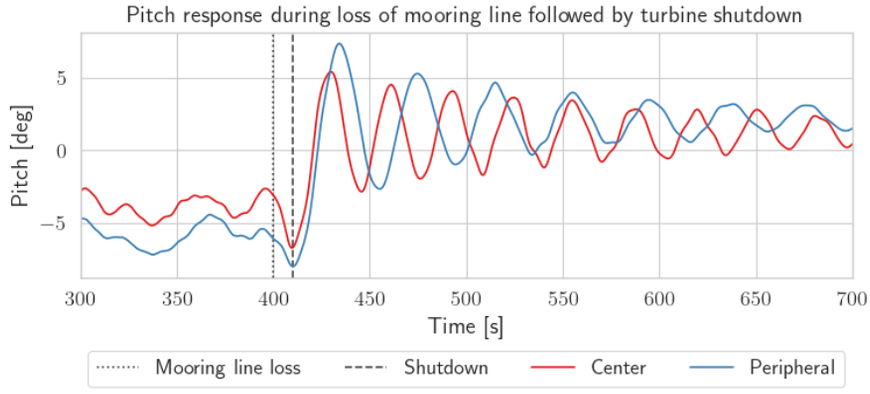

Figure 12.12: Comparison of pitch response following loss of mooring line followed by shutdown

A sudden reduction in the pitch restoring while the rotor thrust remains equal will increase the static pitch angle. It is further seen that this decrease of the negative pitch angle is canceled when the turbine shutdown is initiated, and reversal of thrust occurs. This suggests that the reaction time of the controller from the occurrence of damage to the turbine shutdown is initiated may be an important variable in the simulation of such damage cases. A single variable variation was performed for the case with the largest response, considering an increased controller response time of 60 s. As shown in Figure 12.13, the variation does not appear to lead to a progressive collapse but rather a new quasi-static equilibrium before the shutdown is initiated.

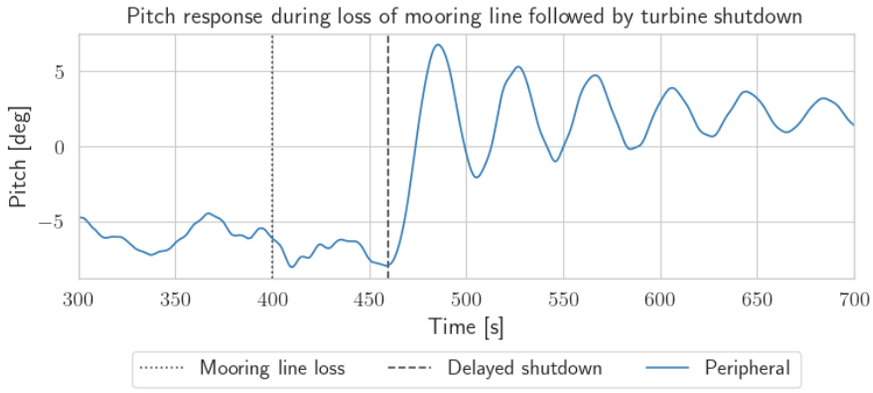

Figure 12.13: Delayed controller response time, DLC 2.6

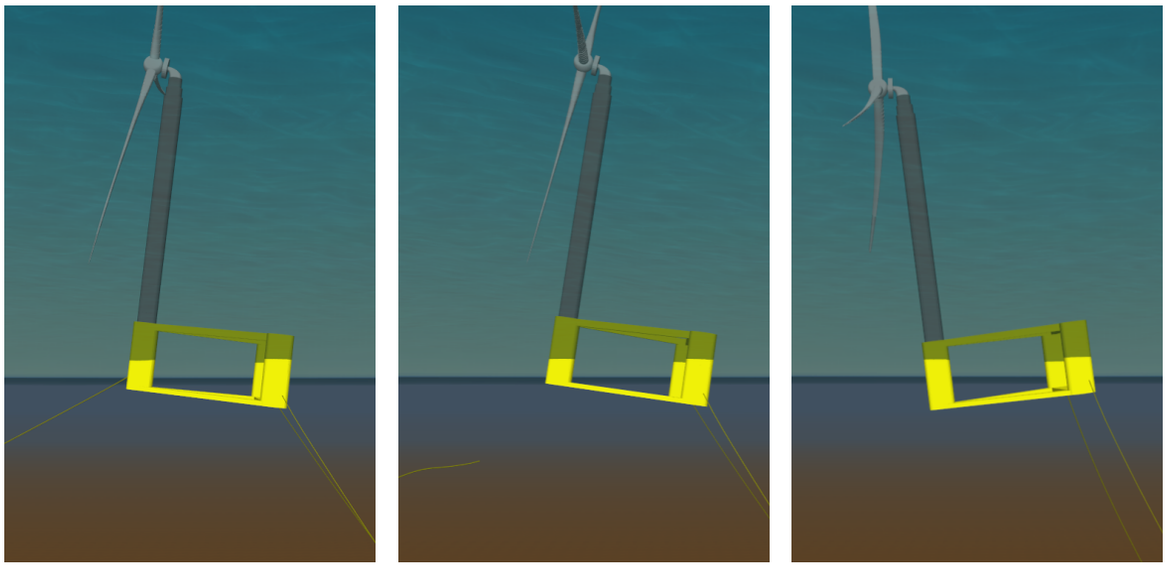

(a) Before damage (T=400.0 s)

(b) Min pitch (T=410.1 s)

(c) Max pitch (T=414.8 s)

Figure 12.14: Transient shutdown after mooring line loss snapshots, peripheral tower design

CHAPTER 13

Discussion

This chapter debates the impact, significance, and validity of the obtained results. Numerous assumptions and simplifications have been made throughout the thesis, which might affect the results to some degree.

13.1 Environmental conditions

Throughout the thesis, the correlation between wind and wave conditions is included and excluded, depending on the nature of the loading conditions. In the cases where disjoint probability models are used, a single mean wind speed with a certain return period is used along with discrete points of H_s and T_p along a contour line with the corresponding return period. This reduces the number of different simulations, as the alternative would be to consider all combinations of mean wind speeds and sea states with the combined return period. The disjoint method is conservative, which is normally desirable in engineering applications. However, it also leads to an overestimation of the probability of failure and prevents cost-effective lean designs.

13.2 Global responses

Allen et al. (2020) present some reference time-domain results for the UMaine VolturnUS-S Semi, which is the concept the center tower design is based on. Before comparing the results, several differences must be mentioned. Firstly, the mass matrix has been modified by introducing a mass model based on calculated steel weight and explicit modeling of ballast water. It is not specified in the reference report whether modifications to the stiffness matrix are made due to internal free surface effects. The report specifies that the pitch restoring stiffness disregarding the mass contribution is $2.19 \cdot 10^9$ Nm/rad. Hand calculations with the same assumptions give a close but not equal pitch restoring stiffness of $2.23 \cdot 10^9$ Nm/rad. The difference is smaller than the difference caused by internal free surfaces in this thesis, but it cannot be concluded without knowing their applied compartmentalization. In addition, they consider a water depth of 200 m with a pure chain catenary mooring system. In their study, only aligned wind and waves are considered, acting along the direction referred to as 180° in this thesis (0° in their study). In their report, six random seeds are simulated for several load cases, including DLC 1.6 and 6.1. Their study uses environmental conditions from Stewart et al. (2016) and Viselli et al. (2015) based on a peak-over-threshold method. In comparing the environmental conditions shown in Table 13.1, the applied environmental conditions are generally in agreement. The 50-year return period wind speed is in a complete agreement between the locations and methods, while more severe sea states are observed. This can either be caused by differences in the applied methods, or oceanographic differences between the North Sea and the Gulf of Maine.

Table 13.1: Comparison of applied environmental conditions

	Allen et al. (2020)			This thesis[a]		
Design load case	$\bar{U}_w{}^{hub}$ [m/s]	H_s [m]	T_p [s]	$\bar{U}_w$ [m/s]	H_s [m]	T_p [s]
DLC 1.6	10	8.10	12.80	10.59	8.65	16.95
DLC 1.6	12	8.50	13.10	12.59	8.92	16.83
DLC 6.1	47.50	10.70	14.20	47.52	14.60	17.48

[a] The sea states represented for this thesis is the sea state with the largest significant wave height along the environmental contour. Sea states better coinciding with the values in Allen et al. (2020) are found along the contour.

In their report, the maximum horizontal offset (surge) value is observed in DLC 6.1, with a value of 24 m. This is the same load case as this thesis documented the largest offset. The value of the maxima cannot be compared, as the mooring system is completely changed. It is further noted that this thesis showed that the maximum horizontal offset does not occur with wind and waves acting along the 180° direction. The maximum vertical rotation found in Allen et al. (2020) was a pitch response of 7.3°, observed in DLC 1.6. This response is larger than the response seen in DLC 1.6 in this thesis, but less than the extreme response seen in DLC 6.1. It must be stated that the extreme rotation observed in this thesis occurs for a combination of environmental conditions not considered in Allen et al. (2020). Lastly, the maximum tower base bending moment found in the reference report is a fore-aft bending moment of 620 MNm, occurring in DLC 1.6. This agrees with the maximum moment found in this thesis for the given DLC. This is, however, not the maximum moment observed in this thesis, which occurs at DLC 6.1 in a loading condition not considered in the reference report. The general agreement between the results provides added confidence in the model, but also displays the need for analysis of multiple directions and sea states.

13.3 Comparison of concepts

Throughout the comparison of the concepts, some important discoveries have been made. During the design of the internal compartments, it was found that the peripheral tower design requires additional internal structures to limit the reduction in metacentric height and to direct sloshing periods away from the maximum wave energy. Among the most compelling arguments for using a peripheral tower design is often the lesser steel weight resulting from one less column. The increased need for internal compartments may offset some of that gain. Another important observation is that the level of ballast filling is less flexible for the peripheral tower design, as the ballast is needed to provide the correct draft and trim. This implies that changes in the ballast filling level cannot be directly compensated by the fixed ballast in the columns. As a result, the sloshing periods in the pontoons cannot be controlled in the same manner as for the center tower design. A solution to this could be different filling levels in different pontoon compartments, although this will introduce an asymmetric loading on the bulkheads.

The most striking difference between the concepts is the inferior stability of the peripheral tower design. In retrospect, the selected design from the upscaling procedure is too lean, and a design with increased stability should be considered for further studies. As seen from the presented Pareto frontier, this would imply a larger steel mass. The identified quasi-static yaw mechanism for wind direction of 180° is possibly the most important finding in the time-domain simulations, which displays a clear disadvantage of a peripheral tower placement. The cause appears to be related to insufficient restoring in all rotational modes, as increasing the metacentric heights and mooring yaw stiffness appear to improve the behavior somewhat. This further illustrates the importance of including the restoring correction due to internal free surfaces, as the behavior is far less critical with the correction omitted.

The pontoon design of the peripheral tower design appears to be beneficial, as its shape provides a large added mass in heave and pitch. This shifts the natural periods of the responses towards longer wave periods, away from periods of significant wave energy. The results also indicate that the peripheral tower design gives smaller horizontal offsets. This is beneficial for the design of power cables, which often is a limiting factor for the design of FOWTs. The reason behind the

smaller offsets is not studied in detail, but it might be explained by a smaller projected drag area caused by one less column and smaller pontoon heights.

For the applied compartmentalization, good resistance against flooding is observed for both concepts. Neither of the concepts is fully redundant, as flooding of the lower part of the radial columns leads to a progressive collapse. By a quasi-static method, it is found that the center tower design might survive a full flooding of the pontoons, while the peripheral tower design will most likely not. The compartmentalization of the pontoons is found to be conservative for the center tower design, whereas the damage case involving pontoon damage results in the largest tower base bending moment for the peripheral tower design. This must, however, be seen in connection with the large RNA overhang caused by the insufficient rotational restoring. It is further shown that the compartmentalization of the pontoons cannot be further reduced without reducing the rotational stability further. The applied compartmentalization in the columns appears conservative, as the flooding of two compartments is not critical compared to other load cases. It is further noted that these compartments are lifted above the free surface in operating conditions. This implies that in the event of a collision, the lower part of the column will be penetrated, which leads to the total loss of the FOWT. Seen in combination with the conservative response during flooding, the size of the compartments could be increased to improve safety. For the center tower design, boat landings are performed on the central column. This represents an added safety against collisions, as this column may be totally flooded without loss of the structure.

13.4 Effect of sloshing

When estimating the effect of linear sloshing using the method applied in WADAM or WAMIT, one should be careful with the obtained results in heave. All the analyzed models gave an added mass term which increased with increasing periods without approaching an asymptotic value as expected. This behavior does not coincide with the behavior expected within linear sloshing theory, where sloshing should not have an effect on heave. In some time-domain simulations, the effect of sloshing is surprisingly larger. The reduction in the vertical rotation was unexpected and should be verified further along with the yaw mechanism causing the large rotations. The frequency-domain results make the effect on horizontal offsets and mooring line tensions more understandable. The effect on the horizontal offset also causes failure of the constraint introduced to limit damage to the power cable, which is not seen for the quasi-static model.

13.5 Evaluation of mooring system

With the simplified design method in mind, the mooring system performed well. Across all load cases, the minimum breaking strength is not exceeded. This may advocate the use of cheaper mooring line materials, reducing the CAPEX of the system. However, some important remarks must be made. First of all, in moments of extreme mooring line tensions, the entire mooring line is lifted from the seabed. This implies that the anchor has to take up forces directly. Depending on the anchor technology used, this may be unacceptable. In addition, for the leeward mooring lines, the polyester segments are in contact with the seabed during extreme horizontal offsets of the platform. This may be allowable in a ULS scenario. Still, it should be noted that synthetic ropes do not have the same resistance against abrasion as chain segments.

In terms of mooring line redundancy, the results are not straightforward. The loss of a single mooring line will most certainly result in damage to the power cable, which might be a critical failure for the turbine. However, only looking at the remaining mooring lines, the maximum tensions appear to be lower compared to other cases. It is however noted that the structural implications of the mooring line twisting observed for the peripheral tower design are unknown.

13.6 Limitations

Several response variables for both concepts are critical in the steepest sea states. This is not aligned with the hypothesis on which the selection of the sea states along the environmental contour was based. More sea states should therefore be investigated along the low-period side of the environmental contours. As the critical responses also have been observed in the longest sea states, this implies that more sea states should be considered in total.

The time-domain simulations also show a clear dependency on the wind and wave direction, suggesting that the full circle of direction should be considered. It is believed that the considered orientation of the peripheral tower design is the most critical due to the observed yaw mechanism. It should, however, be more thoroughly documented. For the center tower design, the considered directions should be sufficient due to the axisymmetric position of the tower. A full range of wind and wave misalignment could still be critical.

For the results involving the dynamic effects of internal fluids, the method itself is a major limitation. As sloshing is a highly non-linear phenomenon, it cannot be fully described by a linear potential theory approach. For such a problem, there is no way around using CFD or experimental methods. This would also capture other important effects, such as piston-mode resonances and air entrapment effects.

The use of steady flow drag coefficients is also a limitation in the thesis. In reality, the KC dependency of the coefficient must be taken into account. To assess the implication, the KC number is estimated for the simulation, which gave the largest horizontal offset for the center tower design. Time series of the relative velocity between the incident wave kinematics and body motions were extracted. Three separate time series were considered horizontally across the middle of the submerged columns and horizontally and vertically across the middle of the pontoons. The maximum velocity was extracted, and the discrete Fourier transform was used to find the most protruding periods of the signals. Through this approach, KC numbers of 1.98, 1.13, and 0.86 were found for the horizontal velocity across the column and the horizontal and vertical velocity across the pontoons, respectively. Given in the same order, the wake amplification factors are found as 0.45, 0.57, 0.62. This could significantly affect the results, both in terms of experienced current loads, wave loads, and damping.

CHAPTER 14

Conclusions

The objective of the thesis was to compare the response of two semi-submersible FOWT concepts. The comparison should be related to survivability for both intact and damaged conditions, and the effect of internal fluid effects should also be investigated.

The frequency domain calculations show the importance of considering the effect of internal fluid effects in the design of FOWTs. The quasi-static reduction of metacentric height due to internal free surfaces is a simple and straightforward approach to the topic. Still, it is shown to be an extremely important correction to obtain accurate responses in extreme environmental conditions. Dynamic fluid effects from linear sloshing are documented in all cases comprising partially filled compartments, and it is shown to occur over periods of large wave spectral density. The frequency-domain calculations also show that the internal fluid effects may be of importance to the second-order wave excitation forces.

The time-domain simulations provide added value to the understanding of the concept's behaviors, as the thesis considers several directions, wind-wave misalignment, and load cases not considered in the previous studies. The results are shown to agree well with the available reference results, but more extreme responses are found outside the environmental conditions considered in previous studies. Steep sea states are found to be critical for selected response variables, which proves the need for an environmental contour approach.

It must be concluded that the rotational responses seen across several load cases are undesirable. The obtained responses shed light on an important effect of the tower placement, where quasi-static instability is experienced in headings with the tower facing the wind direction. This effect causes large rotational responses in both intact and damaged conditions, which increases the possibility of capsizing. It also causes a yaw displacement of 180° in the damage cases considering mooring line failures, leading to tangling of the remaining mooring lines.

The effect of the included sloshing excitation in the time domain is larger than anticipated, which displays the need for further studies. The reduction seen in the maximum pitch and roll responses was unexpected and found to be caused by changes in loading conditions provided by yaw responses. The inclusion of sloshing also causes an increase in horizontal offsets and mooring line tensions, which is critical design variables.

With regard to the methodology, it may be concluded that the quasi-static effect of internal fluid effect on a FOWT may be well described by simple hand calculations. This also holds for the location of resonant sloshing frequencies when the compartments are idealized as simple, regular geometries. It is further concluded that OrcaFlex is overall a suitable tool for analyzing the effect of internal fluid effect in the time domain in a simplified manner, mainly due to the ability to include custom external functions. However, it is noted that a substantial amount of programming is needed, both for the transfer of frequency-domain coefficients and for the external functions themselves. The upside is that there is little limit to what one can include with these functions, which allows for the analysis of challenging situations in the time domain.

CHAPTER 15

Further work

Although the extent of this thesis is large, it is merely the start of a full design study of the selected concepts. For such a study, all load cases prescribed by DNV should be considered with environmental actions from every direction, with full misalignment between wind and waves and with an increased number of random seeds. For the obtained load effects, a full limit state analysis should be performed to ensure structural resistance against the expected extreme loads. Such a limit state analysis must consider fatigue, as it may very well be design-driving for a FOWT.

However, before a more detailed limit state analysis is performed, several parts of the design must be altered, particularly for the peripheral tower design. As concluded, restoring stiffness for the selected concept is insufficient in the rotational degrees of freedom. An increase in rotational stiffness implies changes to both static and dynamic responses, which implies that a full dynamic simulation should be redone.

The steady-state load cases show that steep sea states with wind and wave misalignment may be critical for both concepts. This should be further investigated by considering full misalignment wind and wave misalignment, two-peaked swell and wind sea spectra, and short-crested waves.

With regard to the flooding and internal fluid effects, the accurate prediction of response and load amplitudes is limited by the bounds of potential theory. The studies performed in this thesis show that the effect may be of great importance in accurately determining the response of a FOWT. Therefore, CFD should be used to obtain better estimates of the amplitudes of the sloshing-induced forces. A more accurate method would be coupling a global time-domain simulation with a local CFD solver for the internal tank domains.

For the transient load cases involving a shutdown of the turbine, the effect of the shutdown strategy itself should be investigated further. Dependent on the selected strategy, this may both amplify and mitigate the transient effect of the damage. For cases considering flooding, the analysis should be further extended to also model the cause of the flooding. For instance, if the hull is punctured as a result of a ship collision, significant kinetic energy must be accounted for.

Bibliography

Aarsnes, Lars Holterud (2015). 'Estimation of Extreme Response'. PhD thesis. NTNU.

Abbas, Nikhar J., Daniel S. Zalkind, Rafael M. Mudafort et al. (2023). *NREL/ROSCO: Version 2.8.0*.

Abbas, Nikhar J., Daniel S. Zalkind, Lucy Pao et al. (2022). *A Reference Open-Source Controller for Fixed and Floating Offshore Wind Turbines*.

Abdelmoteleb, Serag-Eldin et al. (2022). *Preliminary Sizing and Optimization of Semisubmersible Substructures for Future Generation Offshore Wind Turbines*.

Acteon (2021). *Maximising power cable reliability for offshore wind*. https://acteon.com/blog/maximising-power-cable-reliability-for-offshore-wind/.

Aker Solutions (2021). *Hywind Tampen – Floating Offshore Wind*. https://www.akersolutions.com/what-we-do/projects/hywind-tampen/.

Allen, Christopher et al. (2020). *Definition of the UMaine VolturnUS-S Reference Platform Developed for the IEA Wind 15-Megawatt Offshore Reference Wind Turbine*.

Anaya-Lara, Olimpo et al. (2018). *Offshore Wind Energy Technology*. Wiley.

Bachynski-Polić, Erin (2022). *Integrated dynamic analysis of wind turbines (module within TMR4505)*. Lecture Notes.

Bachynski-Polić, Erin E. and Lene Eliassen (2019). 'The effects of coherent structures on the global response of floating offshore wind turbines'. In: *Wind Energy* 22.2, pp. 219–238.

Brittanica, Encyclopedia (n.d.). *Ferrel cell*. https://www.britannica.com/science/Ferrel-cell.

Brown, David T. (2005). 'Chapter 8 - Mooring Systems'. In: *Handbook of Offshore Engineering*. Ed. by Subrata K. Chakrabarti. London: Elsevier, pp. 663–708.

Burton, Tony et al. (2001). *Wind Energy Handbook*. Wiley.

Cheng, Zhengshun et al. (2019). 'Long-term joint distribution of environmental conditions in a Norwegian fjord for design of floating bridges'. In: *Ocean Engineering* 191, p. 106472.

Choi, Junhwan et al. (Oct. 2019). 'Improved environmental contour methods based on an optimization of hybrid models'. In: *Applied Ocean Research* 91, p. 101901.

Christakos, Konstantinos (2022). *MET_waves*. https://github.com/KonstantinChri/MET_waves.

Chung, J. and G. M. Hulbert (1993). 'A Time Integration Algorithm for Structural Dynamics With Improved Numerical Dissipation: The Generalized-αMethod'. In: *Journal of Applied Mechanics*.

ClassNK (2019). *Guidelines for Floating Offshore Wind Turbines - Classification Survey*. Standard.

Collett News (2016). *UK's Largest Blades for Muirhall Wind Farm*. https://www.collett.co.uk/index.php/our-story/news/80-muirhall-wind-farm.

Cradden, Lucy, Gareth Harrison and John Chick (2012). *Will climate change impact on wind power development in the UK?*

Cruz, Joao and Mairead Atcheson (2016). *Floating Offshore Wind Energy - The Next Generation of Wind Energy*. Springer.

Cummins, W.E. (1962). *The impulse response function and ship motions*.

DNV (2014). *SESAM GeniE*. Brochure.

— (2018). *DNV-ST-0437 Loads and site conditions for wind turbines*.

— (2019a). *DNV-RP-0286 Coupled analysis of floating wind turbines*.

— (2019b). *DNV-RP-C205 Environmental conditions and environmental loads*.

— (2021a). *DNV-OS-E301 Position mooring*.

— (2021b). *DNV-ST-0119 Floating wind turbine structures*.

— (2021c). *DNV-ST-0119 Floating wind turbine structures*. Standard.

ECMWF (2020). *Fact sheet: Reanalysis*. URL: https://www.ecmwf.int/sites/default/files/medialibrary/2020-06/ecmwf-fact-sheet-reanalysis.pdf.

EIA (2022). *History of wind power - U.S. Energy Information Administration (EIA)*. https://www.eia.gov/energyexplained/wind/history-of-wind-power.php.

Engebretsen, Espen, Zhiyuan Pan and Nuno Fonseca (2020). *Second-Order Difference-Frequency Loads on FPSOs by Full QTF and Relevant Approximations*.

Equinor (2022). *Equinor og partnere utreder 1 GW havvindpark utenfor Bergen - Equinor*. https://www.equinor.com/no/nyheter/20220617-utreder-1gw-havvindpark-utenfor-bergen.

ETIP-WIND, WindEurope (2021). *Getting fit for 55 and set for 2050*. URL: https://etipwind.eu/publications/getting-fit-for-55/.

Faltinsen, Odd Magnus (1990). *Sealoads on Ships and Offshore Structures*. Cambridge University Press.

Faltinsen, Odd Magnus and A. N. Timokha (2009). *Sloshing*. Cambridge University Press.

Ferziger, Joel H. and Milovan Perić (2012). *Computational Methods for Fluid Dynamics*. 3rd. Berlin: Springer.

Gaertner, Evan et al. (2020). *IEA Wind TCP Task 37: Definition of the IEA 15-Megawatt Offshore Reference Wind Turbine*.

Gao, Zhen (n.d.). *Time-domain equations of motions*. Lecture note TMR4505.

Greco, Marilena (2022). *TMR4215: Sea Loads*. Lecture Notes.

Haakenstad, Hilde, Øyvind Breivik, Birgitte R. Furevik et al. (1st Oct. 2021). 'NORA3: A Non-hydrostatic High-Resolution Hindcast of the North Sea, the Norwegian Sea, and the Barents Sea'. In: *Journal of Applied Meteorology and Climatology* 60.10, pp. 1443–1464.

Haakenstad, Hilde, Øyvind Breivik, Magnar Reistad et al. (2020). 'NORA10EI: A revised regional atmosphere-wave hindcast for the North Sea, the Norwegian Sea and the Barents Sea'. In: *International Journal of Climatology* 40.10, pp. 4347–4373.

Hansen, M.O.L. (2015). *Aerodynamics of Wind Turbines*. Taylor & Francis.

Hauteclocque, Guillaume de et al. (1st July 2012). 'Review of Approximations to Evaluate Second-Order Low-Frequency Load'. In: Proceedings of the International Conference on Offshore Mechanics and Arctic Engineering - OMAE.

Haver, S. (1980). *Analysis of Uncertainties Related to the Stochastic Modelling of Ocean Waves*.

— (2019). *Metocean modelling and prediction of extremes*. UiS, NTNU.

IEA (2022). *IEAWindTask37/IEA-15-240-RWT*. https://github.com/IEAWindTask37/IEA-15-240-RWT.

IEC (2019a). *IEC 61400-1: Wind energy generation systems. Part 1: Design requirements*.

— (2019b). *IEC61400-3-2: Design requirements for floating offshore wind turbines*.

Isermann, R. and P. Ballé (1997). *Trends in the application of model-based fault detection and diagnosis of technical processes*.

Jiang, Zhiyu, Torgeir Moan and Zhen Gao (1st Feb. 2015). 'A Comparative Study of Shutdown Procedures on the Dynamic Responses of Wind Turbines'. In: *Journal of Offshore Mechanics and Arctic Engineering* 137.11904.

Jin, Jingzhe et al. (25th June 2017). 'Internal Fluid Effect Inside a Floating Structure: From Frequency Domain Solution to Time Domain Solution'. In: *Volume 7B: Ocean Engineering*. ASME 2017 36th International Conference on Ocean, Offshore and Arctic Engineering. Trondheim, Norway: American Society of Mechanical Engineers.

Johannessen, Kenneth, Trond Stokka Meling and Sverre Hayer (17th June 2001). 'Joint Distribution For Wind And Waves In the Northern North Sea'. In: The Eleventh International Offshore and Polar Engineering Conference. OnePetro.

Jonkman, B. (2014). *TurbSim User's Guide v2.00.00*.

Jonkman, J. and M. L. Buhl (2007). 'Loads Analysis of a Floating Offshore Wind Turbine Using Fully Coupled Simulation: Preprint'. In: WindPower 2007 Conference & Exhibition. NREL.

Kikuchi, Yuka and Takeshi Ishihara (Oct. 2019). 'Upscaling and levelized cost of energy for offshore wind turbines supported by semi-submersible floating platforms'. In: *Journal of Physics: Conference Series* 1356.1. Publisher: IOP Publishing, p. 012033.

Klingan, Kristine Ekeli (2016). 'Automated Optimization and Design of Mooring Systems for Deep Water'. Master thesis. NTNU.

Kong, Xiangjun (2009). 'A Numerical Study of a Damaged Ship in Beam Sea Waves'. Doctoral thesis. Norges teknisk-naturvitenskapelige universitet, Fakultet for ingeniørvitenskap og teknologi, Institutt for marin teknikk.

Kong, Xiangjun and Odd Magnus Faltinsen (2008). 'Coupling between Ship Motions and Flooding of a Damaged Ship in Waves'. In: 8th International Conference on HydroDynamics (ICHD'08).

— (2010). 'Piston Mode and Sloshing Resonances in a Damaged Ship'. In: ASME 2010 29th International Conference on Ocean, Offshore and Arctic Engineering.

Landbø, Trond (2018). *OO-STAR WIND FLOATER THE FUTURE OF OFFSHORE WIND?* https://www.sintef.no/globalassets/project/eera-deepwind-2018/presentations/closing_landbo.pdf.

Larsen, Carl M. et al. (2009). *Marin Dynamics*. Compendium.

Larsen, Kjell (2021). *Marine Operations of Installing a Floating Wind Turbine Park (Equinor's Hywind Tampen)*. Lecture Notes (TMR4225).

Leimester, Mareike et al. (2016). *Rational upscaling of a semi-submersible floating platform supporting a wind turbine*.

Li, Lin, Zhen Gao and Torgeir Moan (2013). 'Joint Environmental Data at Five European Offshore Sites for Design of Combined Wind and Wave Energy Devices'. In: Journal of Offshore Mechanics and Arctic Engineering.

Lifes50+ (2016). *Next generation floating wind technologies*. https://lifes50plus.eu/next-generation-floating-wind-technologies/.

Luan, Chenyu, Zhen Gao and Torgeir Moan (June 2016). 'Design and Analysis of a Braceless Steel 5-MW Semi-Submersible Wind Turbine'. In: vol. Volume 6: Ocean Space Utilization; Ocean Renewable Energy. International Conference on Offshore Mechanics and Arctic Engineering.

Ludvigsen, Arild and Zhi Yuan Pan (2015). 'Extensions and Improvements to the Solutions for Linear Tank Dynamics'. In: *Volume 1: Offshore Technology; Offshore Geotechnics*. ASME 2015 34th International Conference on Ocean, Offshore and Arctic Engineering. St. John's, Newfoundland, Canada: American Society of Mechanical Engineers.

Ludvigsen, Arild, Zhi Yuan Pan et al. (2013). 'Adapting a Linear Potential Theory Solver for the Outer Hull to Account for Fluid Dynamics in Tanks'. In: *Volume 9: Odd M. Faltinsen Honoring Symposium on Marine Hydrodynamics*. ASME 2013 32nd International Conference on Ocean, Offshore and Arctic Engineering. Nantes, France: American Society of Mechanical Engineers.

Moan, Torgeir (1994). *Design of Marine Structures*. Lecture Notes TMR4195.

— (2009). 'Development of accidental collapse limit state criteria for offshore structures'. In: *Structural Safety*.

Moan, Torgeir, Zhen Gao and Efren Ayala-Uraga (2005). 'Uncertainty of wave-induced response of marine structures due to long-term variation of extratropical wave conditions'. In: *Marine Structures*.

Moriarty, P.J. and A.C. Hansen (2005). *AeroDyn Theory Manual*. Tech. rep. National Renewable Energy Laboratory (NREL).

Myrhaug, Dag (2006). *TMR4230 - Oceanography: Wind & Waves*. NTNU.

Næss, Arvid and Torgeir Moan (2012). *Stochastic Dynamics of Marine Structures*. Cambridge University Press.

National Park Service (2019). *A History of Dempster Windmills (U.S. National Park Service)*. https://www.nps.gov/articles/history-of-dempster-windmills.htm.

Nejad, Amir R. and Jone Torsvik (2021). *Drivetrains on floating offshore wind turbines: lessons learned over the last 10 years*.

Newman, J. N. (2005). 'Wave effects on vessels with internal tanks'. In: 20th Workshop on Water Waves and Floating Bodies. Spitsbergen.

— (2017). *Marine Hydrodynamics (40th anniversary edition)*. Massachusetts Institute of Technology.

Ning, S. A. et al. (2015). *Development and Validation of a New Blade Element Momentum Skewed-Wake Model within AeroDyn*. Tech. rep. National Renewable Energy Laboratory (NREL).

NORSOK (2017a). *N-003 Actions and action effects*.

— (2017b). *N-003:2017 Action and action effects*.

— (2021). *N-001:2020+A1+AC Integrity of offshore structures*.

— (2022). *N-004:2022 Design of offshore structures*.

Norwegian Ministry of Petroleum and Energy (2021). *Electricity production - Energy facts Norway*. https://energifaktanorge.no/en/norsk-energiforsyning/kraftproduksjon/.

Offshore Wind Innovation Hub (2020). *Floating wind: Cost modelling of major repair strategies*.

Orcina (2023a). *OrcaFlex - User Manual*.

— (2023b). *OrcaWave - User Manual*.

Recharge News (2022). *Rescue dash as rudderless cargo ship hits foundation at giant North Sea wind farm*. https://www.rechargenews.com/wind/video-rescue-dash-as-rudderless-cargo-ship-hits-foundation-at-giant-north-sea-wind-farm/2-1-1160591.

— (2023). *Cargo ship hits turbine at North Sea wind farm*. https://www.rechargenews.com/wind/cargo-ship-hits-turbine-at-north-sea-wind-farm-orsted-investigates/2-1-1442789.

Rhinoceros (2023). *Rhino - Features*. https://www.rhino3d.com/features/mesh-tools.

Robertson, A., J. Jonkman, M. Masciola et al. (2014). *Definition of the Semisubmersible Floating System for Phase II of OC4*.

— (2015). *Definition of the Semisubmersible Floating System for Phase II of OC4*. Tech. rep. National Renewable Energy Laboratory (NREL).

Robertson, A., J. Jonkman, F Vorpahl et al. (2014). 'Offshore Code Comparison Collaboration Continuation Within IEA Wind Task 30: Phase II Results Regarding a Floating Semisubmersible Wind System'. In: ASME 2014 33rd International Conference on Ocean, Offshore and Arctic Engineering.

Roddier, Dominique et al. (2010). 'WindFloat: A floating foundation for offshore wind turbines'. In: *Journal of Renewable and Sustainable Energy*.

Rognebakke, Olav F. and Odd Magnus Faltinsen (2003). 'Coupling of Sloshing and Ship Motions'. In: *Journal of Ship Research*.

Rypestøl, Martin (2020). *Analysis of Floating Offshore Wind Turbine Subjected to Ship Collisions*.

Sarlak, Hamid and Jens N. Sørensen (2016). 'Analysis of throw distances of detached objects from horizontal-axis wind turbines'. In: *Wind Energy*.

Sartori, Luca et al. (2020). 'A Research Framework for the Multidisciplinary Design and Optimization of Wind Turbines'. In: *Design Optimization of Wind Energy Conversion Systems with Applications*.

Sathe, A. et al. (2013). 'Influence of atmospheric stability on wind turbine loads'. In: *Wind Energy*.

Schlipf, D et al. (2010). *Testing of Frozen Turbulence Hypothesis for Wind Turbine Applications with a Scanning LIDAR System*.

Siddiqui, Mohd Atif (2020). 'Experimental and Numerical Hydrodynamic Analysis of a Damaged Ship Section In Waves'. PhD thesis. NTNU.

Silva de Souza, Carlos Eduardo (2021). *Definition of the INO WINDMOOR 12 MW base case floating wind turbine*.

Importance of Control Strategies on Fatigue Life of Floating Wind Turbines (2007). Vol. Volume 5: Ocean Space Utilization; Polar and Arctic Sciences and Technology; The Robert Dean Symposium on Coastal and Ocean Engineering; Special Symposium on Offshore Renewable Energy. International Conference on Offshore Mechanics and Arctic Engineering.

Stewart, Gordon M. et al. (2016). 'The creation of a comprehensive metocean data set for offshore wind turbine simulations'. In: *Wind Energy*.

Taghipour, Reza, Tristan Perez and Torgeir Moan (2008). 'Hybrid frequency–time domain models for dynamic response analysis of marine structures'. In: *Ocean Engineering*.

Therin-Weise, M & G (n.d.). *Mill Network at Kinderdijk-Elshout - Gallery - UNESCO World Heritage Centre*. https://whc.unesco.org/en/list/818/gallery/.

Twidell, Jown and Gaetano Gaudiosi (2009). *Offshore Wind Power*. Multi-Science Publishing.

U.S. Department of Energy (2010). *Wind Power Today*.

Viselli, Anthony M. et al. (2015). 'Estimation of extreme wave and wind design parameters for offshore wind turbines in the Gulf of Maine using a POT method'. In: *Ocean Engineering*.

WAMIT, Inc. (2013). *WAMIT User Manual - Version 7.0*. URL: https://www.wamit.com/manualupdate/history/V70_manual_old.pdf.

Wilkinson, Michael (2011). *Measuring Wind Turbine Reliability-Results of the Reliawind Project*.

Wind Europe (2022a). *The energy transition goes together with nature protection — WindEurope*. https://windeurope.org/newsroom/news/the-energy-transition-goes-together-with-nature-protection/.

— (2022b). *Wind energy in Europe - 2021 Statistics and the outlook for 2022-2026*.

Yu, Zhaolong et al. (2022). *Numerical modelling and dynamic response analysis of a 10 MW semi-submersible floating offshore wind turbine subjected to ship collision loads*.

Appendix

APPENDIX A

Environmental modeling

In this appendix, results from the environmental modeling is presented.

A.1 Distribution fitting

A Marginal distribution of mean wind speed

Figure A.1 shows the fitted two-parameter Weibull model against the sample hindcast wind data. As seen from the results, the model appears to describe the sample very well.

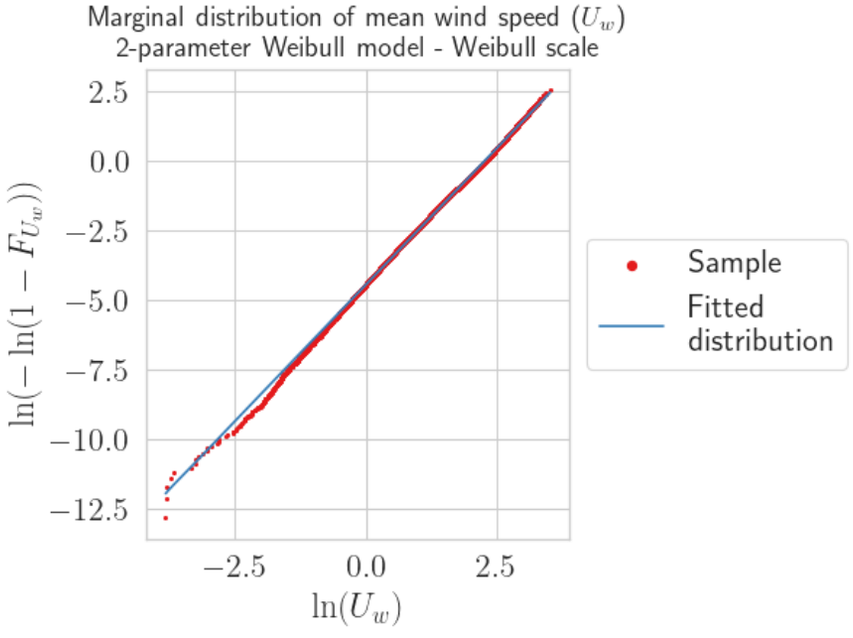

Figure A.1: Marginal distribution of mean wind speed, Weibull scale

B Joint distribution of significant wave height and spectral peak period

Marginal distribution of significant wave height

Figure A.2 shows the fitted Lonowe model for the marginal distribution of the significant wave height. As seen from the results, the fitted model represents the sample well. Compared to the fitted Weibull model, the Lonowe is superior.

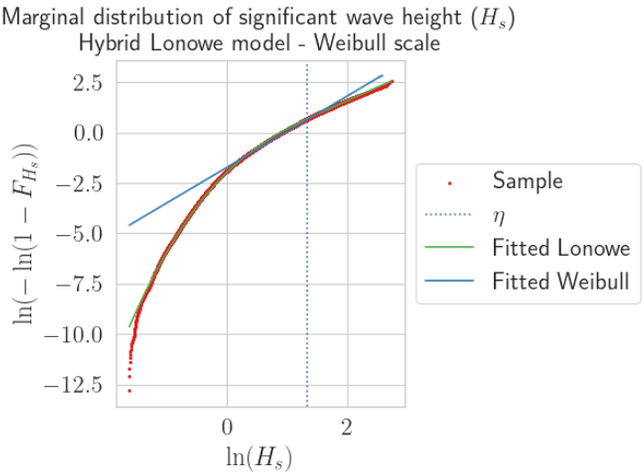

Figure A.2: Marginal distribution of significant wave height, Weibull scale

Conditional distribution of spectral peak period on significant wave height

In Figure A.3, the conditional model for the spectral peak period is plotted against the sample data for two selected wave height bins. Generally, the sample appears to be well described by the model.

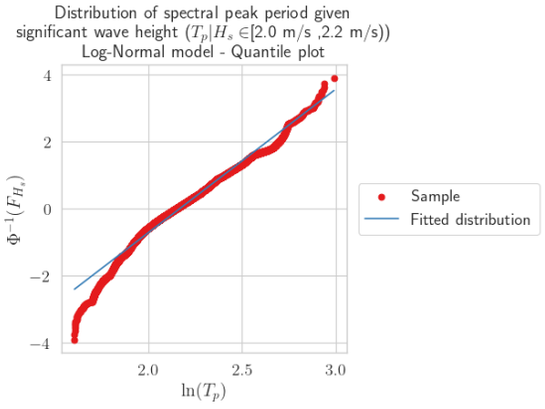

(a) $F_{T_p|H_s}(t|h)$ for $H_s \in [2.0, 2.2)$m

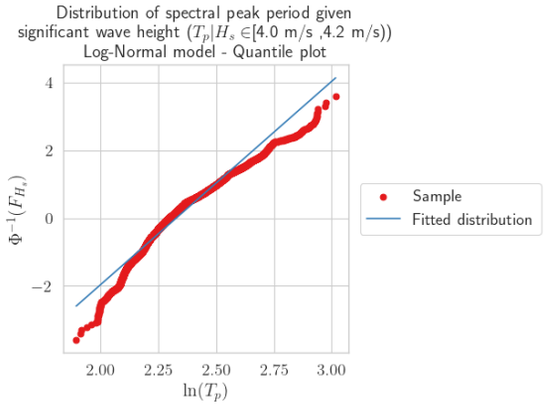

(b) $F_{T_p|H_s}(t|h)$ for $H_s \in [4.0, 4.2)$m

Figure A.3: Log-Normal model fitted inside two separate significant wave height bins, standard normal quantile plot

The curve fittings of the distribution parameters as a function of the significant wave height are shown in Figure A.4. As seen from the result, the fitted curves describe the underlying trend in a good manner.

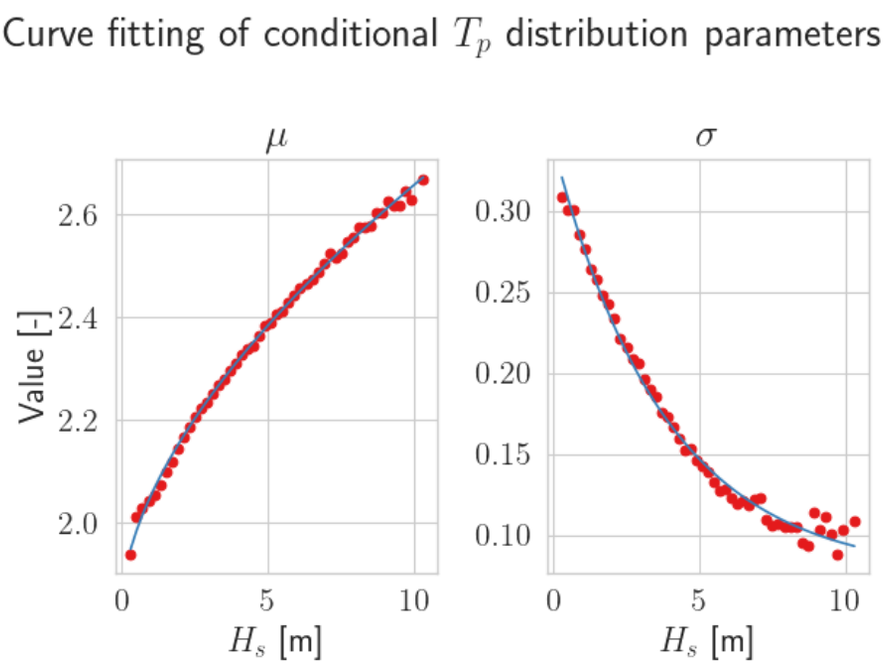

Figure A.4: Curve fitting of Log-normal parameters

C Joint distribution of mean wind speed, significant wave height and spectral peak period

Conditional distribution of significant wave height given mean wind speed

The results plotted in Figure A.5, show the fitted parameters of the Lonowe model applied in the joint distribution of mean wind speed, significant wave height, and spectral peak period. Generally, for all three variables, the variations are well described by the fitted curves.

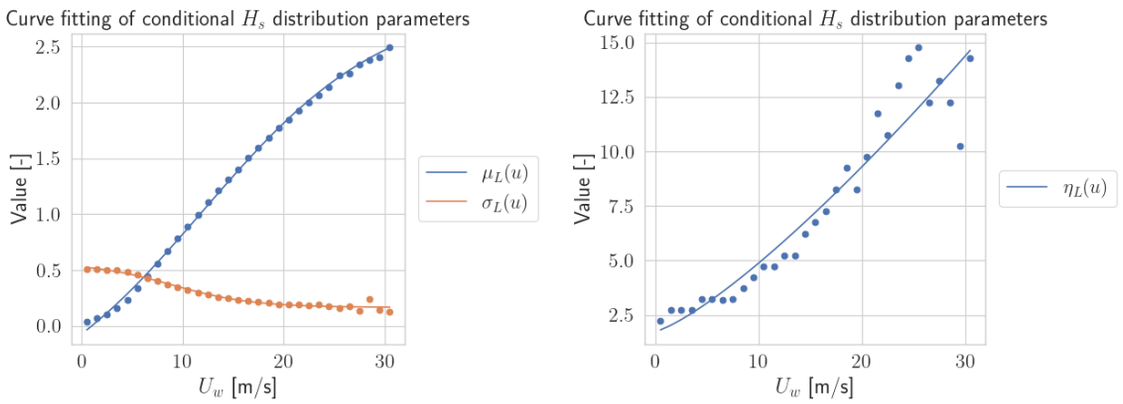

(a) $\mu(u)$ & $\sigma(u)$ (b) $\eta(u)$

Figure A.5: Curve fitting of parameters, conditional distribution of H_s given $\bar{U}_w$

In the same manner as before, the Lonowe model is compared with the sample data alongside a Weibull model. For this case as well, the Lonowe model outperforms the Weibull model. Note that these plots are plotted on a quantile scale.

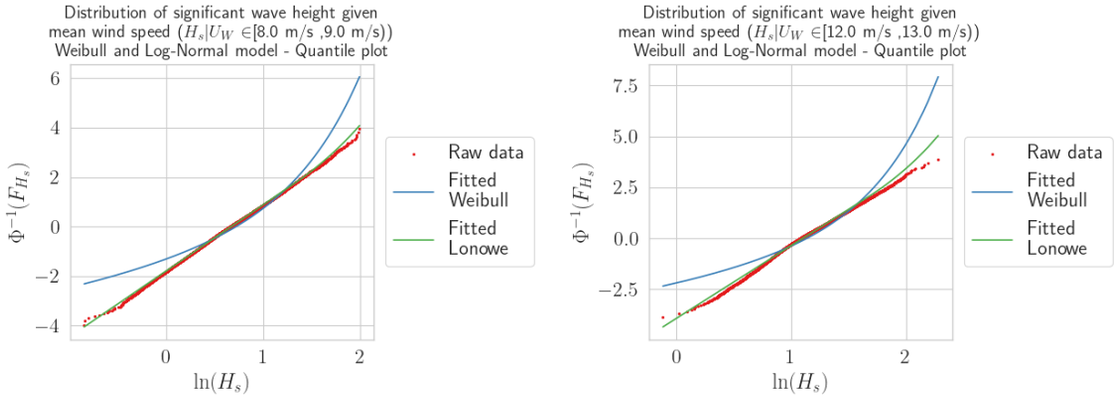

(a) $F_{H_s|U_w}(h|u)$ for $U_w \in [8.0, 9.0)$m/s

(b) $F_{H_s|U_w}(h|u)$ for $U_w \in [12.0, 13.0)$m/s

Figure A.6: LoNoWe and Weibull model fitted inside two separate mean wind speed bins, quantile plot

Conditional distribution of spectral peak period given mean wind speed and significant wave height

In Figure A.7 and Figure A.8, the distribution parameters of the log-normal model that describe the spectral peak period conditional on the mean wind speed and significant wave height are presented.

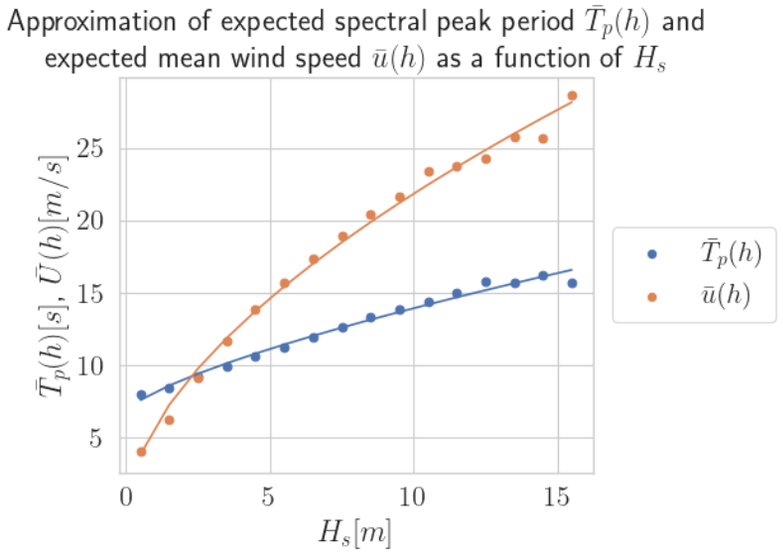

Figure A.7: Curve fitting of expected T_p and expected $\bar{U}_w$ as a function of H_s

In Figure A.8a, the approximation of θ as a function of the significant wave height is shown. The mean approximation applied in Johannessen et al. (2001) is also shown.

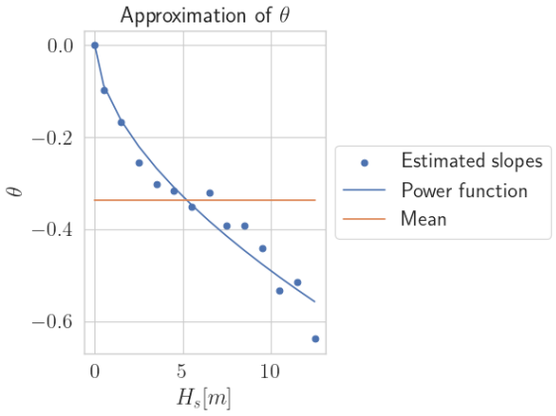

(a) Approximation of θ as power function of H_s versus mean

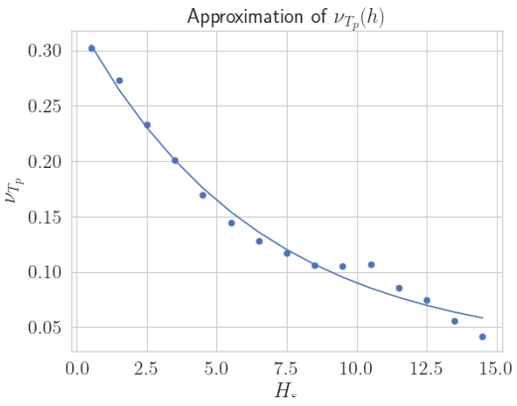

(b) Curve fitting of coefficient of variance as a function of H_s

Figure A.8: Curve fitting of conditional T_p parameters

The difference in error committed when predicting the expected spectral peak period based on a set of $\bar{U}_w$ and H_s using either the power function or the mean to describe θ is shown in Figure A.9. It is noted that the power function delivers a reduced error.

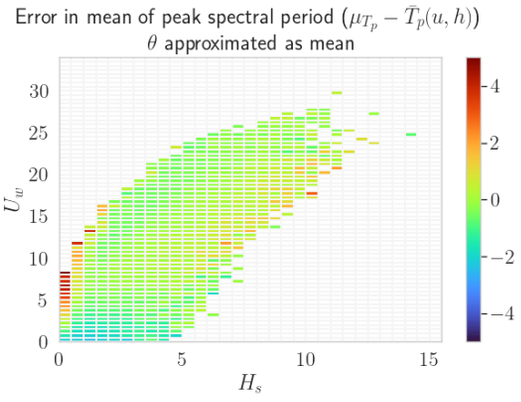

(a) θ as constant approximated as mean

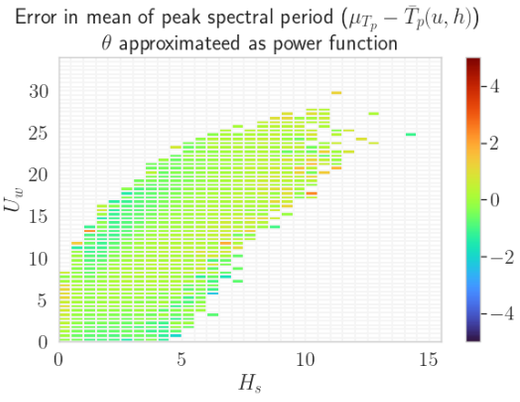

(b) θ as fitted power function

Figure A.9: Error of mean T_p based on choice of approximation for θ

APPENDIX B

Environmental contours

In this section, the different environmental contours are presented. The severe sea state contour is produced with the joint distribution of mean wind speed, significant wave height, and spectral peak period, while the extreme sea states are from the joint distribution of only significant wave height and spectral peak period.

B.1 Severe sea states

Table B.1: Severe sea state 1

#	H_s [m]	T_p [s]	γ [-]
1A	5.34	7.95	5.00
1B	7.33	12.42	5.00
1C	8.25	16.9	1.61
1D	7.33	20.24	1.00
1E	5.34	25.78	1.00
1F	1.71	28.08	1.00

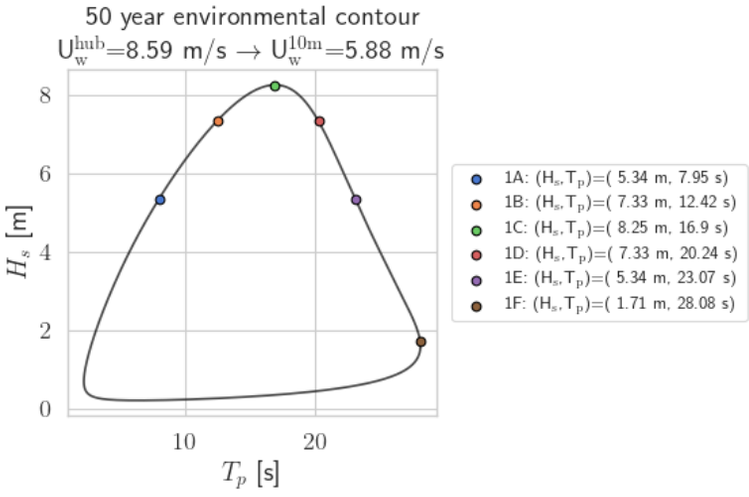

Figure B.1: Contour line severe sea state 1

Table B.2: Severe sea state 2

#	H_s	T_p	γ [-]
2A	5.68	8.14	5.00
2B	7.72	12.59	1.71
2C	8.65	16.95	1.00
2D	7.72	20.10	1.00
2E	6.68	22.70	1.00
2F	1.80	27.47	1.00

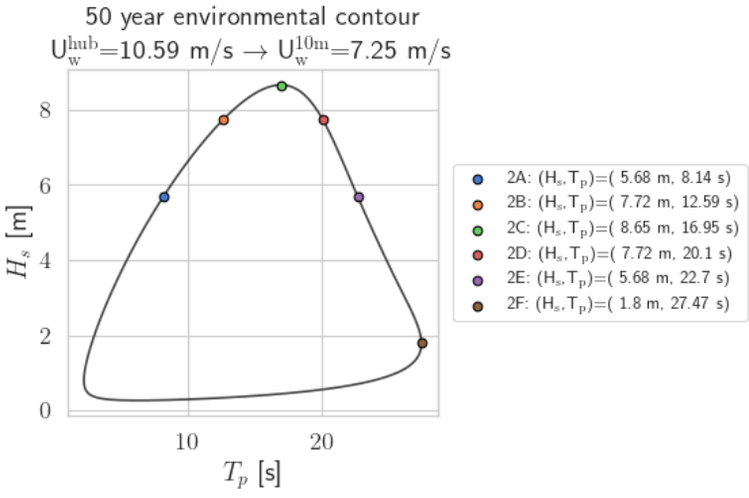

Figure B.2: Contour line severe sea state 2

Table B.3: Severe sea state 3

#	H_s	T_p	γ
3A	5.98	8.29	5.00
3B	8.00	12.63	1.85
3C	8.92	16.83	1.00
3D	8.00	19.85	1.00
3E	5.98	22.25	1.00
3F	2.01	26.67	1.00

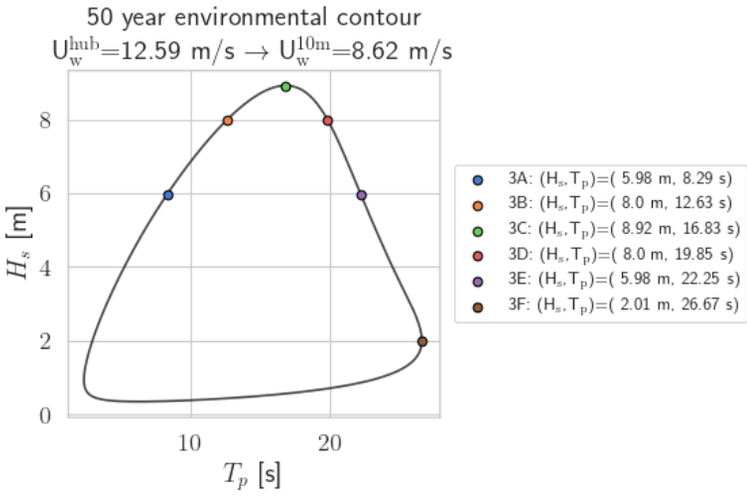

Figure B.3: Contour line severe sea state 3

Table B.4: Severe sea state 4

#	H_s	T_p	γ
4A	8.58	9.99	5.00
4B	10.23	13.23	2.70
4C	10.92	16.25	1.10
4D	10.23	18.34	1.00
4E	7.28	20.05	1.00
4F	5.03	20.73	1.00

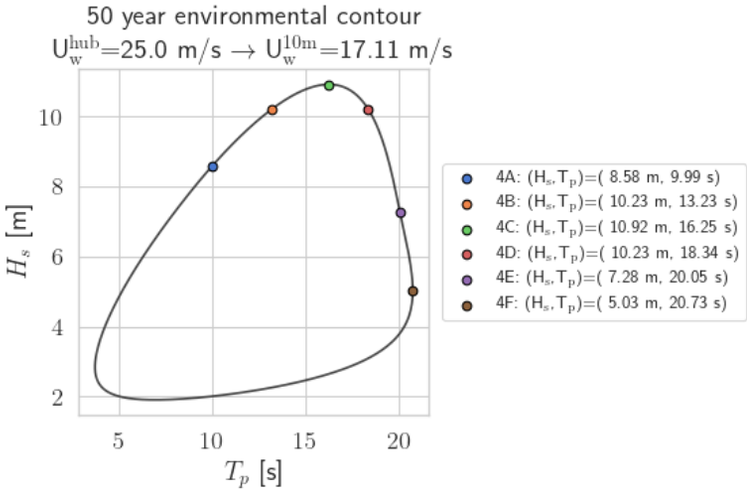

Figure B.4: Contour line severe sea state 4

B.2 Extreme sea states

Table B.5: 1-year extreme sea state

#	H_s	T_p	γ
1yA	7.52	9.13	5.00
1yB	10.36	12.42	3.72
1yC	11.70	15.43	1.75
1yD	10.36	16.93	1.00
1yE	5.55	17.76	1.00
1yF	2.68	20.04	1.00

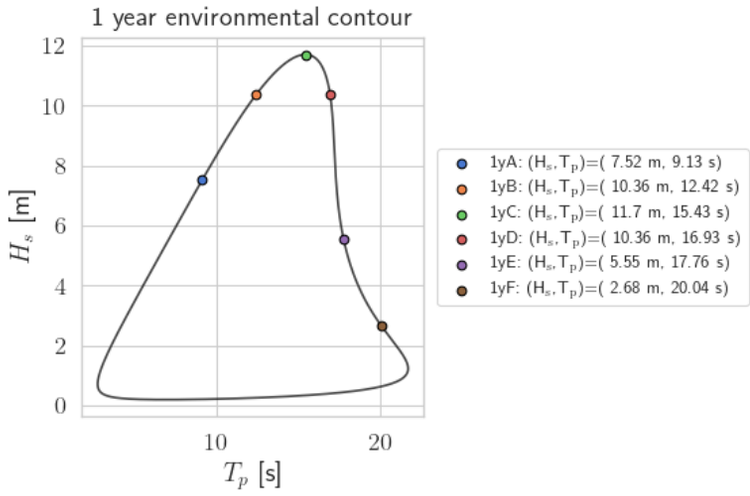

Figure B.5: Contour line 1-year extreme sea state

Table B.6: 50-year extreme sea state

#	H_s	T_p	γ
50yA	9.14	9.71	5.00
50yB	12.85	13.70	3.88
50yC	14.60	17.48	1.63
50yD	12.85	19.24	1.00
50yE	5.73	19.91	1.00
50yF	1.02	27.03	1.00

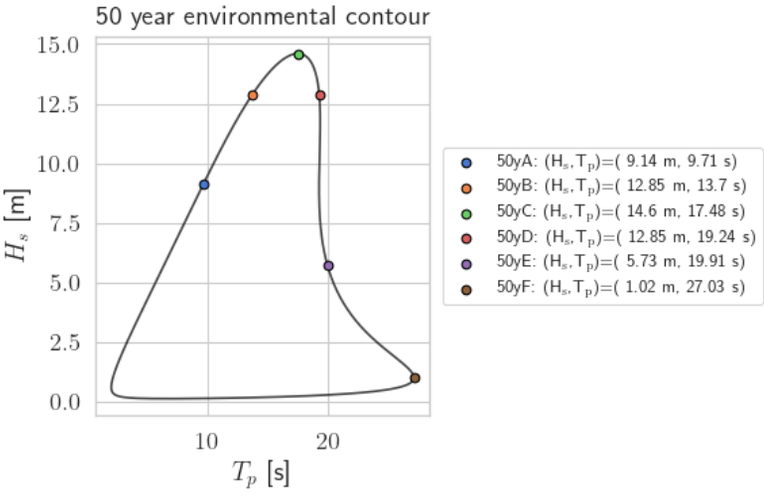

Figure B.6: Contour line 50-year extreme sea state

APPENDIX C

Model verification

This chapter includes supplementary results to those presented in chapter 9.

C.1 Panel model convergence study

In this section, the hydrodynamic coefficients for different levels of hull discretization are included. The estimated discretization errors are shown in chapter 9.

A Center tower design

Added mass

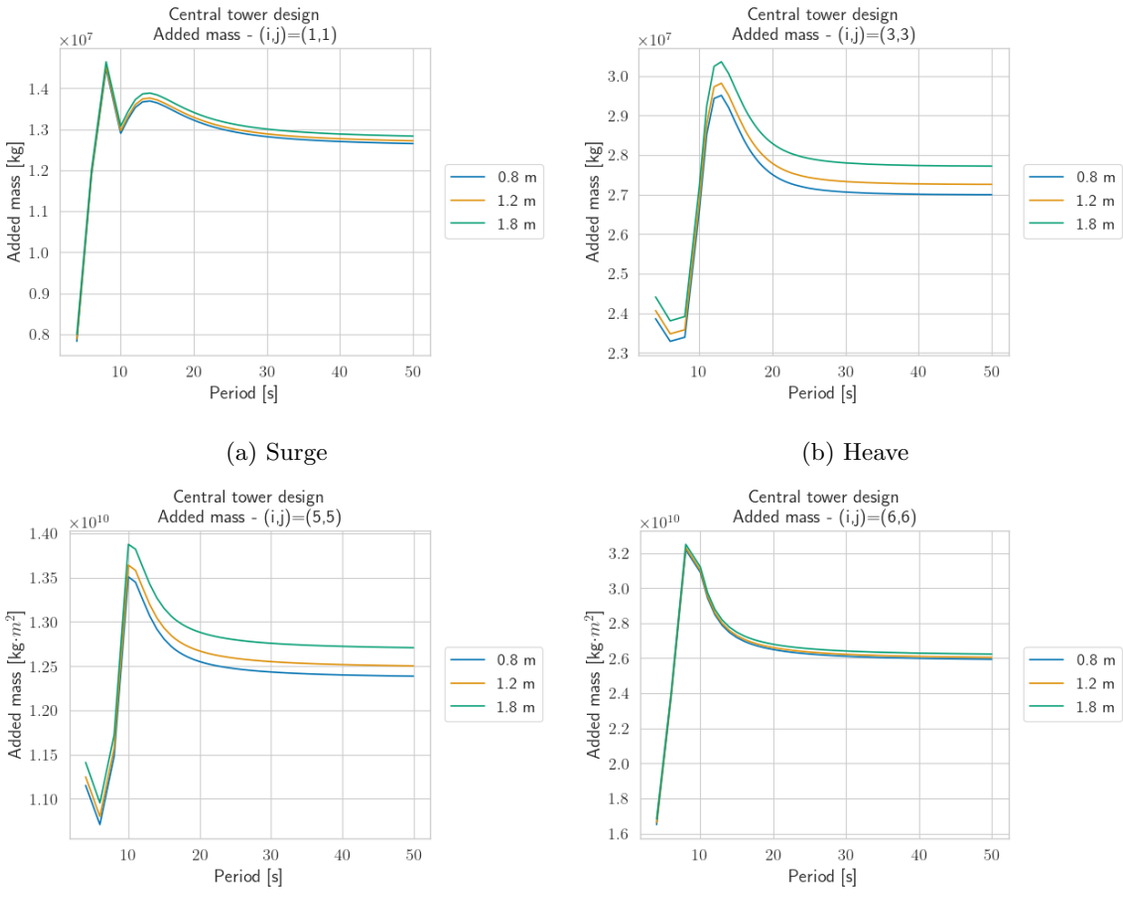

(a) Surge

(b) Heave

(c) Pitch

(d) Yaw

Figure C.1: Added mass diagonal terms

Potential damping

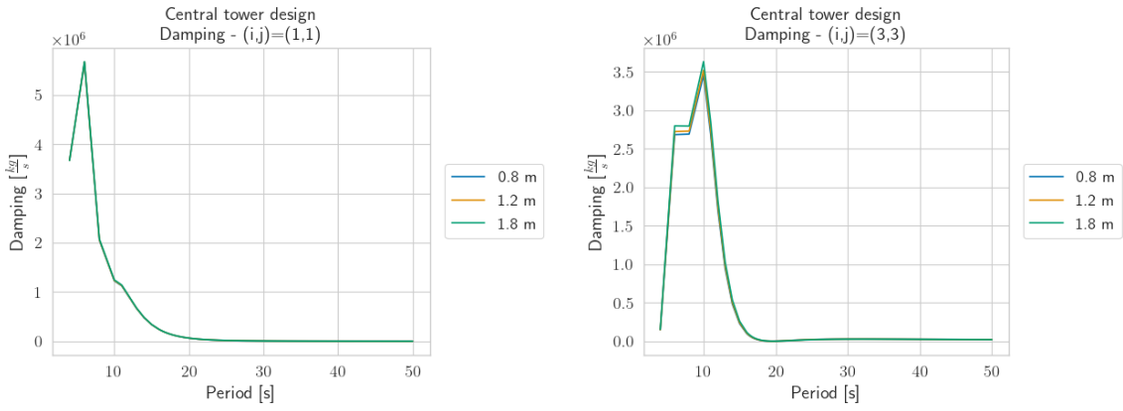

(a) Surge

(b) Heave

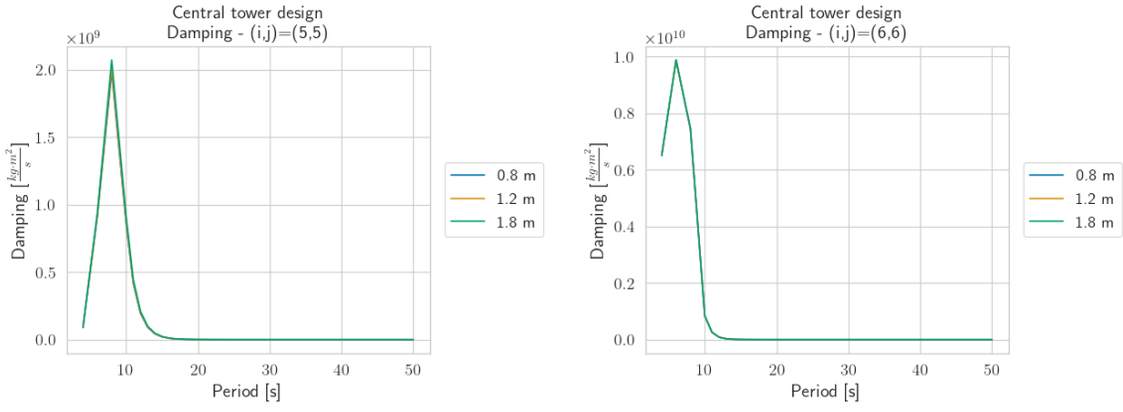

(c) Pitch

(d) Yaw

Figure C.2: Potential damping diagonal terms

Wave load excitation

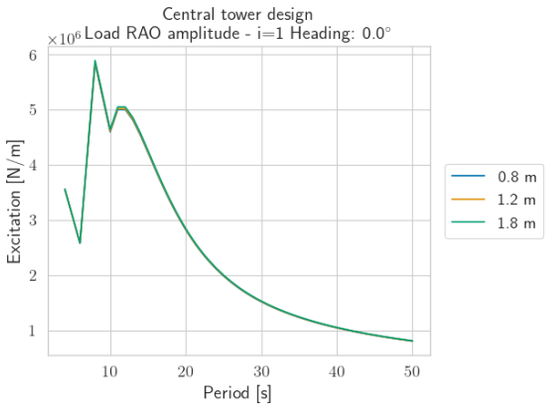

(a) Surge

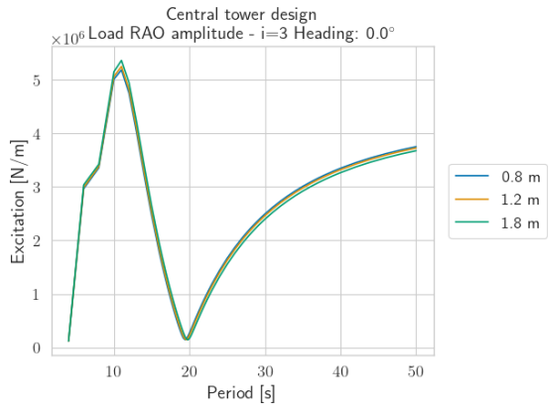

(b) Heave

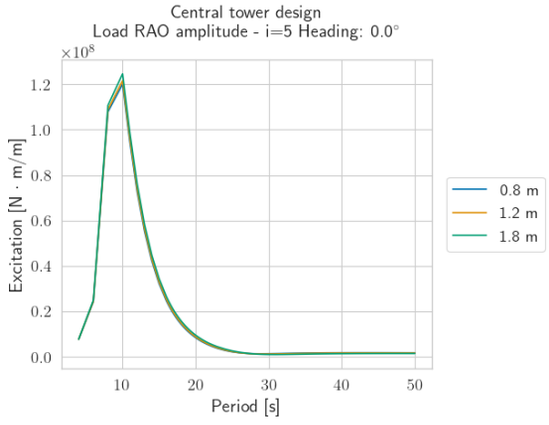

(c) Pitch

Figure C.3: First order wave load excitation transfer functions

Displacement RAOs

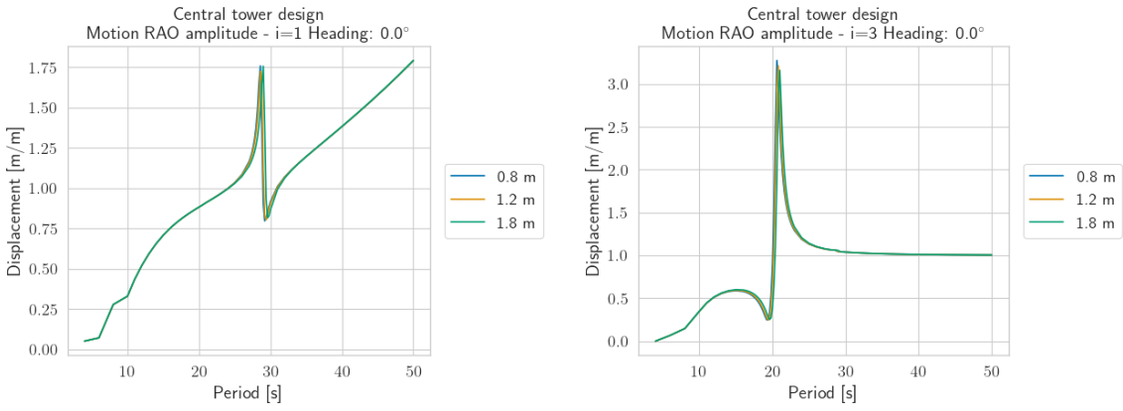

(a) Surge

(b) Heave

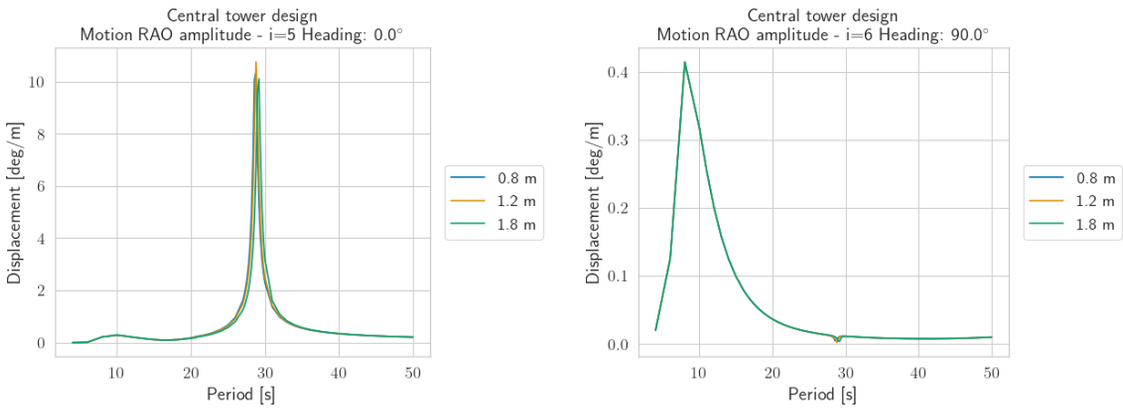

(c) Pitch

(d) Yaw

Figure C.4: Selected RAOs

B Peripheral tower design

Added mass

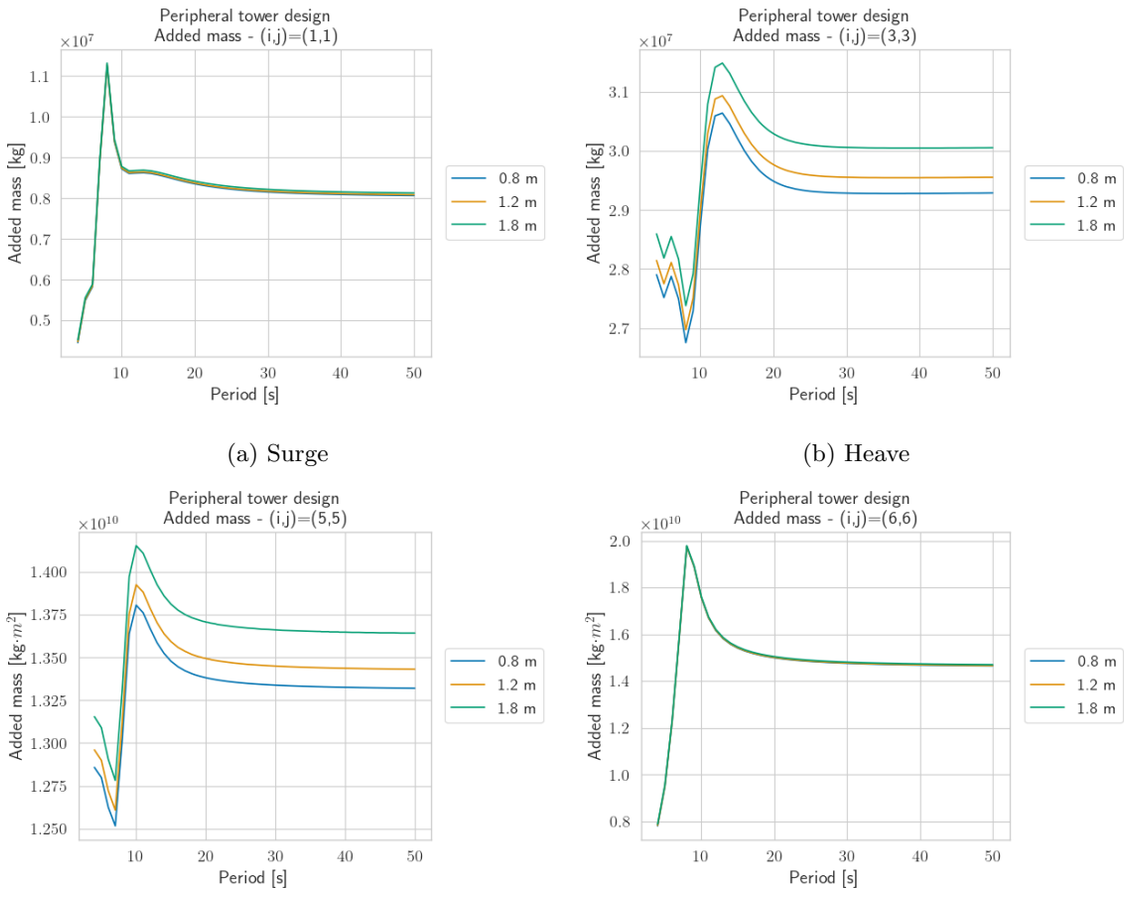

(a) Surge

(b) Heave

(c) Pitch

(d) Yaw

Figure C.5: Added mass diagonal terms

Potential damping

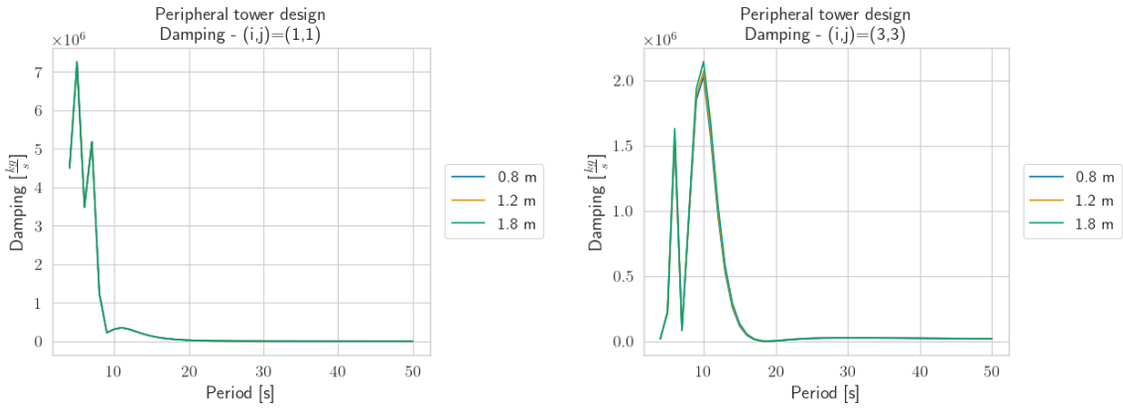

(a) Surge

(b) Heave

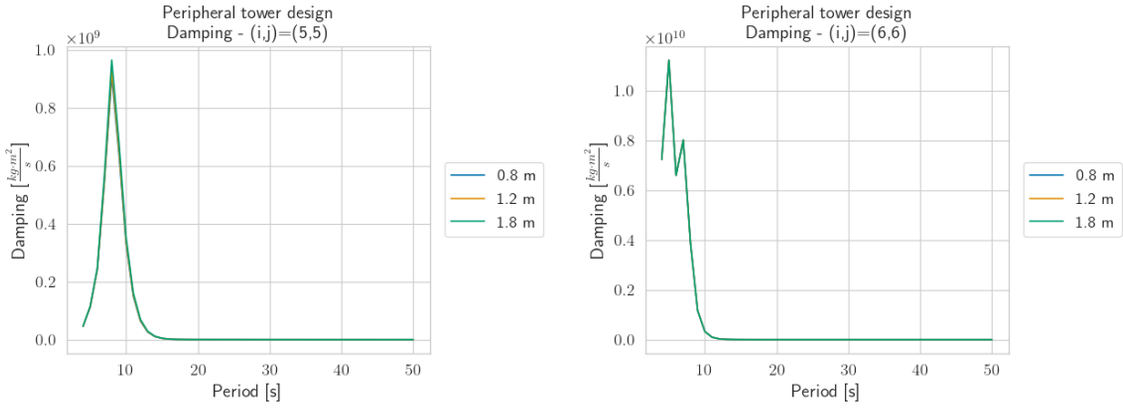

(c) Pitch

(d) Yaw

Figure C.6: Potential damping diagonal terms

Wave load excitation

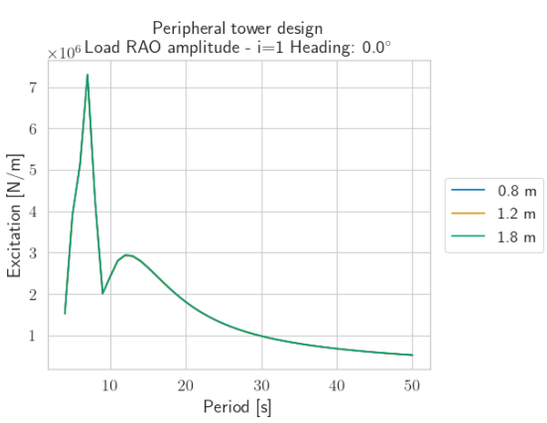

(a) Surge

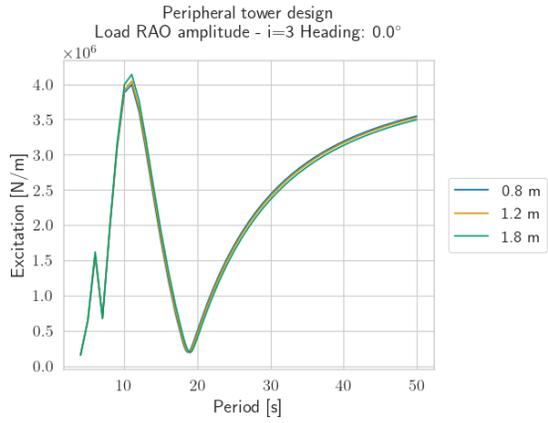

(b) Heave

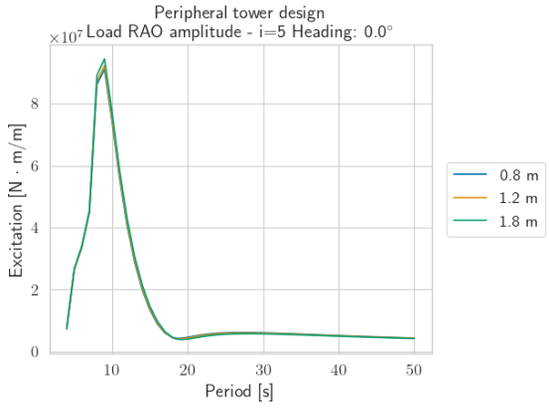

(c) Pitch

Figure C.7: First order wave load excitation transfer functions

Displacement RAOs

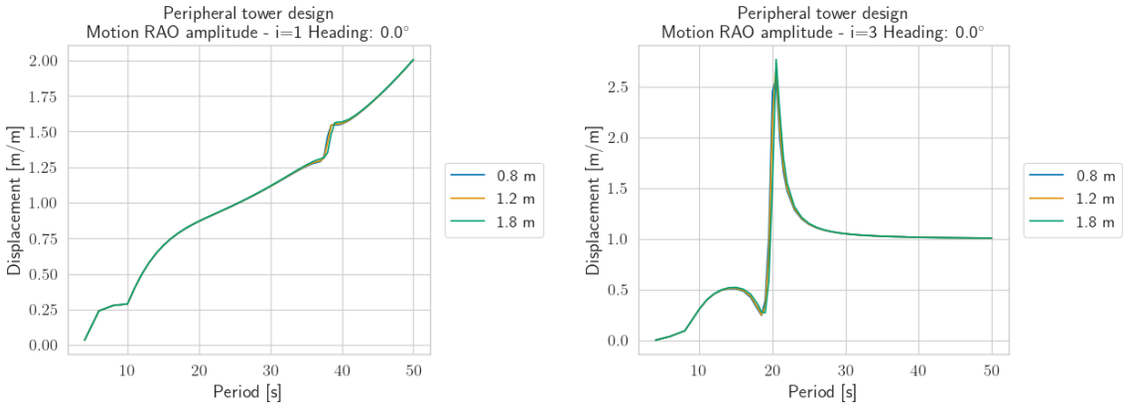

(a) Surge

(b) Heave

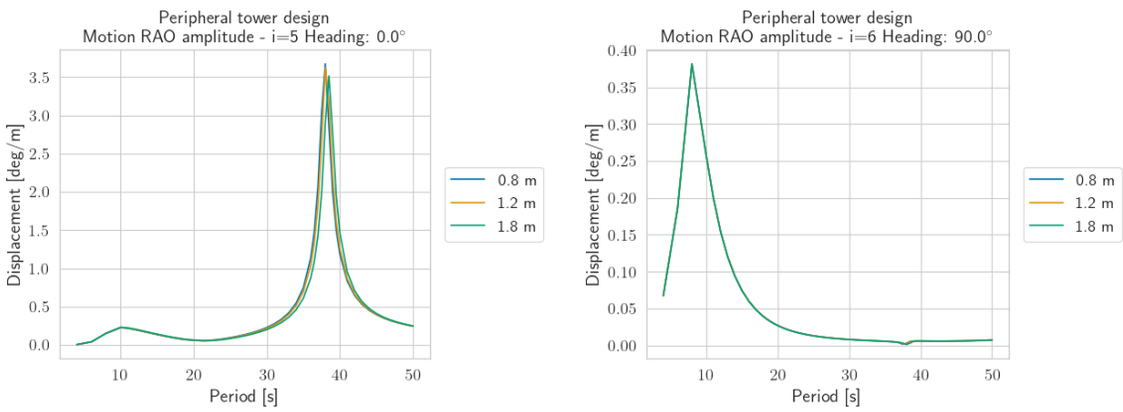

(c) Pitch

(d) Yaw

Figure C.8: Selected RAOs

C.2 Comparison with reference results

In this section, the hydrodynamic coefficients of the center tower design are compared with the reference result from IEA (2022). The results are commented on in chapter 9.

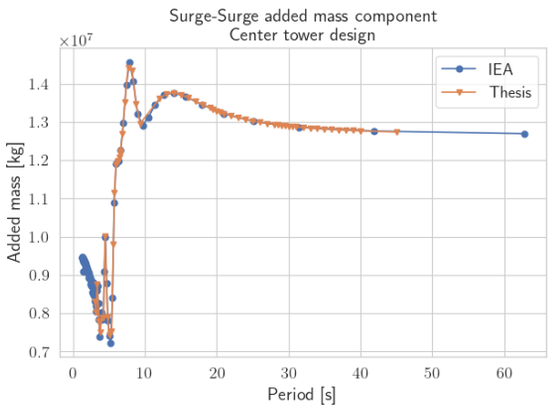

(a) Added mass

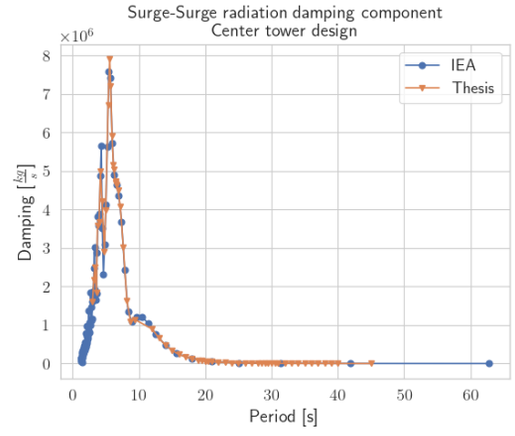

(b) Damping

Figure C.9: Added mass and damping, surge diagonal terms

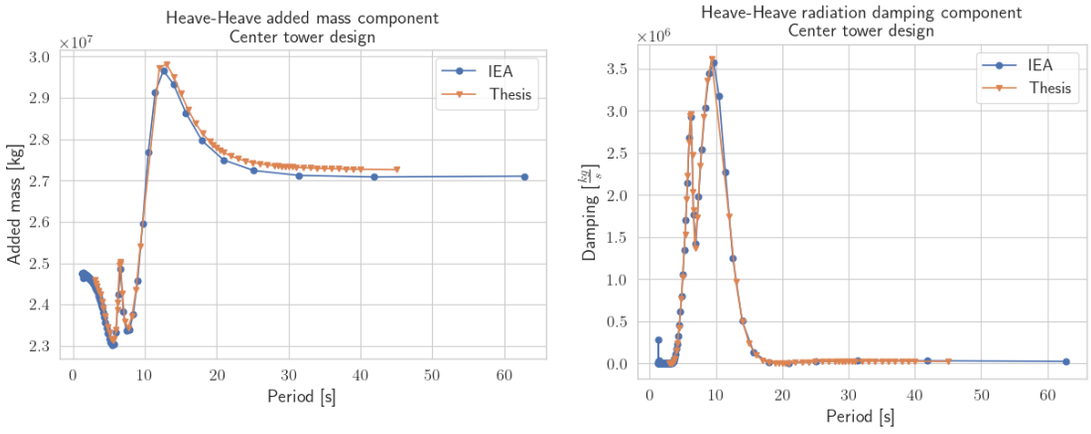

(a) Added mass (b) Damping

Figure C.10: Added mass and damping, heave diagonal terms

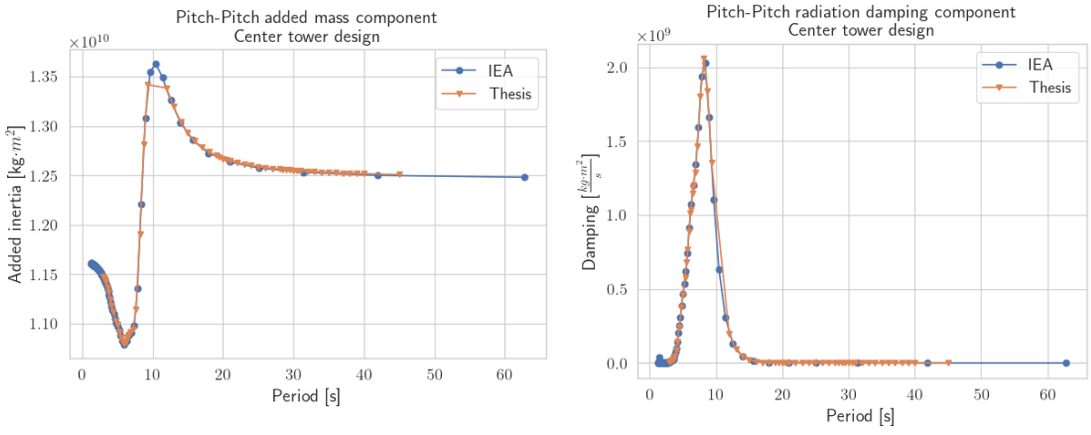

(a) Added mass (b) Damping

Figure C.11: Added mass and damping, pitch diagonal terms

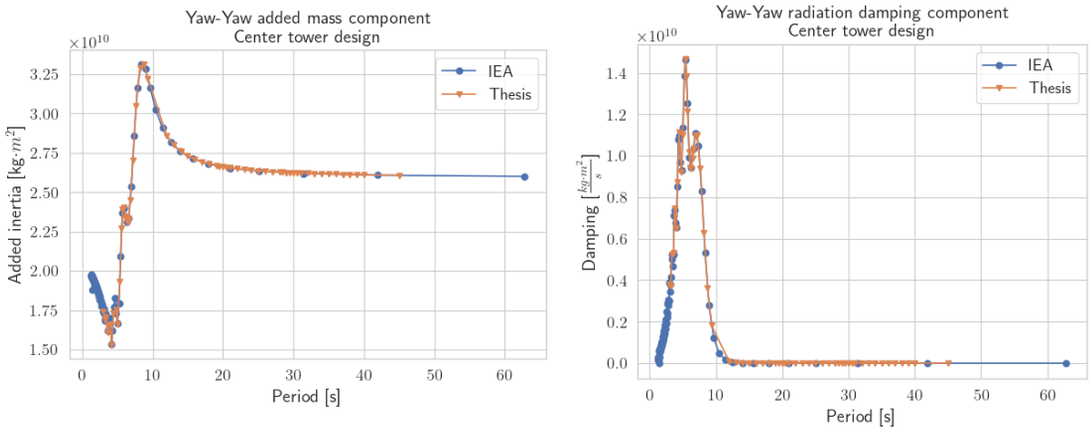

(a) Added mass (b) Damping

Figure C.12: Added mass and damping, yaw diagonal terms

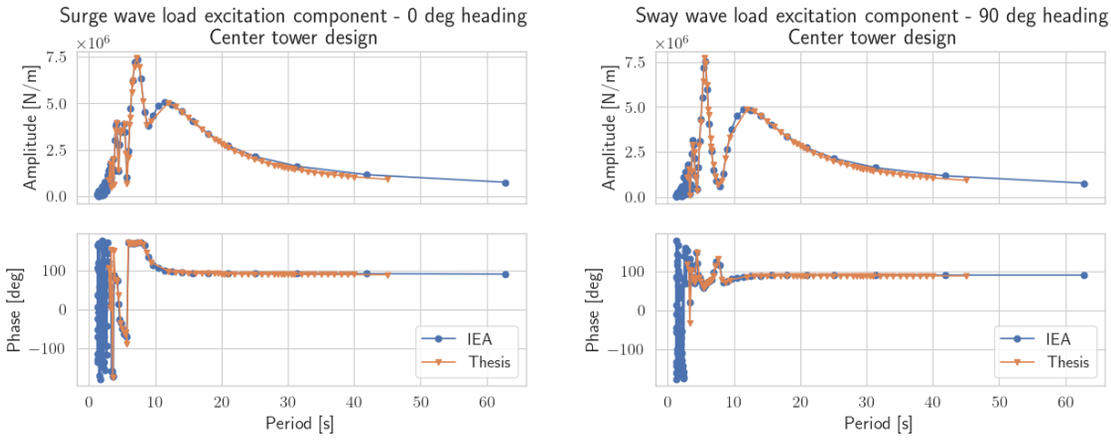

(a) Surge, 0°heading (b) Sway, 90°heading

Figure C.13: Wave load excitation

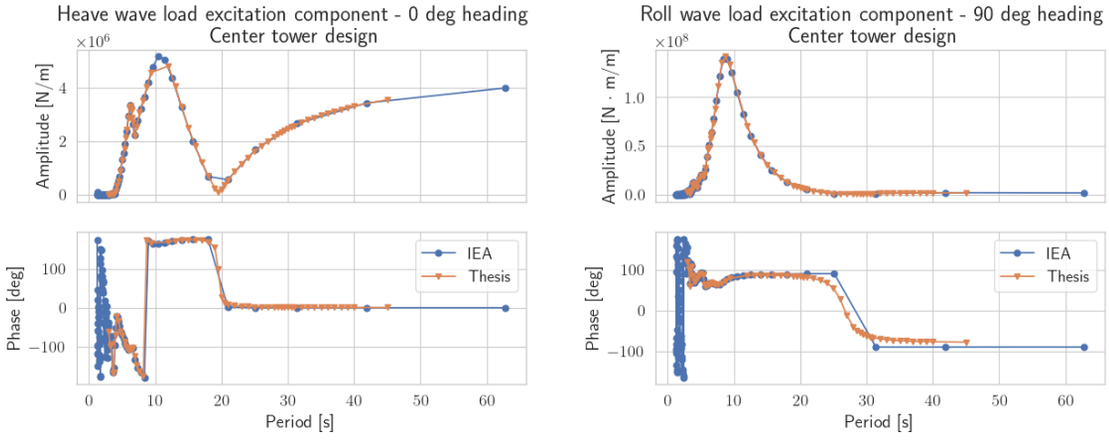

(a) Heave, 0°heading (b) Roll, 90°heading

Figure C.14: Wave load excitation

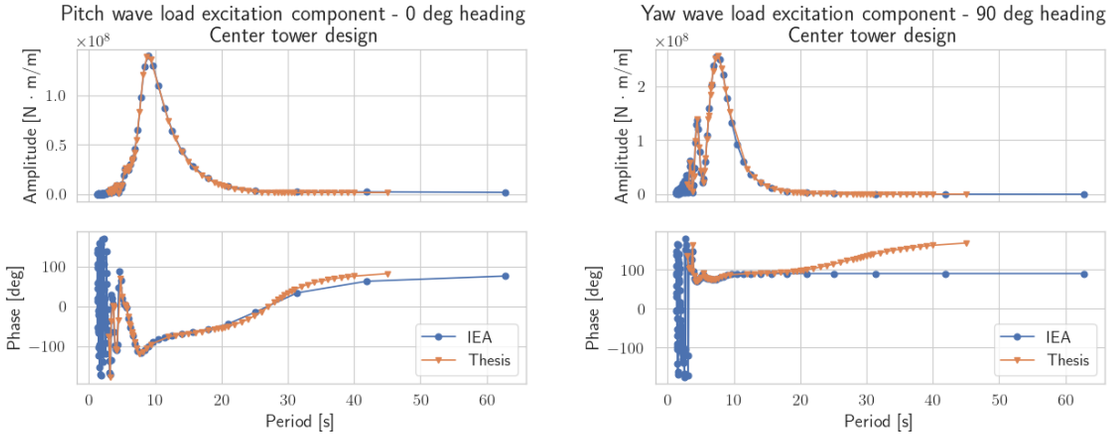

(a) Pitch, 0°heading (b) Yaw, 90°heading

Figure C.15: Wave load excitation

C.3 Time step sensitivity

In Table C.1, the results of the time-step sensitivity study are provided. For all variables and time steps, a good agreement is found.

Table C.1: Time step sensitivity study

	Time step [s]	Mean	Std.dev	Max	Min
Surge [m]	0.050	-15.904	2.901	-9.684	-21.315
	0.025	-15.895	-2.905	-9.651	-21.324
	0.010	-15.893	-2.911	-9.640	-21.336
	0.005	-15.893	-2.912	-9.631	-21.343
Heave [m]	0.050	-0.181	0.075	0.071	-0.389
	0.025	-0.181	0.075	0.071	-0.390
	0.010	-0.181	0.075	0.070	-0.390
	0.005	-0.181	0.075	0.070	-0.390
Pitch [deg]	0.050	-2.938	0.839	-1.167	-4.779
	0.025	-2.934	0.841	-1.165	-4.777
	0.010	-2.933	0.841	-1.163	-4.776
	0.005	-2.933	0.842	-1.162	-4.775
Tower bottom bending moment [MNm]	0.050	236.314	67.486	439.943	64.707
	0.025	236.054	67.631	440.142	59.943
	0.010	236.012	67.707	438.713	60.440
	0.005	236.000	67.727	438.595	60.579
Windward fairlead tension [kN]	0.050	2456.984	274.972	3051.004	1877.319
	0.025	2456.055	275.374	3053.521	1877.108
	0.010	2455.886	275.837	3056.949	1876.484
	0.005	2455.934	276.000	3056.525	1874.211
Rotor thrust [kN]	0.050	1424.951	247.127	2047.704	815.075
	0.025	1423.824	247.517	2053.771	804.203
	0.010	1423.600	247.847	2062.436	814.985
	0.005	1423.672	247.958	2062.071	816.001

C.4 Investigation of damping in regular wave tests

In this section, the results of several variations of the regular wave tests are shown. Several damping contributions are included, and the time domain results coincide with the frequency domain results for the case with linearized damping matrix from WADAM and mooring line with neglected drag contributions.

Morison model and mooring line drag

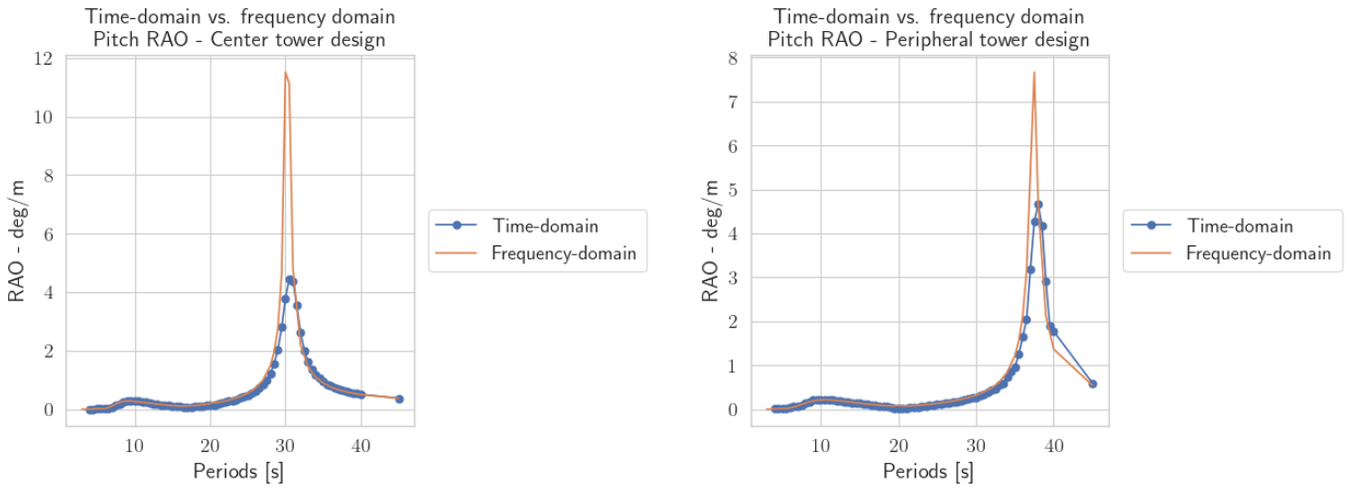

(a) Center tower concept

(b) Peripheral tower concept

Figure C.16: Frequency- and time-domain pitch RAO comparison

Drag-less mooring lines

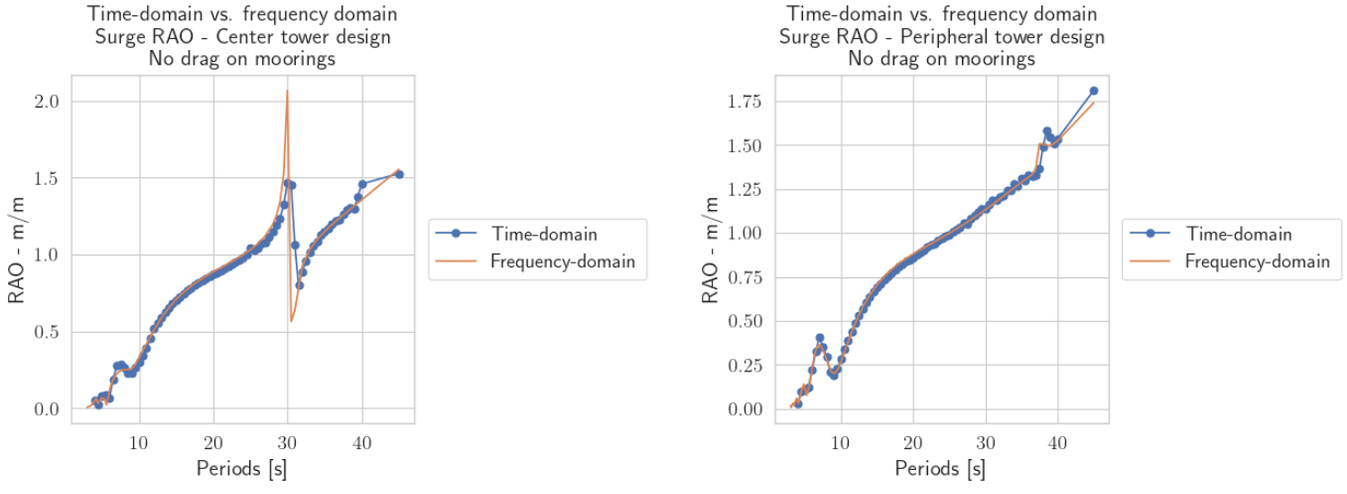

(a) Center tower concept

(b) Peripheral tower concept

Figure C.17: Frequency- and time-domain surge RAO comparison, with drag-less mooring lines

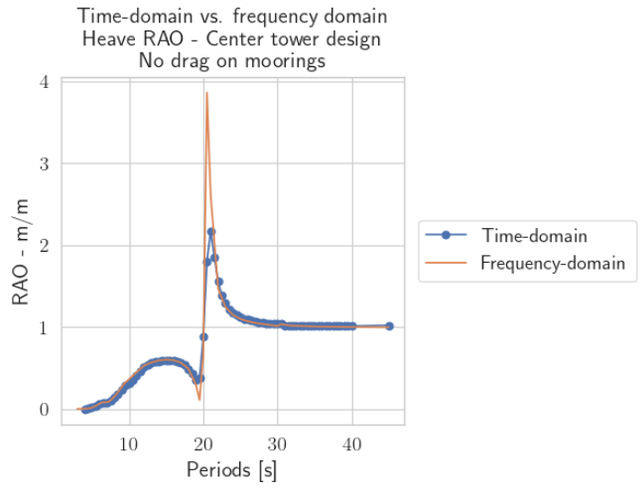

(a) Center tower concept

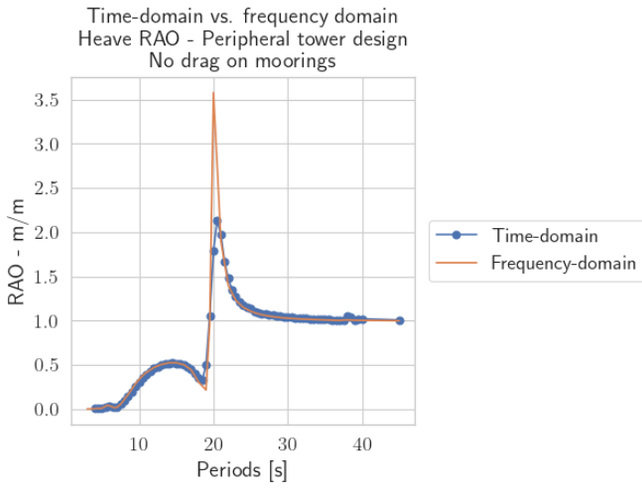

(b) Peripheral tower concept

Figure C.18: Frequency- and time-domain heave RAO comparison, with drag-less mooring lines

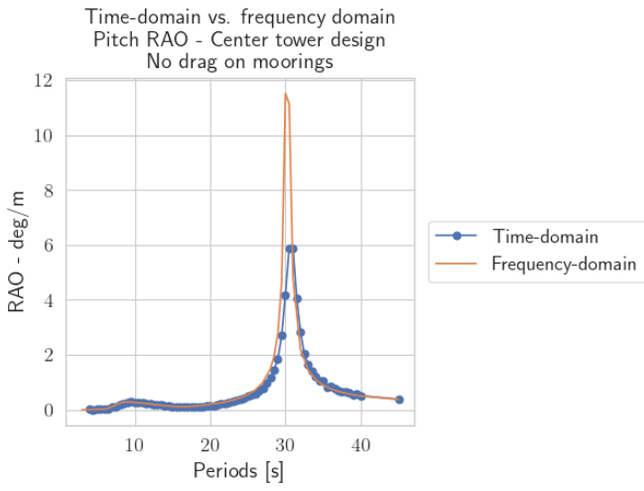

(a) Center tower concept

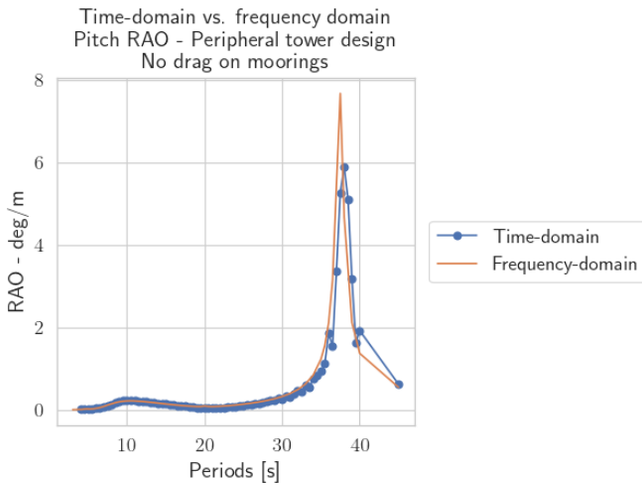

(b) Peripheral tower concept

Figure C.19: Frequency- and time-domain pitch RAO comparison, with drag-less mooring lines

Linearized damping matrix from WADAM

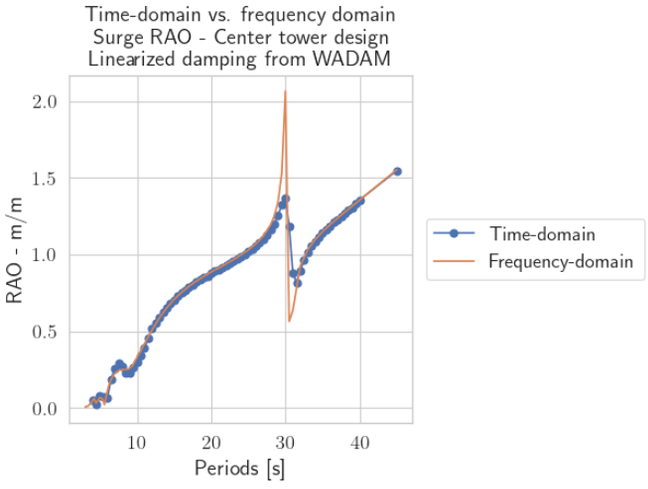

(a) Center tower concept

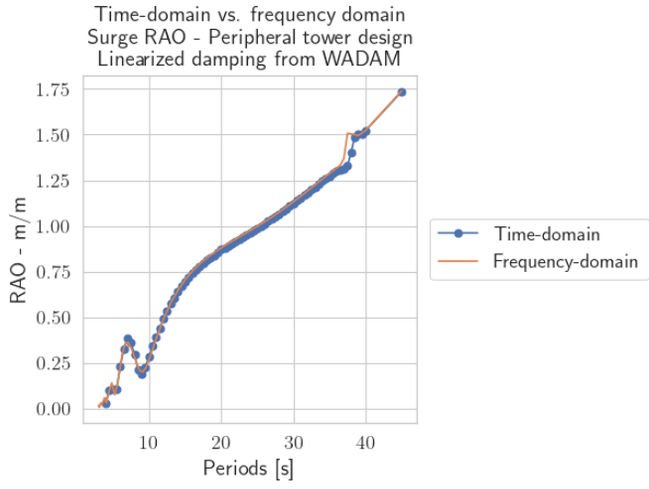

(b) Peripheral tower concept

Figure C.20: Frequency- and time-domain surge RAO comparison, with linearized damping matrix

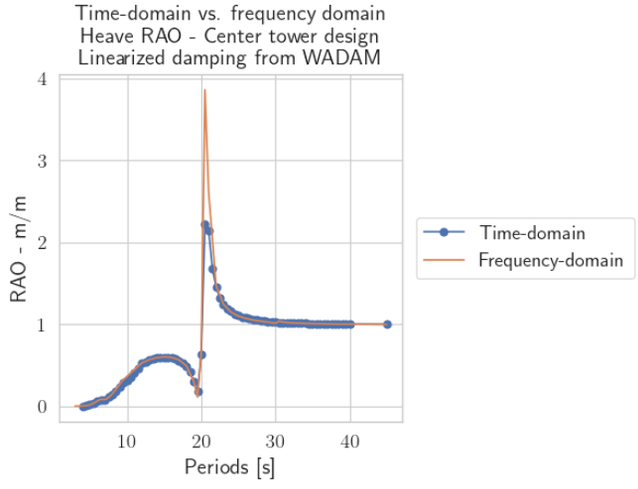

(a) Center tower concept

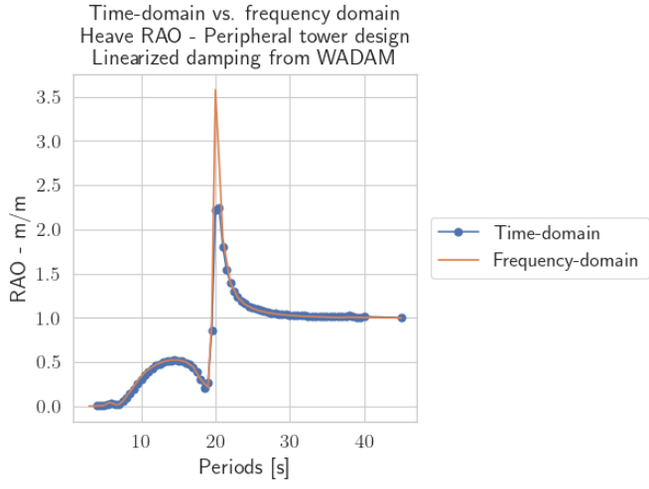

(b) Peripheral tower concept

Figure C.21: Frequency- and time-domain heave RAO comparison, with linearized damping matrix

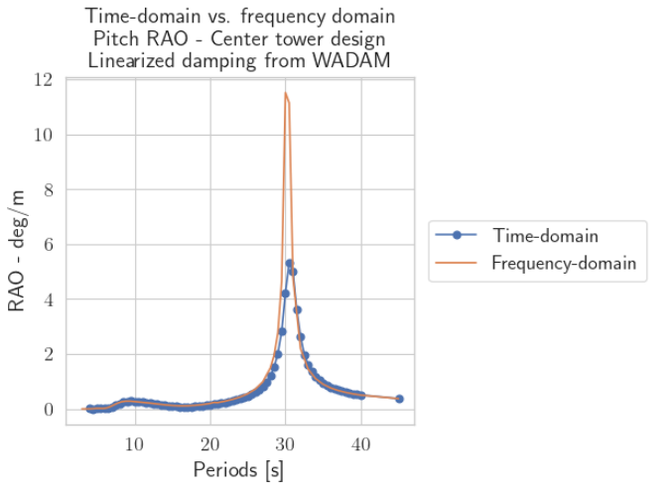

(a) Center tower concept

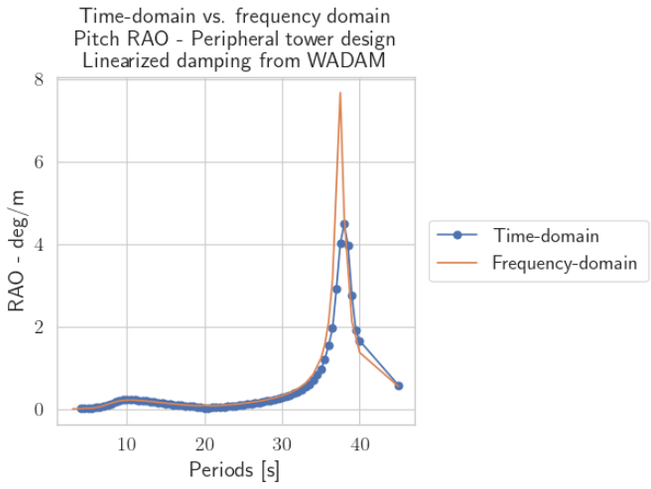

(b) Peripheral tower concept

Figure C.22: Frequency- and time-domain pitch RAO comparison,, with linearized damping matrix

Linearized damping matrix from WADAM and drag-less mooring lines

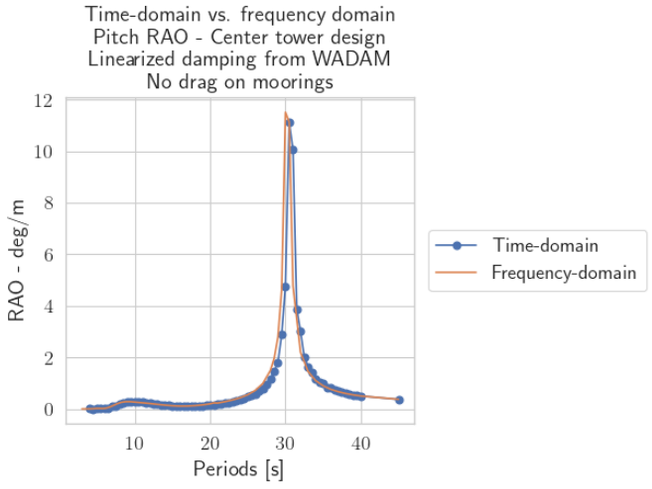

(a) Center tower concept

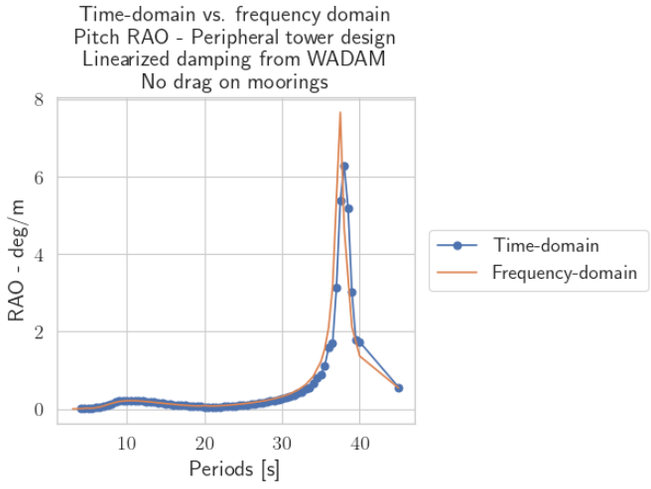

(b) Peripheral tower concept

Figure C.23: Frequency- and time-domain pitch RAO comparison, with linearized damping matrix from WADAM and drag-less mooring lines

APPENDIX D

Frequency discretization for sloshing

In Figure D.1, the effect of internal tank sloshing on the global surge motion is apparent. The extreme responses are linked to the singular added mass behavior at internal tank natural sloshing frequencies.

As this behavior is clearly non-physical, the extreme peaks are removed from the dataset. This must be categorized as an "engineering"-approach to the problem.

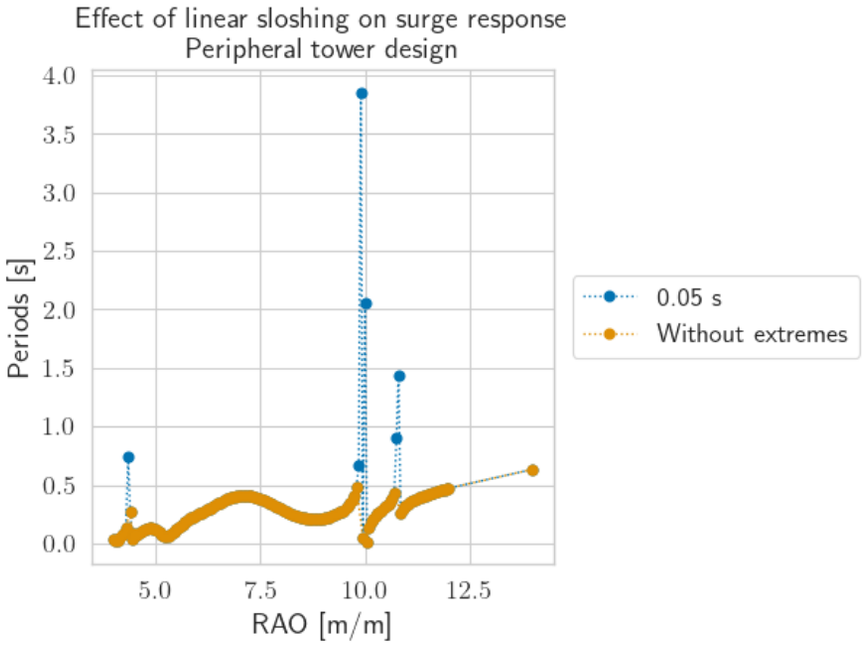

Figure D.1: Removal of sloshing response extreme values

Due to the number of frequencies is limited to 60 for second-order analysis in WADAM, a coarser discretization must be used to be able to cover the full range of important frequencies. In one chooses constant step lengths, one risks not capturing the violent sloshing that happens at distinct periods. Therefore, a very fine discretization with ΔT =0.05 s was applied to capture all important peaks. Further, a set of distinct periods was selected which gives the same approximate response. In this manner, the same dynamics are captured using 20 % of the periods.

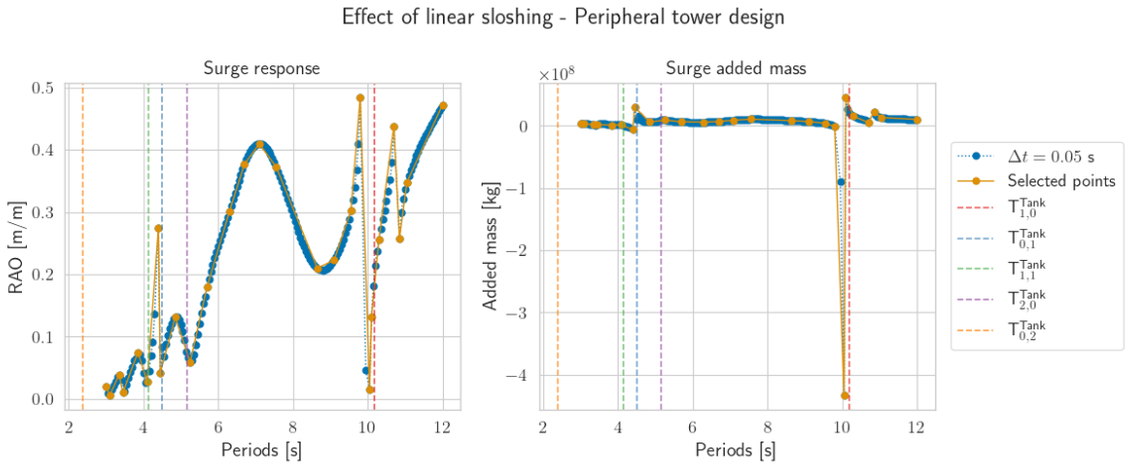

Figure D.2: Frequency discretization for sloshing, Peripheral tower design

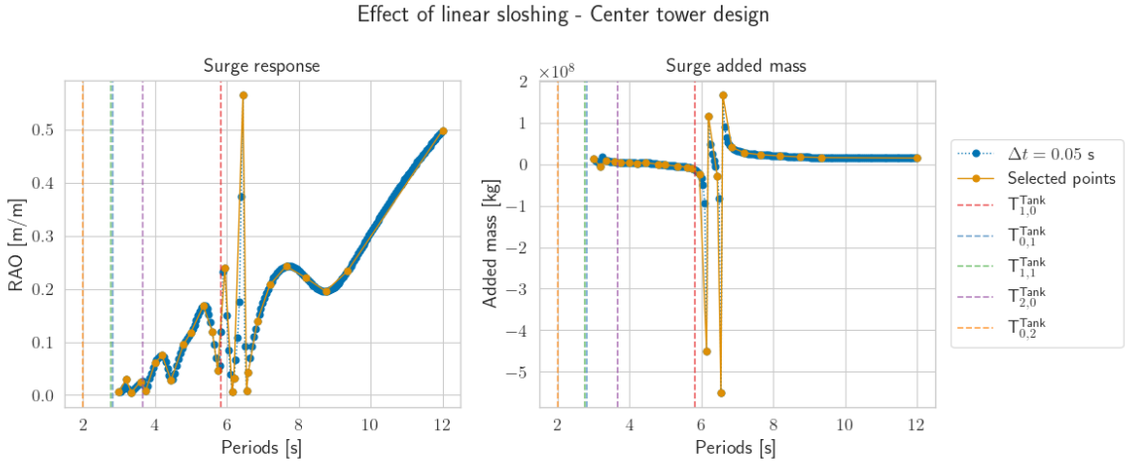

Figure D.3: Frequency discretization for sloshing, Center tower design

APPENDIX E

Linear sloshing effect on heave added mass

Figure E.1 documents the erroneous increase in heave added mass when the dynamic method for internal fluid effects is applied. It is concluded in the thesis that the results from the quasi-static method should be applied instead.

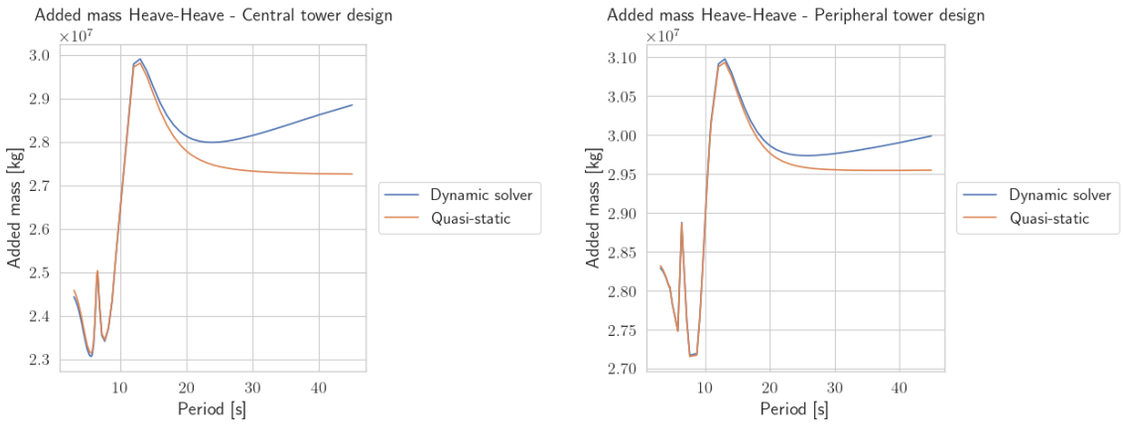

(a) Center tower design

(b) Center tower design

Figure E.1: Comparison of total added mass using quasi-static and dynamic methods

APPENDIX F

Constant wind controller test

This appendix shows the constant wind tests performed for a fixed rotor. Tests performed with floating substructures are included in the main body.

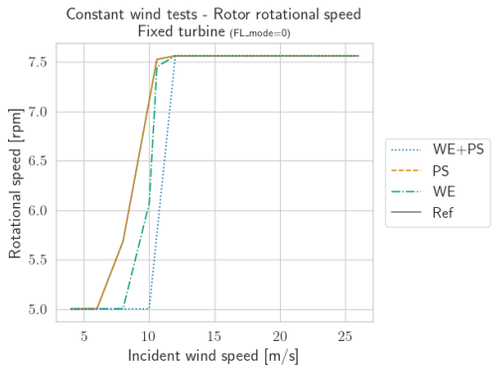

(a) Rotor speed

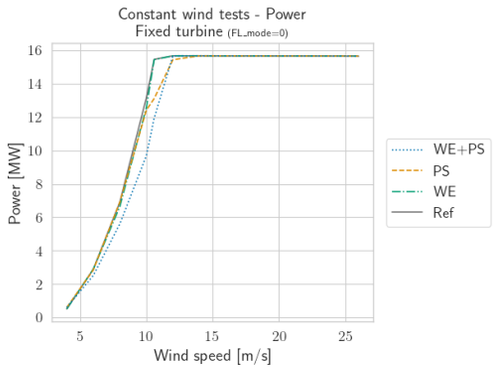

(b) Power

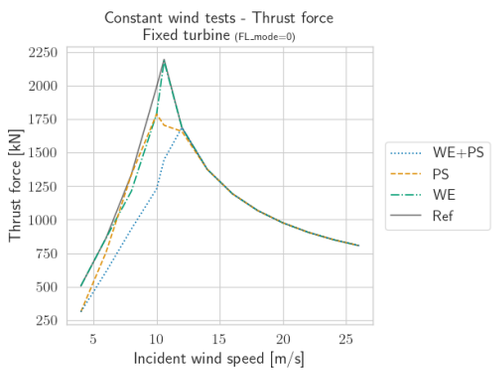

(c) Thrust

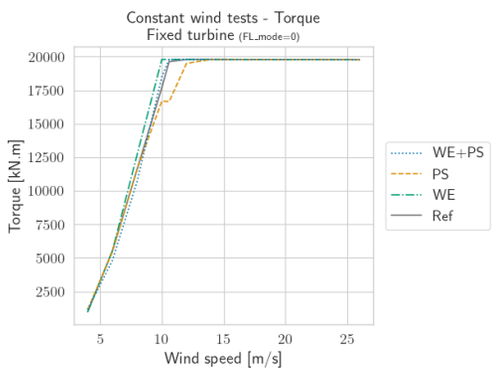

(d) Torque

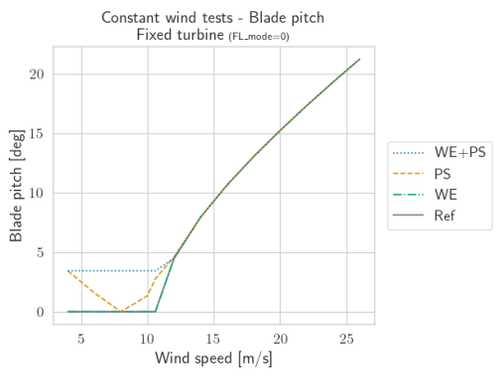

(e) Blade pitch

Figure F.1: Constant wind test for a fixed RNA-tower configuration. "WE" refers to wind speed estimation and "PS" refers to pitch saturation.

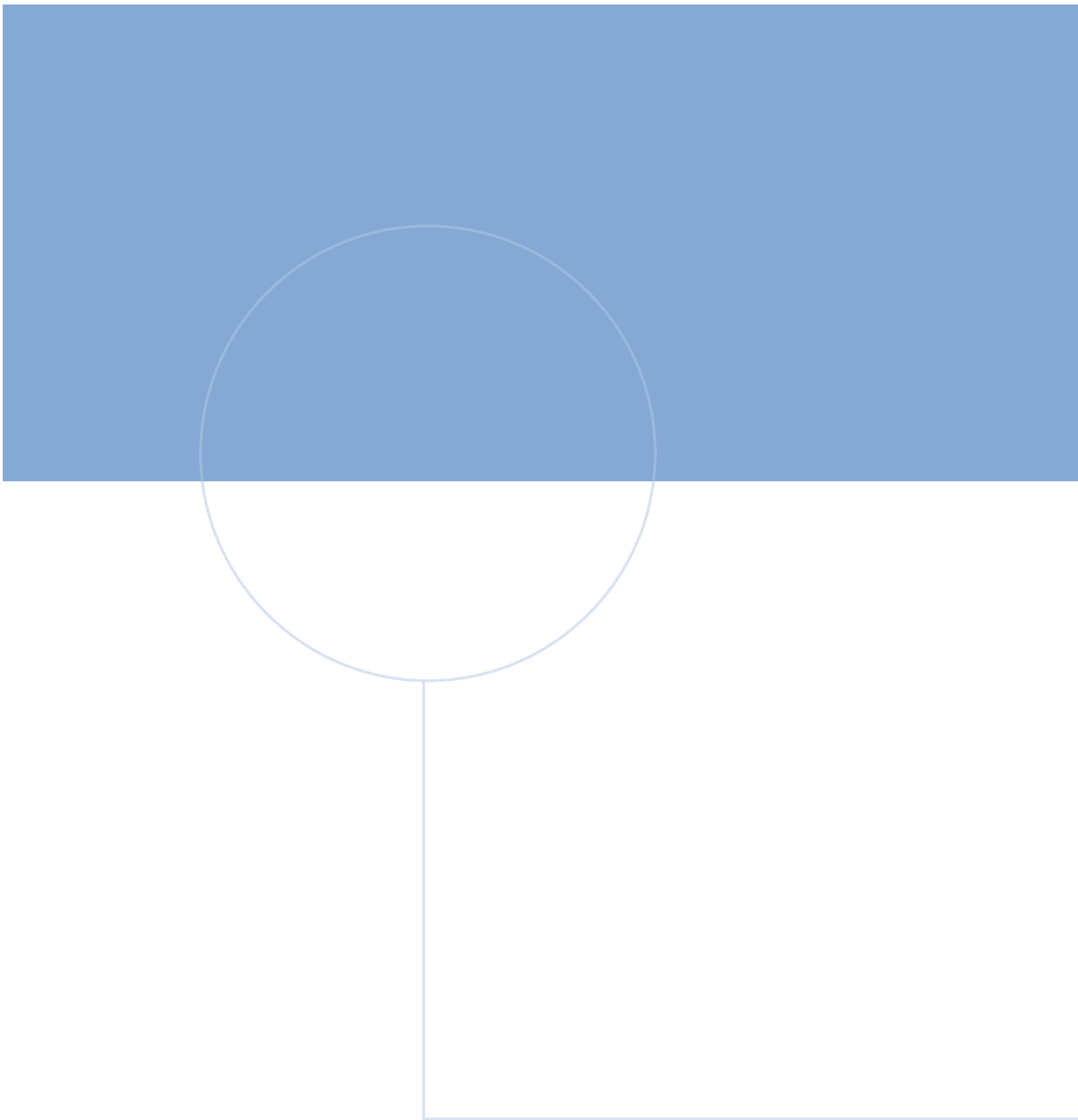

NTNU

Norwegian University of
Science and Technology